



TUM School of Life Sciences

Numerical simulation of CH₄ and its stable isotopologues on regional and global scale

Anna-Leah Nickl

Vollständiger Abdruck der von der TUM School of Life Sciences
der Technischen Universität München
zur Erlangung des akademischen Grades einer
Doktorin der Naturwissenschaften (Dr. rer. nat.)
genehmigten Dissertation.

Vorsitzende: Prof. Dr. Annette Menzel

Prüfer der Dissertation:

1. Prof. Dr. Hans Peter Schmid
2. apl. Prof. Dr. Robert Sausen

Die Dissertation wurde am 30.11.2021 bei der Technischen Universität München eingereicht
und durch die TUM School of Life Sciences am 06.05.2022 angenommen.

Numerical simulation of CH₄ and its
stable isotopologues on regional and
global scale

Anna-Leah Nickl

Zusammenfassung

Methan (CH_4) ist das zweitwichtigste anthropogen beeinflusste Treibhausgas in der Atmosphäre. Es wird an der Erdoberfläche aus anthropogenen und natürlichen Quellen emittiert und hauptsächlich durch das Hydroxylradikal (OH) in der Troposphäre entfernt. Aufgrund seiner relativ kurzen atmosphärischen Lebensdauer birgt die Verringerung der CH_4 Emissionen ein großes Potenzial für die Eindämmung des Klimawandels. Die atmosphärische Wachstumsrate von CH_4 stagnierte zwischen 2000 und 2007 und nimmt seit 2007 weiter zu. Hauptursachen dafür könnten Emissionen aus biogenen Quellen (vor allem Feuchtgebiete, Landwirtschaft, Mülldeponien) oder thermogenen Quellen (vor allem die Produktion fossiler Brennstoffe) sein. Darüber hinaus könnten auch Änderungen der OH-Konzentrationen eine wichtige Rolle spielen. Die vorliegende Modellstudie soll unser Verständnis des globalen CH_4 Budgets verbessern. Die Arbeit ist in drei Teile gegliedert, in denen regionale und globale numerische Modelle zur Simulation des atmosphärischen CH_4 und seiner stabilen Isotopenverhältnisse in Bezug auf Kohlenstoff-13 ($\delta^{13}\text{C}(\text{CH}_4)$) verwendet werden.

Der erste Teil befasst sich mit unserem derzeitigen Verständnis lokaler anthropogener CH_4 Emissionen aus Punktquellen und der atmosphärischen CH_4 Verteilung auf regionaler Ebene. Er umfasst die Entwicklung eines Vorhersagesystems zur Unterstützung der Flugplanung der CoMet 1.0 Messkampagne, die im Jahr 2018 stattfand. Ziel von CoMet war die Quantifizierung von CH_4 Emissionsflüssen aus Kohleminen-Belüftungsschächten im USCB (Polen). CH_4 wird mit dem online dreifach "genesteteten" globalen und regionalen Klima-Chemie-Modell MECO(3) simuliert. Die Modellergebnisse werden im Hinblick auf flugzeuggetragenen Messungen analysiert. MECO(3) kann die Ausbreitung im Windschatten von Punktquellen, vertikale integrierte Werte und vertikale Gradienten von CH_4 gut simulieren. Dies zeigt die Zuverlässigkeit der untersuchten Emissionskataster. Außerdem liefert MECO(3) bis zu vier Tage im Voraus vernünftige Vorhersage-Ergebnisse.

Je nach Entstehungsprozess von CH_4 , variiert auch die $\delta^{13}\text{C}(\text{CH}_4)$ Signatur. $\delta^{13}\text{C}(\text{CH}_4)$ kann deshalb dabei helfen, atmosphärisches CH_4 auf einzelne Quellen zurückzuführen. Die Simulation von $\delta^{13}\text{C}(\text{CH}_4)$ mit MECO(3) und deren Vergleich mit CoMet 1.0 Messungen zeigen, dass die Variabilität von $\delta^{13}\text{C}(\text{CH}_4)$ auf regionaler Ebene gut verstanden wird und, dass Veränderungen im Vergleich zum Hintergrund $\delta^{13}\text{C}(\text{CH}_4)$ auf Kohleminenemissionen zurückzuführen sind. Im Vergleich mit Beobachtungen konnte eine durchschnittliche $\delta^{13}\text{C}(\text{CH}_4)$ Signatur von -51 ‰ für die Emissionen aus Kohleminen im USCB bestimmt werden.

Auf globaler Ebene wurde der CH_4 Anstieg seit 2007 im Hinblick auf negativer werdende $\delta^{13}\text{C}(\text{CH}_4)$ Werte analysiert. Diese weisen auf einen veränderten relativen Beitrag der einzelnen CH_4 Quellen zum erneuten CH_4 Anstieg hin. Sensitivitätssimulationen mit dem "state-of-the-art" globalen Klima-Chemie-Modell EMAC, die insbesondere die Rolle von unkonventioneller Gasförderung ("fracking") untersuchen, zeigen, dass der globale CH_4 -Anstieg nicht allein auf diese Emissionen zurückzuführen ist. Stattdessen spielen biogene Emissionen eine wichtige Rolle. Darüber hinaus reagiert $\delta^{13}\text{C}(\text{CH}_4)$ sehr empfindlich auf Änderungen der Emissionen aus Biomassebrennen, was die Bedeutung der in den Simulationen verwendeten Emissionsabschätzungen unterstreicht.

Der Einfluss einer OH Konzentrationssenkung auf das globale $\delta^{13}C(\text{CH}_4)$ ist eher gering. Darüber hinaus wirkt sich die troposphärische latitudinale OH Verteilung nicht auf den relativen Beitrag der verschiedenen Quellen zum globalen Anstieg von CH_4 und dem globalen mittleren Oberflächen- $\delta^{13}C(\text{CH}_4)$ aus. Mögliche Rückkopplungen auf OH wurden jedoch nicht berücksichtigt und müssen in künftigen Simulationen einbezogen werden.

Abstract

Atmospheric methane (CH_4) is the second most important greenhouse gas in terms of anthropogenic forcing. It is emitted at the Earth's surface from anthropogenic and natural sources, and mainly removed by the hydroxyl radical (OH) in the troposphere. Due to its relatively short atmospheric lifetime, the reduction of CH_4 emissions has a great potential for climate change mitigation. Atmospheric CH_4 growth rate stagnated between 2000 and 2007 and continues to grow since 2007. The major drivers could be emissions from biogenic (mainly wetlands, agriculture, waste) or thermogenic (mainly fossil fuel production) sources. In addition, changes in OH might play an important role. The presented modelling study aims to improve our understanding of the global CH_4 budget. The thesis is divided into three parts, applying regional and global numerical models for the simulation of atmospheric CH_4 and its stable isotopic ratio with respect to 13-carbon ($\delta^{13}\text{C}(\text{CH}_4)$).

The first part addresses our current understanding of local anthropogenic CH_4 point source emissions and the atmospheric CH_4 distribution on regional scales. It comprises the development of a forecast system supporting the flight planning of a measurement campaign in 2018, called CoMet 1.0. CoMet aimed to quantify CH_4 emissions from coal mining ventilation shafts in the USCB (Poland). CH_4 is simulated with the online three-fold nested global and regional chemistry-climate model MECO(3). Model results are analysed with respect to CoMet airborne observations. MECO(3) simulates the dispersion downwind of point sources, vertical integrated values and vertical gradients of CH_4 reasonably well. This implies that the investigated emission inventories are reliable. Moreover, MECO(3) delivers reasonable forecast results up to forecast day four.

Since $\delta^{13}\text{C}(\text{CH}_4)$ depends of the type of CH_4 formation, it can help to constrain atmospheric CH_4 to individual sources. Simulations of $\delta^{13}\text{C}(\text{CH}_4)$ with MECO(3) and comparisons with results of CoMet 1.0 measurements show that we understand the $\delta^{13}\text{C}(\text{CH}_4)$ variability on regional scales, and that changes relative to the background $\delta^{13}\text{C}(\text{CH}_4)$ are attributable to coal mining emissions. In comparison with observations, an average $\delta^{13}\text{C}(\text{CH}_4)$ signature for coal mining emissions in the USCB of -51‰ was found.

On the global scale, the CH_4 rise has been analysed with respect to a $\delta^{13}\text{C}(\text{CH}_4)$ decline since 2007, indicating changes in the relative contribution of CH_4 sources to the renewed CH_4 rise. Sensitivity simulations with the state-of-the-art global chemistry climate model EMAC, which particularly investigate the role of shale gas, show that the global CH_4 increase is not attributable to shale gas emissions alone. Instead, biogenic emissions play an important role. Additionally, $\delta^{13}\text{C}(\text{CH}_4)$ is very sensitive to changes in biomass burning emissions, which underlines the importance of their emission estimates used in the simulations.

The influence of an OH reduction on the global $\delta^{13}\text{C}(\text{CH}_4)$ is rather small. Moreover, the latitudinal tropospheric OH distribution does not impact the relative contribution of different emission source categories to the global rise CH_4 and the global mean surface $\delta^{13}\text{C}(\text{CH}_4)$. However, potential feedbacks on OH were not considered and need to be included in future simulations.

Publications

Parts of this thesis were published in the following article:

- Nickl, A.-L., Mertens, M., Roiger, A., Fix, A., Amediek, A., Fiehn, A., Gerbig, C., Galkowski, M., Kerckweg, A., Klausner, T., Eckl, M., and Jöckel, P.: Hindcasting and forecasting of regional methane from coal mine emissions in the Upper Silesian Coal Basin using the online nested global regional chemistry–climate model MECO(n) (MESSy v2.53), *Geosci. Model Dev.*, 13, 1925–1943, <https://doi.org/10.5194/gmd-13-1925-2020>, 2020.

Contribution of the thesis' autor to the article: Anna-Leah Nickl, Mariano Mertens and Patrick Jöckel planned and carried out the forecast simulations. Anna-Leah Nickl performed the hindcast simulations, analyzed the model results and wrote the article.

Contents

Zusammenfassung	i
Abstract	iii
1 Introduction	1
1.1 Motivation	1
1.2 Methodology and approach	4
2 Scientific background	7
2.1 Methane in the atmosphere	7
2.1.1 Sources of methane	9
2.1.2 Sinks of methane	10
2.2 Methane isotopologues	13
2.2.1 Isotope chemistry	13
2.2.2 Stable isotopologues of methane	16
3 Description of the models and forecast system	21
3.1 The global chemistry climate model EMAC	22
3.1.1 The modular earth submodel system MESSy	22
3.1.2 The EMAC model system	23
3.1.3 The submodel CH4	23
3.2 The global/regional n-times nested chemistry climate model MECO(n) . .	25
3.3 The forecast system	26
4 Hind- and forecasting of regional methane emissions with MECO(n)	29
4.1 The CoMet Campaign	30
4.2 Model setup	32
4.2.1 The MECO(3) setup for the CoMet 1.0 simulations	32
4.2.2 Methane tracer	33
4.2.3 Simulations of the CoMet 1.0 campaign	34
4.3 Evaluation of the model skill	36
4.3.1 Observations	36
4.3.2 Evaluation of the analysis simulation	38

4.3.3	Evaluation of the forecast skill	48
4.4	Summary and outlook	52
5	Simulation of $\delta^{13}\text{C}(\text{CH}_4)$ in coal mining emission with the regional model MECO(3)	55
5.1	Simulation of stable isotopologues with MECO(n)	56
5.1.1	Model Setup	56
5.1.2	Results and discussion of the ANA.ISO simulations	58
5.2	Comparison to CoMet 1.0 observations	60
5.2.1	Sensitivity simulations w.r.t. the $\delta^{13}\text{C}_{\text{CH}_4}$ of coal mining emissions in the USCB	62
5.3	Summary	66
6	Simulation of the recent methane increase and the corresponding $\delta^{13}\text{C}(\text{CH}_4)$ decrease with EMAC	69
6.1	Regional segmentation of methane isotopologues and base simulation	71
6.1.1	Model setup and isotopologues	71
6.1.2	Results and discussion of the base simulations	83
6.2	Sensitivities towards shale gas emissions	96
6.2.1	SDISO sensitivity simulations	99
6.2.2	Influence of tropospheric lifetime on the global mean $\delta^{13}\text{C}$	109
6.3	Sensitivity simulations towards OH variations	112
6.4	Summary and outlook	114
7	Summary, discussion and conclusions	117
7.1	Summary of the methodology	118
7.2	Discussion and conclusions	119
	Bibliography	125
	A Appendix	143

List of Figures

1.1	Global methane mixing ratios and growth rate (1984-2020)	2
2.1	Diagram of the main methane sources categories	11
2.2	Stable isotopes of carbon	14
2.3	$\delta^{13}\text{C}(\text{CH}_4)$ and $\delta\text{D}(\text{CH}_4)$ source signatures	19
3.1	Overview: COSMO/MESSy model domains of MECO(3) used for CoMet 1.0	26
3.2	Initial and boundary data exchange of MECO(n)	27
3.3	Illustration of MECO(n) forecast system	28
4.1	Position of coal mining ventilation shafts and their CH_4 emission rates in the USCB	32
4.2	Illustration of submodels used for the two methane tracers $\text{CH}_4\text{-FX}$ and PCH_4	34
4.3	Snapshot of the methane forecasts during CoMet 1.0	35
4.4	Flight routes and pressure at flight level for JIG data J1 and J2	38
4.5	Flight routes and pressure at flight level for D-FDLR data P4 and P5	39
4.6	Taylor diagram summarizing the statistical analysis of MECO(3)	41
4.7	Comparison of MECO(3) model results with CHARM-F observations	42
4.8	Comparison of MECO(3) model results with JIG observations	44
4.9	Comparison of MECO(3) model results with JIG observations (vertical profiles)	44
4.10	Comparison of MECO(3) model results with D-FDLR observations	46
4.11	D-FDLR CH_4 mixing ratios of P2 and MECO(3) model output sampled above the PBLH	47
4.12	Actual skill scores S_V of the MECO(3) forecasts with respect to CoMet 1.0 observations	49
4.13	Actual skill scores S_C of the MECO(3) forecasts with respect to CoMet 1.0 observations	50
4.14	Expected skill score of the MECO(3) forecasts	51
5.1	Results of the ANA.ISO simulation: CH_4 mixing ratios and three different $\delta^{13}\text{C}$ along P4	59
5.2	Keeling plot of the three different ANA.ISO simulations	60
5.3	Observed and simulated (ANA.ISO) $\delta^{13}\text{C}$ versus CH_4 mixing ratios.	62

5.4	Results of “ANA.ISO simulation (-50 ‰)”, (-51 ‰) and flask samples . . .	65
5.5	Results of “ANA.ISO simulation (-51 ‰)”, #2 (-51 ‰), #3 (USCB) and flask samples	66
6.1	Global methane and atmospheric $\delta^{13}\text{C}$ (1998-2007)	71
6.2	Tropospheric methane lifetime with respect to transient OH field or OH climatology (SDISO)	75
6.3	Global $\delta^{13}\text{C}$ distribution of biomass burning and livestock emissions based on C-4 plant distribution	77
6.4	Global $\delta^{13}\text{C}$ distribution of wetland emissions	79
6.5	Transient flux-weighted $\delta^{13}\text{C}$ source signatures in SDISO-base simulations .	81
6.6	Global $\delta^{13}\text{C}$ and δD distribution of fossil fuel emissions	82
6.7	Map showing CH_4 and $\delta^{13}\text{C}(\text{CH}_4)$ ground-based sampling sites	84
6.8	Global averaged surface $\delta^{13}\text{C}$ of SDISO-base-c / -v.	85
6.9	Global distribution of surface $\delta^{13}\text{C}$ (SDISO-base-c average: 2000-2015) . .	87
6.10	Global distribution of surface methane mixing ratios and $\delta^{13}\text{C}$ (SDISO-base average: 2000-2015)	88
6.11	Observed and simulated surface zonal mean methane mixing ratio and $\delta^{13}\text{C}$ (SDISO-base average: 2000-2015)	89
6.12	Zonal mean methane mixing ratio and $\delta^{13}\text{C}$ of (SDISO-base-c average: 2000-2015)	89
6.13	SDISO-base globally averaged surface CH_4	91
6.14	Comparison of EDGAR v5.0 inventory and EMAC-y-03 CH_4 emissions . .	91
6.15	SDISO-base CH_4 emissions per sector	92
6.16	Taylor diagram of the statistical analysis of the SDISO-base-c simulation .	93
6.17	Zonal mean CH_4 of SDISO-base simulation (2000-2007, 2008-2014 and difference)	96
6.18	Zonal mean $\delta^{13}\text{C}$ of SDISO-base simulation (2000-2007, 2008-2014 and difference)	97
6.19	Map of US shale plays	98
6.20	$\delta^{13}\text{C}$ result of sens sensitivity studies	101
6.21	$\delta^{13}\text{C}$ result of gfd sensitivity studies	104
6.22	$\delta^{13}\text{C}_{surf}^{sim}$ of SDISO base and sensitivity simulations compared to observations	105
6.23	$\delta^{13}\text{C}_{surf}^{sim}$ of SDISO base and gfd sensitivity simulations compared to observations	106
6.24	Comparison of CH_4 mixing ratios at different US sampling sites	107
6.25	Results of the OH sensitivity simulations	114

List of Tables

2.1	Isotopic standards	16
2.2	KIE of methane sink reactions	20
4.1	Overview: CoMet 1.0 instrumentation and models	31
4.2	Overview: CoMet 1.0 observations used for the evaluation of MECO(3) . .	37
4.3	Results of the statistical analysis of MECO(3)	40
5.1	Isotopic source signatures in ANA.ISO simulation setup	58
5.2	Sensitivity simulations of ANA.ISO	63
6.1	Fluxes of individual methane sources used in the SDISO-base simulation .	73
6.2	Isotopic global mean signatures of methane sources used in SDISO-base-c and SDISO-base-v	80
6.3	Nomenclature and overview model setup (SDISO simulations)	83
6.4	Sensitivity studies I - III (-sens)	100
6.5	Sensitivity studies IV - VI (-gfed)	103
6.6	Tropospheric lifetimes of individual methane sources of the SDISO simulations	111

Acronyms

A-GCM	General Circulation Model of the Atmosphere
AIRSPACE	Aircraft Remote Sensing of Greenhouse Gases with combined Passive and Active instruments
CAM	Crassulacean Acid Metabolism
CCM	Chemistry Circulation Model
CCMI	Chemistry-Climate Model Initiative
CoMet	Carbon Dioxide and Methane Mission
COSMO	Consortium for Small Scale Modelling
CRDS	Cavity Ring Down Spectroscopy
ECMWF	European Centre for Medium-Range Weather Forecasts
EMAC	ECHAM/MESSy Atmospheric Chemistry
EMPA	Eidgenössische Materialprüfungs- und Forschungsanstalt (Swiss Federal Laboratories for Materials Science and Technology)
ENSO	El Niño-Southern Oscillation
ESM	Earth System Model
GCM	General Circulation Model
HPC	High Performance Computing
INSTAAR	Institute of Arctic and Alpin Research
IPDA	Integrated Path Differential Absorption
JAS	Jena Air Sampler
KIE	Kinetic Isotopic Effect

LGM	Last Glacial Maximum
MECO(n)	MESSyified ECHAM and COSMO models nested n times
MERLIN	Methane Remote Sensing Lidar Mission
MESSy	Modular Earth Submodel System
NIWA	National Institute of Water and Atmospheric Research
NMHCs	non-methane hydrocarbons
NOAA	National Oceanic and Atmospheric Adminis- tration
O-GCM	General Circulation Model of the Ocean
PBLH	Planetary Boundary Layer Height
SWP	stratospheric water vapour
UAV	unmanned aerial vehicle
UHei	Heidelberg University, Germany
USCB	Upper Silesian Coal Basin
VPDB	Vienna Pee Dee Belemnite
VSMOW	Vienna Standard Mean Ocean Water

Symbols

$\delta^{13}\text{C}$	short for $\delta^{13}\text{C}(\text{CH}_4)$: delta value concerning ^{13}C in CH_4 relative to the standard VPDB
δD	short for $\delta\text{D}(\text{CH}_4)$: delta value concerning D in CH_4 relative to the standard VSMOW
CH4_FX	CH4 submodel tracer for CH_4
CH4_12C	CH4 submodel tracer for isotopologue $^{12}\text{CH}_4$
CH4_13C	CH4 submodel tracer for isotopologue $^{13}\text{CH}_4$
CH4_D0	CH4 submodel tracer for isotopologue CH_4
CH3_D1	CH4 submodel tracer for isotopologue CH_3D
$\tau_{\text{CH}_4}(\text{OH})$	CH_4 lifetime with respect to OH

Chapter 1

Introduction

1.1 Motivation

Methane (CH_4) is one of the most abundant organic trace gases, which plays an important role in atmospheric chemistry. Next to water vapour (H_2O) and carbon dioxide (CO_2), it is an effective greenhouse gas, having a direct radiative forcing of about 0.61 W m^{-2} (1750–2011 RF, Etminan et al., 2016). Furthermore, atmospheric CH_4 affects the abundance of other greenhouse gases and thereby contributes to an additional indirect radiative forcing (Myhre et al., 2013). It is an important sink of the hydroxyl radical (OH), the major oxidant of pollutants and greenhouse gases in the troposphere (Crutzen, 1995; Lelieveld et al., 2004). OH is also the major sink of methane. Moreover, the oxidation of CH_4 produces stratospheric water vapour (SWP), which in turn influences global surface temperatures on decadal scales (Solomon et al., 2010).

Since pre-industrial times atmospheric CH_4 has more than doubled, whereby the global average mixing ratio increased from 695 ppb (Etheridge et al., 1998) to a present level of 1873.4 ppb (Dlugokencky et al., 2020, mixing ratio in January 2020). The increase is accompanied by growing human activity (mainly agriculture, waste management and fossil fuel exploitation), and can be partially attributed to emissions from these activities. Next to anthropogenic sources (currently about 60 % of the total emissions, Saunio et al., 2020), CH_4 is also emitted from natural sources, such as wetlands, wild animals, volcanoes, oceans, termites and permafrost. Emissions from wetlands are the largest natural source and account for about one third of the total CH_4 emissions (Saunio et al., 2020). Moreover, a considerable amount of CH_4 is also emitted from biomass burning, which is both, anthropogenically and naturally induced.

Growing Earths' human population and the emerging role of anthropogenic activities will likely increase the emissions of CH_4 and impact global climate change. In addition, future global warming will presumably feedback in further emissions from wetlands and thawing permafrost and gas hydrates (Gedney et al., 2004; Dean et al., 2018; Nisbet et al., 2019). Since the atmospheric lifetime of CH_4 ranges between only 8 to 10 years (Prinn et al., 2005; Jöckel et al., 2006; Prather et al., 2012; Frank, 2018), it is relatively quickly

removed from the atmosphere. Reducing CH_4 emissions is therefore an attractive target for mitigating global warming (Dlugokencky et al., 2011). To do so, a precise knowledge of the individual sources and their emission fluxes is essential.

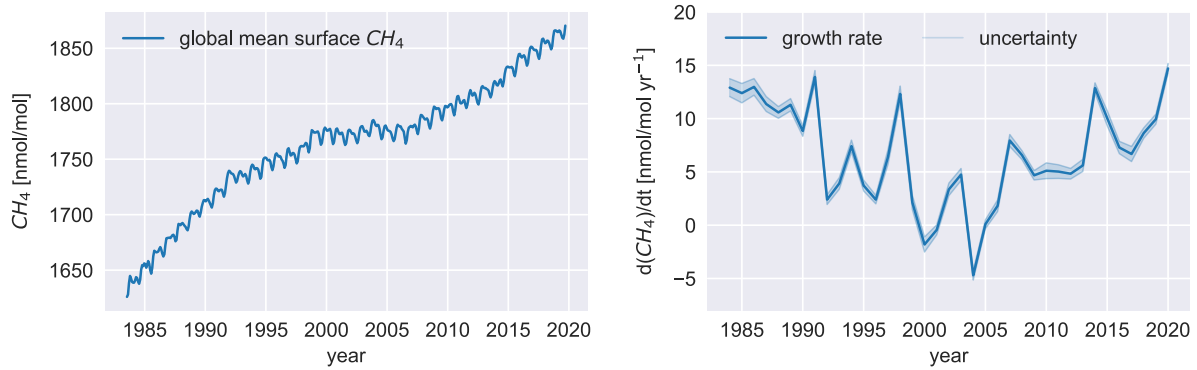


Figure 1.1: Global averaged monthly marine near surface methane mixing ratio (left panel) and annual growth rate (right panel) between 1984 and 2020 derived from https://gml.noaa.gov/ccgg/trends_ch4/ (Dlugokencky et al., 2020).

Figure 1.1 shows the evolution of the global average CH_4 mixing ratio over the last decades. Mixing ratios increased until 2000 (see left panel), whereas between 2000 and 2007 the atmospheric growth rate (right panel) stagnated. After 2007 CH_4 mixing ratios increased with a considerable growth rate of 12.7 ± 0.5 ppb/year in 2014 (Nisbet et al., 2019). The reasons for the stagnation and the renewed rise after 2007 are still unknown and debated in the literature. Until today, large uncertainties appear in the estimates of the individual source emission fluxes. Emission inventories differ from each other, and estimates of the so called bottom-up and top-down approaches deviate strongly (bottom-up: $576 \text{ Tg}(\text{CH}_4)/\text{yr}$ [550-594] and top-down: $737 \text{ Tg}(\text{CH}_4)/\text{yr}$ [594-881], Saunio et al., 2020, see Chapter 2 for an explanation on the top-down and bottom-up approaches). Moreover, uncertainties in the atmospheric OH concentration (the major sink of CH_4) exist (Nicely et al., 2020; Zhao et al., 2020).

Understanding the global methane budget requires precise emission flux estimates and a good representation of the CH_4 chemistry and physics in chemistry climate models. Long-term monitoring, as well as global and regional atmospheric observations help to identify and quantify different CH_4 sources. Accurate measurements of strong point source emissions are quite feasible, but still subject to uncertainties. Moreover, we lack comprehensive observations of diffuse emissions, e.g. from wetlands or due to leakage from fossil fuel exploitation, transport and usage. Furthermore, due to its high reactivity and associated very short lifetime, the concentration and distribution of OH in the atmosphere is highly variable, which makes it difficult to calculate the total methane loss based on measurements. To close the gap of uncertainties in the estimates of emission fluxes and OH concentration, and to better constrain atmospheric observations, regional and global numerical models are used.

A powerful tool for tracing back CH₄ emissions and identifying the sources of the recent global increase, is the study of stable isotopes. Sources of CH₄ can be categorized according to the type of formation (biogenic, thermogenic and pyrogenic). Depending on this type of formation, the ratio between light and heavy isotopes in a CH₄ sample (i.e. ¹³C/¹²C and D/¹H) differs. The isotopic composition of a sample is expressed relative to a standard (VPDB¹ for carbon and VSMOW² for hydrogen isotopes) in a so called “delta notation”, i.e. $\delta^{13}\text{C}$ and δD for carbon and hydrogen, respectively. Biogenic emissions (e.g. from wetlands, agriculture, waste, wild animals, termites, permafrost) have relatively negative $\delta^{13}\text{C}(\text{CH}_4)$ signatures. The $\delta^{13}\text{C}(\text{CH}_4)$ signatures of thermogenic emissions (e.g. from fossil fuels, volcanoes) are less negative, and the pyrogenic emissions (biomass burning) show least negative values. The global averaged $\delta^{13}\text{C}(\text{CH}_4)$ increased until 2000, which suggests a larger contribution of methane with less negative $\delta^{13}\text{C}(\text{CH}_4)$ signatures. The isotopic signature was relatively constant between 2000 and 2007, followed by a decrease since 2007. This indicates a change in the composition of the methane sources contributing to the current methane emissions.

Previous studies analysed the globally averaged $\delta^{13}\text{C}(\text{CH}_4)$ with respect to the methane rise after 2007. Decreasing $\delta^{13}\text{C}(\text{CH}_4)$ implies larger emissions from wetlands (Nisbet et al., 2019) and agricultural activities (Schaefer et al., 2016). In addition, thermogenic emissions, predominantly due to fossil fuel exploitation, could have contributed to the CH₄ rise (Hausmann et al., 2016). This assumption is, for example, supported by a possible reduction of pyrogenic emissions with relative high $\delta^{13}\text{C}(\text{CH}_4)$ (Worden et al., 2017). Fossil fuel production (Höök et al., 2012) and in particular, the extraction of shale gas (fracking, EIA, 2015) prevailed over the last decades. Howarth (2019) suggests, that shale gas may have lower $\delta^{13}\text{C}(\text{CH}_4)$ signatures compared to methane from other fossil sources. Therefore, a considerable contribution of shale gas emissions may also partly explain the observed decrease in the global mean surface $\delta^{13}\text{C}(\text{CH}_4)$. In contrast, Milkov et al. (2020) suggest very negative $\delta^{13}\text{C}(\text{CH}_4)$ signatures in shale gas methane, which opposes the findings of Howarth (2019). Finally, a reduction of the OH concentration could lead to the observed increase of CH₄ and a change of the isotopic composition due to the oxidation of CH₄ (Rigby et al., 2017; Turner et al., 2017).

Scientific questions

The presented study aims to investigate and identify sources and sinks of atmospheric CH₄ on the global and regional scale by using different modelling approaches. The overarching goal is to improve our knowledge of the global CH₄ budget and further enable supporting numerical simulations for future measurement campaigns. Four scientific questions result from the motivation described above. The first two are related to regional and local CH₄ emissions. The two last scientific questions addressed in this study concern the recent global atmospheric CH₄ rise since 2007 and the simultaneous decrease in global $\delta^{13}\text{C}$.

¹Vienna Pee Dee Belemnite

²Vienna Standard Mean Ocean Water

- Regional and local CH₄ emissions
 1. How well do we understand the CH₄ distribution on regional scale? How good can we simulate and forecast regional CH₄ distributions with a regional model? Is there an improvement of the models' skill with increasingly finer model resolution?
 2. How well do we understand stable CH₄ isotopologues on regional scale and how good can we simulate them? Do we see differences in the isotopic signatures relative to the background signature?
- Stable CH₄ isotopologues and the recent CH₄ rise:
 3. How do different CH₄ source categories, and in particular shale gas emissions, contribute to the global CH₄ budget?
 4. How does the global OH concentration and its atmospheric distribution influence the global mean surface $\delta^{13}\text{C}(\text{CH}_4)$ signature?

1.2 Methodology and approach

In order to answer these questions, and to examine various aspects of atmospheric methane, I apply a combined global and regional numerical model of the atmosphere. On the regional scale, the focus is on accompanying an extensive measurement campaign, called CoMet 1.0. The global methane budget is assessed with a global chemistry climate model.

To resolve small-scale patterns and CH₄ point sources in a specific area, the models' spatial and temporal resolution must be as fine as possible. Moreover, to simulate the total methane mixing ratios in the area, the variability in background methane should be correctly represented. Regional models usually prescribe methane climatologies at their boundaries. To simulate the methane background variations, the models' boundary conditions must however, be consistent with the actual meteorology. This can be achieved with a global/regional on-line nested chemistry climate model. Such models allow for a so called "nesting" of several model instances into each other, covering a progressively smaller area with an increasingly finer resolution. Each model instance receives its' boundary conditions from the respective coarser resolved model instance. Thereby, only the area of interest is simulated with a high temporal and spatial resolution. The surrounding area is less resolved, which saves computational resources.

The Carbon Dioxide and Methane Mission (CoMet) campaign is a measurement campaign, carried out in May and June 2018. One of the objectives of the CoMet campaign was to quantify localized methane emissions from coal mining activities in the Upper Silesian Coal Basin (USCB) in Poland. It combined airborne and ground-based measurements (active and passive remote sensing, in-situ, flask sampling), as well as regional and global atmospheric models. A major part of the presented thesis was to develop a forecast

system that provided numerical simulations of methane in the atmosphere. These forecasts supported the research aircraft flight planning throughout the campaign. Numerical simulations further help with the interpretation of the observed methane mixing ratios afterwards (hindcasting).

For future studies and measurement campaigns, it is crucial to investigate how well these regional simulations can reflect the actual CH₄ distribution in the atmosphere.

The first part of this study therefore includes the analysis of hind- and forecast simulations conducted with a global/regional on-line nested chemistry climate model. The model results are compared to the observational data sampled during CoMet 1.0. These results are already published by Nickl et al. (2020) and the corresponding Chapter 4 in this thesis is mainly based on this publication. The second part covers the assessment of methane isotopologues with the regional model. The simulation results are analysed and compared to CoMet observations (CH₄ mixing ratios and stable isotopes) in Chapter 5.

The last part in Chapter 6 concerns the simulation of the global methane budget by global modelling. It investigates the influence of different source emission fluxes and the OH field onto the recent CH₄ rise with respect to the observed global averaged $\delta^{13}\text{C}(\text{CH}_4)$ signature. A state-of-the-art global chemistry climate model is applied, using a simplified approach to simulate methane loss, as well as the physical and chemical processes of methane isotopologues. Based on recent emission inventories, CH₄ emissions and the respective isotopic signatures are systematically varied within the range of their uncertainties, in order to reproduce the observed global trends in $\delta^{13}\text{C}(\text{CH}_4)$ and CH₄ mixing ratios.

Chapter 2

Scientific background

2.1 Methane in the atmosphere

Methane (CH_4) is a major greenhouse gas in the atmosphere, along with H_2O (vapour), carbon dioxide (CO_2) and nitrogen dioxide (N_2O). Furthermore it plays an important role in atmospheric chemistry, as it effects the concentration of tropospheric hydroxyl radical (OH), a key oxidant or "cleaner" in the atmosphere, which removes other trace gases, such as carbon monoxide (CO), nitrous oxide (NO_x) and organic compounds (Crutzen, 1995; Lelieveld et al., 2004).

In terms of anthropogenically induced radiative forcing methane is the second most important greenhouse gas after CO_2 . Its direct radiative forcing is estimated at 0.61 W m^{-2} (Etminan et al., 2016). Atmospheric concentrations are about 200 times lower than CO_2 concentration. Yet, methane's absorption of infrared radiation is stronger and its 100-year global warming potential (GWP) is 28 times larger than the GWP of CO_2 (GWP=1). Methane has a relatively short atmospheric lifetime of ~ 10 years (see Section 2.1.2). On a shorter time horizon of 20 years its GWP is therefore even higher with a value of 84 (Myhre et al., 2013). Besides the direct effect to radiative forcing, the oxidation of methane leads to a production of further greenhouse gases such as O_3 , CO_2 and stratospheric water vapour (Myhre et al., 2013). This again contributes to the radiative forcing (indirectly) and results in a GWP of 34 and 86 for the 100-year and 20-year time horizon, respectively (Myhre et al., 2013).

Since the atmospheric methane lifetime is relatively short, a reduction of anthropogenic methane emissions would rapidly effect the global methane budget. This is an attractive target in terms of climate change mitigation strategies (Dlugokencky et al., 2011). Understanding the behaviour of atmospheric methane and its chemical feedbacks, as well as the causes of the recent methane growth is therefore crucial.

Atmospheric methane concentrations are determined by emission fluxes and sink processes. Both can be subject to different feedbacks. Palaeo records show that natural methane emissions are sensitive to temperature variations (Etheridge et al., 1998). Bo-

real wetland emissions, for example, decreased during the Last Glacial Maximum (LGM), when temperatures were low (Fischer et al., 2008). In contrast, increasing temperatures, accompanied by rising soil water tables, will enhance the production and therefore also the emission of methane. Moreover, permafrost or gas hydrates possibly thaw or become destabilized due to higher temperatures. This implies, that emissions from wetlands, gas hydrates and permafrost likely respond to a future warming climate (Gedney et al., 2004; Dean et al., 2018; Nisbet et al., 2019). Apart from this warming climate feedback, methane is also involved in a complex interplay of processes determining its atmospheric lifetime. The oxidation of methane with OH, which is the primary sink, affects for example methane's own tropospheric lifetime. Methane and its oxidation products are also major sinks for OH. Thus, higher methane concentrations increase the tropospheric lifetime of methane (Lelieveld et al., 1998; Winterstein et al., 2019; Stecher et al., 2021).

Methane sources are predominantly located in the Northern Hemisphere. Currently, 64 % of total emissions appear in the tropics, 32 % in the mid latitudes and 4 % in the Northern high latitudes (Saunio et al., 2020). The concentrations of sink reactants also vary globally with latitude. This results in a South-North gradient of the global methane surface mixing ratios. Atmospheric transport, in turn, impacts the interhemispheric and inter-polar difference (Pandey et al., 2019) and reduces the gradient between both Hemispheres. A detailed description of the individual methane sources and the different sink processes are given in section 2.1.1 and 2.1.2, respectively.

Analyses from ice core records reconstructed global averaged methane mixing ratios of about 695 ppb during the late pre-industrial Holocene (Etheridge et al., 1998). Since then global methane mixing ratios in the atmosphere increased rapidly to currently 1873.4 ppb (Dlugokencky et al., 2020, mixing ratio in January 2020). This sharp increase during the 20th century is most likely attributed to enhanced human activity. Figure 1.1 in Chapter 1 shows the global methane mixing ratios from the early 1980s until present (left panel). The corresponding methane growth (right panel) began to slow down in 1983 and during the 1990s, presumably due to reduced anthropogenic emissions (Bousquet et al., 2006). Emissions from the Mt. Pinatubo eruption in 1992 resulted in decreasing temperatures (Dutton and Christy, 1992), whereupon wetlands likely responded with lower emissions. This might have led to the observed drop in the methane growth rate. Additionally, the disintegration of the former Soviet Union presumably weakened the methane rise at this time (Dlugokencky et al., 1994). Between 1997 and 1998, enhanced biomass burning from Indonesian wildfires resulted again in larger methane emissions (Dlugokencky et al., 2011). The growth rate stagnated between 1999 until 2006 (Dlugokencky et al., 2011) and in 2007 methane mixing ratios increased again, with the highest growth rate of 12.7 ± 0.5 ppb/year in 2014 (Nisbet et al., 2019). However, although single events that induced changes in methane emissions during the last decades have been identified, the interannual variability of methane mixing ratios is still poorly understood. Wetlands and variations of tropical OH are assumed to contribute largely to the previous changes (Bousquet et al., 2006). Still, the recent increase after 2007 is heavily debated in the literature. The various hypotheses, trying to explain the causes of the renewed methane growth, have been already

shortly described in the introduction (see Chapter 1). The use of stable isotopologues can help to constrain individual sources and sinks of methane. An introduction to the stable isotope chemistry is therefore given in Section 2.2.2. Chapter 6 addresses the recent increase between 2007 and 2014 and discusses the global observed isotopic signature of methane in more detail.

2.1.1 Sources of methane

Methane is emitted by natural and anthropogenic sources. Depending on the type of formation, they can be further divided into biogenic, thermogenic and pyrogenic sources. Biogenic or "microbial" methane is produced due methanogenesis by *archaea* under anoxic conditions (Cicerone and Oremland, 1988), such as in coastal sediments, wetlands and rice paddies, the rumen of livestock (enteric fermentation) or organic waste deposits. Thermogenic methane is generated under high pressure and temperature conditions due to a thermal breakdown of organic matter. This applies for example to fossil fuels or volcanic gases which are formed in great depths. Pyrogenic methane forms during incomplete combustion of biomass during wildfires or biomass burning.

The individual natural and anthropogenic sources of methane are well known. Yet, their relative contribution to the global methane budget is uncertain. Methane emissions are either constrained by bottom-up inventories, which scale individual source data to a global emissions, or they are estimated by top-down inversions using satellite and other atmospheric measurements. Depending on the approach, the methane emissions differ widely. While for the total methane emission, top-down estimates between 2008 and 2017 are 576 Tg(CH₄)/yr [550-594], bottom-up inventories suggest much larger emissions of 737 Tg(CH₄)/yr [594-881] (Saunio et al., 2020). Figure 2.1 lists the emission fluxes per source based on top-down estimates.

Natural sources include wetlands, freshwater systems, oceans, termites, wild animals, geological sources, methane hydrates and wild fires. Wetlands are the largest natural source and are mainly located in tropical South America (Amazonas region) and in boreal regions. Between 2008 and 2017 emission fluxes, derived from bottom-up and top-down estimates, are 149 Tg(CH₄)/yr [102-182] and 181 Tg(CH₄)/yr [159-200], respectively (Saunio et al., 2020). Wetland and freshwater emissions estimates show the highest uncertainties (Kirschke et al., 2013) and differences between the estimates may arise from double counting of freshwater as wetland emissions (Saunio et al., 2020). Since methane formation in wetlands depends on the water table (depth of anoxic zone), temperature, and degradable material it may be possibly impacted by a changing climate and can be important in terms of future climate feedbacks (Gedney et al., 2004). Geological sources including emissions from volcanoes, mudvolcanoes and sediment basins (onshore and offshore) are less constrained and again lead to discrepancies between bottom-up and top-down estimates (Saunio et al., 2020). Together with all other natural sources, they make up only a minor part of the total methane emissions.

Anthropogenic emissions arise from gas, oil and coal extraction, agriculture, waste disposal, and biomass (incl. biofuel) burning. They account for about 60 % of the total

emissions (Saunois et al., 2020) and seem to be better constrained than natural emissions, since the differences between bottom-up and top-down estimates are smaller. However, estimates for the individual sectors are only from bottom-up estimates and are based on local informations and inventories. Uncertainties can still be there. A major part of the anthropogenic methane is attributed to agricultural activity, mostly livestock farming, manure and rice cultivation, the latter being predominant in South East Asia (Carlson et al., 2016). Another large source is the waste sector, where methane is produced during the decay of biogenic waste in landfills or waste water. Agriculture and waste account for 206 Tg(CH₄)/yr [191-223] in bottom-up and for 217 Tg(CH₄)/yr [207-240] in top-down estimates of the emissions between 2008 and 2017 (Saunois et al., 2020). Between 2000 and 2008 nearly 63 % of the fossil fuel emissions were due to oil and natural gas exploitation. Methane escapes as fugitive emission from productive and abandoned wells, as well as during transport. Natural gas include conventional and shale gas emissions. Since 2007, one can observe a growing shale gas activity especially in Northern America. The remaining part of fossil fuel emissions is mainly attributed to coal mining, where methane is mostly directly emitted from the ventilation shafts. However, fugitive emissions escape also from not-operated mines and during transport. Coal related methane emissions increased largely in China in the 2000s (Thompson et al., 2015). Minor fossil fuel emissions arise from road traffic and industry. All fossil fuel emissions sum up to 128 Tg(CH₄)/y [113-154] (bottom-up) or 111 Tg(CH₄)/y [81-131] (top-down) during 2008 to 2017 (Saunois et al., 2020).

Methane is further emitted during biomass and biofuel burning. Most emission are attributed to wild and large-scale fires, which are strongly influenced by environmental and climate conditions. Between 2001 and 2016 the global fire activity decreased (Earl and Simmonds, 2018), likely due to an expansion of agriculture (Andela et al., 2017). Increasing fire activity is observed in India and China (Earl and Simmonds, 2018), which is attributed to increasing crop residue burning (Andela et al., 2017). Human induced fires, such as agricultural waste burning, appear mainly in the subtropic and tropics and are often difficult to detect (Saunois et al., 2020). Biofuel burning make up between 30 to 50 % of the total biomass burning emissions and arise for example, from domestic cooking, heating and open fires (Saunois et al., 2020). Biomass burning including the natural burning emissions make up 30 Tg(CH₄)/y [22-36] (top down, Saunois et al., 2020).

2.1.2 Sinks of methane

Methane is removed from the atmosphere by various photochemical reactions, i.e. the oxidation with hydroxyl radical (OH), chlorine (Cl) and the excited oxygen atom O(¹D). The following equations taken from Ravishankara (1988) describe the corresponding chemical reaction:



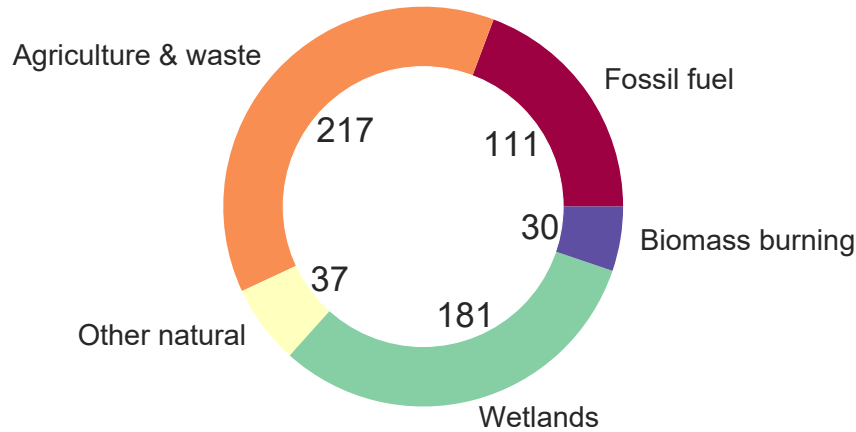


Figure 2.1: Emission fluxes of the main methane sources categories in Tg(CH₄)/yr. Numbers are based on the data of Saunois et al. (2020) top-down estimates from the period 2008-2017.



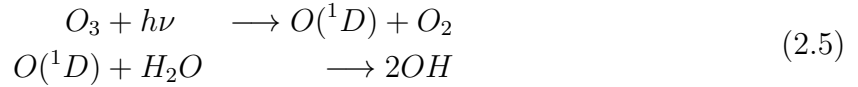
About 90 % of methane is removed in the troposphere. The main sink here is the oxidation with OH. Between 2000 and 2009 the tropospheric oxidation by OH removed about 553 [476-677] Tg(CH₄)/yr (Saunois et al., 2020). Tropospheric methane is also oxidized by Cl in the marine boundary layer (Allan et al., 2007), however, as recently reported by Gromov et al. (2018), this is only a small amount of the global atmospheric methane. About 5 % escape to the stratosphere, where methane is oxidized by OH, Cl and O(¹D). The stratospheric loss of methane is about 31 [12-37] Tg(CH₄)/yr (Saunois et al., 2020). Furthermore methane is removed by photolysis, which takes place above the mesosphere (Ravishankara, 1988) and is described by the reaction:



Equation 2.4 is taken from (Turco, 1975). The remaining sink is due to biological consumption in soils, where methane is oxidized by methanotrophic bacteria (Curry, 2007).

OH radical and tropospheric lifetime of methane

OH is the primary sink of methane in the atmosphere. As a result of its high reactivity, it is also a major oxidant for CO, NO_x species and other trace gases (Crutzen, 1995). This makes OH an important compound of atmospheric chemistry. OH is formed from photodissociation of tropospheric ozone (O₃) and water vapour:



The equation 2.5 is taken from Crutzen (1995). The photolysis of ozone provides the O(¹D) for the reaction with water vapour resulting in OH. This primary production of OH is subject to various feedbacks in the atmosphere. It relies on the supply of water vapour and O₃ and depends additionally on the incoming UV radiation, which is highest in the tropics (Crutzen, 1995). Tropospheric O₃ is produced in NO rich regions, such as near industrial zones or the continental tropics and mid latitudes, where NO forms due to lightning (Crutzen, 1995). The OH formation is further influenced by the methane oxidation products. Thereby, water vapour is produced, which is again needed for the reaction with O(¹D) in the troposphere and therefore favours OH production. Counteracting to this, CO is formed during the sink reaction with OH, which is along with CH₄, a major sink of OH. Consequently, both affect again the OH abundance in the troposphere. However, oxidation products in the stratosphere influence OH concentration differently. Stratospheric ozone for example reduces the short wave radiation reaching the troposphere, which is needed for the photolysis of ozone (Voulgarakis et al., 2013). These feedbacks also affect the tropospheric methane lifetime τ_{CH_4} . Enhanced methane mixing ratios lead to a reduction of OH and an increase in the methane lifetime (Lelieveld et al., 1998; Winterstein et al., 2019). This enhancement is again weakened by slow warming feedbacks, that involve the production of more water vapour in the troposphere due to CH₄ oxidation, resulting in the production of OH (Stecher et al., 2021). Furthermore, since the oxidation reactions depend on temperature, the lifetime responds to temperature changes. El Niño-Southern Oscillation (ENSO) events for example, lead to higher temperatures and more water vapour. They may result in both, production of OH due to higher water vapour, or loss of OH due to warmer temperatures (Prinn et al., 2005). Additionally, during el Niño events, enhanced biomass burning in tropical regions lead to large emissions of CO. Due to these higher concentrations of CO, OH is removed rapidly and leads to an average longer lifetime of methane (Crutzen, 1995; Prinn et al., 2005; Zhao et al., 2020).

Understanding the global methane budget and interpreting the recent methane increase requires the consideration of the methane sink processes and lifetime estimates. Zhao et al. (2020) found that an OH underestimation likely led to an underestimation of methane emissions during 1986 and 2010. Recent studies link the recent growth of methane to an reduced oxidation capacity (Turner et al., 2016; Rigby et al., 2017). The atmospheric OH concentrations are afflicted with high uncertainties due to low the sparsity of measurements, the complex feedbacks, and fast reactivity of OH in the troposphere. The most uncertainties are the OH concentrations in the tropics (Zhao et al., 2020). Consequently,

the tropospheric lifetime of methane with respect to OH varies among different studies. Estimated lifetimes range from short lifetimes, i.e.: 8.02 yr (Jöckel et al., 2006), 8.11 ± 0.13 (Frank, 2018) over 9.1 ± 0.9 yr (Prather et al., 2012, measurement-based), 9.8 ± 1.6 (Voulgarakis et al., 2013) to longer estimates of for example 10.2 [9.5-11.1] (Prinn et al., 2005). Differences of the simulated methane lifetime between models are mainly caused by different photolysis frequencies of ozone to the excited O^1D ($J O^1D$), O_3 and chemical mechanisms in these models (Nicely et al., 2020).

2.2 Methane isotopologues

2.2.1 Isotope chemistry

Atoms consist of a nucleus which is surrounded by a number of electrons. The atomic nucleus in turn is composed of protons and neutrons. The number of protons, also called atomic number, and the number of electrons characterise a chemical element. While a specific element always has the same atomic number, its number of neutrons can vary. Atomic nuclei of an element with different numbers of neutrons are called isotopes. Molecules that contain the same elements but different isotopes are denoted as isotopologues. Isotopes can either be stable or subject to radioactive decay (radiogenic isotopes). Most elements have two naturally occurring stable isotopes, the lighter one being generally the most abundant. Figure 2.2 shows a sketch of the two stable carbon isotopes carbon-12 (^{12}C) and carbon-13 (^{13}C), with a nucleus consisting of either six or seven neutrons, respectively. Different isotopes of the same element mainly equal in most chemical reactions, but neutrons contribute to the total mass of the nuclei, resulting in a small mass difference and therefore slightly different chemical and physical properties. Chemical compounds with "heavier" (i.e. with larger mass) isotopes have lower mobility and stronger chemical bounds, compared to those containing "lighter" (i.e. with lower mass) isotopes. This leads to a relative partitioning of the heavier and lighter isotopes during physical phase transition or chemical reactions, and is defined as isotopic fractionation (Mook, 2000). The distribution of isotopes can therefore contain information about the origin and transport of a sample or may record chemical reactions. The abundance of heavier isotopes relative to the abundance of lighter isotopes can be measured by cavity ring down or mass spectroscopy. The study of isotopes and isotopologues became an important tool in Earth and Environmental Sciences. Both, radiogenic and stable isotopes serve as tracers, marking for example transport in hydrological studies (Mook, 2000). Additionally, radioactive decay is used for age determination, such as the ^{14}C or the uranium/thorium methods. Stable isotopes are widely used in palaeo environmental reconstruction and can help to identify geo- and biochemical processes that cause isotopic fractionation. Stable oxygen isotopes for example, sampled from ice core air bubbles or marine sediment foraminifera are often used to derive palaeo temperature records. Methane sources have different source signatures and stable isotope analyses can be used to constrain individual sources and to understand the atmospheric composition of methane.

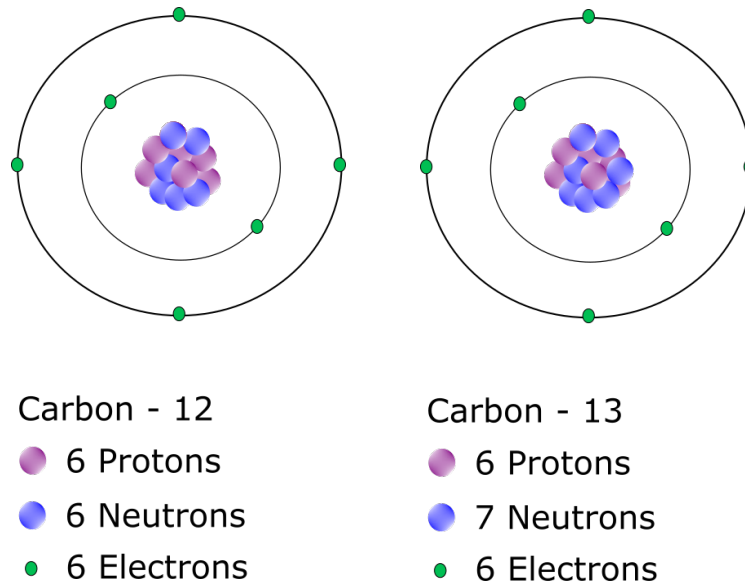


Figure 2.2: Sketch of the stable isotopes carbon-12 (left) and carbon-13 (right). Red (protons) and blue (neutrons) form the atomic nucleus and green dots show the surrounding electrons. Carbon consists of 6 electrons and 6 protons. In nature carbon has two stable isotopes with either 6 neutrons (carbon-12) or 7 neutrons (carbon-13).

Isotopic fractionation of stable isotopes

The isotopic ratio R of a sample is defined as the ratio between the rare isotope I_{rare} and the abundant isotope I_{abundant} of a specific element I :

$$R_{\text{Sample}} = \frac{I_{\text{rare}}}{I_{\text{abundant}}} \quad (2.6)$$

with I_{rare} being the heavier isotope and I_{abundant} being the lighter isotope. The ratio of the rare and the abundant isotope changes as the sample is subject to isotopic fractionation during physical or chemical reactions. As described above, the isotopic fractionation is a result of the mass differences between heavy and light isotopes. Chemical compounds with heavier isotopes are in general less mobile and have a higher binding energy than the compounds with lighter isotopes. During the evaporation of water, for example, the heavier isotope oxygen-18, is favoured by the liquid phase where it is bound more stably, while the lighter isotope oxygen-16 evaporates preferably into the gas phase. The difference between the binding energies becomes smaller with higher temperatures and results in smaller fractionation effects (Mook, 2000). The isotopic fractionation is mathematically described as isotopic fractionation factor α :

$$\alpha_A(B) = \frac{R_B}{R_A} \quad (2.7)$$

with R_A and R_B being the isotopic ratios of a chemical compound before and after the

physical phase transition or chemical reactions, respectively. It can be further described as the fractionation:

$$\varepsilon_A(B) = \alpha_A(B) - 1 \quad (\cdot 10^3 \text{ ‰}) \quad (2.8)$$

The $\varepsilon_A(B)$ value can be either negative or positive and refers to a depletion or an enrichment of the heavier isotope in compound B relative to compound A, respectively. We distinguish between two different fractionation processes, i.e. the equilibrium and the kinetic fractionation. Equilibrium fractionation takes place in closed systems in which two compounds are in chemical and isotopic equilibrium. While the isotopes are exchanged back and forward, the isotopic ratio is kept constant. An equilibrium occurs for example between gaseous carbon dioxide and dissolved bicarbonate (Mook et al., 1974) or between calcite and ocean water as seen for some benthic foraminifera (Shackleton, 1974). Kinetic isotopic fractionation occurs during irreversible one-way chemical and physical processes, such as it is true for many biological reactions. In most cases, the compounds with the lighter isotopes have higher velocities and smaller binding energies. These compounds react faster, which leads to an enrichment of the heavier isotope in the remaining compound and a depletion in the resulting compound. For example, when atmospheric methane is oxidized by OH in the troposphere, molecules with the lighter carbon isotope react faster. The remaining methane becomes isotopically enriched in the heavier carbon isotope. The ratio between the reaction rate of the lighter compound k_L and the reaction rate of the heavier compound k_H is called Kinetic Isotopic Effect (KIE) (Bigeleisen, 2005):

$$KIE := \frac{k_L}{k_H} \quad (2.9)$$

The delta notation

The isotopic distribution of a sample is not given as absolute value. For a better comparability, the isotopic ratio is reported in the so called delta notation describing the relative abundance of the raw isotope and the abundant isotopes relative to a standard. The delta notation is given by McKinney et al. (1950) and defined as follows:

$$\delta = \frac{R_{Sample} - R_{Standard}}{R_{Standard}} * 1000 = \frac{R_{Sample}}{R_{Standard}} - 1 * 1000 \quad (2.10)$$

The universally used standard for hydrogen and oxygen isotopes is the isotopic ratio of mean ocean water, named Vienna Standard Mean Ocean Water (VSMOW). Carbon isotopes are typically reported relative to the Vienna Pee Dee Belemnite (VPDB), a fossil containing a relatively large amount of the heavier isotope ^{13}C . The exact values of the standards are listed in Table 2.1. Throughout the chapters of this study, the two terms δD and $\delta^{13}\text{C}$ always refer to the standards VSMOW and VPDB, respectively (i.e. $\delta\text{D}_{\text{VSMOW}}$ and $\delta^{13}\text{C}_{\text{VPDB}}$).

Table 2.1: Values of the two isotopic standards VSMOW and VPDB for hydrogen and carbon isotopes, respectively.

Standard	Value	values taken from:
Vienna Standard Mean Ocean Water (VSMOW)	0.00015576	Fry (2006)
Vienna Pee Dee Belemnite (VPDB)	0.0111802	Werner and Brand (2001)

2.2.2 Stable isotopologues of methane

The interannual variability of methane and particularly the causes of the recent increase in the atmosphere are heavily discussed in the recent literature. Since the isotopic signature of methane (reported as $\delta^{13}\text{C}(\text{CH}_4)$ and $\delta\text{D}(\text{CH}_4)$) differ according to its type of formation, i.e. biogenic, thermogenic and pyrogenic, the analysis of stable isotopes can help to constrain different sources of methane. Moreover, sink reactions have characteristic fractionation effects, which alter the isotopic composition and may therefore be identified. Yet it is not possible to distinguish between anthropogenic and natural sources. The recent global methane increase is accompanied by a decrease in $\delta^{13}\text{C}(\text{CH}_4)$. A shift in the atmospheric $\delta^{13}\text{C}(\text{CH}_4)$ indicates a change in the source composition or atmospheric sink. The observed trend in atmospheric $\delta^{13}\text{C}(\text{CH}_4)$ has been subject to many debates (see Chapter 1). It is also a main scientific question of the present study and further discussed in Chapter 6. Since the main focus of this study lies on the investigation of $\delta^{13}\text{C}(\text{CH}_4)$, most explanations in this section are given with respect to $\delta^{13}\text{C}(\text{CH}_4)$. Moreover, $\delta^{13}\text{C}(\text{CH}_4)$ is measured globally at various marine and continental surface sampling sites. The measurements are organized by the National Oceanic and Atmospheric Administration (NOAA), the Institute of Arctic and Alpin Research (INSTAAR), the National Institute of Water and Atmospheric Research (NIWA) and the Heidelberg University, Germany (UHei). $\delta\text{D}(\text{CH}_4)$ measurements are unfortunately very sparse. However, for the sake of completeness, $\delta\text{D}(\text{CH}_4)$ signatures and fractionation are also described here.

The isotopic composition of methane in the atmosphere is influenced by the individual source signatures emitted from the surface and the isotopic fractionation during the sink reactions in soils, troposphere and stratosphere. The emitted flux weighted mean $\delta^{13}\text{C}(\text{CH}_4)$ is about -53.5 ‰ (Schwietzke et al., 2016). Yet, as a result of isotopic fractionation during the sink processes, the atmospheric global mean signature becomes enriched in the heavier isotopes with only -47.33 ‰ (Quay et al., 1999, between 1990-1995). Both, $\delta^{13}\text{C}(\text{CH}_4)$ and $\delta\text{D}(\text{CH}_4)$ show a decreasing South-North gradient in the near surface atmosphere, which becomes less pronounced with altitude. Most sources are located in the Northern hemisphere and mainly determine the isotopic signatures near the surface here. The isotopic signatures in the Southern hemisphere are mainly altered due to interhemispheric transport of methane (Quay et al., 1999). The impact of the fractionation by oxidation becomes more important with increasing altitude, especially in the stratosphere (Quay et al., 1999). Besides the spatial variability, $\delta^{13}\text{C}(\text{CH}_4)$ is further affected by seasonal cycles. Whereas

the temperate and polar Northern Hemisphere is mostly influenced by the composition of methane sources, the monthly changes in the tropics can be explained by OH oxidation (Quay et al., 1999).

The next paragraph introduces the stable isotopologues of methane and summarizes the different source signatures and fractionation processes.

Methane isotopologues

In the present model study, the chemistry climate model simulates mixing ratios of the entire molecules, rather than the single elements of which a molecule is composed off. The analysis presented in relation to isotope chemistry therefore refers to stable isotopologues. Methane molecules can be composed of four different stable isotopes: the carbon isotopes ^{12}C and ^{13}C , and the hydrogen isotopes ^1H and D. The most abundant stable isotopologues of methane, which are formed by these isotopes, are: CH_4 , CH_3D , CH_2D_2 and CHD_3 .

The isotopic ratio of a CH_4 sample with respect to C is calculated as follows:

$$R_C(\text{CH}_4) = \frac{^{13}\text{CH}_4}{^{12}\text{CH}_4} \quad (2.11)$$

Since CH_4 contains more than one hydrogen isotope, the isotopic ratio with respect to D is calculated slightly differently:

$$R_D(\text{CH}_4) = \frac{|\text{CH}_3\text{D}| + 2 \cdot |\text{CH}_2\text{D}_2| + 3 \cdot |\text{CHD}_3| + 4 \cdot |\text{CD}_4|}{4 \cdot |\text{CH}_4| + 3|\text{CH}_3\text{D}| + 2 \cdot |\text{CH}_2\text{D}_2| + |\text{CHD}_3|} \quad (2.12)$$

Isotopologues consisting of more than one rare isotope occur rarely in nature and are usually neglected in the calculation. This results in the following simplification of equation 2.12:

$$R_D(\text{CH}_4) = \frac{|\text{CH}_3\text{D}|}{4 \cdot |\text{CH}_4| + 3|\text{CH}_3\text{D}|} \quad (2.13)$$

The isotopic signatures are reported in the delta notations $\delta^{13}\text{C}(\text{CH}_4)$ and $\delta\text{D}(\text{CH}_4)$. The standards Vienna Pee Dee Belemnite (VPDB) and Vienna Standard Mean Ocean Water (VSMOW) are used for carbon and hydrogen, respectively. $\delta^{13}\text{C}(\text{CH}_4)$ and $\delta\text{D}(\text{CH}_4)$ of atmospheric methane are usually negative, which is due to the lower content of the heavier isotopes compared to the standards. In the presented study I use the terms "isotopically enriched" or "isotopically depleted", which means that a sample is enriched or depleted in the heavier isotope relative to another sample. The corresponding $\delta^{13}\text{C}(\text{CH}_4)$ and $\delta\text{D}(\text{CH}_4)$ become consequently either less or more negative. Throughout the chapters of this study, I abbreviate $\delta^{13}\text{C}(\text{CH}_4)$ as $\delta^{13}\text{C}$, and $\delta\text{D}(\text{CH}_4)$ as δD .

Isotopic sources signatures

As described in Section 2.1.1, methane sources can be distinguished with respect to the formation of methane, i.e. biogenic, thermogenic or pyrogenic. Since the isotopic signature of a methane sample depends, among other factors, on the kinetic isotopic fractionation happening during formation, the different isotopic source signatures can also be roughly classified into these categories. Figure 2.3 shows this classification and the corresponding $\delta^{13}\text{C}$ and δD . The mean isotopic signatures, which I report here, were calculated by Frank (2018) using the following references: Kiyosu (1983); Quay et al. (1999); Snover et al. (2000); Mikaloff-Fletcher et al. (2004); Whiticar and Schaefer (2007); Monteil et al. (2011); Rigby et al. (2012); Zazzeri et al. (2015).

Biogenic methane is in general isotopically most negative. Kinetic effects occur due to the anaerobic metabolism of microorganisms and lead to a depletion of the heavier isotope in the resulting methane. The mean signatures are -59.0‰ and -324.5‰ for $\delta^{13}\text{C}$ and δD , respectively (Frank, 2018, and references therein). Thermogenic methane is isotopically less depleted in the heavier isotopes with a mean $\delta^{13}\text{C}$ of -41.8‰ , and a mean δD of -192.0‰ (Frank, 2018, and references therein). Pyrogenic methane is isotopically most enriched. During the combustion of organic material, $\delta^{13}\text{C}$ is not subject to any kinetic fractionation and the isotopic signature of the source material is maintained. Contrary, a significant fractionation occurs for deuterium during combustion (Snover et al., 2000). Mean signatures are -23.9‰ and -213‰ for $\delta^{13}\text{C}$ and δD , respectively (Frank, 2018, and references therein). $\delta^{13}\text{C}$ and δD also depend on the isotopic signature of the source material, such as different plant types that incorporated the individual carbon isotopes differently. This applies for example to biomass burning or livestock emissions. Furthermore, methane can be subject to secondary fractionation due to oxidation during migration in rock formations or soils. Chapter 6 deals with a more detailed description of the individual source signatures and describes the individual processes behind their formation.

Isotopic fractionation during sink reactions

During its removal in the atmosphere, methane is subject to isotopic fractionation. The isotopically lighter molecules $^{12}\text{CH}_4$ and CH_4 react preferentially with the oxidation partners, which leads to an enrichment of the heavier molecules $^{13}\text{CH}_4$ and CH_3D in the remaining methane. The extent of the fractionation and the corresponding KIE depend, as described above, on the reaction rates and consequently, vary with the different methane sink reactions. Additionally they are partly temperature dependent. The corresponding KIEs were analysed by various studies. Yet, differences remain between experimentally and theoretically derived KIEs (Gupta et al., 1997; Quay et al., 1999). Table 2.2 presents, among others, the KIEs used in the present study. The upper part lists the experimentally derived KIEs for the reactions with OH, Cl and $\text{O}(^1\text{D})$. The strongest fractionation for carbon and hydrogen isotopes is observed for the reaction with Cl (Saueressig et al., 1996). The smallest KIE is found for the reaction with $\text{O}(^1\text{D})$ (Saueressig et al., 2001). The

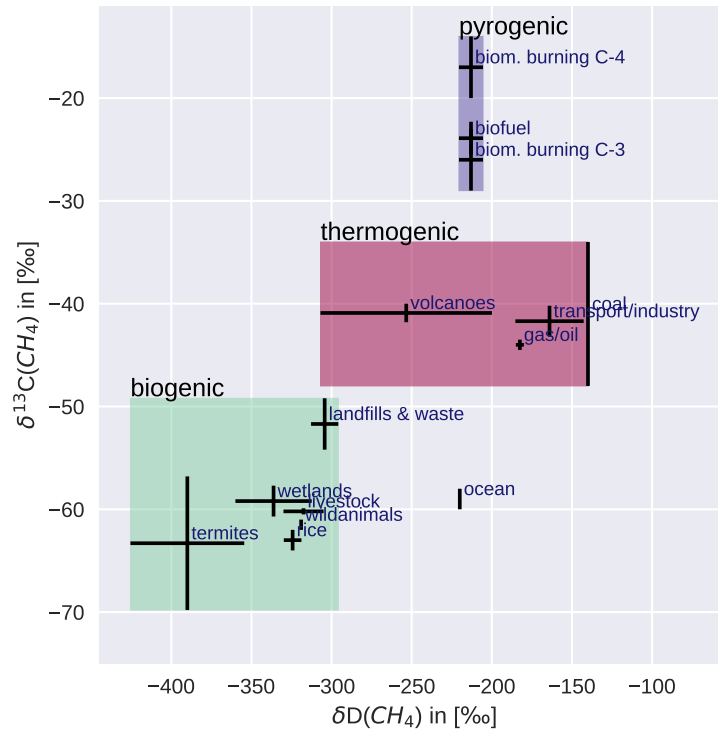


Figure 2.3: Overview of the $\delta^{13}C(CH_4)$ and $\delta D(CH_4)$ source signatures in ‰. Signatures are grouped into pyrogenic (purple rectangle), thermogenic (red rectangle) and biogenic (green rectangle) sources. The overview including the isotopic signatures and uncertainty ranges is adapted from Frank (2018). Pyrogenic emissions are additionally separated into C-3 and C-4 plants. Signatures are taken from Dlugokencky et al. (2011).

fractionations by Cl and O(1D) oxidation become important when considering the isotopic composition in the stratosphere. Both fractionations are sensitive to temperature changes. This also applies for the hydrogen isotope fractionation during OH oxidation. On the contrary, the carbon isotope fractionation during the reaction with OH shows no temperature dependency (Cantrell et al., 1990). OH loss plays a major role in the troposphere and influences in particular the isotopic composition and its monthly variations in the tropics (Quay et al., 1999). The fractionation for carbon differ largely between different studies. Table 2.2 lists two experimentally derived ^{13}C KIE_{OH}. Even stronger KIEs are reported by theoretical studies (Gupta et al., 1997). The presented study uses the most recent KIE given by Saueressig et al. (2001). Since the fractionation during photolysis is only important in the mesosphere and the KIE are relatively small (as shown by the results for the Martian atmosphere determined by Nair et al. (2005)), the fractionation by photolysis is neglected in the present model setup (similar to the setups described by Frank, 2018; Winterstein and Jöckel, 2021). The KIE of soil loss depends on the fractionation during both, the diffusion into the soil and the microbial oxidation. It further varies with the type of soil, such as the soils of boreal tundra, forests or grasslands. Snover and Quay

(2000) presents KIE measurements in forest and grassland soils (see Table 2.2, lower part). Although soil uptake responds to the seasonal cycle, the effect the seasonal variations of $\delta^{13}\text{C}$ is negligible (Quay et al., 1999). For soil uptake, the two mean values, $^{13}\text{C}\text{KIE}_{\text{soil}} = 1.0196$ (Frank, 2018, mean calculated with values taken from Snover and Quay (2000); Maxfield et al. (2009)) and $^{\text{D}}\text{KIE}_{\text{soil}} = 1.0825$ (Frank, 2018, mean calculated with values taken from Snover and Quay (2000)), are used.

Table 2.2: KIEs for different methane sink reactions. The upper part lists the KIE at a temperature of 296 K for the reactions with OH, Cl and $\text{O}(^1\text{D})$. Since the KIE are partly temperature dependent the coefficient A and B are given, to calculate the KIE according to $\text{KIE} = A \cdot \exp(B/T)$ (adapted from Saueressig et al., 2001). The lower part lists the KIEs for forest and grassland soil uptake.

Reaction	KIE	A	B	Reference
$^{13}\text{C}\text{KIE}_{\text{OH}}$	1.0054	-	-	(Cantrell et al., 1990)
$^{13}\text{C}\text{KIE}_{\text{OH}}$	1.0039	-	-	(Saueressig et al., 2001)
$^{13}\text{C}\text{KIE}_{\text{Cl}}$	1.066	1.043	6.46	(Saueressig et al., 1995)
$^{13}\text{C}\text{KIE}_{\text{O}^1\text{D}}$	1.013	1.013	0	(Saueressig et al., 2001)
$^{\text{D}}\text{KIE}_{\text{OH}}$	1.294	1.1	49	(Saueressig et al., 2001)
$^{\text{D}}\text{KIE}_{\text{Cl}}$	1.508	1.278	51.31	(Saueressig et al., 1996)
$^{\text{D}}\text{KIE}_{\text{O}^1\text{D}}$	1.06	1.060	0	(Saueressig et al., 2001)
Reaction	KIE			Reference
$^{13}\text{C}\text{KIE}_{\text{soil}}$	1.0181 (forest)			(Snover and Quay, 2000)
	1.0173 (grassland)			(Snover and Quay, 2000)
$^{\text{D}}\text{KIE}_{\text{soil}}$	1.066 (forest)			(Snover and Quay, 2000)
	1.099 (grassland)			(Snover and Quay, 2000)

Chapter 3

Description of the models and forecast system

Our climate system encompasses a wide variety of components of the Earth system, i.e. atmosphere, biosphere, cryosphere, lithosphere and hydrosphere. Numerical modelling is a suitable tool to understand the complex interplay between those components. Although comprehensive measurements of climate variables are carried out globally, they only represent local snapshots. Moreover, at some locations continuous data sets are rare or even difficult to capture. Hence, in order to fill this gap and additionally understand the involved processes leading to the observations, numerical models became essential in climate sciences. Modelling of the past climate helps to interpret palaeo records and understand the mechanisms, feedbacks and driving forces of long-term changes, such as the interglacial and glacial variability. Furthermore, climate models are used to study the impacts on the recent climate, the role of human activities and the evolution of greenhouse gases. Finally, future environmental changes and climate evolution can be projected by numerical simulations.

General Circulation Models (GCM) describe the basic physical processes of atmosphere and ocean. These processes are, for example, related to clouds, ice, ocean currents or wind. In general, we distinguish between General Circulation Models of the Atmosphere (A-GCM) and General Circulation Models of the Ocean (O-GCM). If they are "coupled", the feedbacks between atmosphere, ocean and often sea-ice are simulated. These coupled models are then called Climate Models. However, chemical and biological processes, as well as the various other feedbacks between the different Earth system components are not considered in a simple A-GCM or O-GCM. In contrast, Chemistry Circulation Model (CCM) are A-GCMs that include atmospheric chemistry. CCMs consider feedbacks on dynamics of radiatively compounds (traces gases and aerosols) and feedbacks of chemical reactions on the atmospheric hydrological cycle. A CCM "coupled" to an O-GCM is called Earth System Model (ESM). ESMs include the online coupling of different compartments of the Earth system and consider feedbacks between them. Such numerical ESMs are computationally very demanding, w.r.t. to both, computing time and storage capacity. Simulations are therefore carried out at High Performance Computing (HPC) Centers.

Global chemistry climate models, such as the numerical global chemistry climate model ECHAM/MESSy (EMAC, Jöckel et al., 2010) simulate the chemistry of the atmosphere explicitly and are suitable to investigate the mixing ratios and chemical processes of methane, such as it is the aim of this study. Section 3.1 describes the EMAC model in more detail and introduces the submodel CH4, which calculates the basic methane chemistry.

Due to the computational demands for atmospheric chemistry processes, mainly for solving the kinetic equation system, CCMs are usually coarser resolved as their GCM counterparts, when simulating comparable time spans. Simulating smaller scale features with a global CCM would consume large amounts of computational time. It therefore makes sense to only simulate the region and time span of interest, using a regional model at higher resolutions. Yet, regional models need proper boundary conditions. A regional model can therefore be coupled to a global model and exchange the boundary conditions online. As described in Chapter 1, the presented study involves the regional modelling and forecasting of very localized methane plume evolutions. Therefore, simulations with the model system MESSyified ECHAM and COSMO models nested n times (MECO(n), Kerkweg and Jöckel, 2012a,b; Mertens et al., 2016) were performed. MECO(n) is described below in Section 3.2. Section 3.3 presents the forecast system, which was developed as part of this study and published by Nickl et al. (2020).

3.1 The global chemistry climate model EMAC

3.1.1 The modular earth submodel system MESSy

The Modular Earth Submodel System MESSy (Jöckel et al., 2005) allows for comprehensive studies of chemistry and dynamics in stratosphere and troposphere, as well as the interaction between stratosphere and troposphere, atmosphere and biosphere, and atmosphere and ocean. It encompasses a set of individual submodels and a modular interface structure that connects the various submodels (currently 60, <https://www.messy-interface.org>, last access: July 2021) to a base model (such as a box model or a GCM). Different physical, dynamical and chemical processes are comprised in individual submodels, that are all coded according to the modular structure and the underlying coding standard. The submodels can be applied independently from each other and are further largely independent from the base models' temporal and spatial resolution. Data can be exchanged between the individual submodels, and between the submodels and the base model. A two-way coupling (data exchange in both directions) allows to study feedbacks between the submodels. The modularity of MESSy provides a high flexibility, since submodels can be switched on and off individually, or extended by newly developed submodels.

3.1.2 The EMAC model system

The numerical global chemistry climate model ECHAM/MESSy (EMAC, Jöckel et al., 2010) is a state-of-the-art chemistry climate model, which consists of the Modular Earth Submodel System, coupled to the general circulation model ECHAM5 (Roeckner et al., 2006). The various MESSy submodels calculate the physical and chemical processes in the troposphere and middle atmosphere, as well as the interaction between the atmospheric layers.

EMAC can be applied in different vertical and horizontal resolutions. The present study uses the T42L90MA resolution, which corresponds to a quadratic Gaussian horizontal grid of about $2.8^\circ \times 2.8^\circ$ in latitude and longitude and 90 vertical layers between the surface and approximately 80 km altitude. Furthermore, EMAC can be operated in different configurations: 1. as a GCM, 2. as the Idealized model (EMIL, Garny et al., 2020), 3. as a GCM including a simplified chemistry mechanism, as it is done in the current study (basic methane chemistry using the CH₄ submodel, described below), or 4. with a comprehensive, interactive multi-phase (i.e., gas, liquid, aerosol) atmospheric chemistry, involving the submodels Module Efficiently Calculating the Chemistry of the Atmosphere (MECCA, Sander et al., 2005, 2011), SCAVening (SCAV, Tost et al., 2006), as well as the aerosol submodels GMXE (Pringle et al., 2010) or MADE3 (Kaiser et al., 2014), and various submodels for on- and offline emissions. Moreover, EMAC can be optionally coupled to an O-GCM (Pozzer et al., 2011) or to a mixed layer ocean (Kunze et al., 2014; original code by Roeckner et al., 1995). In order to represent the observed or forecasted meteorology, EMAC can be nudged by Newtonian relaxation towards the reanalysis, analysis and forecast data provided by the European Centre for Medium-Range Weather Forecasts (ECMWF).

The present study applies the MESSy submodels CH₄ (Eichinger et al., 2015; Winterstein and Jöckel, 2021) to calculate the basic chemical processes of methane and its isotopologues. Section 3.1.3 introduces the CH₄ submodel and includes a description of those submodels, which are additionally related to either methane sink processes or the inclusion of methane emission inventories, i.e. the submodels JVAL (Sander et al., 2014), for calculating the methane photolysis rate, Dry DEposition (DDEP, Kerkweg et al., 2006a), and the submodels OFFEMIS (Kerkweg and Jöckel, 2012b) and IMPORT_GRID (Kerkweg and Jöckel, 2015). For my studies, I additionally used the MESSy submodels TREXP (Jöckel et al., 2010) for defining new point source tracers and the submodel S4D (Jöckel et al., 2010) concerning the online sampling of the model output along flight tracks (e.g. of research aircraft). These submodels are described as part of the model setup description in the respective Chapter 4.

3.1.3 The submodel CH₄

The MESSy submodel CH₄ (Eichinger et al., 2015; Winterstein and Jöckel, 2021) calculates a simplified methane chemistry, i.e. the main sink reactions of CH₄ with OH, Cl, O(¹D) and direct photolysis. The sink reactants OH, Cl, O(¹D) are provided offline as

prescribed fields, which can be derived from previous atmospheric chemistry simulations. The MESSy submodel MECCA (Sander et al., 2005) in contrast, solves the system of ordinary differential equations (ODEs), which describe a detailed kinetic system of chemical reactions. In this way, OH, O(¹D) and Cl concentrations are simulated interactively. The CH₄ submodel can also be one-way coupled to MECCA. Thereby, the sink reaction partners are online calculated by MECCA and used by the CH₄ submodel. Conversely, MECCA is not affected by the CH₄ submodel. Thus, no feedbacks onto the sinks and between the hydrological cycle are considered. However, there is an option of the CH₄ submodel to feedback onto H₂O, in order to account for the water vapour produced by methane oxidation, which is an important water source in the stratosphere. The simulation of only the basic methane mechanisms, has the advantage of reducing the computational demand. About 8.3 times less nodes-h per simulated year are consumed by using the CH₄ submodel compared to the simulation with MECCA (Winterstein and Jöckel, 2021). In the present study all simulations use prescribed reactant fields in the submodel CH₄. The comprehensive chemistry submodels, such as MECCA or SCAV, are not used. Yet, the setup of the global simulations described in Chapter 6, considers the feedback onto H₂O.

The photolysis rate of methane is calculated by the MESSy submodel JVAL (Sander et al., 2014). The submodel CH₄ uses the methane photolysis rate calculated by JVAL. Alternatively, the photolysis rate could be prescribed offline. For the deposition of methane in soils, a constant deposition rate is normalized to a specific CH₄ mixing ratio of 1800 ppb (derived from Spahni et al., 2011) and multiplied with the actual CH₄ mixing ratio per grid cell. It is then prescribed via the MESSy submodel IMPORT_GRID.

The CH₄ submodel defines a methane master tracer, called CH₄_FX. Methane emission fluxes are read in via the MESSy submodel IMPORT_GRID (Kerkweg and Jöckel, 2015), which transforms emission fluxes to the computational grid of EMAC. The MESSy submodel OFFEMIS (Kerkweg and Jöckel, 2012b, therein described as OFFLEM) converts the emission fluxes into tracer tendencies and adds these to the CH₄_FX tracer tendency. In addition to the master tracer, tracers for different age and emission classes can be defined. Emission classes allow to split the CH₄_FX tracer into different sub tracers, e.g. total emission fluxes are subdivided according to their source category or regions where they are emitted. The allocation of emission fluxes to the individual emission class tracers is again handled via OFFEMIS. Similarly, different age classes can be defined to study the evolution of specific emissions over time. A single age class covers a defined time period. By the expiry of this time period, methane is moved from a previous age class to next age class (Winterstein and Jöckel, 2021). All emission and age classes are altered by the same sink reactions as the master tracer.

The CH₄ submodel can further simulate the four major methane carbon and hydrogen isotopologues, i.e. ¹²CH₄, ¹³CH₄, CH₄ and CH₃D. Therefore, emission fluxes are split into the respective fraction of the light and the heavy isotopologues and assigned to the corresponding tracers via OFFEMIS (CH₄_12C, CH₄_13C, CH₄_D0, CH₃_D1). In each case, they sum up to the master tracer CH₄_FX. All four tracers are subject to the same sink reaction by oxidation with OH, Cl, O(¹D) and by photolysis. The submodel CH₄ calculates the isotopic fractionation during these sink reactions by using the respective KIEs for the

reactions (see Table 2.2 in Chapter 2):

$$KIE = \frac{k_{12^C H_4+educt}}{k_{13^C H_4+educt}} \quad (3.1)$$

$$KIE = \frac{k_{CH_4+educt}}{k_{CH_3D+educt}} \quad (3.2)$$

with k being the reaction rate coefficient of the reaction with the respective educt OH, Cl, O(¹D) or $h\nu$. The submodel CH4 uses a constant KIE (listed Table 2.2) for the fractionation during the oxidation of methane in soils.

3.2 The global/regional n-times nested chemistry climate model MECO(n)

In order to simulated small scale meteorology and chemistry, down-scaling of the global EMAC model to smaller domains is required. The smaller model domains need suitable lateral boundary conditions. The regional COSMO/MESSy (Kerkweg and Jöckel, 2012a) model comprises the MESSy infrastructure, which is connected to the regional weather prediction and climate model of the Consortium for Small Scale Modelling (COSMO-CLM further denoted as COSMO, Rockel et al., 2008). The COSMO-CLM is the community model of the German regional climate research community jointly further developed by the CLM-Community. The implementation of the MESSy infrastructure allows for a coupling of the regional COSMO/MESSy model to the global EMAC model, which is realized as the model system MESSyified ECHAM and COSMO models nested n times (MECO(n), Kerkweg and Jöckel, 2012a,b; Mertens et al., 2016). The COSMO/MESSy model is thereby on-line coupled (so called "nesting") to EMAC. The on-line nesting approach is performed by the Multi-Model-Driver (MMD), which exchanges boundary conditions and initial conditions between the different model domains by using computer memory instead of off-line providing data from external files (Kerkweg and Jöckel, 2012b). The sub-submodel INT2COSMO interpolates the data of one model domain to match with the respective coarser or finer grid of the other model domain (Kerkweg and Jöckel, 2012b).

The COSMO/MESSy model domains can cover areas of different sizes and can have different spatial and temporal resolutions. Several domains can be applied at the same time. They are either distributed globally without any connection, or nested into each other. The latter implies an on-line nesting of two or more COSMO/MESSy model domains with decreasing size and increasing resolution, in order to reach a regional refinement at a specific location. Figure 3.1 shows an example of this nesting for three regional COSMO/MESSy domains (MECO(3)) covering the area over Europe, Central Europe and South-Western Poland, respectively. The global EMAC model serves as a driving model and provides the initial and boundary conditions for the largest COMSO/MESSy model domain over Europe. The subsequent COMSO/MESSy model domains derive their initial and boundary conditions from the respective coarser model domain. The simulation of chemical processes

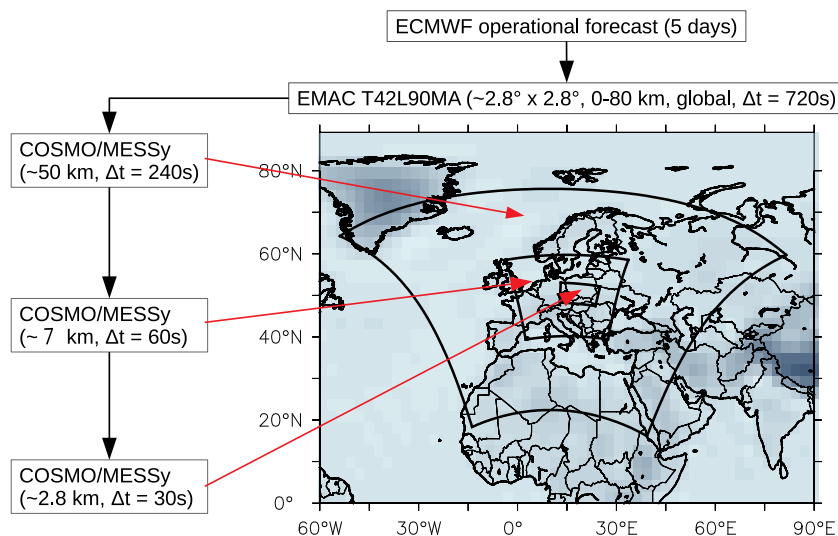


Figure 3.1: Example of the three-fold nesting with MECO(3), as it is applied for the study in Chapters 4 and 5: Overview of the different COSMO/MESSy model domains over Europe (CM50), Central Europe (CM7) and South-Western Poland (CM2.8). Each has a different spatial resolution and a different time step length. The exchange of initial and boundary conditions between the different COSMO/MESSy model domains is shown by the black arrows. The driving model EMAC is nudged towards ECMWF data for temperature, vorticity, divergence and the logarithm of surface pressure. Sea surface temperature (SST)/sea ice temperature (SIC) are prescribed as boundary conditions. The figure is derived from Nickl et al. (2020).

requires a high frequent data exchange between the individual model domains. Figure 3.2 illustrates the data exchange for the MECO(3) presented in Figure 3.1, which occurs at every time step of the respective coarser model domain. The shown example refers to the MECO(3) setup applied in Chapter 4 and 5. A detailed description of the setup of the model is therefore provided in the corresponding chapters.

3.3 The forecast system

As introduced in Chapter 1, parts of the presented study aims at forecasting the evolution of very localized methane emissions arising from coal mining ventilation shafts. To provide the forecasts with the appropriate initial conditions, a forecast system was developed, which is introduced in the following section. It has been already described and evaluated in the publication by Nickl et al. (2020): Hindcasting and forecasting of regional methane from coal mine emissions in the Upper Silesian Coal Basin using the online nested global regional chemistry–climate model MECO(n) (MESSy v2.53), *Geosci. Model Dev.*, 13, 1925–1943, <https://doi.org/10.5194/gmd-13-1925-2020>.

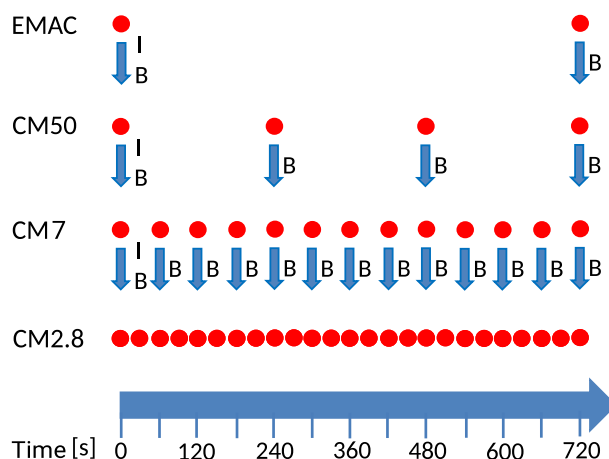


Figure 3.2: The illustration shows the initial (I) and boundary (B) data exchange (blue arrows) between EMAC and the different COSMO/MESSy model domains, shown in Figure 3.1. Data is exchanged at every model time step (red circles), of the respective coarser model domain. The illustration is taken from Nickl et al. (2020).

The forecasts are simulated by the three-fold nested global regional chemistry-climate model MECO(3). The global EMAC model (driving model) is nudged by Newtonian relaxation towards the ECMWF operational forecast data. The nudging is applied for temperature, vorticity, divergence and the logarithm of surface pressure. Additionally, the ECMWF operational forecast data of sea surface temperatures (SST) and sea ice temperatures (SIC) are prescribed as boundary conditions. Each forecast simulates a time period of 6 days. A forecast simulation, performed on an Intel Xeon E5-2680v3 based Linux Cluster (6 nodes à 12 dual cores) with 144 message passing interface (MPI) tasks, runs about 8 hours (Nickl et al., 2020).

The forecasts require initial conditions, which can be derived from a continuous analysis simulation. The analysis simulation uses the same model setup as the forecasts, but is nudged towards the ECMWF operational analysis data. Since operational analysis data include observations of the current state of the atmosphere, they are assumed to represent the real meteorology best. Every 12 hours a restart file is written, which triggers the forecast simulation and initializes all tracers. The nudging of EMAC is applied at every model time step (here 720 seconds). Yet, the nudging fields and the SST/SIC data for the analysis simulation are only available every 6 and 12 hours, respectively. Therefore, the nudging data is linearly interpolated in time. This, in turn, requires the data of two nudging time steps (i.e. 12 hours) ahead of the simulation time. An analysis simulation that starts a forecast at for example 00:00 UTC, uses the nudging data of the subsequent time steps 06:00 UTC and 12:00 UTC (Nickl et al., 2020). Consequently, a 6-day forecast is ready for post-processing 12 (two nudging time steps) plus 8 (simulation run time) hours after the forecast start time 00:00 UTC.

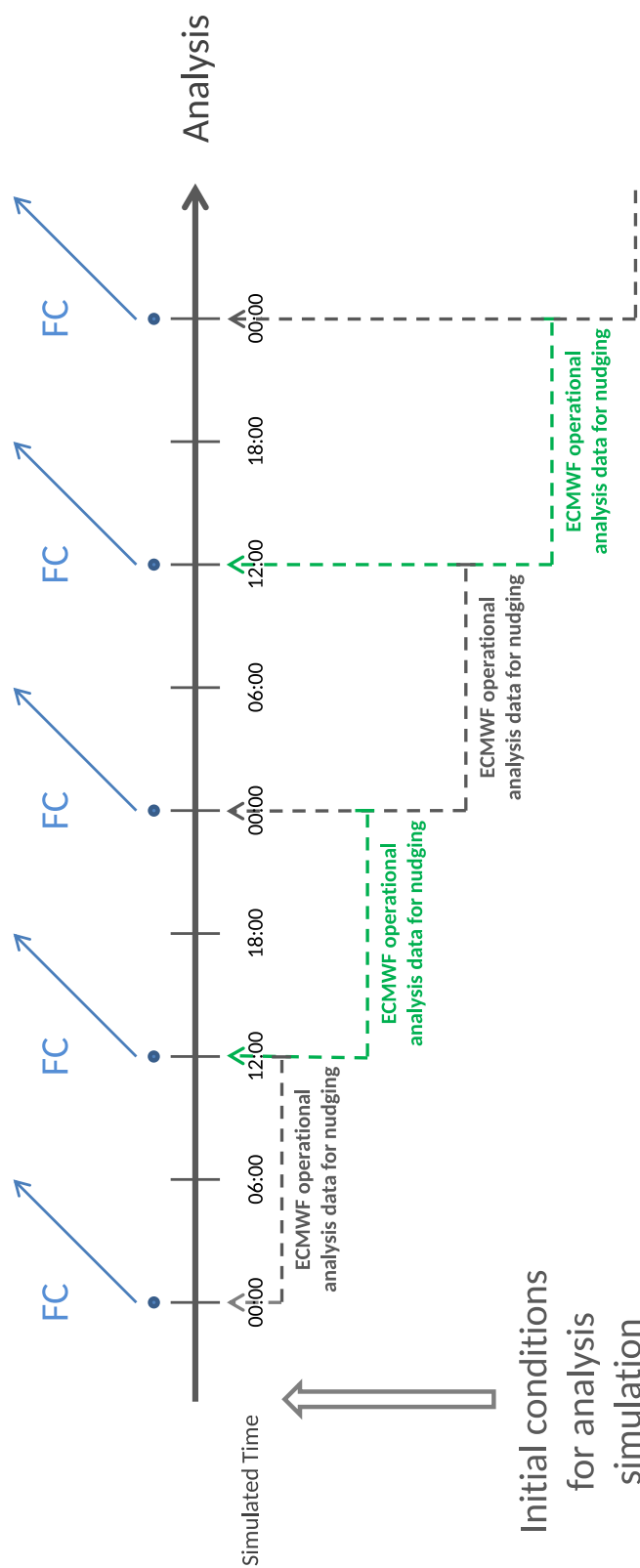


Figure 3.3: The illustration shows the nudging procedure of the 3-times nested global regional chemistry-climate MECO(3) forecast system. The dark grey arrow indicates the time evolution of an analysis simulation, which is nudged towards the ECMWF operational analysis data. Every 12 hours a forecast (blue arrows) branches from this analysis using its calculated tracer field for initialisation. By the time a forecast starts, the analysis simulation requires two time steps of the nudging data ahead this starting time (shown by the dotted green and grey arrows). Graphic derived from Nickl et al. (2020).

Chapter 4

Hind- and forecasting of regional methane emissions with MECO(n)

As introduced in Chapter 1 atmospheric methane is steadily increasing since 2007 and its growth even accelerated since 2014 (Nisbet et al., 2019; Fletcher and Schaefer, 2019). The causes of the recent methane increase are still under debate (Schwietzke et al., 2016; Schaefer et al., 2016; Nisbet et al., 2016, 2019; Worden et al., 2017; Rigby et al., 2017; Turner et al., 2017; Thompson et al., 2018; Howarth, 2019), i.e. uncertainties exist in the emission flux estimates of the individual sources, as well as in the quantification of the atmospheric sink (e.g. changes in OH concentrations). Top-down and bottom-up methane estimates still deviate strongly from each other (Saunois et al., 2020, see also Chapter 2). Filling the gap of these large uncertainties in the methane budget is essential for further action on climate change mitigation. Comprehensive measuring campaigns can help to better understand sources and sinks on regional scales and thereby contribute to a more precise data coverage on global scale. Such a measuring campaign, named Carbon Dioxide and Methane Mission (CoMet) 1.0, was carried out in 2018 to quantify local anthropogenic methane emissions in the Upper Silesian Coal Basin (USCB) in Poland, where high amounts of methane are emitted due to coal mining. Section 4.1 describes the CoMet 1.0 campaign and the corresponding study area in Poland.

To support the campaigns measurement strategies and to interpret the observed methane mixing ratios afterwards, reliable model-based forecasts and analysis simulations (i.e. model is constrained with observed meteorology after campaign to receive a “best guess” of the actual conditions) are required, respectively. To localize the methane plumes that arise from the coal mining ventilations shafts, the model needs to resolve small-scale features on regional scale. Yet, due to the coarse resolution, global climate models cannot resolve this. Therefore, the online coupled global and regional chemistry-climate model system “MESSy-fied ECHAM and COSMO models nested n times” (MECO(n); Kerkweg and Jöckel, 2012a,b; Mertens et al., 2016) is applied (see Chapter 3 for a detailed description of the MECO(n) model). Three COSMO/MESSy instances are nested into each other to simulate the region over the USCB. The finest resolved model domain has a spatial resolution of 2.8 km. Section 4.2 presents the corresponding model set-up and the implementation of

different methane tracers.

The presented study evaluates how well the MECO(3) model simulates the regional methane plumes and their distribution in the atmosphere. Thereby the results of the two finest resolved model instances are analysed with respect to several airborne observations taken during the CoMet 1.0 campaign. Since high-resolution simulations require a lot of computing time, it is further tested whether the results of the second model instance (spatial resolution of 7 km) performs equally well as the smallest model instance. Section 4.3.1 and Section 4.3.2 describe the different observations and their comparison to the model results, respectively. Moreover, for future campaigns it is also important to know until which day a forecast provides reliable results. Section 4.3.3 determines a forecast skill by comparing the individual forecast days with the analysis simulation, as well with the measurements sampled during the campaign.

The presented results have been already published by Nickl et al. (2020): Hindcasting and forecasting of regional methane from coal mine emissions in the Upper Silesian Coal Basin using the online nested global regional chemistry–climate model MECO(n) (MESSy v2.53), *Geosci. Model Dev.*, 13, 1925–1943, <https://doi.org/10.5194/gmd-13-1925-2020>.

The publication discusses the performance of MECO(3) to simulate local methane emissions and evaluates a forecast skill of the model. The same contents are presented in the current chapter. Most of the presented tables and figures are also taken or reconstructed from Nickl et al. (2020).

4.1 The CoMet Campaign

The Carbon Dioxide and Methane Mission (CoMet) is part of the AIRSPACE (Aircraft Remote Sensing of Greenhouse Gases with combined Passive and Active instruments) project, which is in turn involved in the validation of the French-German climate mission MERLIN (Methane Remote Sensing Lidar Mission). The project comprises data collection and evaluation for the validation and verification of satellite products (see <http://www.pa.op.dlr.de/AIRSPACE>).

CoMet aims to quantify carbon dioxide and methane emissions by using different measuring techniques, such as in-situ instruments, active and passive remote sensing and flask sampling. The measurements are accompanied by global and regional atmospheric modelling. Table 4.1 shows an overview of all involved instruments and models. A list of the involved research institutes and further information can be found on the CoMet website: <https://www.halo.dlr.de/science/missions/comet>. The mission concentrates on Central Europe and, particularly on the Upper Silesian Coal Basin (USCB) in Poland, next to the Czech and Slovenian borders (see map in Fig. 4.1). The USCB emits roughly 502 kt CH₄ yr⁻¹ due to hard coal mining (CoMet internal CH₄ and CO₂ emissions over Silesia, version 2 (2018-11), further denoted as CoMet ED v2). Since this is about 3 % of all European methane emissions, the region belongs to one of Europe's largest methane sources. Figure 4.1 shows the exact location of all known coal mining ventilation shafts, including

their approximate emission fluxes in the USCB.

Table 4.1: Overview of CoMet instrumentation (i.e. CHARM-F, JIG, JAS, MAMAP, CRDS, QCLS, C-AS, EM27/SUN) and the involved atmospheric models. The table lists only those instruments, that measure CH₄ and/or stable isotopes in CH₄.

Instrument	Technique	Measurement
Airborne on HALO		
CHARM-F (Amediek et al., 2017)	Active remote sensing	CH ₄ total column
JIG	Cavity Ring Down Spectroscopy (in-situ)	CH ₄ in-situ
JAS	Air sampler	CH ₄ , $\delta^{13}C(\text{CH}_4)$, $\delta D(\text{CH}_4)$ flasks
Airborne on FUB Cessna		
MAMAP (Gerilowski et al., 2011)	Passive remote sensing	CH ₄ total column
Airborne on DLR Cessna		
CRDS G1301-m	Cavity Ring Down Spectroscopy	CH ₄ in-situ
QCLS (Kostinek et al., 2019)	Quantum Cascade Laser Spectroscopy	CH ₄ in-situ
C-AS	Air sampler	CH ₄ , $\delta^{13}C(\text{CH}_4)$, $\delta D(\text{CH}_4)$ flasks
Ground-based		
EM27/SUN (mobile/stationary)	Passive remote sensing	CH ₄ total column
Modelling		
MECO(n)	regional/global modelling of CH ₄ and stable isotopologues, forecasts	
WRF-Stilt	regional modelling, inverse modelling	

The first campaign CoMet 0.5 took place in August 2017 and comprised ground-based passive remote sensing and in-situ measurements, as well as air core samples. CoMet 1.0 was carried out during May and June 2018 and additionally included airborne measurements collected in-situ, by flask sampling, and by active and passive remote sensing. Next to CH₄ and CO₂, stable isotopes were sampled within detected methane plumes and in the individual coal mine ventilation shafts. First results of the ground-based and airborne passive remote sensing measurements are published by Luther et al. (2019) and Krautwurst et al. (2021), respectively. Fiehn et al. (2020) and Kostinek et al. (2021) present methane emission estimates of the USCB based on in-situ observations. Gałkowski et al. (2021b) presents airborne in-situ and laboratory analysed air samples, including also stable isotope measurements of methane. Wolff et al. (2021) provides CO₂ emission estimates based on airborne active remote sensing of coal-fired power plants. Additionally, wind was measured by stationary ground-based active remote sensing (wind lidar). The results are discussed by Wildmann et al. (2020). Throughout the campaign, 12-hourly 6-day forecasts simulated by the MECO(3) model were successfully provided. The forecasts simulated the distribution of the methane plumes, which are emitted by the ventilation shafts and helped to develop flight planning strategies. Nickl et al. (2020) analysed the forecast and model performances. Further model activities are carried out with respect to CO₂ emissions. Chen et al. (2020) presents short-term forecasts of biospheric CO₂.

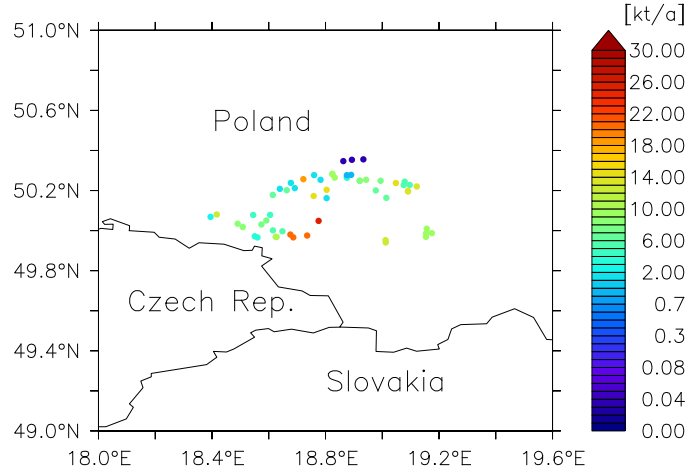


Figure 4.1: Exact locations of the coal mining ventilation shafts in the USCBA (Poland), including the annual emitted CH₄ in tons per year (according to CoMet ED v1 inventory based on E-PRTR, 2014). Map from Nickl et al. (2020).

4.2 Model setup

As described above, the presented study aims to simulate very localized methane emissions on regional scale. Therefore the global/regional 3-times nested, on-line coupled chemistry climate model MECO(3) is used for the simulation. A detailed description of MECO(n) is provided in Chapter 3. The following section describes the specific model setup as used for all analysis and forecast simulations.

4.2.1 The MECO(3) setup for the CoMet 1.0 simulations

The global chemistry climate model EMAC is used as a driving model for the MECO(3) model. It is operated with a 90-layer vertical resolution covering the atmosphere from the surface up to an altitude of 80 km, a T42 spectral resolution and a time step length of 720 s. Three COSMO/MESSy model instances are nested into each other to simulate the USCBA area over Poland (see Figure 3.1 in Section 3.2). The first COSMO/MESSy instance covers the area over Europe and has a spatial resolution of 0.44° (~50 km) and a time step length of 240 s (it is further denoted as CM50). The next finer resolved instance (further denoted as CM7) covers the area over Central Europe and has a spatial resolution of 0.0625° (~7 km) and a time step length of 60 s. The finest resolved instance simulates the USCBA with a spatial resolution of 0.025° (~2.8 km) and a time step length of 30 s. It is further denoted as CM2.8. CM50 and CM7 are operated with 40 vertical layers. The model instance CM2.8 is operated with 50 vertical layers up to an altitude of 22 km. At 11

km a sponge zone begins, which reaches the model top and nudges the model prognostic variables with increasing weights towards the driving model.

4.2.2 Methane tracer

To quantify the coal mining emissions in the USCB, it is important to identify those emissions, which actually arise from the coal mining. Therefore, two independent tracers are used to simulate the methane fluxes in the conducted simulations of the presented study. The first tracer, called CH4_FX, includes all emission fluxes, i.e. anthropogenic and natural emissions, as well as an influx of methane at the lateral domain boundaries from the respective coarser model. In addition to the local emissions (presumably from coal mining), this results in a background level of methane, which is emitted globally from all methane sources and advects into the USCB area. The second tracer is called PCH4 and only simulates the local methane emissions from the various coal mining ventilations shafts in the USCB (see Figure 4.1). Comparing the results of this second PCH4 tracer to the results of the CH4_FX tracer, or to observations, allows for tracing back simulated or observed methane enhancements to the coal mine emissions. The tracers are initialized equally for the EMAC model and the three COSMO/MESSy instances. The following section describes the emission inventories and MESSy submodels used for the simulation of the two tracers. Figure 4.2 presents how the two tracers are defined and handled by the different submodels.

The master tracer CH4_FX

The CH4_FX tracer uses gridded methane emissions from a combined emission inventory. The natural emissions are derived from the EMPA inventory (Frank, 2018) and are available as monthly averages on a $1.0^\circ \times 1.0^\circ$ grid. For the anthropogenic emissions, the EDGAR v2FT2010 (Janssens-Maenhout et al., 2013) inventory is used. These emissions are monthly averages with a finer grid resolution of $0.1^\circ \times 0.1^\circ$. Since both inventories are only available until the year 2012, this year is used to simulate the year 2018, when the CoMet 1.0 campaign took place. For the initialization of the CH4_FX tracer, a monthly climatological average (2007 to 2016) derived from the simulation SC1SD-base-01 (similar to the RC1SD-base-10 simulation, described by Jöckel et al., 2016), is used. The MESSy submodels IMPORT_GRID (Kerkweg and Jöckel, 2015) and OFFFEMIS (OFFFEMIS, Kerkweg and Jöckel, 2012b, therein described as OFFLEM) are used to transform the emissions to the actual computational grid and convert the emission fluxes into tracer tendencies of the CH4_FX tracer, respectively. The CH4 submodel calculates the basic methane chemistry, as described in Chapter 3. The reaction partners OH, O¹D and Cl for the oxidation of methane (chemical loss) are predefined and derived as monthly averages (2007-2016) from a previous interactive chemistry simulation. They are read in again via the submodel IMPORT_GRID. The rate for the depletion by photolysis is calculated by the submodel JVAL (Sander et al., 2014).

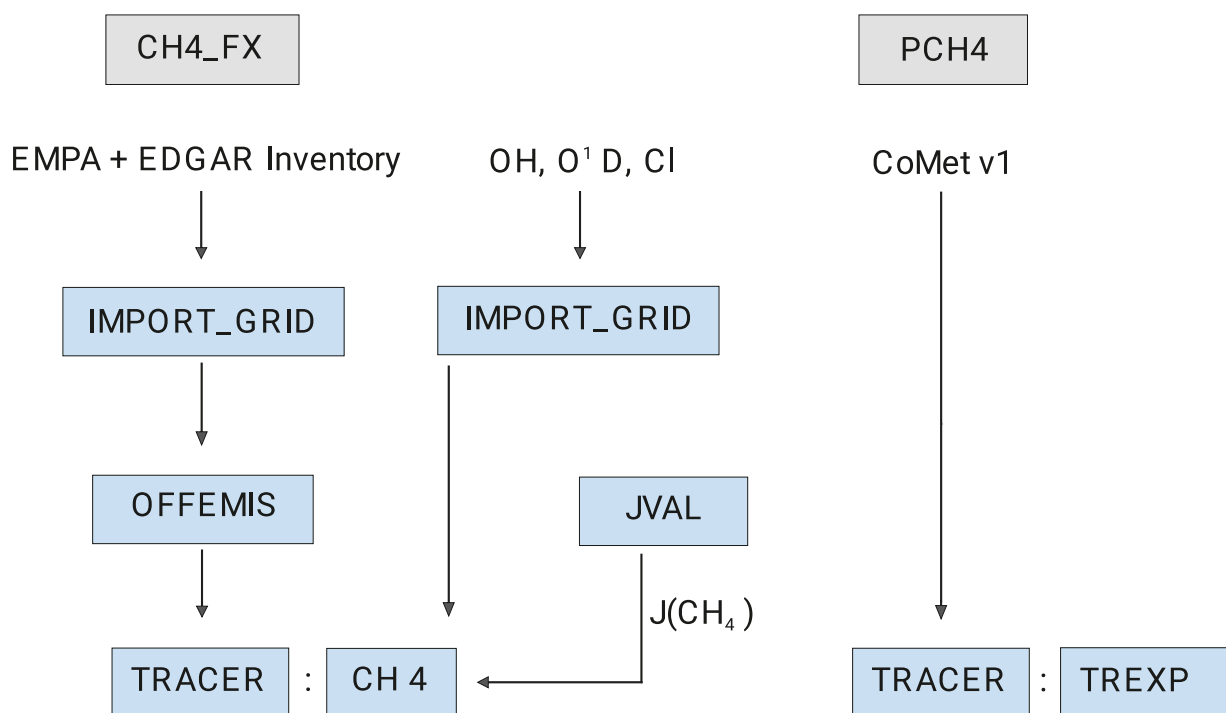


Figure 4.2: Illustration of submodels which are used for the different methane tracers. CH4_FX tracer (left side): Methane emission data and the oxidation reaction partners OH, O¹D and Cl are read from the netcdf files and transformed to the computational grid by the submodel IMPORT_GRID. OFFFEMIS converts the emission fluxes into tracer tendencies, and the CH4 submodel simulates the chemical loss of methane using the predefined fields of the oxidation partners and the calculated photolysis rate from the submodel JVAL. PCH4 (right side): submodel TRESP is used for the point source emissions and tracer definition. Illustration and caption from Nickl et al. (2020).

The point source tracer PCH4

The point source emission fluxes for the PCH4 tracer are taken from the CoMet ED v1 inventory, which is mainly based on the European Pollutant Release and Transfer Register (E-PRTR, 2014) and on data from Wyzszy Urzad Gorniczny 2014 (2017). The emissions are given for the single coal mines, and are split equally between the corresponding ventilation shafts. The exact locations of the ventilation shafts are shown in Figure 4.1. The point sources are defined by the submodel TRESP (Jöckel et al., 2010), which DESCRIPTION HERE. The initial conditions are zero and no chemical sink reactions are calculated for the PCH4 tracer. Furthermore, it is independent from the CH4_FX tracer.

4.2.3 Simulations of the CoMet 1.0 campaign

Throughout the CoMet 1.0 campaign 6-day forecasts were delivered every 12 hours. Chapter 3 describes the forecast system, which is used to perform the forecast simulations. A

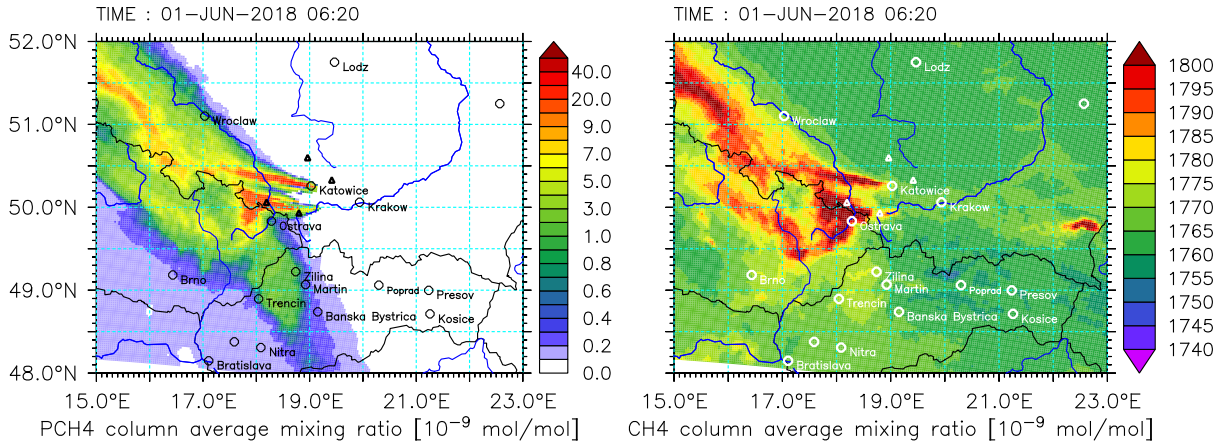


Figure 4.3: Snapshot of a CMet 1.0 forecast showing the total column dry air average mixing ratio in nmol/mol in the USC in Poland. In both panels CH_4 was simulated with the finest resolved COSMO/MESSy instance CM2.8, by the point source tracer PCH4 (left panel) and by the total methane tracer CH4_FX (right panel). Note that the colour bar on the left panel is pseudo logarithmic for a better visualization. Figure from Nickl et al. (2020).

continuous analysis simulation is performed starting in April, 1st 2018. Since the campaign started on May, 15 2018, this results in a spin up time of 45 days. The EMAC model is nudged by Newtonian relaxation of temperature, vorticity, divergence and the logarithm of surface pressure towards the 6-hourly ECMWF operational analysis data. SST and SIC are prescribed and derived from the same data set. The forecasts branch from the analysis simulation every twelve hours and are thereby initialized from its restart files. In the forecast simulations, the EMAC model is nudged towards the ECMWF operational forecast data. A detailed explanation is given in Section 3.3.

The forecasts assisted the flight planing strategy (for airborne measurements) during the CoMet 1.0 campaign and were made available on a website. Figure 4.3 gives an example of one of the forecast products, i.e. the vertical integrated methane mixing ratios X_{PCH_4} (left side) and X_{CH_4} (right side), simulated over the smallest model domain by the CM2.8 instance for the PCH4 and the CH4_FX tracer, respectively:

$$X_{\text{PCH}_4}, X_{\text{CH}_4} = \frac{\sum(\chi_{\text{CH}_4} \cdot m_{\text{dry}})}{\sum m_{\text{dry}}} \quad (4.1)$$

with χ_{CH_4} being the methane mixing ratio PCH4 or CH4_FX and m_{dry} being the mass of dry air in a grid box. The summation is carried out over all vertical levels (or a specific altitude, see Section 4.3.2).

S4D model output

In the presented study, the analysis simulation is evaluated to determine the general performance of MECO(3) to simulate the small scale pattern and local methane emissions. Due to the applied nudging with the ECMWF operational analysis data, the analysis simulation is assumed to reproduce the observed meteorology best. The forecast ability of MECO(3) is tested by analysing the individual forecast days. In each case, model results are compared to the observations sampled during the campaign on board of two research aircraft (HALO and D-FDLR Cessna). The MESSy submodel S4D (Jöckel et al., 2010) allows for the online sampling of the model results along a specific track of a moving object, such as aircraft or ships. Therefore, the analysis simulation, as well as all forecast simulations are repeated, including the specific geographical flight track coordinates (in degrees), pressure altitudes (in hPa) and time steps (in UTC) of all flights (see Table 4.2) for the S4D submodel. The S4D submodel interpolates the simulation data horizontally (and optionally also vertically) to the track and samples the output at every time step of the model, i.e. every 720 s, 240 s, 60 s and 30 s for EMAC, CM50, CM7 and CM2.8, respectively.

4.3 Evaluation of the model skill

As described above, the analysis simulation is evaluated with respect to the general performance of MECO(3) to reproduce the observed methane mixing ratios in the atmosphere and the local methane emissions. Therefore the simulations are compared to the observations sampled during the CoMet Campaign 1.0. Section 4.3.1 gives an overview of the different measurements used for the analysis. Moreover, results from the different COSMO/Modular Earth Submodel System (MESSy) instances are compared to each other. The evaluation in this study only considers the two finest COSMO/MESSy instances CM7 and CM2.8. The aim is to examine which model instance is sufficient for the purpose of the campaign. Section 4.3.2 discusses the results of the analysis comparison. Finally, for the campaign planning it is important to know, how long a forecast is reliable. In Section 4.3.3 a forecast skill is calculated and discusses.

4.3.1 Observations

To evaluate the models' performance and forecast skill, observational data of three different measuring techniques (during CoMet 1.0) are compared to the model results:

- Active remote sensing using the Integrated Path Differential Absorption (IPDA) Lidar called CHARM-F (Amediek et al., 2017) on board of HALO, operated by the German Aerospace Center (DLR) in Oberpfaffenhofen (personal communication A. Amediek).

Table 4.2: Overview of all observational methane data sets used for the comparison with the model results. It lists the name of aircraft, date of flight, respective measuring instrument and type of measurement, i.e. XCH_4 (integrated vertically) or in-situ).

Name	Aircraft	Flight date	Instrument	Measurement type
C1	HALO	6th of June 2018	CHARM-F	total column
C2	HALO	7th of June 2018	CHARM-F	total column
J1	HALO	6th of June 2018	JIG (with Picarro CRDS G2401-m)	in-situ
J2	HALO	7th of June 2018	JIG (with Picarro CRDS G2401-m)	in-situ
P1	D-FDLR	29th of May 2018	Picarro CRDS G1301-m	in-situ
P2	D-FDLR	1st of June 2018	Picarro CRDS G1301-m	in-situ
P3	D-FDLR	5th of June 2018	Picarro CRDS G1301-m	in-situ
P4	D-FDLR	6th of June 2018, morning	Picarro CRDS G1301-m	in-situ
P5	D-FDLR	6th of June 2018, afternoon	Picarro CRDS G1301-m	in-situ
P6	D-FDLR	7th of June 2018	Picarro CRDS G1301-m	in-situ
P7	D-FDLR	11th of June 2018	Picarro CRDS G1301-m	in-situ

- In-situ by Cavity Ring Down Spectroscopy (CRDS) using a JIG instrument (Jena Instrument for Greenhouse Gases, Filges et al., 2015) on board of HALO and operated by the Max-Planck Institute for Biogeochemistry in Jena (Gałkowski et al., 2021b).
- In-situ by Cavity Ring Down Spectroscopy (CRDS) installed on board of DLR Cessna and operated by the atmospheric trace gas research group of the Institute of Atmospheric Physics (DLR, P4 and P5 published in Fiehn et al., 2020, all other: personal communication with A. Fiehn).

Table 4.2 lists the different observations including the date, they were sampled.

Total column

Measurements taken with the CHARM-F lidar (Amediek et al., 2017) on board of HALO D-ADLR provide weighted atmospheric columns of the methane dry-air mixing ratio from the surface to the flight altitude of the research aircraft (XCH_4). During the two flights C1 and C2 (on 6th and 7th of June 2018, respectively; see Table 4.2), HALO flew within the USCB area and sampled several methane plumes arising from the coal mining ventilation shafts. The data sets have a temporal resolution of 1 s and are smoothed horizontally with a box window corresponding to 2 km of flight distance.

In-situ

Additionally, on board of HALO, methane was sampled in-situ by Cavity Ring Down Spectroscopy (CRDS) with a Picarro CRDS G2401-m instrument. The two flights J1 and J2 (see Table 4.2) are compared to the model results. Again, J1 and J2 were sampled on the 6th and the 7th of June 2018, respectively. However, the samples were collected in the

afternoon, when HALO flew larger scale patterns within the USCB, and outside Poland in the Czech Republic (see Figure 4.4). Due to descending and ascending flight pattern, measurements were sampled at different altitude representing the vertical distribution of methane in the atmosphere. The data sets have a temporal resolution of 1 s.

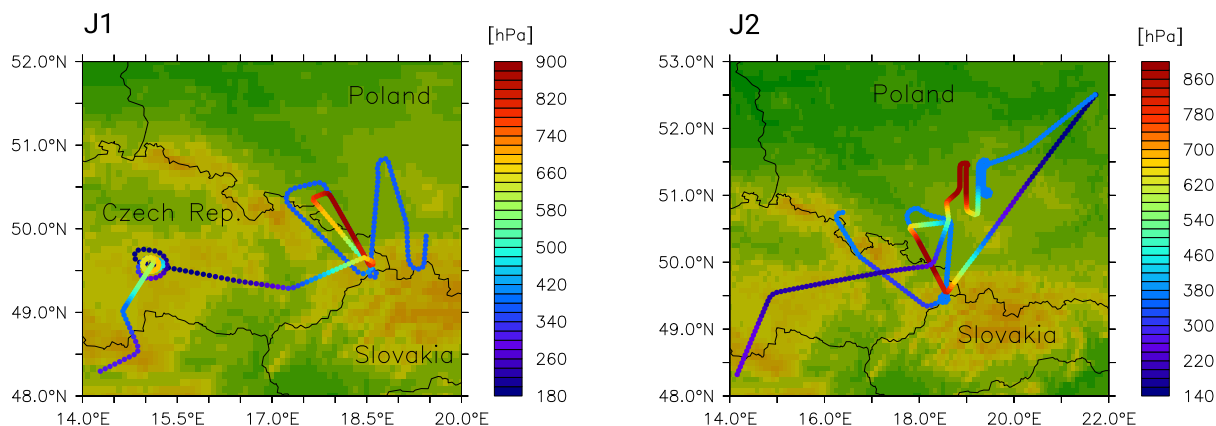


Figure 4.4: HALO flight routes of J1 (left panel) and J2 (right panel) over Czech Republic and Poland. The colour bar gives the atmospheric pressure at flight level. Maps from Nickl et al. (2020).

Further in-situ measurements are derived from the Picarro CRDS G1301-m instrument on board of the Cessna 208B (D-FDLR). Seven airborne observations (P1-P7, see Table 4.2) are compared to the model results. The aircraft flew only within the USCB area, close to the coal mines (see Figure 4.5). In contrast to the JIG data, here smaller-scaled patterns and the methane plumes arising from the ventilation shafts were sampled. The aircraft surrounded the USCB and flew a back-and-forth patterns (so called “walls”) along horizontal tracks downwind of the coal mines. Thereby it crossed the methane plumes several times at different heights. The data are derived in a temporal resolution of 1 s.

4.3.2 Evaluation of the analysis simulation

The above described observations are now compared to the analysis simulations. Since the three datasets differ in terms of geographical extent, duration and sampling patterns, the performance of the model is analysed depending on the measurement type; i.e. vertically weighted integrated methane (CHARM-F), vertical distribution of methane in the atmosphere (in-situ, JIG), and representativeness of local methane emissions on small scales (in-situ, D-FDLR).

All data are analysed with respect to pattern similarity and amplitude of the CH₄FX tracer, i.e. root mean square error (RMSE), standard deviation, correlation coefficient and

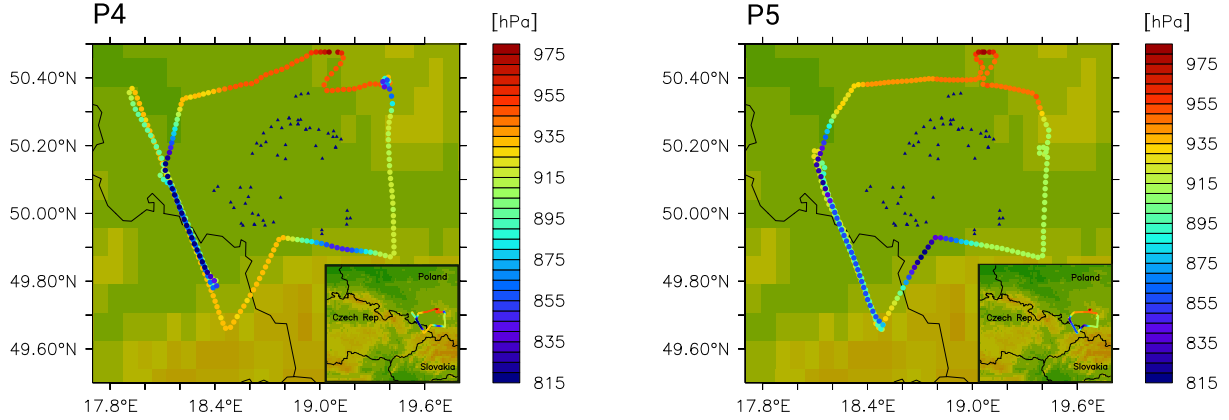


Figure 4.5: D-FDLR flight routes of P4 (left panel) and P5 (right panel) in the USCIB. The colour bar gives the atmospheric pressure at flight level. Maps from Nickl et al. (2020).

normalized mean bias error (NMBE). The NMBE is calculated as follows:

$$NMBE = \frac{\sum_{i=1}^n (\chi_{sim} - \chi_{obs})_i}{n \cdot \bar{\chi}_{obs}} \cdot 100 \quad (4.2)$$

with χ_{sim} being the simulated methane mixing ratio, χ_{obs} being the observed methane mixing ratio, and n being the number of the models' time steps. Since the observed data have a finer temporal resolution than the model output, they are averaged over 60 s for the CM7 and over 30 s for the CM2.8 inter comparison, respectively.

The first comparison to the observations revealed a systematic bias towards lower methane mixing ratios of all simulated CH₄FX results. The initial conditions used for the CH₄FX tracer were derived as monthly climatological average of the time period 2007 until 2016. The CoMet 1.0 campaign, however, took place in 2018. Since global methane mixing ratios are increasing steadily since 2007 (Nisbet et al., 2019), this bias is likely caused by lower initial methane mixing ratios, taken from the time period before 2016. The OH field is also initialized as a monthly climatological mean (2007-2016) from the same simulation. Furthermore, methane emissions are taken from the year 2012 instead of the year 2018. However, the MECO(3) simulations only cover a short time period of three months. An overestimation of the OH sink or an underestimation of emission fluxes should therefore not have a significant influence on global background methane mixing ratios, and do not explain the observed bias.

The deviations in the background methane are neglected for the rest of the evaluation. This is justified by the fact that the main objective of the study is, to investigate how well MECO(3) is able to simulate the regional distribution of the methane plumes from

Table 4.3: Results of the statistical analysis of the measurements compared to the model results of the two model instances CM7 and CM2.8. Listed are the root mean square error (RMSE) in $\mu\text{mol mol}^{-1}$, the normalized mean bias error (NMBE) in percent, and the correlation coefficient (R). Values taken from Nickl et al. (2020).

Name	RMSE _{CM7}	RMSE _{CM2.8}	NMBE _{CM7}	NMBE _{CM2.8}	R _{CM7}	R _{CM2.8}
C1	0.08	0.08	-4.1	-4.2	0.47	0.47
C2	0.10	0.10	-5.3	-5.3	0.75	0.75
J1	0.02	0.02	-0.29	-0.06	0.78	0.70
J2	0.02	0.03	0.08	-0.04	0.88	0.77
P4	0.06	0.07	1.30	1.88	0.77	0.84
P5	0.05	0.05	1.17	1.18	0.76	0.68

local sources. Therefore, a bias correction is applied to all model results involved in the statistical comparisons with the in-situ observations. For the bias correction the most frequently occurring difference between all D-FDLR in-situ observations and the model results of instance CM2.8 (i.e. $0.108 \mu\text{mol mol}^{-1}$) is used.

The offset between the CHARM-F observations and the model results is less than $0.108 \mu\text{mol mol}^{-1}$. Moreover, it is difficult to determine a definite bias. For the comparison with the CHARM-F measurements, the S4D submodel output is vertically integrated between the surface and aircraft altitude (see Equation 4.1, further denoted as $X_{fl}\text{CH}_4$). The irregularities in the background bias might occur due to the integration over a varying number of model levels or due to changes of topography, which are not resolved by the model. The bias correction is therefore not applied to the simulated $X_{fl}\text{CH}_4$.

The Table 4.3 lists the results of the statistical analysis for the 6 flights that took place on the 6th and 7th of July. These two days were the most successful measurement days of the campaign. Although several other in-situ measurements were carried out on board of the D-FDLR Cessna, only the flights P4 and P5 on the 6th of June (morning and afternoon) are listed. Both measurements were used for the estimation of the USCB emissions in the study by Fiehn et al. (2020). The meteorological conditions here were most favourable to measure the methane plumes downwind the ventilation shafts (personal communication A. Fiehn). However, the following discussion also addresses the other flights, in order to explain mismatches between model and observations.

RMSE and NMBE provide information on how far the model and the observations deviate from each other on average. In the case of the CHARM-F data, this is mostly owed to the overall offset in the background (discussed above). However, due to the bias correction applied for the comparison with the in-situ observations, RMSE and NMBE also indicate differences in amplitudes. Of course, this also applies to the CHARM-F data.

The Taylor diagram in Figure 4.6 summarizes the comparison of all three analyses,

including also the comparisons to P1, P2, P3, P6 and P7. It combines three statistical metrics: standard deviation (radial distance from the origin), correlation coefficient (angle) and centered RMSE (dashed semi circles) in a single diagram (Taylor, 2001). The standard deviation and the centred RMSE (NRMSE) are normalized, to become non-dimensional. This allows for the comparison of the different model results, with respect to amplitude (standard deviation) and pattern (correlation) similarity. In the following section, the results of all individual comparisons with the observations are discussed.

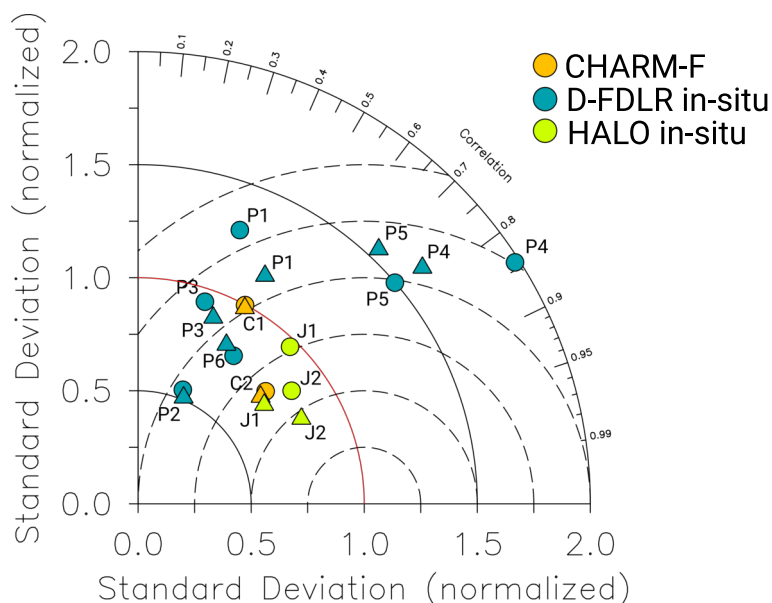


Figure 4.6: Taylor diagram summarizing the statistical comparison of the MECO(3) model results (analysis simulation) with the observations. It combines the normalized standard deviation (radius), correlation coefficient (angle) and centered NRMSE (dashed semi circles). Triangles and circles mark the results for the model instances CM7 and CM2.8, respectively. The comparisons to C1 and C2 are shown in orange, those to P1 until P6 in blue, and those to J1 and J2 in green. The normalized standard deviation of 1 outlines the point where model results fit perfectly the observations. Figure from Nickl et al. (2020).

Comparison to CHARM-F measurements

Figure 4.7 shows the observed $X_{fl}CH_4$ of the two data sets C1 and C2 compared to the simulated $X_{fl}CH_4$. The results are shown for the two instances CM7 and CM2.8, respectively. All model results are biased towards smaller values compared to the observations. The corresponding NMBEs in Table 4.3 range from -4.1 % to -5.3 % for C1 and C2, respectively. The differences between the two model instances are rather small. Besides the overall bias, which is already discussed above, the model results agree well with the observed patterns. All $X_{fl}CH_4$ peaks are represented by the simulations and show similar amplitudes. For C2 the observed amplitudes are larger than those of the model results.

This is also confirmed by the normalized standard deviations presented in the Taylor diagram (Figure 4.6). The corresponding data points are slightly below the reference line, which means that the standard deviation of the model results are lower than the standard deviation of the observations. In contrast, data points of C1 lie on the reference line, indicating that both, observations and simulations have the same mean amplitude. The calculated NMBE and RMSE (see Table 4.3) mainly represent the continuous bias between model results and observations. However the values are lower for C1, which shows, that the simulated amplitudes agree best with the C1 observations. In contrast, the correlation is higher with the C2 observation. The correlation coefficient for the comparison with C1 is only 0.47. Around 09:30 UTC on June 6th (C1), the model results are slightly shifted in time. Additionally, the observed $X_{fl}CH_4$ follow a negative trend until 10:10 UTC, which is not represented by the model.

However, in general the MECO(3) model is able to simulate the observed $X_{fl}CH_4$ reasonably well. Overall, the two model instances CM7 and CM2.8 yield similar results. The performances in comparison with the measurements are of equal quality. Therefore, and as the simulation of the finest model instance CM2.8 consumes more computational time, it is sufficient to conduct future simulations (for this campaign purpose or similar campaign analyses) with the CM7 model instance only.

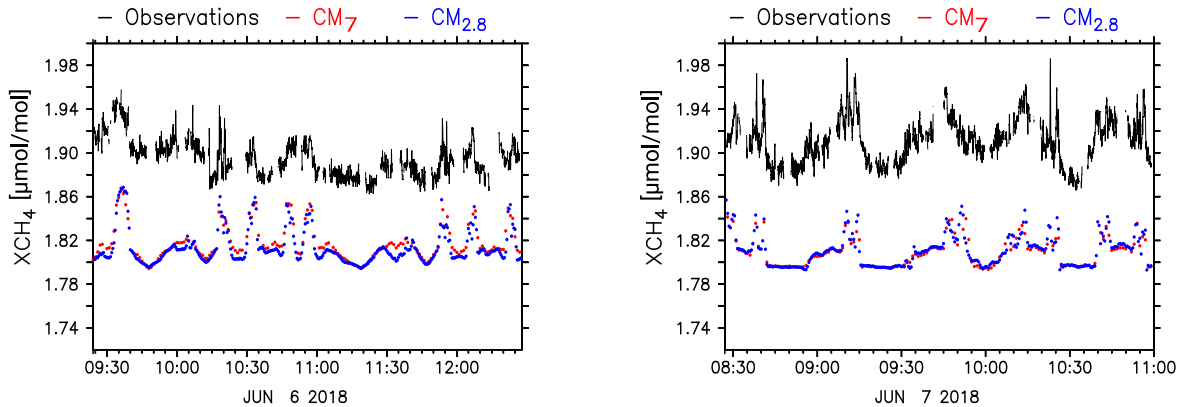


Figure 4.7: Comparison of the CHARM-F measurements and the S4D submodel output (CM7 and CM2.8) sampled along C1 (left panel) and C2 (right panel). The results show the vertically integrated mixing ratios $X_{fl}CH_4$ in $\mu\text{mol}/\text{mol}$. The time axes is in UTC. Figure from Nickl et al. (2020).

Comparison to JIG measurements

For the comparisons with the in-situ observation, the S4D submodel output is sub-sampled onto the flight altitude by linear interpolation. Figure 4.8 (upper panels) compares the re-

sulting methane mixing ratios of the CH₄.FX tracer to the data sets J1 and J2. Again, only the results of the two model instances CM7 and CM2.8 are shown. Since the measurements cover larger areas outside the USCB, the mixing ratios simulated by the CM2.8 model instance, have several gaps in the model output. These gaps mark the aircraft leaving the model domain (i.e. the USCB area) temporally. In the lower panels, the aircrafts' atmospheric pressure altitude along the respective flight tracks is plotted. The pressure follows a steep up-and-down movement between 900 and 200 hPa, indicating changes in the flight altitude. As mentioned in Section 4.3.1, these flight patterns were chosen to sample the vertical profile of methane in the atmosphere. Both, observed and simulated methane mixing ratios correlate closely with atmospheric pressure, i.e. lower mixing ratios with higher altitudes and higher mixing ratios with lower altitudes. This shows that the vertical gradient of methane in the atmosphere is well represented by both model instances (see also Figure 4.9). The data points of J1 and J2 in the Taylor diagram (see Figure 4.6) are close to the reference point on the horizontal axis. The correlation coefficients are very high, which is especially true for the CM7 model instance. The methane variability at low altitudes is well represented by both model instances CM7 and CM2.8, which are generally in good agreement with each other and the observations.

However, the model does not resolve the fine structures of the observations around 200 hPa (e.g. at 13:20 UTC (J1) or at 12:00 and 14:30 UTC (J2) in Figure 4.8). The methane mixing ratios at these altitudes are strongly influenced by the global models' boundary conditions, which makes it difficult for the model to reproduce the observed features. Furthermore, the small-scale fluctuations, which are measured at 400 hPa, are not simulated by the two model instances CM7 and CM2.8.

Overall, the comparison to J1 and J2 is the best in the Taylor diagram. Presumably because the horizontal distribution of the methane plumes plays only a minor role in the JIG observations in contrast to the CHARM-F and D-FDLR Cessna observations. Similar to the comparison with the CHARM-F measurements, the two model domains CM2.8 and CM7 perform equally well.

Comparison to Cessna

Similar to the comparison with the JIG observations, the curtains sampled with the S4D submodel along the flight tracks, are further sub-sampled onto the flight altitude by linear interpolation. Figure 4.10 (upper panels) shows the comparison of the CH₄.FX tracer simulated by the two model instances CM7 and CM2.8 with the observations P4 and P5. The measurements feature several enhancements in the methane mixing ratio relative to the background. These peaks are indicative of the methane plumes sampled along the flight paths near the USCB coal mines. The background methane shows little variations.

In general, the patterns of the model results and the observations agree well. The simulated peaks along the P4 trajectory are close to or larger than the observations. In particular, the peaks simulated by the CM2.8 model instance exceed those of the observations and those of the CM7 model instance. Consequently, the resulting NMBE are positive and differ between the CM7 and CM2.8 model instance, with 1.30 % and 1.88 %, respectively.

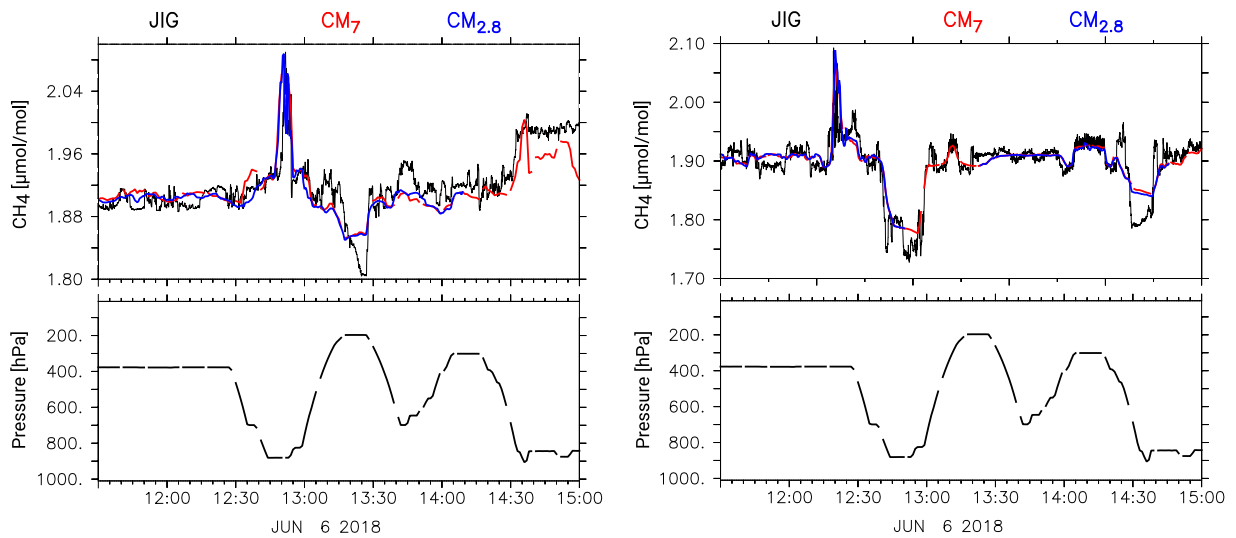


Figure 4.8: Comparison of the JIG in-situ measurements and the S4D submodel output (CM7 and CM2.8) sampled along J1 (left panel) and J2 (right panel). Results show methane mixing ratios in $\mu\text{mol/mol}$. Note that the model results are bias corrected. The lower panels display the aircrafts' atmospheric pressure altitude along the flight tracks in hPa. The time axis is in UTC. Figure from Nickl et al. (2020).

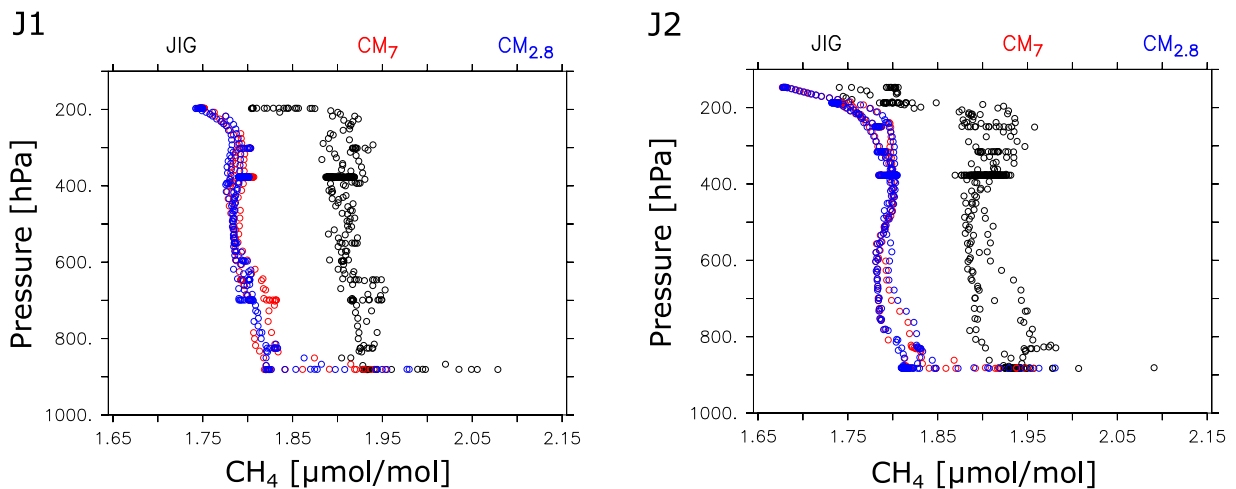


Figure 4.9: Comparison of the JIG in-situ measurements and the S4D submodel output (CM7 and CM2.8) sampled along J1 (left panel) and J2 (right panel). Results show methane mixing ratios in $\mu\text{mol/mol}$ versus the aircrafts' atmospheric pressure altitude along the flight tracks in hPa.

respectively. The difference between the two model instances is possibly related to their different grid cell size. The methane mixing ratios in a methane plume are not distributed evenly. The smaller grid cells of the CM2.8 model instance may have captured only parts of locally very enhanced methane mixing ratios in the a plume. In contrast, since the coarser grid cells, cover a larger part of the methane plume, the mixing ratios could be more diluted here. Additionally, the methane emissions fluxes used in the simulation are most likely overestimated. A comparison of the applied anthropogenic emission inventory EDGAR v4.2FT2010 to a more recent release from the year 2019, (EDGAR v4.3.2, Crippa et al., 2018), shows that the total methane emissions of the applied EDGAR v4.2FT2010 inventory in the USCB (longitude: 18.30-19.40 °E, latitude: 49.90-50.40 °N) are larger by 1030.4 kt a⁻¹ compared to EDGAR v4.3.2.

Similarly to the comparison with the P4 observations, the simulated peaks along the P5 flight track exceed those of the observations. This is not as significant as for the P4 observations and therefore resulted in lower NMBEs of 1.17 % and 1.18 % for the CM7 model instance and the CM2.8 model instance, respectively. The sharp increase of the methane mixing ratios, observed around 13:30 UTC, is not simulated by the CM7 model instance, and only to a small extent by the CM2.8 model instance. This peak was measured very close to a coal mine ventilation shaft (personal communication with A. Fiehn). Presumably, MECO(3) is not able to resolve these localized methane emissions. Especially the large grid cells of the CM7 model instance blur these emissions in the background methane.

Apart from these inconsistencies, the comparisons between model results and the observation, P4 and P5 are good. However, this is not always true for the comparisons with the other smaller scaled D-FDLR observations (i.e. other than P4 and P5). The statistical results summarised in Figure 4.6 demonstrate the low correlation between simulated and observed methane mixing ratios along the respective flight tracks. A graphical comparison can be found in the Appendix A.1. In the case of P3 and P6, the observed methane peaks can be simulated but are slightly shifted in time. This results in a similar mean amplitude height (normalized standard deviation close to reference line), but a low correlation between model results and observations. Additionally, other factors, such as the wind speed could play an important role. The P7 data were sampled during very high wind speed conditions and the model output shows considerable deviations from the observations. The corresponding data point lies outside the range of the Taylor diagram in Figure 4.6. For comparison, during the 6th and 7th of June, when the observations P4, P5 and P6 were sampled, wind conditions were very stable. Figure 4.11 displays the results for the comparison with the P2 observations. Both model domains are not able to simulate the observed methane peaks M1 and M2 (left panel). During this time, the flight track of P3 is above the simulated methane plumes (see right panel). Sampling the model output at this altitude consequently does not detect any of the observed methane peaks. This is because MECO(3) simulates a too shallow Planetary Boundary Layer Height (PBLH) during the morning. Around 09:30 UTC the simulated PBLH has risen already and the observed peak M3 can be seen in the S4D submodel output. However, with a smaller amplitude, which is also seen by the low normalized standard deviation in Figure 4.6. Previous studies

(i.e. Collaud Coen et al., 2014; Mertens et al., 2016) analysed the simulated PBLH of the COSMO model. In contrast to the results presented here, their results show an excessively high simulated PBLH. However, in the present study we only consider a single moment of a short-term simulation. A detailed investigation of the PBLH would go beyond the scope of the study.

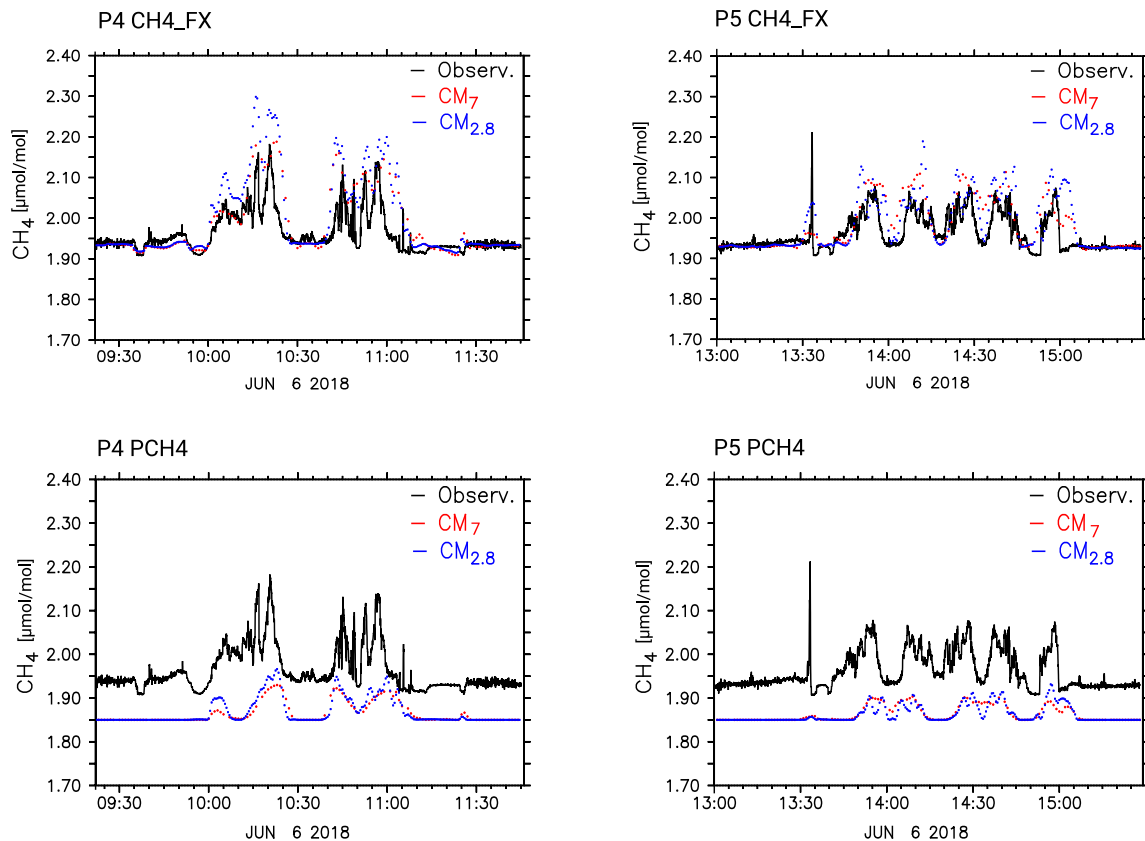


Figure 4.10: Comparison of the D-FDLR in-situ measurements and the S4D submodel output (CM7 and CM2.8) sampled along P4 (left panel) and P5 (right panel). Upper panels: methane mixing ratios in $\mu\text{mol/mol}$ simulated by the CH4_FX tracer. Note that the model results are bias corrected with $0.108 \mu\text{mol/mol}$. Lower panels: methane mixing ratios in $\mu\text{mol/mol}$ simulated by the PCH4 tracer. An offset of $1.85 \mu\text{mol/mol}$ is added to PCH4 for a better visualization. The time axis is in UTC. Figure from Nickl et al. (2020).

Figure 4.10 (lower panels) displays the methane mixing ratios simulated by the PCH4 tracer compared to the observations P4 and P5. Since the PCH4 tracer only considers those emissions which actually arise from the coal mining ventilation shafts, no background

methane is present and all simulated methane peaks can be attributed to the coal mining. The timing of the simulated methane mixing ratio peaks agree well with the observations, as well as with the CH₄.FX tracer (upper panel). This implies that the observed plumes of P4 and P5 indeed arise from the coal mines. However, the amplitudes of the simulated PCH₄ mixing ratios are below those of the observations. Again, this can be explained by the applied emission inventory. The sum of all methane emissions in CoMet ED v1 used for PCH₄ is 465 kt a⁻¹. This is less than the sum of the updated emission inventory CoMet ED v2 (based on E-PRTR, 2016), which is 502 kt a⁻¹. In addition, changes in emission distribution and structural and operational changes in the mining sector may have occurred in the time between the reporting years (2014 and 2016 for CoMet ED v1 and v2, respectively). The fact that the simulations assume a constant methane release from the ventilation shafts over time could also have a small influence on model results. In reality, these emission fluxes vary from day to day.

In contrast to the CH₄.FX tracer, the differences between the model instances CM2.8 and CM7 are more pronounced in the tracer PCH₄. The CM2.8 model instance is able to simulate the finer structure within the methane peaks better.

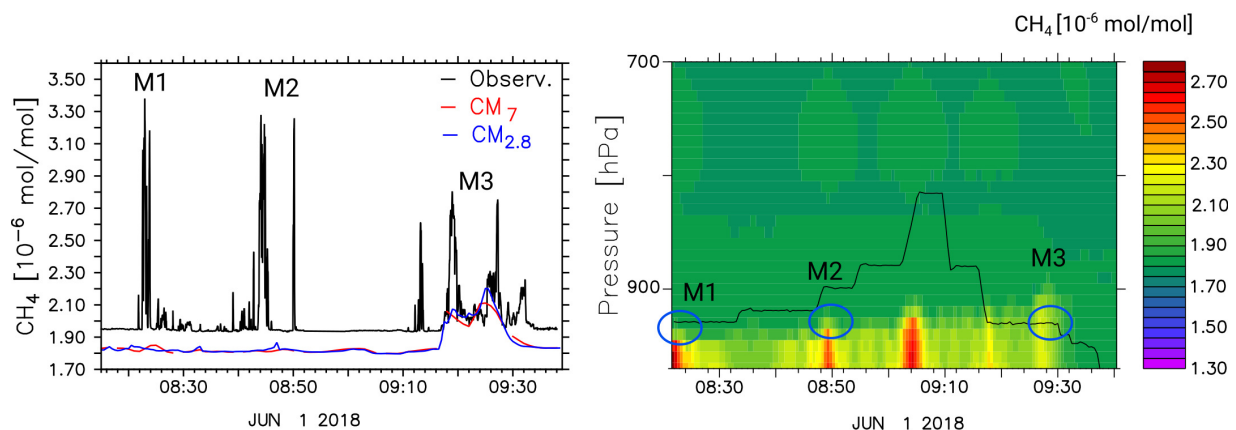


Figure 4.11: The left panels shows D-FDLR in-situ sampled CH₄ mixing ratios (black lines) of P2, as well as the S4D submodel output of CH₄.FX at flight altitude for CM7 (red) and CM2.8 (blue). The right panel displays the corresponding flight altitude of P2 (black line) and the simulated profile (CM2.8) of the methane mixing ratio along this flight track. All mixing ratios are in $\mu\text{mol/mol}$. The time axes is in UTC. M1, M2 and M3 mark specific methane peaks seen in the observation (left panel) and in the simulated methane profile (right panel), but not necessarily in the sampled S4D output at flight altitude (left panel). Figure and caption from Nickl et al. (2020).

4.3.3 Evaluation of the forecast skill

In order to determine the overall forecast skill, and to estimate the deviation of each proceeding forecast day from the actual conditions, a so called skill score can be calculated. A good forecast for a measurement campaign needs to simulate both, the observed amplitudes and the observed pattern variability. Therefore a single skill score should be able to make statements about the standard deviation and the correlation coefficient between the observations and the forecasts. The presented study uses two skill scores after Taylor (2001), that fulfil these criteria. Both skill scores include the two parameters, but either emphasize the similarity of the amplitudes (S_V), or the similarity of the patterns (S_C). They are calculated as follows:

$$S_V = \frac{4(1 + R)}{(\sigma_f + 1/\sigma_f)^2(1 + R_0)} \quad (4.3)$$

and

$$S_C = \frac{4(1 + R)^4}{(\sigma_f + 1/\sigma_f)^2(1 + R_0)^4} \quad (4.4)$$

with R being the correlation coefficient between forecast and observation, R_0 being the maximum attainable correlation coefficient, and σ_f being the ratio of the standard deviation of the forecast to that of the observation. R_0 is assumed to be 1. In reality, however, the maximum correlation coefficient between observations and simulations does not reach the value 1 due to differences in spatial and temporal resolution. In the following, each forecast day is analysed accordingly to estimate the evolution of forecast quality.

Actual forecast skill

The actual forecast skill of MECO(3) is obtained by comparing the observations (total column and in-situ) to the forecasts. The calculated skill scores S_V and S_C are presented in Figure 4.12 and Figure 4.13, respectively. The skill scores are calculated for the two model instances CM7 (left panels) and CM2.8 (right panels) and for each forecast day I to VI.

The previous Section 4.3.2 showed that the models' skill differs between the three observational data sets. This is mainly due to different flight patterns (e.g. small-scale pattern, vertical pattern) and measurement techniques. As expected, these differences can be also observed in the forecast skills. Overall, the skill scores for the comparison with the CHARM-F and JIG observations (upper panels) are larger than the skill scores received from the comparison with the D-FDLR observations (lower panels). This applies in particularly for the S_C skill score (see Figure 4.13), that emphasizes the correlation between observation and simulation. As discussed in the previous section, the integrated methane mixing ratios and the vertical methane gradient are well simulated by MECO(3). The smaller-scale measurements in contrast, barely correlate with the simulations (see Figure 4.6). Again, the best correlation (with the D-FDLR Cessna observations) is achieved for P4 and P5, where wind conditions were favourable to sample the methane plumes

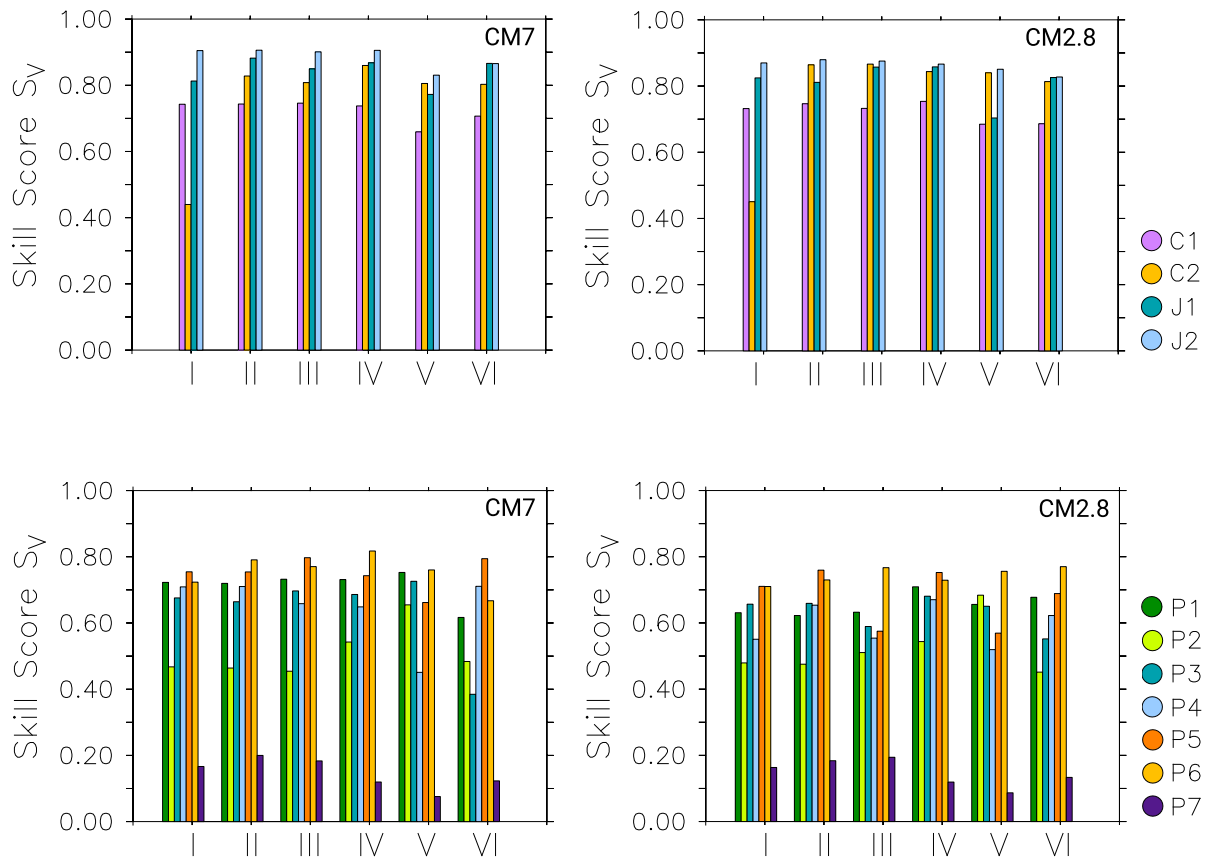


Figure 4.12: Skill scores S_V resulting from the comparison of the forecast days I to VI (horizontal axis) with the observations. The coloured bars refer to the individual observations: C1, C2, J1, and J2 (upper panels) and P1 until P7 (lower panels). The skill scores are calculated for the two model instances CM7 and CM2.8 on the left and right panels, respectively. Figure from Nickl et al. (2020).

downwind the coal mining shafts. However, the observations C1, C2, J1 and J2 have been also sampled during these two days. If the CHARM-F and JIG observations had been measured on days with less stable meteorological conditions, this could also have led to poorer forecast qualities. The skill score S_V is very similar for both model instances (CM2.8 and CM7, see Figure 4.12). Furthermore, there is little variability between the different forecast days I to VI, neither a noticeable decrease of the forecast skill. The S_V is highest for the JIG observations with values above 0.8. The skill is also good for C1, C2, P1, P4, P5 and P6 with values above 0.6 (except for C2 at forecast day I).

The skill score S_C in Figure 4.13 is in general lower than the skill score S_V , and slightly higher for the bigger and coarser resolved model instance CM7 (left panel). The variability

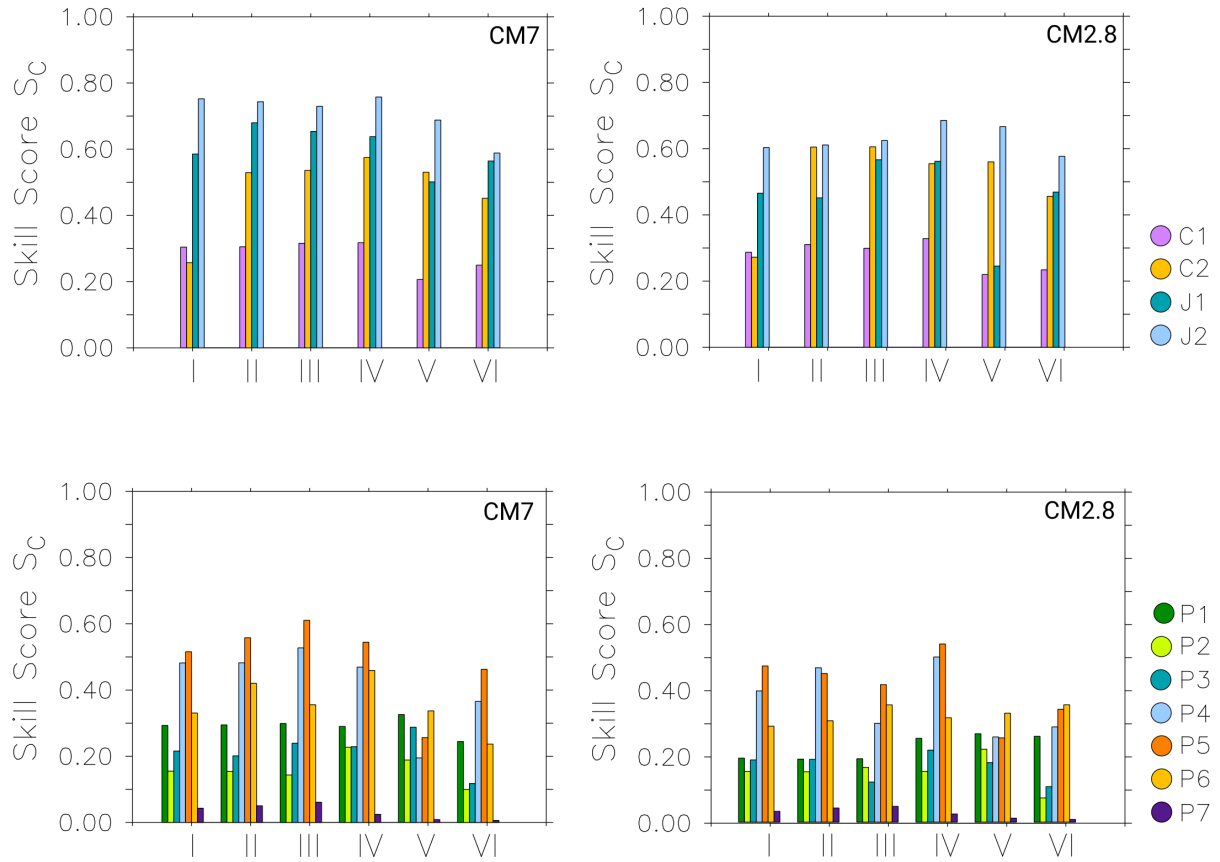


Figure 4.13: Skill scores S_C resulting from the comparison of the forecast days I to VI (horizontal axis) with the observations. The coloured bars refer to the individual observations: C1, C2, J1, and J2 (upper panels) and P1 until P7 (lower panels). The skill scores are calculated for the two model instances CM7 and CM2.8 on the left and right panels, respectively. Figure from Nickl et al. (2020).

between the individual forecast days is again low, at least until forecast day IV, from which on the skill score decreases. Forecast day V has the lowest skill. However, since most observations were sampled during only two days (6th and 7th of June) the forecasts are related to the same days of the analysis simulation and the meteorological conditions during these days. To make a general statement about the forecast skill, it would be necessary to compare additional observations within a broader time span.

Theoretical forecast skill

To evaluate how the forecasts evolve over the entire model domains, the forecasts cannot be solely compared to the observations along a flight track. Therefore, each forecast day

is compared to the analysis simulation and covering the entire model domains. Thereby a theoretical forecast skill is obtained. As described above, XCH_4 is the dry air weighted average methane mixing ratio of the total atmospheric column. Since, XCH_4 thereby covers the entire vertical extent of the model domains CM2.8 and CM7, it is used for the comparison between the forecasts and the analysis simulation.

The XCH_4 values are compared at each grid point on the respective two-dimensional model grid and the corresponding skill scores S_V and S_C are calculated. In order to compare the CM7 results with the CM2.8 results, the analysed area only covers the area obtained by removing the outermost 15 grid points of the CM2.8 domain (relaxation zone). The average area containing a skill score > 0.7 is estimated for each forecast day. Figure 4.14 shows the results for the S_V (left panel) and S_C (right panel). The skill is calculated for the CH4.FX tracer, as the PCH4 tracer does not cover the entire model domain (no background methane).

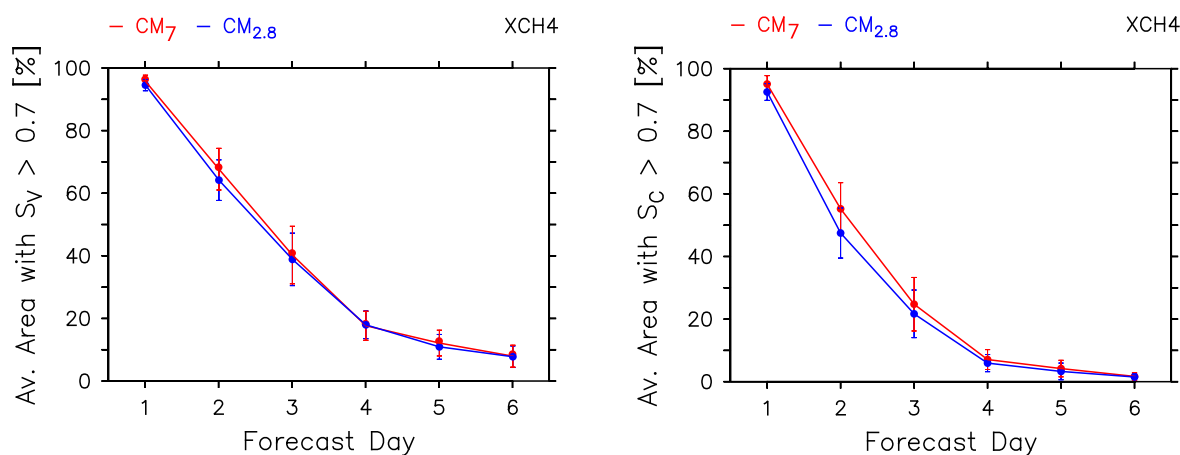


Figure 4.14: The graphic shows the evolution of the theoretical forecast skill with increasing forecast day for CM7 (red) and CM2.8 (blue). The vertical axis displays the average area (in %), according to the smallest model domain, with a Skill Score > 0.7 . The horizontal axis shows the specific forecast days 1 to 6. The Skill Scores are calculated for each day at each grid point from 1st to 22th June 2018 (CoMet 1.0). It compares the CH4.FX total column mixing ratios of the forecast simulations to the CH4.FX total column mixing ratios of the analysis simulation. The error bars indicate the interval which contains 95% of all skill scores per day. S_V (left panel) emphasizes variability and S_C (right panel) emphasizes the correlation. Figure and caption from Nickl et al. (2020).

The differences between the two model instances are very small. The skill of the model instance CM7 is slightly higher, which can be explained by the lower amount of larger-sized grid cells that need to be compared (and match) within the regarded area. The skill score S_C is lower than the skill score S_V . The lower correlation in the area could be attributed to a displacement of a simulated plume in time or space, which would also explain the fact that the standard deviations of analysis and forecasts remain similar.

However, in contrast to the actual forecast skill, the theoretical skill decreases faster with each proceeding forecast day. At forecast day IV less than 20 % (S_V) or 10 % (S_C) of the area shows a skill larger than 0.7. Whereas the theoretical skill score is defined to measure the skill averaged over the entire model domain, the actual skill score compares the model results to the measured methane plumes downwind the ventilation shafts. The latter are easier to forecast than the variability of the methane background in the overall model domain.

4.4 Summary and outlook

The presented study describes the MECO(3) setup for the simulation of localized methane emissions from coal mining activity in the USCB. Next to the methane master tracer CH4_FX, which comprises all methane emissions, the point source tracer PCH4 is implemented. The PCH4 tracer includes only emissions from the coal mining ventilations shafts. Comparing both tracers with each other, as well as to the observations, allows for a more precise assignment of methane peaks (either of the CH4_FX tracer or the observations) to a specific source (here: coal mining). Moreover, the PCH4 point sources can be switched on and off individually, which provides a good tool for further investigations of single methane plumes.

Throughout the CoMet 1.0 campaign, 12-hourly 6-day forecast simulations have been successfully performed and helped to plan the campaigns' measuring strategy. In addition, an analysis simulation has been conducted and was analysed with respect to the observations.

The evaluation of the analysis simulation showed, that, even though EMAC is nudged towards the ECMWF data at a coarser resolution (T42 spectral truncation), and all three COSMO/MESSy instances are only driven by relaxation at their boundaries by the next coarser model instance, the MECO(3) model is able to simulate the observed methane plumes reasonably well. The timing of the simulated peaks in the methane mixing ratios is in good agreement with the observations. Both, the vertically integrated methane (derived from the CHARM-F lidar), as well as the vertical gradient of methane in the atmosphere (measured in-situ by JIG) are well represented by the CH4_FX tracer. Furthermore, the CM7 instance simulates these larger-scale observations as precise as the finest resolved CM2.8 instance.

The simulation of the smaller-scale in-situ measurements is however, challenging in some cases. Although most of the observed peaks in the methane mixing ratio can be simulated, the amplitudes differ from their observed counterparts, and the correlation is low due to shifts in time or in space. This can be seen in the Taylor diagram in Figure 4.6 as well as in the statistical results presented by Table 4.3. The CH4_FX tracer overestimated the amplitudes of the observed peaks. As mentioned above, methane emission fluxes of the applied emission inventory (EDGAR v4.2FT2010) are larger compared to what is reported by recent emission inventories. This is particularly seen from the results obtained with

the finer-resolved CM2.8 instance. Depending on the model domains' grid cell size, very localized methane enhancements can be either more diluted (CM7) or more intensified (CM2.8) in the model results. Moreover, those mixing ratios sampled very close to the ventilation shafts are often not resolved by the model. Furthermore, the MECO(3) model simulates a too low PBLH during the morning. Therefore, the observed methane peaks cannot be seen in the S4D submodel output.

Apart from that, a continuous and constant offset of the simulated CH₄FX compared to all observations exists. Since the vertical gradient of methane in the atmosphere is well represented in the model output, this bias is most likely not caused by shortcomings in the vertical transport. Instead, the bias could be explained by the fact, that the applied emission inventory is based on the anthropogenic EDGAR v4.2FT2010 and natural EMPA (Frank, 2018) emissions from the year 2012. Between 2012 and 2018 global methane increased steadily (Nisbet et al., 2019), resulting in an overall increase in the methane background level at the time when CoMet 1.0 took place.

The PCH₄ tracer is in very good agreement with the CH₄FX tracer and the in-situ observations measured on board D-FDLR. However, simulated amplitudes are lower than the observed, which is again explained by the applied "not-up-to-date" emission inventory' (i.e. CoMet ED v1). Moreover, the CM2.8 simulated the fine structure of the observed methane mixing ratios better than the CM7 instance. For the campaigns' flight planning, however, it is sufficient to perform the forecast with the CM7 instance only.

For future simulations, the bias could be reduced by updating the emission inventories to the recent EDGAR v5.0 (Crippa et al., 2020) inventory for anthropogenic emissions. Thereby a better agreement of the small-scale simulated methane amplitudes with the observations may also be achieved. Similarly, the most recent point source emission inventory CoMet ED v4.01 (Gałkowski et al., 2021a) would improve the simulated amplitudes of the PCH₄ tracer. Furthermore, the CAMS-GLOB-ANT inventory (Granier et al., 2019), which extrapolates the emissions to the current year by using EDGAR v4.3.2 as a basis for 2010 and by projecting emission trends for 2011 to 2014 from the Community Emissions Data System (CEDS) inventory (Hoesly et al., 2018) until 2018, could be used.

Finally, the evaluation of the forecast skill showed, the MECO(3) model for this specific campaign, is able to provide reliable forecast until forecasts day four.

Chapter 5

Simulation of $\delta^{13}\text{C}(\text{CH}_4)$ in coal mining emission with the regional model MECO(3)

In order to reduce future methane emissions it is important to identify the emission fluxes of individual sources. Assigning methane emissions to a specific local source is, however, fraught with quantitative uncertainties. Inverse modelling, such as it is done for top-down approaches, can constrain emission estimates with ground-based, airborne or satellite-based atmospheric measurements. However, this method often does not allow for a separation of sources that are spatially or temporally close to each other (Saunois et al., 2020). Moreover, also small-scale measurements of specific plumes may capture methane that originates from various sources. Thus, it is often not possible to distinguish between the origin of methane emitted in the same area.

Since the isotopic signatures $\delta^{13}\text{C}$ and δD of thermogenic, pyrogenic and biogenic methane differ from each other (see Chapter 2), they can be used to identify the origin of atmospheric methane. This requires a comprehensive knowledge of the various local source signatures. A country- and sector-based inventory of isotopic source signatures has been already provided by Sherwood et al. (2017). Nevertheless, the isotopic source signature of a single emission sector (e.g. coal) can vary widely also within smaller regions (Kotarba, 2001; Zazzeri et al., 2016). Therefore, further regional measurements are needed.

Modelling the stable isotopologues of methane on regional scales could additionally support the evaluation of such measurements. As shown in Chapter 4, the MECO(3) model allows for the regional simulation of point sources explicitly emitted by a single sector, e.g. coal. The comparison of this model output and observations already helps to assign measured plumes to the specific sector. Such simulations were carried out in parallel to the CoMet 1.0 campaign in the Upper Silesian Coal Basin (USCB) in Poland, where methane measurements are associated with coal mining. Similarly, the simulation of stable isotopologues with MECO(3) could help to interpret the $\delta^{13}\text{C}$ or δD values, which are measured in a methane plume, and further determine a specific isotopic source signature.

The extension of the MESSy submodel CH4 (Frank, 2018; Winterstein and Jöckel, 2021)

simulates the four main methane isotopologues CH_4 , CH_3D , $^{12}\text{CH}_4$ and $^{13}\text{CH}_4$ and applies the kinetic fractionation, occurring during the sink reactions of methane in the atmosphere and in soils (see Chapter 3 for a detailed description). This submodel extension has been tested and evaluated on the global scale (Frank, 2018; Winterstein and Jöckel, 2021). It is further applied in the global simulations of the presented study in Chapter 6. However, so far, it has not been tested on regional scale, e.g. with the MECO(3) model.

Here, I test the performance of MECO(3) including stable isotopologues on the example of the CoMet 1.0 campaign. In particular, I analyse the model output along the flight track of the research aircraft D-FDLR Cessna (see Chapter 4); i.e. the flight tracks P1 to P7 (see Table 4.2). The aim of those measurement flights was to detect methane emitted from the coal mine ventilation shafts in the USCB. In-situ (Fiehn et al., 2020) and flask samples (personal communication with A. Fiehn) were collected up- and downwind relative to the methane plumes. The flask samples were collected with the Jena Air Sampler (JAS) and later analysed for CH_4 mixing ratios, $\delta^{13}\text{C}$ and $\delta^{13}\text{D}$ using the JRAS-M16 (Sperlich et al., 2016) in Jena. In the presented study, I simulate the CoMet campaign including $\delta^{13}\text{C}$. For the comparison of the simulated and the observed signatures, I online sample the MECO(3) output along the flight tracks P1 until P7 using the MESSy submodel S4D (Jöckel et al., 2010).

The first part of this chapter concentrates on the question to which extend the regional model MECO(3) represents the stable isotopic composition in methane plumes associated with coal mining. Therefore, I make three different assumptions on the applied $\delta^{13}\text{C}$ for the coal sector (throughout this chapter denoted as $\delta^{13}\text{C}_{\text{Coal}}$). Afterwards I examine whether the simulated $\delta^{13}\text{C}$ in the observed methane plumes differs from the signatures in the background methane. The results are discussed in Section 5.1. In the second part, I compare the model results to the observations. The simulations are adjusted stepwise, in order to match best with the observed $\delta^{13}\text{C}$ signatures and determine an isotopic source signature for coal-related methane in the USCB. This is described in Section 5.2.

5.1 Simulation of stable isotopologues with MECO(n)

5.1.1 Model Setup

For the regional modelling of stable methane isotopologues, I performed several simulations, named ANA.ISO, using the MECO(3) setup, which is introduced and discussed in Chapter 4. The simulations are analysis simulations of the CoMet 1.0 campaign and cover the time period between 04/2018 and 06/2018 (spin-up and campaign period). The driving model EMAC is again operated in the T42L90MA resolution with a time step length of 720 s. The three on-line coupled COSMO/MESSy instances are nested into each other over the USCB in Poland: CM50, CM7 and CM2.8 with 50 km, 7 km and 2.8 km spatial resolution and time step lengths of 240 s, 60 s and 30 s, respectively (see Section 4.2.1). To constrain the model with the observed meteorology, the EMAC model is nudged by Newtonian relaxation towards the six-hourly ECMWF operational analysis data. The

sink reactant fields are again predefined and derived as monthly averages from a previous ESCiMo simulation (described in Jöckel et al., 2016).

I simulate the methane tracer CH4_FX, which comprises all methane emission fluxes, and the point source tracer PCH4, which includes only methane emitted from coal mining in the USCB (see Chapter 4). The CH4_FX tracer uses gridded methane emissions, which are analogues to the previous setup, a combination of the EMPA inventory (Frank, 2018) for all natural emissions, and the EDGAR inventory for all anthropogenic emissions. However, other than in the previous setup, I use the at-that time most recent version EDGAR v5.0 (Crippa et al., 2020). The EMPA and EDGAR v5.0 inventories are only available until the year 2012 and 2015, respectively. For consistency reasons, I use the EMPA emissions (monthly) from 04/2012 to 06/2012 and the EDGAR v5.0 emissions (yearly) from 2012, to simulate the time period from 04/2018 until 06/2018. The initial conditions are derived from a previous global simulation named EMAC-y-02, which uses a simplified methane chemistry (conducted by Frank, 2018).

The PCH4 tracer uses the methane emission fluxes provided by the CoMet ED v2 inventory (based on E-PRTR, 2016, personal communication M.Galkowski).

The stable isotopologue tracers CH4_12C and CH4_13C

As described in Chapter 3, the CH4 submodel simulates the four main methane isotopologues as separate tracers. Methane emissions are split according to their ratio of light and heavy isotopologues given by the respective isotopic source signature. The resulting proportions are then assigned via the MESSy submodel OFFEMIS (Kerkweg and Jöckel, 2012b) to the corresponding tracers CH4_12C and CH4_13C for $\delta^{13}\text{C}$, and CH4_D0 and CH3_D1 for δD .

In the presented study, I intend to simulate the $\delta^{13}\text{C}$ signatures in atmospheric methane, i.e. the two tracers CH4_12C and CH4_13C. Table 5.2 list all methane sources and their corresponding $\delta^{13}\text{C}$ signatures, which are used for the ANA.ISO simulations. The anthropogenic emissions of the EDGAR v5.0 inventory are provided as several individual emission sectors (see Appendix A.2 for a detailed list). Here, they are grouped into only four categories, i.e. rice, livestock, landfills and fossil fuels. Emissions from agricultural waste burning (in EDGAR v5.0) are considered as biomass burning emissions. Since the fossil fuel emissions within the investigated area in Poland arise predominantly from coal mining, I use the isotopic signatures reported for coal-derived methane, as an overall signature for fossil fuel emissions. I conducted three ANA.ISO simulations, which make different assumptions on this isotopic signature, i.e. $\delta^{13}\text{C}_{\text{Coal}}$. Based on values reported in the literature, I chose a maximum of -35‰ , an average of -41.7‰ and a minimum of -50‰ for the coal mining emissions (see Table 5.1). The initial conditions for the isotopologue tracers are again taken from the analysis simulation EMAC-y-02 (Frank, 2018). The stable isotopologues are not simulated for the point source emission tracer PCH4.

5. Simulation of $\delta^{13}\text{C}(\text{CH}_4)$ in coal mining emission with the regional model 58 MECO(3)

Table 5.1: The table lists the individual isotopic source signatures of the CH_4 emission sectors used in the ANA.ISO setup. For fossil fuel emissions three different values are applied, covering the range of isotopic signatures reported in the literature for coal mine emissions.

Source	$\delta^{13}\text{C}$ [‰]		Source	$\delta^{13}\text{C}$ [‰]	
Biomass Burning	-23.0	(*)	Rice	-63.0	(*)
Wetlands	-59.4	(*)	Livestock	-60.2	(*)
Termites	-63.3	(*)	Landfills	-51.7	(*)
Wildanimals	-61.5	(*)	Fossil fuels	max -35.0	Monteil et al. (2011)
Volcanoes	-40.9	(*)		ave -41.7	(*)
Ocean	-59.0	(*)		min -50.0	Zazzeri et al. (2015)

(*)calculated by Frank (2018) using the following references:

Kiyosu (1983); Quay et al. (1999); Snover et al. (2000); Mikaloff-Fletcher et al. (2004); Whiticar and Schaefer (2007); Monteil et al. (2011); Rigby et al. (2012); Zazzeri et al. (2015).

5.1.2 Results and discussion of the ANA.ISO simulations

Figure 5.1 shows the simulated methane mixing ratios (upper panel) and the corresponding $\delta^{13}\text{C}$ (lower panel) sampled along the selected flight P4. All results are simulated by the finest resolved COSMO/MESSy domain CM2.8. The upper panel depicts the results of the two methane tracers $\text{CH}_4.\text{FX}$ and PCH_4 . As described above, the PCH_4 tracer only simulates methane emissions from the coal mining point sources. Since both tracers agree well with each other and have similar amplitudes, the enhancements seen in the $\text{CH}_4.\text{FX}$ tracer clearly arise from coal mining. Simultaneously, in the lower panel, all ANA.ISO simulations show a difference in $\delta^{13}\text{C}$ relative to the background. The two tracers $\text{CH}_4.12\text{C}$ and $\text{CH}_4.13\text{C}$, which define the isotopic composition, use the same emissions as the master tracer $\text{CH}_4.\text{FX}$. It can therefore be concluded that the relative changes in $\delta^{13}\text{C}$ here, actually result from the coal mining emissions. In the given example, the MECO(3) model is clearly able to resolve stable isotopic signatures on small scales. Moreover, the three different $\delta^{13}\text{C}_{\text{Coal}}$ signatures, chosen for the coal-related methane emissions, can be clearly distinguished and lead to three different simulated $\delta^{13}\text{C}$ amplitudes. Since the background methane within the USCB region is strongly influenced by the coal mining emissions, these differences appear to a lesser extend also in the simulated background $\delta^{13}\text{C}$.

To further test whether the isotopic composition of coal-derived methane emissions is reflected by the simulated $\delta^{13}\text{C}$ of atmospheric methane, I apply the so called "Keeling plot" approach (first applied by Keeling, 1958, 1961). This method is usually used to interpret stable isotopic measurements and determine individual source signatures. It is based on the assumption, that the atmospheric methane mixing ratio is a combination of

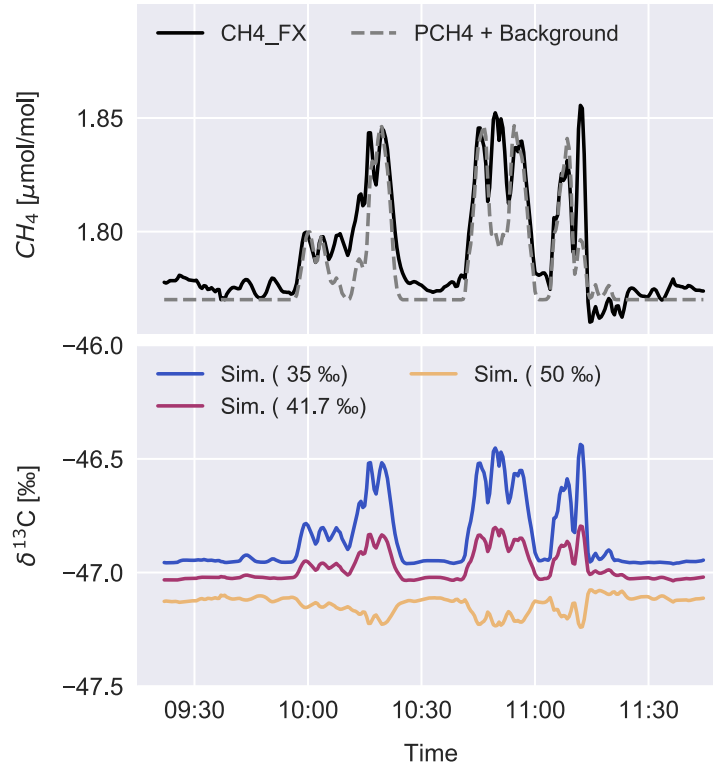


Figure 5.1: Simulated CH₄ mixing ratios (upper panel) and δ¹³C (lower panel) of the ANA.ISO simulations along the D-FDLR flight track P4 (see previous Chapter 4). The upper panel shows the resulting mixing ratios of the CH₄.FX tracer (solid line) and the point sources tracer PCH₄ (dashed line). A constant background value of 1.77 μmol/mol is added to the PCH₄ tracer. The lower panel shows the resulting δ¹³C values for three different assumptions on the isotopic fossil fuel source signature, i.e. -50 ‰(ochre), -41.7 ‰(red-purple) and -35 ‰(blue).

the background methane and the amount of methane emitted from a specific sources. This additional methane leads to an enhancement relative to the background mixing ratio level (see Figure 5.1, upper panel). Similarly, the atmospheric δ¹³C reflects a mixture between the background isotopic composition (δ¹³C_B) and the source isotopic composition δ¹³C (δ¹³C_S):

$$\delta^{13}C_A = \alpha \cdot \delta^{13}C_B + \beta \cdot \delta^{13}C_S \quad (5.1)$$

with δ¹³C_A being the atmospheric isotopic composition, α being the proportion of the background methane and β being the proportion of the source methane. Calculating the linear regression between the reciprocal values of the methane mixing ratios and the corresponding isotopic signatures (see Figure 5.2) results in an interception, which represents the isotopic composition of the source (assuming that δ¹³C_S is constant and only from a

single source).

Since in the ANA.ISO simulations the $\delta^{13}\text{C}_\text{S}$ is predefined (i.e. $\delta^{13}\text{C}_\text{Coal}$: -35 ‰, -41.7 ‰ and -50 ‰), I use the Keeling approach in reverse to verify the model output. The simulated methane enhancements along the flight tracks P1-P7 can be almost all directly associated with the emissions from the coal mining ventilation shafts. This has been investigated by comparing the two tracers PCH4 and CH4.FX (see Appendix A.2). Figure 5.2 shows the resulting interceptions for the three ANA.ISO simulations. In each case they are very similar or equal to the initially specified $\delta^{13}\text{C}_\text{S}$ for coal-derived methane emissions ($\delta^{13}\text{C}_\text{Coal}$). Furthermore, in Figure 5.2 the corresponding data points of the three simulations gather very close to the regression line, which indicates again that the regarded methane plumes originate from coal mining. A contribution of other sources would have led to a larger scattering.

These first analyses and results demonstrate, that MECO(3) is able to simulate the stable carbon isotopologues of methane using the CH4 submodel. The local influence of individual source emissions on the atmospheric isotopic composition is well represented.

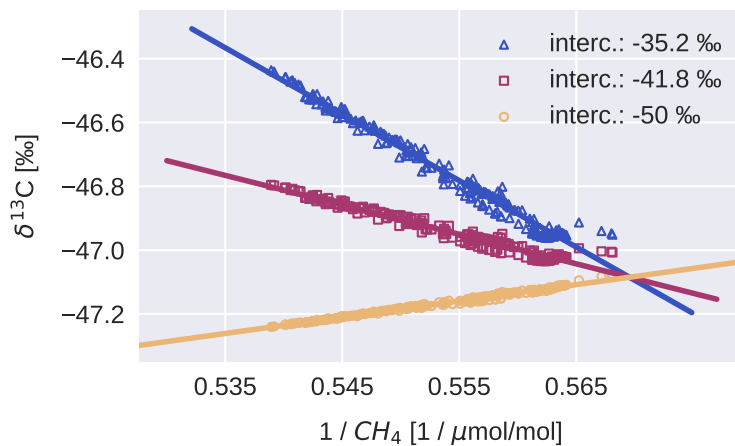


Figure 5.2: The Keeling plot shows the reciprocal of the simulated mixing ratios plotted versus the simulated $\delta^{13}\text{C}$ for the ANA.ISO simulation, assuming either i.e. -50 ‰ (ochre circles), -41.7 ‰ (red-purple rectangles) or -35 ‰ (blue triangles) as isotopic fossil fuel signatures. Additionally, the respective interceptions are listed, indicating the source signatures

5.2 Comparison to CoMet 1.0 observations

The previous section investigated the general ability of MECO(3) to simulate the stable isotopologues on regional scales. Three different isotopic compositions were chosen to simulate the influence of local methane emissions from coal mining. These assumptions were made based on various proposals from the literature and are not specific to coal mining emissions in the USCB. In order to find the most likely isotopic composition of coal-derived methane specifically from the USCB, the model results need to be compared

to observations. This in turn also helps in interpreting observations to determine individual source signatures.

As described in the introduction of this Chapter, several flask samples were collected on board of the aircraft D-FDLR Cessna and later analysed for CH₄ mixing ratios and $\delta^{13}\text{C}$. The data are provided by A. Fiehn (personal communication in 2020). Figure 5.3 (left panel) compares the observations of all flights (P1-P7) to the S4D model output of the three ANA.ISO simulations. $\delta^{13}\text{C}$ is plotted versus the CH₄ mixing ratios. Note that the S4D submodel output of the CM2.8 domain is on-line sampled at each model time step, i.e. every 30 seconds. In contrast, the flask samples are less frequently sampled (4 to 11 flasks per flight). The “ANA.ISO simulation (-50 ‰)” matches the observations best. Both, model results and observations, reveal decreasing $\delta^{13}\text{C}$ signatures with increasing methane mixing ratios. This suggests that the source, responsible for the enhancement over the background methane, has a lighter isotopic composition compared to the background. As described above, the mixing ratio reflects the combination of background methane and source contribution. The previous Section 5.1.2 showed, that the elevated methane mixing ratios simulated by the tracer CH4_FX correspond to the coal mining emissions. Furthermore, the model results are linearly distributed close to the regression line (see Figure 5.3, right panel). This again supports the statement, that the methane plumes arise from the same source.

The observations in Figure 5.3 (right panel) are slightly scattered compared to the model results. This is not surprising, since in reality it cannot be assumed that all coal mines have exactly the same $\delta^{13}\text{C}_{\text{Coal}}$ signature. The detected methane plumes presumably do not only come from one shaft. Even if this were the case, one could assume that the $\delta^{13}\text{C}_{\text{Coal}}$ can also change within a single coal mine. Furthermore, the measured $\delta^{13}\text{C}$ could also be influenced by a change in the background $\delta^{13}\text{C}$, for example due to other environmental factors or daily fluctuations. Finally, the measurements may have captured the contribution of other sources in the vicinity that are not included in the model.

Nevertheless, the regression lines of model results and observations are still in good agreement. Therefore, the $\delta^{13}\text{C}_{\text{Coal}}$ of -50 ‰ seems to correspond most closely to the actual value. It should be noted that this can only be an average $\delta^{13}\text{C}_{\text{Coal}}$ signatures of all here considered coal mines. This value of -50 ‰ is almost in accordance with the study of Zazzeri et al. (2016), who calculated a $\delta^{13}\text{C}_{\text{Coal}}$ of -50.9 ± 0.6 ‰ for the USCB coal mines. An earlier study by Kotarba (2001) reports $\delta^{13}\text{C}_{\text{Coal}}$ signatures ranging from -79.9 to -44.5 ‰ in the USCB coalbeds. These signatures seem to be very negative, compared to those usually found in thermogenic produced methane (see Chapter 2). The coalbed methane in the USCB formed during the bituminous stage, which took place until the end of the Variscan orogeny (Kotarba, 2001). The $\delta^{13}\text{C}_{\text{Coal}}$ signatures of methane in bituminous coal lie between -65 and -55 ‰ (Kotarba, 2001). Furthermore, parts of the USCB have isotopically very light methane (-80 to -60 ‰), which was generated during microbial reduction of carbon dioxide in the Miocene. In addition, methane could have undergone isotopic depletion by diffusion and adsorption, during its’ migration through porous structures (Kotarba, 2001).

However, Figure 5.3 (right panel) also exhibits several biases of the “ANA.ISO simulation (-50 ‰)” relative to the observations. Background methane mixing ratios lie below the observed mixing ratios. This is mainly attributed to the fact, that emissions are taken from the year 2012 to simulate the year 2018 (see model setup description in Section 5.1). The slope of the regression line, calculated for the “ANA.ISO simulation (-50 ‰)”, is slightly lower than the one calculated for the observations. Assuming that the sampled methane plumes originate only from coal mining emissions, the $\delta^{13}\text{C}_{\text{Coal}}$ from the coal mine methane should be somewhat lower than the -50 ‰. As mentioned above, also the $\delta^{13}\text{C}_{\text{Coal}}$ in Zazzeri et al. (2016) is slightly more negative, with -50.9 ± 0.6 ‰.

Finally, the simulated $\delta^{13}\text{C}$ displays a positive bias compared to the observations. This bias is, however, only of about 0.63 ‰, which is within the uncertainty range of most isotopic source signatures (see Figure 2.3 in Chapter 2), used in the presented model setup. However, as seen in Section 5.1, the selected $\delta^{13}\text{C}_{\text{Coal}}$ also influences the simulated background $\delta^{13}\text{C}$ locally. Applying an isotopically more depleted $\delta^{13}\text{C}_{\text{Coal}}$ for the coal mining emissions could therefore also reduce the observed bias in the $\delta^{13}\text{C}$.

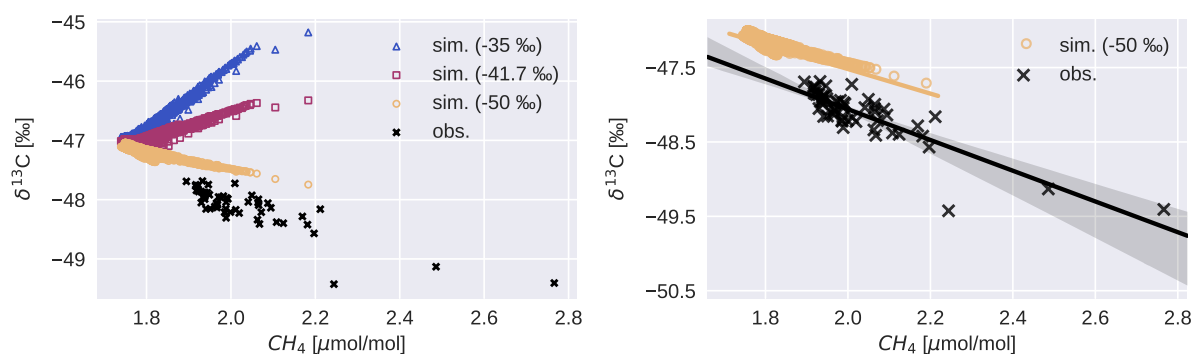


Figure 5.3: $\delta^{13}\text{C}$ plotted against the methane mixing ratio. The left panel shows the results of the flask samples (black crosses) and the three ANA.ISO simulations with different isotopic signatures for fossil fuel emissions, i.e. -50 ‰(ochre), -47.7 ‰(red-purple), -35 ‰(blue). The right panel shows again the results of the flask samples (black crosses) and the ANA.ISO simulation (-50 ‰, ochre). Additionally it displays the linear regression lines, including the 95 % confidence interval.

5.2.1 Sensitivity simulations w.r.t. the $\delta^{13}\text{C}_{\text{CH}_4}$ of coal mining emissions in the USCB

To account for the just described biases, and to find the most likely $\delta^{13}\text{C}_{\text{Coal}}$ signature of the measured methane plumes, I conducted several sensitivity simulations. Thereby emission fluxes are scaled and the $\delta^{13}\text{C}_{\text{Coal}}$ signature is slightly adjusted. Table 5.2 lists all ANA.ISO sensitivity simulations and their specific adjustments. The following section

describes them in more detail and discusses their comparison to the CH₄ mixing ratios and $\delta^{13}\text{C}$ flask samples.

Table 5.2: Overview of the ANA.ISO sensitivity simulations

Name		Description
ANA.ISO sim.	(-35)	ANA.ISO setup with $\delta^{13}\text{C}_{\text{Coal}}$ of -35 ‰, used for all fossil fuel emissions
ANA.ISO sim.	(-41.7)	ANA.ISO setup with $\delta^{13}\text{C}_{\text{Coal}}$ of -41.7 ‰, used for all fossil fuel emissions
ANA.ISO sim.	(-50)	ANA.ISO setup with $\delta^{13}\text{C}_{\text{Coal}}$ of -50 ‰, used for all fossil fuel emissions
ANA.ISO sim.	(-51)	ANA.ISO setup with scaled anthropogenic emissions and $\delta^{13}\text{C}_{\text{Coal}}$ of -51 ‰, used for all fossil fuel emissions
ANA.ISO sim. #2	(-51)	ANA.ISO with scaled anthropogenic and natural emissions and $\delta^{13}\text{C}_{\text{Coal}}$ of -51 ‰, used for all fossil fuel emissions
ANA.ISO sim. #3	(USCB)	ANA.ISO setup with scaled anthropogenic emissions, coal mining emissions and the corresponding $\delta^{13}\text{C}_{\text{Coal}}$ (taken from a previous version of CoMet ED v4.01) are included as point sources, $\delta^{13}\text{C}$ of -51 ‰ used for all other fossil fuel emissions

Description of the ANA.ISO sensitivity simulations

To reduce the bias in the methane mixing ratios, I scaled the initial conditions, as well as the emission fluxes used for the master tracer CH₄_FX. This is similarly applied to both isotopologue tracers, CH₄_12C and CH₄_13C. The scaling factor is calculated by comparing the background mixing ratios of the “ANA.ISO simulation (-50 ‰)” to the in-situ measurements taken on board of D-FDLR Cessna (continuous measurement along the flight track). $\delta^{13}\text{C}$ is not scaled, since the scaling of the emission fluxes and the adjustment of the $\delta^{13}\text{C}_{\text{Coal}}$ already influences the background $\delta^{13}\text{C}$ (see previous Section 5.1.2).

The two sensitivity simulations, named ANA.ISO simulations (-51‰) and ANA.ISO simulation #2 (-51‰), now use a slightly more negative $\delta^{13}\text{C}_{\text{Coal}}$, i.e. -51 ‰. In the “ANA.ISO simulation (-51 ‰)” I only scale the anthropogenic EDGAR v5.0 emissions. For the ANA.ISO simulation #2 (-51‰) the scaling is applied to all anthropogenic and natural emission fluxes.

The third sensitivity simulation, named “ANA.ISO simulation #3 (USCB)”, uses point source emission data from a previous version of the CoMet ED v4.01 inventory (Galkowski et al., 2021a, personal communication A. Fiehn), which provides detailed information on emissions from the individual coal mining ventilation shafts in the USCB. To avoid double

counting of the coal mining emissions, the EDGAR v5.0 emissions are set to zero in the respective gridboxes. The point source emissions are read in via the MESSy submodel TREXP (Jöckel et al., 2010) and contribute to the master tracer CH4_FX. The previous version of CoMet ED v4.01 inventory additionally includes $\delta^{13}\text{C}$ measurements of the individual shafts, which are used as $\delta^{13}\text{C}_{\text{Coal}}$ of the new point source emissions. Therefore, the point source emission fluxes are split again into a light and heavy fraction, which contribute to the CH4_12C and CH4_13C tracers, respectively. This is again done via the TREXP namelist.

Results and discussion of the ANA.ISO sensitivity simulations

The best match with the observations is achieved with the “ANA.ISO simulation (-51 ‰)”. Figure 5.4 shows the corresponding results. Compared to the previous “ANA.ISO simulation (-50 ‰)”, the bias of the simulated methane mixing ratios compared to the observations is reduced. Moreover, the regression line of the “ANA.ISO simulation (-51 ‰)” has a steeper slope and matches with the regression line of the observations. Applying the more negative $\delta^{13}\text{C}_{\text{Coal}}$ of -51 ‰ led to an improvement of the model results. This signature of -51 ‰ seems to be closest to the actual value and agrees with the previously reported signature in the study of Zazzeri et al. (2016, i.e. 50.9 ‰). Other than expected, the bias between the simulated and the observed $\delta^{13}\text{C}$ did not change significantly. However, as described above, this bias is still within the uncertainties of the various $\delta^{13}\text{C}$ source signatures.

This improvement of the model results, cannot be achieved with the two other sensitivity simulations. Figure 5.5 (left panel) shows the results of the ANA.ISO simulation #2 (-51 ‰) compared to the observations. In addition, I plotted the results of the “ANA.ISO simulation (-51 ‰)”. Although both simulations use the same $\delta^{13}\text{C}_{\text{Coal}}$ of -51 ‰, the $\delta^{13}\text{C}$ signatures of the ANA.ISO simulation #2 (-51 ‰) decrease faster with increasing CH₄ mixing ratios (steeper regression line). Other than in the “ANA.ISO simulation (-51 ‰)”, in the ANA.ISO simulation #2 (-51 ‰) all emission fluxes are scaled, i.e. natural and anthropogenic. This could lead to a larger contribution of biogenic emissions, which are in general isotopically more depleted. In the corresponding model output, additional methane plumes may now arise from those isotopically lighter biogenic emissions, resulting in a steeper slope of the regression line. The assumption is also supported by the fact that the confidence interval of the regression line is now broader. This indicates a contribution of other sources with different $\delta^{13}\text{C}$ signatures.

Figure 5.5 (right panel) shows the results of the “ANA.ISO simulation #3 (USCB)” compared to the observations. The isotopic signatures of the “ANA.ISO simulation #3 (USCB)” simulated in the methane plumes are far below those of the observations. This mismatch can have several reasons. The $\delta^{13}\text{C}_{\text{Coal}}$ signatures are taken from a previous version of the CoMet ED v4.0 inventory (Gałkowski et al., 2021a) and lie within the reported range for the USCB coal mines (Kotarba, 2001, see Section 5.1). However, the individual $\delta^{13}\text{C}_{\text{Coal}}$ signatures could still be partly underestimated or variable over time. Since each coal mine was assigned an individual $\delta^{13}\text{C}_{\text{Coal}}$ signature, it is further important

that the model simulates the exact plumes as observed. Here, the “ANA.ISO simulation #3 (USCB)” may have simulated methane plumes, which originate from other coal mines with isotopically lighter methane.

To rule this out, the individual plumes need to be assessed in more detail. In the Appendix A.2, the individually simulated CH_4 mixing ratios and $\delta^{13}\text{C}$ values of the flights P1-P7 are compared to the in-situ observations. The comparisons show that the “ANA.ISO simulation #3 (USCB)” does not always correlate with the observations. Reasons for the difficulties in accurately simulating the local pattern, are discussed in Chapter 4. Here, it can be summarised that most of the discrepancies are due to temporal displacements of the plumes or due to an incorrect Boundary Layer Height (BLH) of the model. This means that the observed methane plumes are either still included in the model output (just at different times), or they are not simulated at all, such as, for example, in the case of the flight P2. The simulated BLH is lower than the actual BHL. Since the flight track of P2 is above the simulated, but below the actual BLH, the observed methane plumes sampled at this height are not visible in the model output. However, in some cases, e.g. during flight P7, “ANA.ISO simulation #3 (USCB)” simulates methane plumes, which are not present in the observations. This could influence the resulting $\delta^{13}\text{C}$, but does not explain the large deviation between the “ANA.ISO simulation #3 (USCB)” results and the observations alone. However, simulating the observed pattern (e.g. the CH_4 plumes) more accurately is crucial for the interpretation of the isotopic measurements. The comparisons of the “ANA.ISO simulation (-51 ‰)” and “ANA.ISO simulation #2 (-51 ‰)” with the in-situ observations along the flight tracks P1-P7 are also shown in the Appendix A.2.

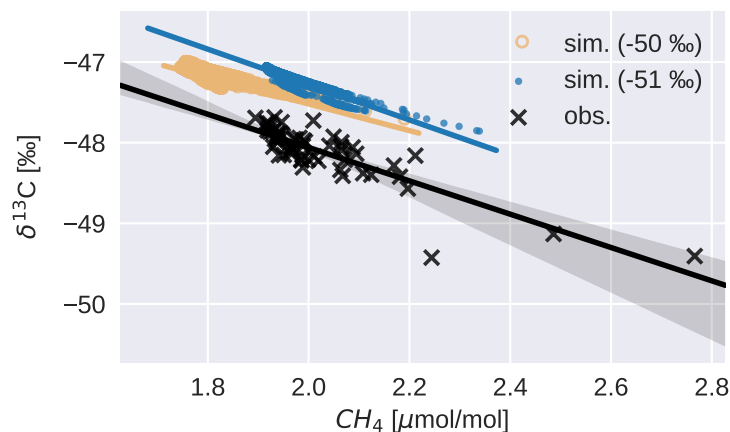


Figure 5.4: $\delta^{13}\text{C}$ plotted versus the methane mixing ratio of the “ANA.ISO simulation (-50 ‰)” in ochre, the “ANA.ISO simulation (-51 ‰)” in blue and the flask samples in black. Additionally the linear regression lines are plotted, including the 95 % confidence interval.

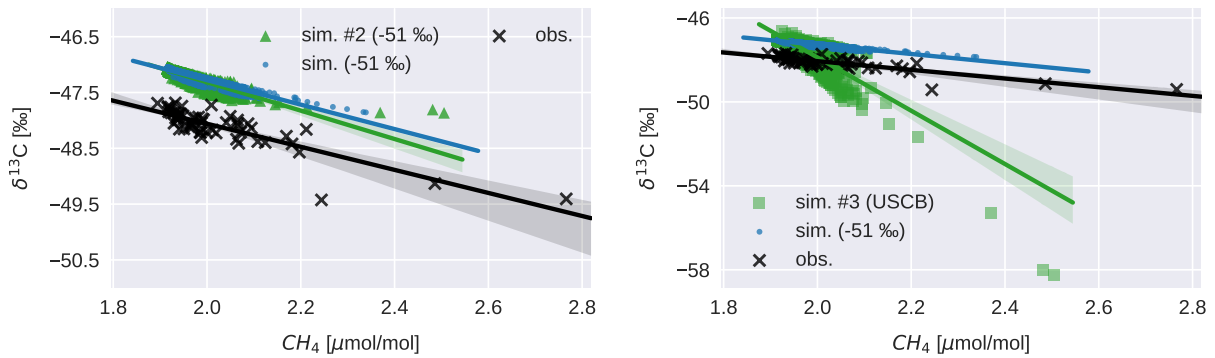


Figure 5.5: $\delta^{13}\text{C}$ plotted versus the methane mixing ratio. The left panel shows the results for the “ANA.ISO simulation (-51 ‰)” in blue, the “ANA.ISO simulation #2 (-51 ‰)” in green and the flask samples in black. The right panel shows the results for the “ANA.ISO simulation (-51 ‰)” in blue, the “ANA.ISO simulation #3 (USCB)” in green and the flask samples in black. Additionally the linear regression lines are plotted in each panel, including the 95 % confidence interval.

5.3 Summary

This chapter describes the simulation of the stable isotopologues with the regional MECO(3) by applying the extension of the MESSy submodel CH4 (Frank, 2018; Winterstein and Jöckel, 2021). Its performance on regional scale is evaluated using the example of local coal mine emissions in the USCB. Therefore, I performed several analysis simulations of the CoMet 1.0 campaign, where CH_4 mixing ratios and $\delta^{13}\text{C}$ were measured.

I assigned different isotopic source signatures, given by the literature, to the individual emission sectors, e.g. livestock, rice, wetlands or coal. In order to investigate the influence of local coal mining emissions to the simulated $\delta^{13}\text{C}$, I assumed different isotopic signatures for the coal mining methane emissions ($\delta^{13}\text{C}_{\text{Coal}}$). The results show that MECO(3) is able to simulate the stable isotopic signatures in methane plumes relative to the background signatures. The Keeling plot approach revealed, that changes in the $\delta^{13}\text{C}$ along with enhanced methane mixing ratios were attributable to the coal mining emissions. Furthermore, the selected $\delta^{13}\text{C}_{\text{Coal}}$, also affected the $\delta^{13}\text{C}$ background value in the area of study.

The simulation results were further compared to the CH_4 mixing ratios and $\delta^{13}\text{C}$ measurements, sampled during the CoMet 1.0 campaign. To determine a specific $\delta^{13}\text{C}_{\text{Coal}}$ of the coal mining emissions in the USCB, the simulation results must match the observations as closely as possible. To do so, emission fluxes and $\delta^{13}\text{C}_{\text{Coal}}$ were slightly adjusted. This estimated a $\delta^{13}\text{C}_{\text{Coal}}$ of -51 ‰ as the average of all those coal mines responsible for the discovered/measured methane plumes. The estimated value agrees with the -50.9 ± 0.6 ‰ suggested by Zazzeri et al. (2016) for the USCB coalbeds.

However, a simulation, that used different $\delta^{13}\text{C}_{\text{Coal}}$ signatures for each coal mine, did not agree well with the observations. Besides the fact that these signatures must also correspond to the actual value, it is also important that the model can simulate the observed

plumes well. The comparisons of the model results and the in-situ measurements revealed several discrepancies. It is therefore important to improve the simulation of local methane plumes in future simulations (see also Chapter 4). The assessment of the individual $\delta^{13}\text{C}_{\text{Coal}}$ emitted from each ventilation shaft is, however, beyond the scope of the study.

The presented study shows that the regional simulation of methane isotopologues with MECO(3) works well. It can support the interpretations of measurements and help to determine an isotopic composition of a specific source.

Chapter 6

Simulation of the recent methane increase and the corresponding $\delta^{13}\text{C}(\text{CH}_4)$ decrease with EMAC

The causes of the recent methane rise after a period of stabilisation from 2000-2007, and the simultaneous decrease in atmospheric $\delta^{13}\text{C}$, are currently subject to debate with a variety of hypotheses. $\delta^{13}\text{C}$ has been risen over the last decades, indicating an increasing contribution of sources relatively enriched in $\delta^{13}\text{C}$, i.e. a significant contribution from thermogenic sources. Fossil fuel production has prevailed over the last centuries with a sharp increase since the 1950s (Höök et al., 2012). During the stabilization period from 2000 to 2007, $\delta^{13}\text{C}$ remains relatively constant (see Figure 6.1 as an example for $\delta^{13}\text{C}$ at Mauna Loa Observatory). After 2007 one observes a decreasing trend, suggesting a higher proportion of emissions depleted in $\delta^{13}\text{C}$ or a change in the tropospheric oxidation capacity. Many studies assume increasing emissions from biogenic sources (Schwietzke et al., 2016; Schaefer et al., 2016; Nisbet et al., 2019), such as tropical wetlands (Nisbet et al., 2019), or enhanced agricultural activity (Schaefer et al., 2016). Worden et al. (2017) propose a decrease in biomass burning emissions of 3.7 Tg(CH₄)/yr. $\delta^{13}\text{C}$ of biomass burning emissions is less negative and a reduction would lead to an overall more negative isotopic signature. This in reverse allows for a higher proportion of thermogenic sources. A key finding in the study of Jackson et al. (2020) is an equal increase in thermogenic and biogenic emissions. Another reason could be a reduced oxidation capacity in the troposphere resulting in higher atmospheric methane lifetimes and less kinetic fractionation, which is caused by the sink reactions (Rigby et al., 2017; Turner et al., 2017). This would lead to lower atmospheric $\delta^{13}\text{C}$. Howarth (2019) proposed that increasing shale gas production with relatively light isotopic signature leads to the latest increase in atmospheric methane. Shale gas is a natural gas trapped beneath non-permeable layers, such as shale rock formation or coalbeds, which prevent shale gas from migrating upwards. Shale gas is exploited by cracking the shale rock formation artificially (hydraulic fracturing). This unconventional method is currently applied by only four countries, the US, Canada, China and Argentina, with the US being the largest producer (EIA, 2015). Since 2008 US shale gas production

has become very popular and makes up 70 % of the US natural gas production in 2018 (EIA, 2019). Since shale gas is prevented from migrating, it is not subject to any secondary fractionation. The isotopic signature originates from the primary produced thermogenic methane and might differ from the conventional fossil fuel signatures. Howarth (2019) suggests that the isotopic signatures of shale gas emissions are slightly lower than the signatures measured in conventional gas and oil emissions. He proposes that increased shale gas production is a major contributor to the renewed methane rise and simultaneous decrease in global $\delta^{13}\text{C}$. In contrast, Milkov et al. (2020) calculated an emission-weighted mean signature of only -41.8 ‰. Their calculation is based on recent measurements, taken at the mostly operated plains in the US. This signature of only -41.8 ‰ is different to the findings of Howarth (2019), who assumes a value of -46.9 ‰ for shale gas emissions. However, other studies on non-methane hydrocarbons (NMHCs), in particular on ethane, show evidence that the US oil and natural gas production has increased (Helmig et al., 2016; Franco et al., 2016; Hausmann et al., 2016). Ethane is the longest lived and most abundant NMHC (the atmospheric lifetime is about 2 - 6 months) released from fossil fuels. Helmig et al. (2016)'s study on ethane, for example, suggests a 4.2 (± 10) % increase of fossil fuel emissions per year since 2009 in the mid latitudes. Turner et al. (2016) found that over 30 % of the renewed increase is from anthropogenic emissions in the US, although not clearly attributed to a distinct source.

The presented study intends to investigate the idea of Howarth (2019) by using the chemistry climate model EMAC and applying a simplified methane chemistry, including the simulation of methane isotopologues (see CH₄ submodel in Chapter 3). In particular, it is tested, whether a state-of-the-art chemistry climate model, using the most recent emission inventories and currently available information on stable isotopic source signatures, is able to reproduce the observed decline in $\delta^{13}\text{C}$. Furthermore, it is tested, if shale gas emissions are the main cause of the decline or at least, which share they have in the increase of methane.

Many studies on atmospheric methane and $\delta^{13}\text{C}$ use flux weighted global mean source signatures and account for regional variations by considering the flux strength. However, temporal changes in regional methane source strengths of a specific source (e.g. enhanced emissions from the tropical wetlands relative to the emissions from high latitudinal wetlands) result in a modified $\delta^{13}\text{C}$ mean of the respective source. Feinberg et al. (2018) evaluated the impact of considering the regional distribution of the source signatures on the global atmospheric $\delta^{13}\text{C}$ and suggest their inclusion in future studies. The first part of this chapter therefore focuses on the refinement of the various isotopic source signatures. Based on a previous simulation (named EMAC-y-03) from Frank (2018) I build up a new setup, including these refinements. I perform two different base simulations with the new setup, which are discussed in Section 6.1.2. The main focus here is to find a suitable setup, that represents realistic results for the methane mixing ratios and $\delta^{13}\text{C}$ values. The simulation serves as a reference simulation for different sensitivity simulations. Six sensitivity simulations are carried out in order to first test the hypothesis described by Howarth (2019), and second test the influence of the applied OH field on the isotopic signatures. Thereby I make different assumptions regarding the source strengths of biogenic, fossil

fuel and shale gas emissions, as well as on the shale gas $\delta^{13}\text{C}$ signatures. The results and discussion are covered by Section 6.2. Finally, in Section 6.3, two sensitivity simulations are described and discussed to assess the potential influence of a reduced OH field on the global $\delta^{13}\text{C}$.

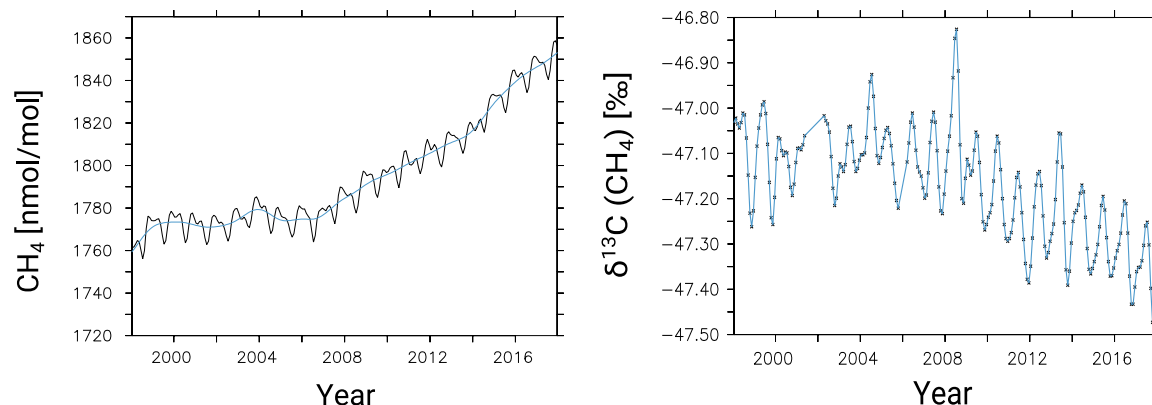


Figure 6.1: Global averaged marine near surface methane mixing ratio in black and trend in blue (left panel) and $\delta^{13}\text{C}$ measured from flask samples sampled at Mauna Loa Observatory (MLO) (right panel), all as monthly mean from 1998 to 2017. Data of the methane global mean are taken from Dlugokencky et al. (2020)) and stable isotopic composition data is taken from White et al. (2018).

6.1 Regional segmentation of methane isotopologues and base simulation

6.1.1 Model setup and isotopologues

For the presented study, several EMAC simulations are conducted in the T42L90MA-resolution, with a spectral triangle truncation at wave number 42, and with 90 vertical hybrid pressure levels between the surface and 0.01 hPa. In order to constrain the model with the observed meteorology, simulations are performed with "specified dynamics" (SD). EMAC is therefore nudged by Newtonian relaxation of temperature, divergence, vorticity and the logarithm of surface pressure towards the ECMWF reanalysis data ERA-Interim (Dee et al., 2011). ERA-Interim data are available from 1979 until August 2019. The EMAC simulations consider four methane isotopologues ($^{12}\text{CH}_4$, $^{13}\text{CH}_4$, CH_4 , CH_3D) by applying the submodel CH4. CH4 (which has been described in Chapter 3) calculates a simplified methane chemistry with predefined sink reactants. I conducted various simula-

tions named SDISO starting from 1990 including a spin up time of 10 years, i.e. the results are analysed from the year 2000 onwards.

6.1.1.1 Emission per sector

The SDISO simulations use the a posteriori inventory from a previous simulation (named EMAC-03) by Frank (2018) for all natural methane emissions between 1990 and 2012. Except for biomass burning emissions, the year 2012 is repeated cyclically from 2013 to 2019, since no better information is currently available. Biomass burning emissions (excluding agricultural waste and biofuel burning) after 2012 are taken from the GFED 4.1s emission inventory (Randerson et al., 2017). Natural emissions from wetlands, wild animals, termites, volcanoes, and the ocean, are prescribed based on monthly average data on a $1.0^\circ \times 1.0^\circ$ grid (Frank, 2018). Anthropogenic emissions including emissions from rice cultivation and ship operations are taken from the inventory EDGAR v5.0 (Crippa et al., 2020). Emission fluxes are available as annual averages on a finer grid with a $0.1^\circ \times 0.1^\circ$ resolution for the period 1990 until 2015. The year 2015 is repeatedly applied for the years 2016 to 2019, since no other inventory for these years was available. Natural and anthropogenic emissions are split into several sectors to assign them their distinct isotopic signature via the submodel OFFEMIS (Kerkweg et al., 2006b; Kerkweg and Jöckel, 2012b). Each sector is allocated to the methane master tracer (CH4_FX) of the submodel CH4. To account for the effect of plume buoyancy for example due to high temperatures of the emitted gas, emissions are not solely emitted at the Earths' surface grid boxes. Anthropogenic emissions are vertically distributed and disaggregated into different emission heights, as described by Mailler et al. (2013). Biomass burning emissions are also emitted at different altitudes and are assigned to the levels according to Dentener et al. (2006). Agricultural waste burning is excluded from the vertical distribution and only emitted at the surface. Table 6.1 lists all methane emissions per sector and their associated fluxes. Additionally, it compares all fluxes to those previously presented by Saunio et al. (2020). Note that biomass burning is not exclusively due to human activity, although here it is subordinated to anthropogenic emissions.

Table 6.1: Methane source fluxes in $\text{Tg}(\text{CH}_4)/\text{yr}$ for the periods 2000-2009 and 2008-2017. Values in the respective first two columns are taken from Saunois et al 2020. Each respected third column lists the fluxes used in the SDISO-base simulations. Fluxes are global averages. The square parentheses show that range from minimum to maximum value of the individual years. The sum of anthropogenic source fluxes includes the fluxes biomass burning.

Sources	2000-2009			2008-2017		
	Saunois et al. 2020 Flux BT	Flux TD	This study Flux	Saunois et al. 2020 Flux BT	Flux TD	This study Flux
Natural total	369 [245-485]	215 [176-243]	185 [169-203]	371 [245-488]	218 [183-248]	181 [175-199]
Wetlands	147 [102-179]	180 [153-196]	146 [134-159]	149 [102-182]	181 [159-200]	145 [140-157]
Other natural	222 [143-306]	35 [21-47]		222 [143-306]	37 [21-50]	
-Termites	9 [3-15]		24 [22-27]			22 [21-25]
-Wildanimals	2 [1-3]		5 [5-6]			5
-Ocean			7 [6-7]			6 [6-7]
-Volcanoes			3 [2-4]			3 [3-5]
Anthropogenic total	334 [321-358]	332 [312-347]	317 [311-379]	366 [349-393]	359 [336-376]	371 [349-396]
Agriculture and waste	192 [178-206]	202 [198-219]	211 [202-224]	206 [191-223]	217 [207-240]	229 [221-235]
-Enf and Mnm(*)	104 [93-109]		107 [102-113]	111 [106-116]		115 [112-118]
-Landfills & Wwt(*)			70 [67-74]			77 [73-79]
-Rice	28 [23-34]		34 [33-37]	30 [25-38]		37 [36-38]
Fossil Fuel	110 [94-129]	101 [71-151]	95 [81-105]	128 [113-154]	111 [81-131]	114 [102-122]
-Coal	32 [24-42]		28 [22-33]	42 [29-61]		37 [32-40]
-Oil and Gas	73 [60-85]		59 [53-64]	80 [68-92]		68 [62-72]
-Transport/Industry	6 [1-17]		7 [6-8]	7 [1-19]		9 [8-10]
Biomass burning	31 [26-46]	29 [23-35]		30 [26-40]	30 [22-36]	
-Awb(*)			1 [1-2]			2
-Biofuel	12 [9-14]		12 [12-13]	12 [10-14]		13
-biomass burning	19 [15-32]		22 [15-35]	17 [14-26]		15 [11-24]
Total	703 [566-842]	547 [524-560]	524 [480-582]	737 [594-881]	576 [550-594]	567 [524-595]

*(Enf = Enteric fermentation, Mnm= Manure management, Wwt=Waste water management, Awb = Agricultural water burning, Bb = Biomass burning)
BT = bottom up estimates, TD= top down estimates

6.1.1.2 Methane sink reactants

The SDISO model setup uses a simplified methane chemistry calculated by the CH₄ sub-model, and thereby predefined sink reactant fields (Cl, OH and O¹D) throughout the simulation. Additionally, the rate for the sink reaction by photolysis is calculated online via the submodel JVAL (see Chapter 3). For the period 1990 to 2012 the applied sink fields are derived from the EMAC-y-03 simulation (Frank, 2018), which was conducted with full interactive chemistry, accounting for atmospheric feedbacks on the hydroxyl radical (OH) and on the other reactants (Cl and O¹D). The applied sink fields are therefore consistent with the EMAC-y-03 a posteriori emission inventory, which is used as the biogenic emissions for the SDISO simulations (see previous section). For the years 2013 to 2017 11 the sink reactant fields are derived from the SD1SD-base-01 simulation (RCP8.5 scenario, Jöckel et al. (2016)). The months 2016/12 until 2017/11 are repeated for the months 2017/12 until 2019/01, since the SD1SD-base-01 simulation ended in 2017/11. Figure 6.2 shows the monthly averaged global mean tropospheric lifetime of methane with respect to the above described transient OH field (SDISO-trans) and to an annually repeated monthly climatological OH distribution (SDISO-clim) being calculated from the composite time series EMAC-y-03 plus SD1SD-base-01 from 1990 until 2017/11. Figure 6.2 shows the respective simulated atmospheric methane surface mixing ratios compared to observations (Dlugokencky et al., 2020). The drop in SDISO-trans methane lifetime is owed to an increase in the OH concentration in 2013, leading to a disproportionately large decrease in the atmospheric methane mixing ratio relative to the time before 2013. The differences between the EMAC-y-03 simulation and the SD1SD-base-01 simulation are due to the different model setups. OH concentration and the methane lifetime are dependent on the interplay of various chemical cycles in the atmosphere. A recent analysis of 10 CCMI (Chemistry-Climate Model Initiative) models revealed that the methane lifetime is influenced by the frequency of photolysis, the abundances of local ozone and NO_x and other components that drive OH. It is further important, how these components are represented in the different models (Nicely et al., 2020). To ensure that variability and uncertainties in atmospheric OH concentration do not impact the $\delta^{13}\text{C}$ throughout the presented study I decided to use the annually repeated monthly climatological OH distribution for all SDISO base and sensitivity simulations. Since the climatology is derived by calculating the monthly means of the time series, the annual variability is maintained. Yet, decreasing atmospheric oxidation capacity could also be a driver for recent methane rise and contribute to the observed changes in $\delta^{13}\text{C}$ (Rigby et al., 2017; Turner et al., 2017). The lighter $^{12}\text{CH}_4$ is preferably removed during OH oxidation. Thus, less OH would result in an overall more negative $\delta^{13}\text{C}$. The examination of $\delta^{13}\text{C}$ with respect to OH variations after 2008 is subject of Section 6.3.

Simulated global atmospheric methane mixing ratios of SDISO-trans and SDISO-const simulations after 1998 (Figure 6.2) lie below the observations. In order to build on a base simulation with a best guess for atmospheric methane mixing ratios, I adjusted the OH field by a factor of 0.96 for the period after 1998. This results in a tropospheric mean $\tau_{\text{CH}_4}(\text{OH})$ of about 9 years (details on the estimation can be found in Section 6.2.2), which is within

the uncertainty range of the tropospheric $\tau_{\text{CH}_4}(\text{OH})$. As described in the introductory part (Chapter 2), tropospheric lifetime with respect to OH varies among different studies. The EMAC tropospheric lifetime calculated by Jöckel et al. (2006) and Frank (2018) is 8.02 years for the period 2000-2004 and 8.11 ± 0.13 years for the period 2000-2010, respectively. The Chemistry-Climate Model Initiative (CCMI) estimated a $\tau_{\text{CH}_4}(\text{OH})$ multi-model mean of 9 years for 2000-2009 [7.2-10.1] (Saunois et al., 2020). Other studies suggest even longer methane lifetimes for this period (see Chapter 2). The lifetimes calculated for EMAC are at the lower end of the scale and are likely underestimated. An assumption of 9 a seems therefore not unrealistic. Furthermore, 9 a lie within the range of uncertainties and equal the CCMI multi-model mean for 2000-2009. However, uncertainties in source strength cannot be ruled out. For instance, in the SDISO model setup, the wetland emissions are small compared to other studies (e.g. Poulter et al., 2017; Saunois et al., 2020) and EDGAR v5.0 anthropogenic emissions fall below those of the optimized EMAC-03 inventory between 1995 and 2005 (further discussed in Section 6.1.2, Figure 6.14).

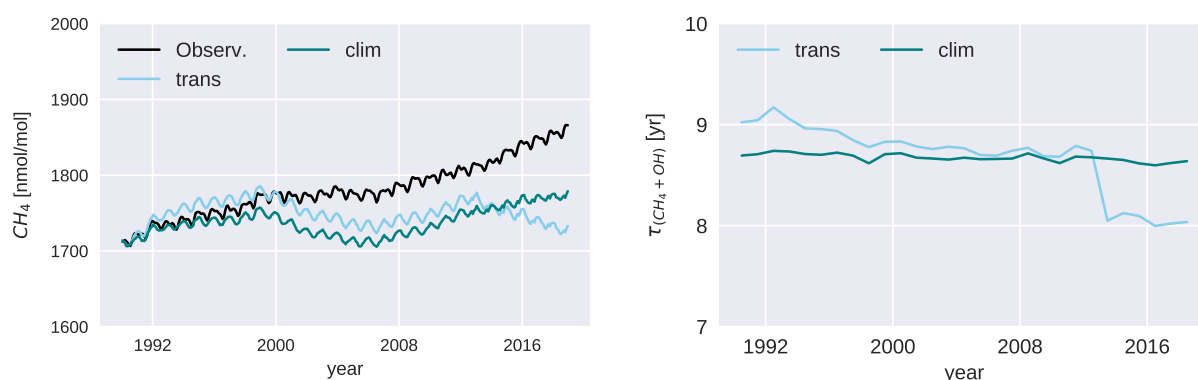


Figure 6.2: Global mean surface methane mixing ratio of the simulations SDISO-trans and SDISO-clim compared to the observed global mean marine surface mixing ratios from Dlugokencky et al. (2020, left panel) and the mean tropospheric methane lifetime with respect to the applied OH field of SDISO-trans and SDISO-clim (right panel).

6.1.1.3 Methane isotopologues in the model setup

Chapter 2 reported on the classification into biogenic, thermogenic and pyrogenic source types and their associated isotopic signatures. Source signatures depend on the precursor organic material, which can vary in its composition of heavy and light isotopes. They further depend on type and magnitude of its formation, i.e. the different pathways of methane production and its consumption by microorganisms, which lead to kinetic isotope effects (Whiticar, 1999). Thus, differences in environmental conditions lead to variations within a particular source and mostly show up as a regional pattern. The present section is dedicated to the regional variation of $\delta^{13}\text{C}$ of the individual sources and how I account for them in the model setup. Regional breakdown of $\delta^{13}\text{C}$ is applied to these sectors: wetlands, biomass and agricultural waste burning, gas, oil, coal, and livestock. Due to lack of information,

the breakdown of δD is only applied to the gas, oil and coal sectors. I created gridded maps with information on the regional distribution of $\delta^{13}\text{C}$ and δD . The creation of these gridded maps and the data on which they are based will be explained separately in the next two subsections for biogenic and pyrogenic sources and for thermogenic sources, respectively. Fluxes in EMAC are prescribed in units of molecules/m² s⁻¹. Natural emission fluxes of the a posteriori EMAC-03 inventory are also prescribed in units of molecules/m² s⁻¹, and can be simply split into the fraction of the abundant ¹²CH₄ and the fraction of the rare ¹³CH₄. The EDGAR v5.0 emission fluxes are provided in units of kg(CH₄) m⁻² s⁻¹. Therefore, special caution needs to be taken to split the emission fluxes according to their signatures. I calculated the number of abundant and rare molecules matching the isotopic signature for each grid cell according to equation in the Appendix A.3.1 before reading them into the model via the submodel IMPORT_GRID. Constant $\delta^{13}\text{C}$ and δD values are assigned to these sectors: industry, ship operations, biofuel burning, wildanimals, termites, oceans, and volcanoes. These constant signatures are the flux weighted global mean signatures calculated by Frank (2018) based on recent literature. All isotopic source signatures used in the SDISO model setup are summarized in Table 6.2. They are read one-by-one via the submodel IMPORT_GRID and handed over to the submodel OFFEMIS, where emission fluxes are split into abundant and rare fraction and contribute to the tracers CH4_12C and CH_13C, respectively (or accordingly to tracers CH4_D0 and CH3_D1).

Regional distribution of isotopic signatures

Biogenic/pyrogenic sources:

The isotopic signature of biogenic sources depends, among others, on the type of bulk material (plants and other organic material). Plants can be categorized according to their pathway of photosynthesis. For an optimal adaptation to different habitats and climatic conditions, they developed different ways of carbon dioxide fixation taking place with or separately from the Calvin Cycle (Ehleringer et al., 1997; Ehleringer and Cerling, 2002). We distinguish between C-3 plants such as trees, crops and rice in moderate climate zones, C-4 plants, like grasses and sedges predominantly in hot regions (subtropics and tropics) and the CAM (Crassulacean Acid Metabolism) plants, such as epiphytes and succulents, which are adapted to dry and hot regions (Ehleringer and Cerling (2002), Still et al. (2009), see Figure 6.3). Whereas C-3 plants preferably use the lighter ¹²C isotopes, the latter two increasingly incorporate the heavier ¹³C isotopes (Farquhar et al., 1989). This results in different distributions of light and heavier carbon isotopes among the different plant types and can be further recognized in the methane emissions from biomass burning or enteric fermentation (Dlugokencky et al., 2011). $\delta^{13}\text{C}$ in methane derived from C-3 plant material constitutes -26 (± 3) ‰ for biomass burning and -70 (± 4) ‰ for enteric fermentation. The $\delta^{13}\text{C}$ of C-4 plant-based emissions is accordingly more positive, -17 (± 3) ‰ and -49 (± 4) ‰, for biomass burning and enteric fermentation, respectively (Dlugokencky et al., 2011). An increase of for example tropical livestock emissions would lead to the emission of

isotopically enriched methane. I therefore account for the regional distribution of C-3 and C-4 plants when adapting emission source signatures. I use the map by Still et al. (2009) shown in Figure 6.3 and calculate the signature per grid-box according to the percentage of C4 plants within the grid-box. Note that I assume that the remaining percentage only consists of C3 plants. CAM plants play a minor role in the carbon cycle and are not considered here. However, while this is just an assumption, one cannot expect that source material (e.g. food for cattle) always correlates with the percentage of C-4 or C-3 plant abundance within the grid-box. The resulting weighted annual means are presented in the upper two panels of Figure 6.5. The signatures of biomass burning (bb) emissions can deviate more than $+1.5\text{‰}$ from the literature mean, but still remain within the range of the uncertainties. The presented $\delta^{13}\text{C}$ correlates well with the El Niño Southern Oscillation (ENSO). Negative values correspond to El Niño events leading to enhanced biomass burning in tree (C-3 plants) dominated regions in South Asia and South America, for example the large Indonesian wildfires in 1998. In contrary, during the La Niña years emissions with a larger C-4 plant fraction appear (e.g. enhanced emissions from savanna regions in 2000, (Randerson et al., 2005)).

$\delta^{13}\text{C}$ resulting from livestock emissions shows less variability over this time period. But a slight increase in $\delta^{13}\text{C}$ indicates a shift to more tropical livestock emissions. Isotopic signatures are generally much more negative than the -60.2‰ reported in other literature (Frank (2018) and references therein: Quay et al. (1999); Snover and Quay (2000); Whiticar and Schaefer (2007)). This negative offset is comparable to results from Feinberg et al. (2018). However, due to the discrepancies between this study and literature values, two simulations are performed, SDISO-base-c using the constant literature value for livestock and SDISO-base-v using the newly calculated lower signatures.

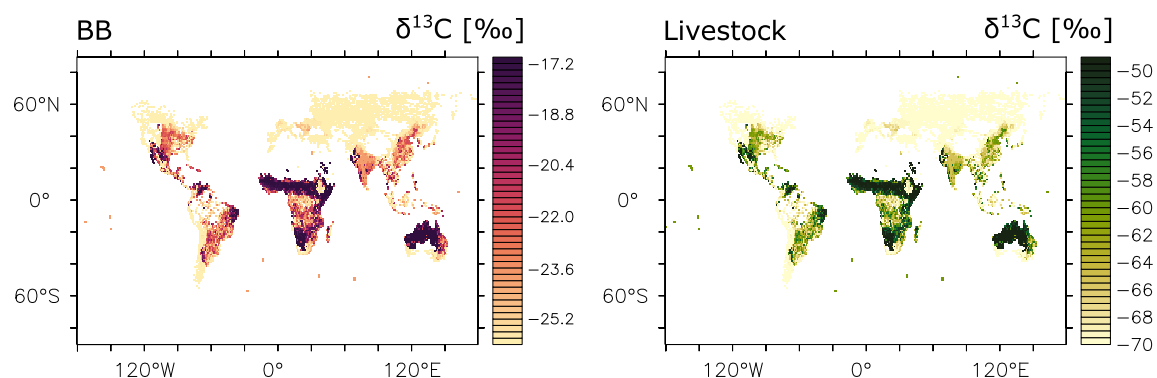


Figure 6.3: Global $\delta^{13}\text{C}$ in $[\text{‰}]$ distribution of biomass burning (left panel) and livestock (right panel) emissions. Data for the fraction of C-4 plants in the total global vegetation is derived from Still et al. (2009) and serves as a basis for the assignment of $\delta^{13}\text{C}$ signatures to livestock and biomass burning emissions.

Isotopic signatures of wetland emissions are associated with the primary isotope com-

position (type of plant) and the environmental conditions under which methanogenesis has taken place. Tropical $\delta^{13}\text{C}$ is in general more enriched than boreal $\delta^{13}\text{C}$, with a mean of -56.7‰ and -67.8‰ , respectively (Ganesan et al., 2018). As described above, initial organic material in the tropics is already more enriched than in high latitudes, which is due to the appearance of C-4 plants in the tropics. Furthermore, two pathways of methanogenesis exist: Methanogenesis by CO_2 reduction, which occurs predominantly in marine sediments, and methanogenesis by acetate fermentation, which occurs mainly in freshwater. CO_2 reduction typically leads to more depleted methane (Whiticar et al., 1986). Which of these two pathways prevails is also dependent on the type of water (i.e. fresh or salt water), depth and acetate availability (pH, Whiticar et al., 1986; Hornibrook, 2009). Additionally, kinetic fractionation appears as methane is oxidized during its transport through the sediment or water column. Methane produced in floating grassmats in the Amazon region for example become isotopically enriched, likely due to oxidation by emerged macrophytes (Chanton et al., 1989). The regional isotopic signatures for this study are derived from the source signature map of Ganesan et al. (2018), which provides spatially resolved wetland $\delta^{13}\text{C}$ on a $0.5^\circ \times 0.5^\circ$ grid (see Figure 6.13). The resulting flux weighted annual means from 1990-2019 are shown in the middle left panel of Figure 6.5. Between 1992 and 2008 $\delta^{13}\text{C}$ lies mainly below the literature mean with a slightly increasing trend, indicating more input from tropical wetlands. The course is in accordance with the study of Poulter et al. (2017), who investigated the period 2000 to 2012 and found wetland emissions to be dominantly from boreal regions with a slightly increasing contribution from the tropics after 2006. Since the emission inventory is limited to the year 2012, no statements can be made for the last period 2013-2019.

Thermogenic sources:

Methane from fossil fuels and volcanoes developed under high pressure and temperatures conditions. The latter influences the kinetic isotopic fractionation and results in enriched $\delta^{13}\text{C}$ and δD relative to the source rock. $\delta^{13}\text{C}$ and δD of these so called thermogenic sources typically range from -50 to -20‰ and -275 to -100‰ , respectively. Besides the thermal maturity level, source material also has an influence on the isotopic ratio. Methane can be produced at very low thermal stress, if the source rock is hydrogen-rich, which results in relatively negative $\delta^{13}\text{C}$ (Whiticar, 1999). Thermogenic signatures vary largely, but contrary to the biogenic sources, they do not show a specific latitudinal pattern. Zazzeri et al. (2016) describe different coal source signatures dependent on maturity and depth (i.e. pressure) under which the coal is formed. They range from low values of $-70 (\pm 10)\text{‰}$ for sub-bituminous coals formed under low pressure and low temperatures conditions over bituminous coal with $-50 (\pm 20)\text{‰}$, to very high pressure-high temperature formed anthracite coal with higher signatures of $-30 (\pm 10)\text{‰}$. Thus, depending on the different coal mines and coal type, which is extracted in different countries, methane signatures can vary within a large range of isotopic signatures. The global data set of Sherwood et al. (2017) provides country specific information on $\delta^{13}\text{C}$ and δD for coal and conventional gas and oil emissions. Based on this data set, I assigned each country its individual source.

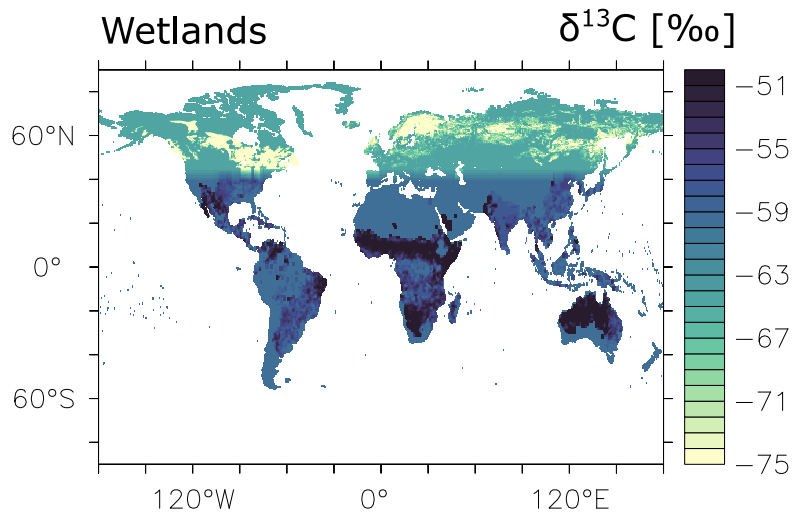


Figure 6.4: Global $\delta^{13}\text{C}$ in [‰] distribution of wetland emissions based on the dataset of Ganesan et al. (2018).

Where no data was available, the global mean is applied. Figure 6.6 shows the resulting regional distribution. For coal I use a mean signature of -50 ‰ (Zazzeri et al., 2016). As literature values differ widely from each other, the mean of -41 ‰ taken from Frank (2018) (and literature therein: Quay et al. (1999); Whiticar and Schaefer (2007); Zazzeri et al. (2015)), is alternatively applied. Resulting $\delta^{13}\text{C}$ are presented in the middle right panel of figure 6.5. $\delta^{13}\text{C}$ based on the -50 ‰ differ up to -3 ‰ from the constant literature value calculated by Frank (2018). However, coal signatures have a wide uncertainty range and all resulting signatures lie within these uncertainties. To account for the differences, the simulation SDISO-base-c is performed with the constant value and SDISO-base-v uses the -50 ‰ transient signatures. The increase after 2002 in both time series is due to the contribution of coal emissions with relatively enriched $\delta^{13}\text{C}$ from China in the EDGAR v5.0 inventory. Thompson et al. (2015) estimated the emissions from China to be responsible for 40 % of the total methane increase after 2000. However, unless Chinese extracted coal type does not move towards less enriched signatures, this increase is not compatible with the observed global $\delta^{13}\text{C}$ (Feinberg et al., 2018). Since the contribution of fossil fuel emissions to the global methane increase is subject to the presented study, this will be covered later in the discussion. For gas and oil emissions I apply a mean signature of -44 ‰ (Schwietzke et al., 2016). Resulting annual signatures (Figure 6.5, lower left panel) show little variations. Note that the scale of the vertical axis scale is very small. A decline of oil emissions with higher $\delta^{13}\text{C}$ potentially leads to the decreasing $\delta^{13}\text{C}$ signatures after 2010.

Table 6.2: Isotopic global mean signatures of the individual methane sources in [‰] used in SDISO-base. Most values are derived from a previous EMAC setup (Frank, 2018) and display flux weighted averages. The two last columns list the adjusted signatures including the consideration of regional variations, which are applied in SDISO-base-v or partly in SDISO-base-c. These values are weighted by the individual regional flux strength and averaged over the period 1990-2019. If not specifically listed in column SDISO-base-c or SDISO-base-v, the global mean is used.

Sources	SDISO-base-c			SDISO-base-v						
	$\delta^{13}\text{C}$ (+/-)	ref. (+/-)	δD (+/-)	$\delta^{13}\text{C}$ (+/-)	δD (+/-)	$\delta^{13}\text{C}$ (+/-)	δD (+/-)			
Biogenic										
Wetlands	-59.2	1.5	(2)	-336.2	23.8	(2)	-44.3	0.5	-44.3	0.5
Termites	-63.3	6.5	(2)	-390.0	35.5	(2)				
Wildanimals	-61.5	0.5	(2)	-319.0	/	(2)				
Ocean	-59.0	1.0	(2)	-220.0	/	(2)				
Livestock	-60.2	0.3	(2)	-317.5	12.5	(2)	-65.7	0.4		
- C3	-70	4.0	(1)							
- C4	-49	4.0	(1)							
-Enf(*)									-65.6	0.4
-Mnm(*)									-66.8	0.3
Landfills & Wwt(*)	-51.7	2.5	(2)	-304.3	8.5	(2)				
Rice	-63.0	1.0	(2)	-324.3	5.5	(2)				
Pyrogenic										
Biomass burning	-23.9	1.6	(2)	-213.0	7.5	(2)	-23.64	1.2	-23.64	1.2
Awb(*)	-23.9	1.6	(2)	-213.0	7.5	(2)	-23.9	0.3	-23.9	0.3
- C3 (awb,bb(*)	-26	3	(1)							
- C4 (awb,bb(*)	-17	3	(1)							
Biofuel	-23.9	1.6	(2)	-213.0	7.5	(2)				
Thermogenic										
Volcanoes	-40.9	0.9	(2)	-253.4	53.5	(2)				
Fossil Fuel	-41.8	7.5	(2)	-154.2	2.5	(2)	-43.2	0.4	-177	22.3
-Coal	-41.0	7.0	(2)	-140.0	0.0	(2)	-43.4	1.1	-150.4	2.2
-Gas	-44.0	0.5	(3)	-182.5	2.5	(2)	-44.1	0.2	-189.6	2.6
-Oil							-44.3	0.5	-189.0	2.8
Transport/Industry	-41.7	1.5		-164.0	21.3					

(¹)Dlugokencky et al. (2011), (²)Frank (2018) and references in there, (³)Schwietzke et al. (2016)

* (Enf = Enteric fermentation, Mnm = Manure management, Wwt = Waste water management, Awb = Agricultural water burning, Bb = Biomass burning)

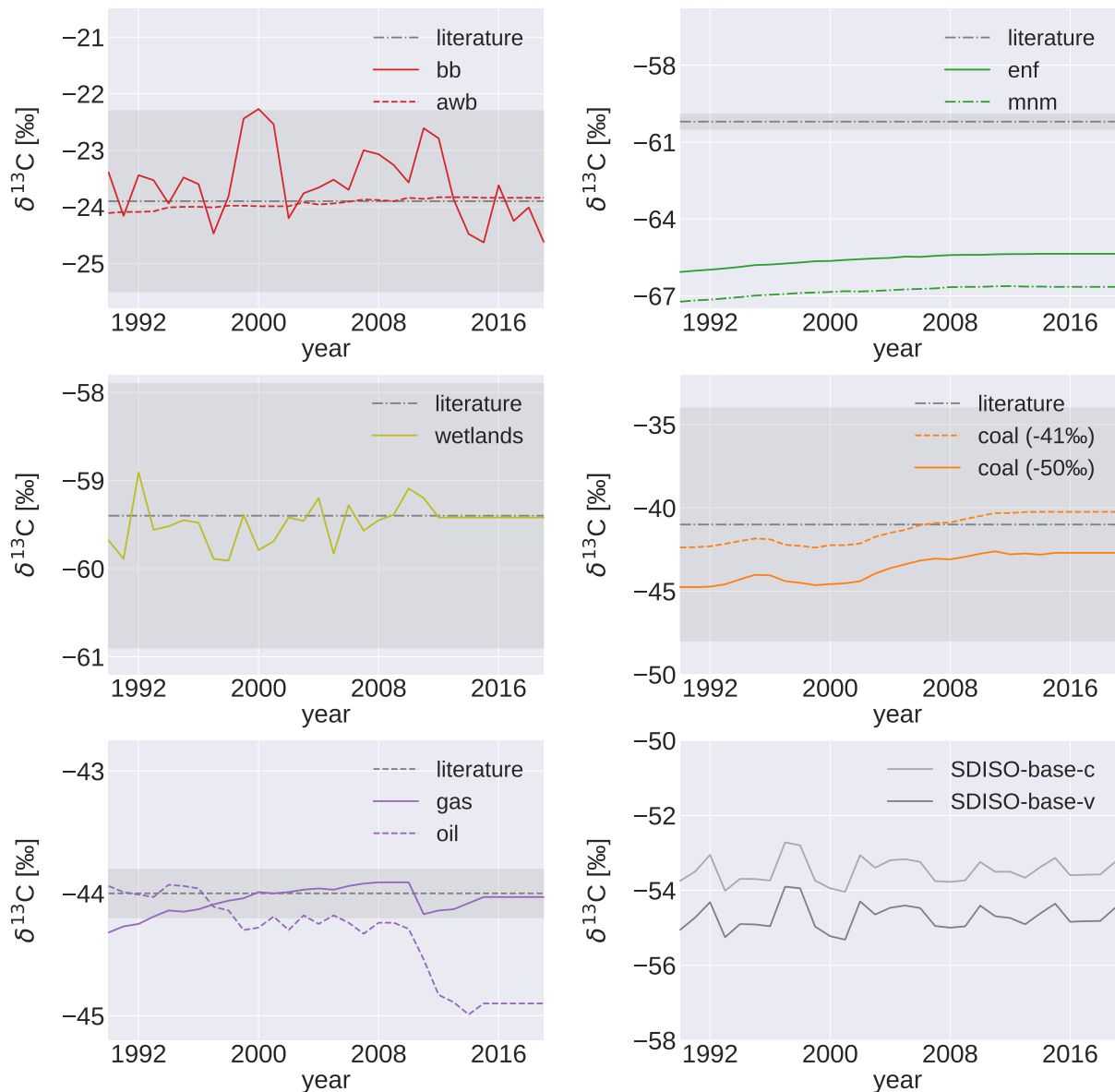


Figure 6.5: Transient flux-weighted $\delta^{13}\text{C}$ for pyrogenic (red), livestock (green), wetlands (olive), coal (orange), and gas and oil (purple) emissions, as well as the flux weighted $\delta^{13}\text{C}$ of all emissions as used in the simulations SDISO-base-c and SDISO-base-v, including those emissions with constant $\delta^{13}\text{C}$ signatures. Grey dashed lines display the corresponding mean literature signatures calculated by Frank (2018). The dark grey area indicates the uncertainty range as reported by Frank (2018). Abbreviations: biomass burning (bb), agricultural waste burning (awb), enteric fermentation (enf), manure management (mnm). The different signatures for coal emissions are the result of assuming two different mean $\delta^{13}\text{C}$ values (-41 or -50 ‰), wherever specific country data is missing.

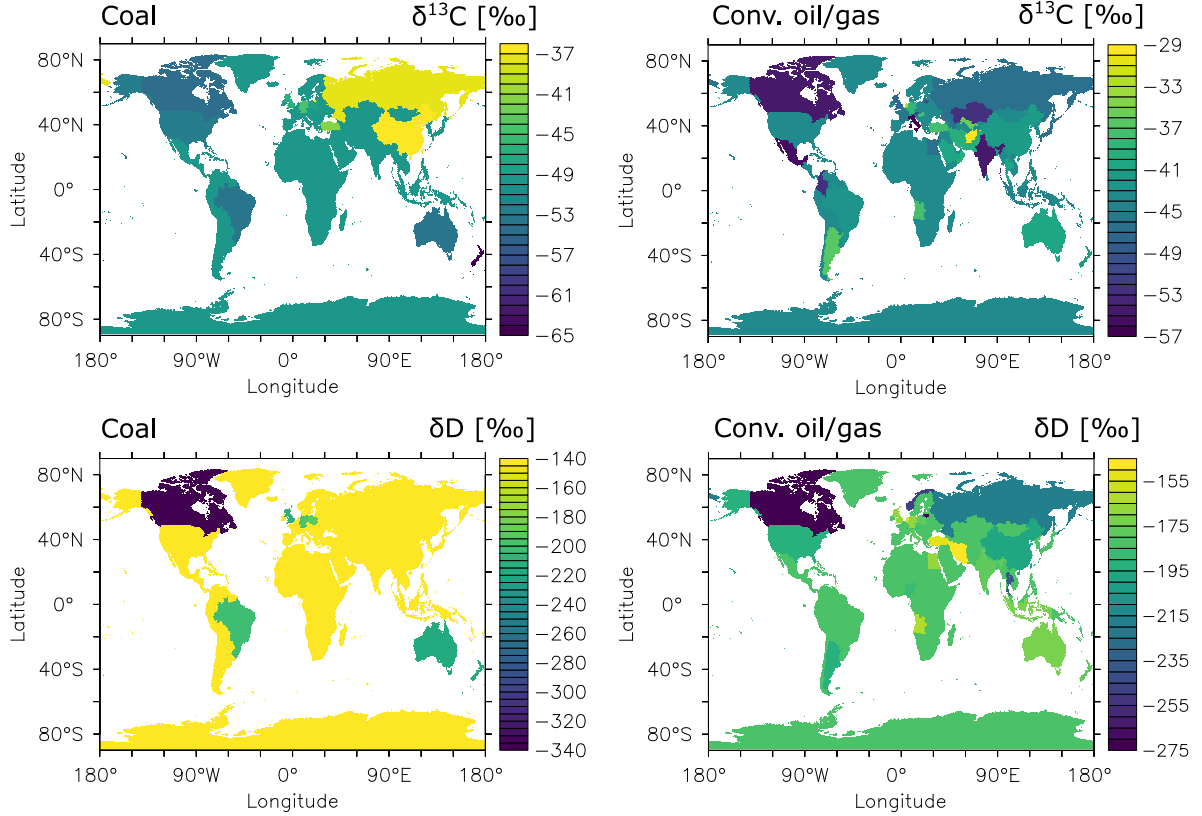


Figure 6.6: Isotopic source signatures for coal (left panels) and conventional gas and oil exploitation (right panel) used in the SDISO model setup. The maps show the regional distribution of $\delta^{13}\text{C}$ (upper panels) and δD (lower panels) in ‰. Values are taken from Sherwood et al. (2017). Missing values are filled with the global mean. Table 6.2 lists the exact values and their corresponding references.

6.1.1.4 Tracer initialization

The methane master tracer, as well as the tracers for all four isotopologues CH_4 , CH_3D , $^{12}\text{CH}_4$ and $^{13}\text{CH}_4$, are initialized with results from the EMAC-y-03 simulation (Frank, 2018) in January 1990. All tracers are scaled by a factor of 0.98 to match the global monthly mean methane observations in January 1990 (Dlugokencky et al., 2020). The initial global mean $\delta^{13}\text{C}$ of -47.75 ‰ approximately corresponds to the observed -47.37 ‰ (Schaefer et al., 2016), with however a small offset of -0.38 ‰. First test simulations of SDISO-base-c and SDISO-base-v showed a drop in the simulated $\delta^{13}\text{C}$ during the spin up phase, resulting in an almost constant offset compared to the observations after 2000. This applies for both simulations, whereby the SDISO-base-v simulation decreases more strongly. Reasons for these biases will be discussed in Section 6.1.2. To avoid the drop during the beginning period, I additionally scale the initial atmospheric methane isotopologues for both simulations according to their mean bias after the spin up time. Details on the bias calculation can be found in the Appendix A.3.1. Carbon isotope signatures of

Table 6.3: Nomenclature and overview of the model setup and the simulations carried out with the EMAC model in this study.

Name	Description
SDISO	Model setup for the EMAC model using "specified dynamics" (SD) and simulating CH ₄ isotopologues.
-trans	Simulation based on the SDISO setup using a transient OH field.
-clim	Simulation based on the SDISO setup using an annually repeated monthly OH climatology (climatology: 1990-2017).
-base -v	Simulation based on the SDISO-clim simulation with regional splitting of the $\delta^{13}\text{C}$ and δD source signatures.
-base -c	Simulation similar to SDISO-base-v, but constant $\delta^{13}\text{C}$ for livestock and coal emissions.
-sens*	Sensitivity simulations towards shale gas emissions based on the SDISO-base-c simulation. Further description see Table 6.4.
-gfed*	Sensitivity simulations towards shale gas emissions based on the SDISO-base-c simulation, using GFED v4.1s data for biomass burning emissions. Further description see Table 6.5.
-OH*	Sensitivity simulations towards OH variations based on the SDISO-base-c simulation using constant emissions after 2007. Further described in Section 6.3.

the initial files are adjusted to fit the observed $\delta^{13}\text{C}$ in 1990 plus a bias, which is -1.74 ‰ and -2.65 ‰ for the SDISO-base-c and the SDISO-base-v simulation, respectively.

6.1.2 Results and discussion of the base simulations

It is important to find a base simulation for the future sensitivity studies, which matches the observed methane mixing ratios and $\delta^{13}\text{C}$ in the atmosphere sufficiently well. In light of this, I compared the two simulations, SDISO-base-c and SDISO-base-v, to define the most suitable base simulation. The selected simulation is then evaluated and compared to observed global-mean data, as well as to observations at individual sampling sites. I use monthly-averages estimated from flask samples, wherever the time series between 2000 and 2015 is available. The map in Figure 6.7 shows the exact locations of these sampling sites. Data for methane mixing ratios and $\delta^{13}\text{C}$ are taken from Dlugokencky et al. (2020, <https://www.esrl.noaa.gov>, April 2020) and White et al. (2018, <https://www.esrl.noaa.gov>,

6. Simulation of the recent methane increase and the corresponding $\delta^{13}\text{C}(\text{CH}_4)$ decrease with EMAC

April 2020), respectively. A main focus also lies on the global distribution of the simulated surface $\delta^{13}\text{C}$, in order to find out how well the regional refinement of the individual source signatures is represented in the model. Furthermore, I explore whether the base simulation can reproduce the observed trend in global methane and $\delta^{13}\text{C}$. Finally, the simulated CH_4 mixing ratios and their corresponding $\delta^{13}\text{C}$ after the stabilization period (i.e. after 2007) are analysed with respect to the flux strengths of the individual sources.

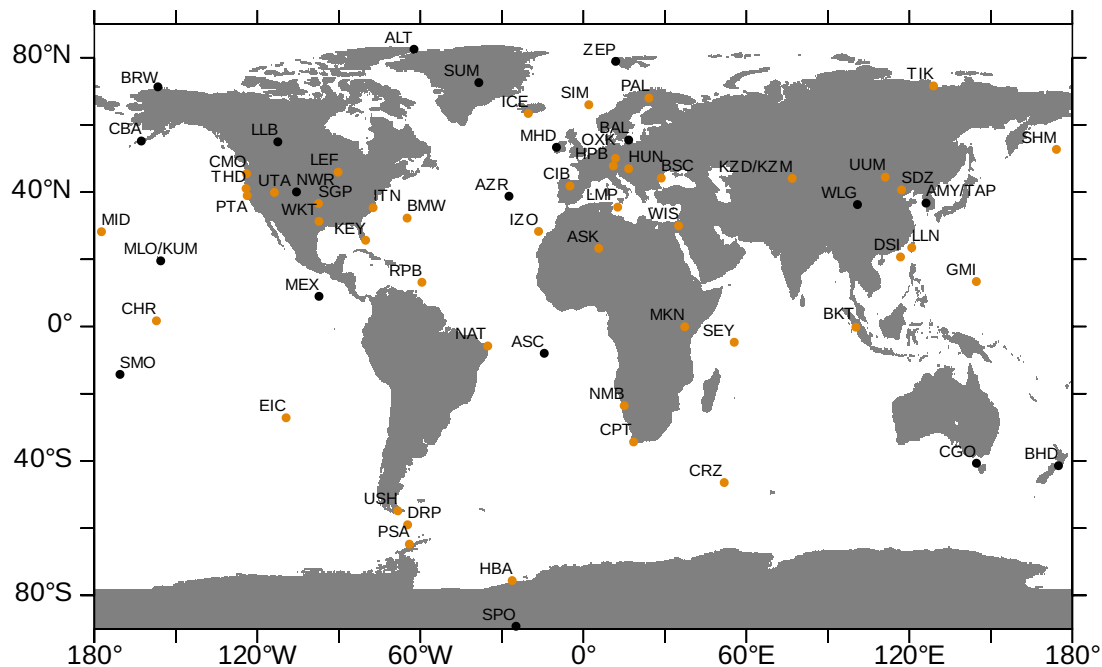


Figure 6.7: Map showing the locations of CH_4 and $\delta^{13}\text{C}(\text{CH}_4)$ ground-based sampling sites. At the orange marked sampling sites the dry mole fraction of atmospheric CH_4 is measured. At the black marked sampling sites, $\delta^{13}\text{C}(\text{CH}_4)$ is additionally measured. The measurement sites are monitored by different groups within NOAA and the Institute of Arctic and Alpine Research (INSTAAR), University of Colorado, Boulder. Data is taken from Dlugokencky et al. (2020) and White et al. (2018) for CH_4 and $\delta^{13}\text{C}(\text{CH}_4)$, respectively (derived from <https://www.esrl.noaa.gov>, April 2020).

Comparison of SDISO-base-c and SDISO-base-v

The two performed base simulations SDISO-base-c and SDISO-base-v only differ with respect to their isotopic source signatures of livestock and coal emission. This results in different emitted flux-weighted mean isotopic source signatures of -53‰ and -55‰ , respectively. Both, methane fluxes and applied sink reactant fields are identical. The discussion on the resulting atmospheric mixing ratios therefore applies to both simulations, and will be part of the next section. I first compare both simulations with respect to the observed $\delta^{13}\text{C}$. The observed annual global-mean is taken from Schaefer et al. (2016), who used different measurements from individual NOAA and INSTAAR (Institute of Arctic and Alpine Research) ground-based sampling sites to estimate five zonal means, and from that an area-weighted global-mean. Most of these sampling site locations are used for the comparison to the model result and are shown in a map in Figure 6.7. For the comparison I use model results at the surface layer (hereinafter referred to as $\delta^{13}\text{C}_{surf}^{sim}$). I derived the area-weighted global-mean $\delta^{13}\text{C}_{surf}^{sim}$ from the zonal means for polar regions (66.5° to 90°) and mid latitudes (23.5° to 66.5°) in both Hemispheres, as well as for the tropical zone (23.5°S to 23.5°N). The zonal means are calculated from the sum of $^{12}\text{CH}_4$ and the sum of $^{13}\text{CH}_4$ of all sampling sites within the respective zone. Additionally, a global-mean $\delta^{13}\text{C}_{surf}^{sim}$ is calculated by taking into account all model surface grid boxes. This value represents the models' best guess and is comparable to that calculated on the basis of the individual sampling site signatures (see Figure 6.8, left panel). However, the latter exhibits a larger standard deviation due to the fewer data points included in the calculation. As both model means are in good agreement, I further use the global-mean $\delta^{13}\text{C}_{surf}^{sim}$ based on all model surface grid boxes for the comparison with the observations (see Figure 6.8, right panel).

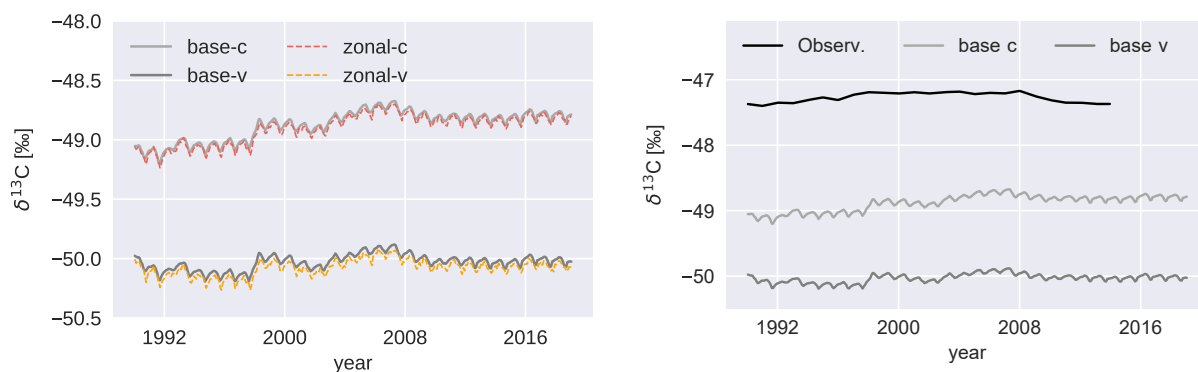


Figure 6.8: Left panel: Comparison of globally averaged $\delta^{13}\text{C}_{surf}^{sim}$ (of SDISO simulations base-c and base-v) estimated in two different ways. Either, by taking into account all model surface grid boxes results (grey), or by calculating the area-weighted mean of five zonal means (coloured). The zonal means are in turn estimated by using the model results at individual measurement stations (see Section 6.1.2). Right panel: Global averaged surface $\delta^{13}\text{C}$ in [‰] of SDISO-base-c / -v and observations. The observed global signatures are taken from Schaefer et al. (2016).

As described before, the emitted flux-weighted mean $\delta^{13}\text{C}$ of the two base simulations differ due to the regional refinement of livestock and coal mining emission signatures. This is reflected by a bias between their resulting $\delta^{13}\text{C}_{surf}^{sim}$ (see Figure 6.8). The SDISO-base-v simulation uses a relatively negative isotopic signature (-55 ‰) compared to previous studies. The emitted $\delta^{13}\text{C}$ of the SDISO-base-c simulation (-53 ‰), in contrast, is comparable to other literature, e.g. -53.5 ‰ from Schwietzke et al. (2016). Due to isotopic fractionation, atmospheric $\delta^{13}\text{C}$ is typically enriched relative to the emitted $\delta^{13}\text{C}$. The SDISO-base-c and SDISO-base-v simulations are able to reproduce this enrichment well, although both $\delta^{13}\text{C}_{surf}^{sim}$ fall below the observations. In the troposphere the enrichment is caused by OH oxidation or soil uptake, yet with uncertainties regarding the extent of kinetic isotope fractionation. In the SDISO setup a $\text{KIE}_{(\text{OH})}$ of 1.0039 reported by Saueressig et al. (2001) is used, which equals a fractionation effect ε of -3.89 ‰ ($\varepsilon = 1/\text{KIE}-1$). Cantrell et al. (1990) for example, calculated a KIE of 1.0054, resulting in a larger ε of -5.4 ‰. The relatively low fractionation factor used in the SDISO setup could explain the negative bias of $\delta^{13}\text{C}_{surf}^{sim}$ in comparison to the observed global-mean. Furthermore, EMAC is operated without interactive chemistry. Consequently, there is no feedback on the tropospheric OH concentration, which in turn affects the degree of fractionation. This is in agreement with Frank (2018), who used a similar EMAC setup and found stronger fractionation when EMAC is operated with full interactive chemistry instead of simplified chemistry. Figure 6.9 shows the global distribution of $\delta^{13}\text{C}_{surf}^{sim}$ averaged over the period 2000-2015 for both simulations (left and middle panel). Both show a North-South gradient, which is slightly larger in the SDISO-base-v simulation. In Eastern China $\delta^{13}\text{C}_{surf}^{sim}$ differences between both simulations (right panel) are very small. Emissions here are dominated by coal mining. Although the two simulations differ in their coal $\delta^{13}\text{C}$ signature, Chinese coal in SDISO-base-v is most enriched in the heavier carbon isotope and is closest to the constant literature value, which is used in SDISO-base-c (see previous Section 6.1.1.3). Apart from that, both simulations show a similar pattern, e.g. time series in Figure 6.8 and global distribution in Figure 6.9 (see also Appendix A.3.2 for the comparison of the two simulations at selected sampling sites). Both simulations include a regional refinement of the isotopic signatures for biomass burning, wetlands, gas and oil. The additional refinement of livestock and coal emission signatures in the SDISO-base-v simulation lead only to a constant offset of the emitted flux-weighted mean $\delta^{13}\text{C}$ (see Figure 6.5) and of the resulting global mean $\delta^{13}\text{C}_{surf}^{sim}$ (see Figure 6.8) relative to the SDISO-base-c simulation. Applying latitudinal changes in the flux strengths of livestock and coal emissions could, however, affect the resulting global mean $\delta^{13}\text{C}_{surf}^{sim}$. But in the present study, sensitivities are performed by down- or upscaling the emissions globally. Consequently, significant differences of the patterns between a sensitivity based on SDISO-base-v and a sensitivity based on SDISO-base-c, are not expected. Therefore, and as livestock $\delta^{13}\text{C}$ in the SDISO-base-v simulation deviates strongly from most literature values, the SDISO-base-c simulation is used as a reference for the subsequent sensitivity studies. The use of an overall too negative isotopic signature for livestock (SDISO-base-v) could, in contrast, induce biases when livestock emissions are reduced or increased globally. Nevertheless, in future studies livestock $\delta^{13}\text{C}$ of SDISO-base-v could be scaled to fit into the range of uncertainties and therefore maintain the regional distribution.

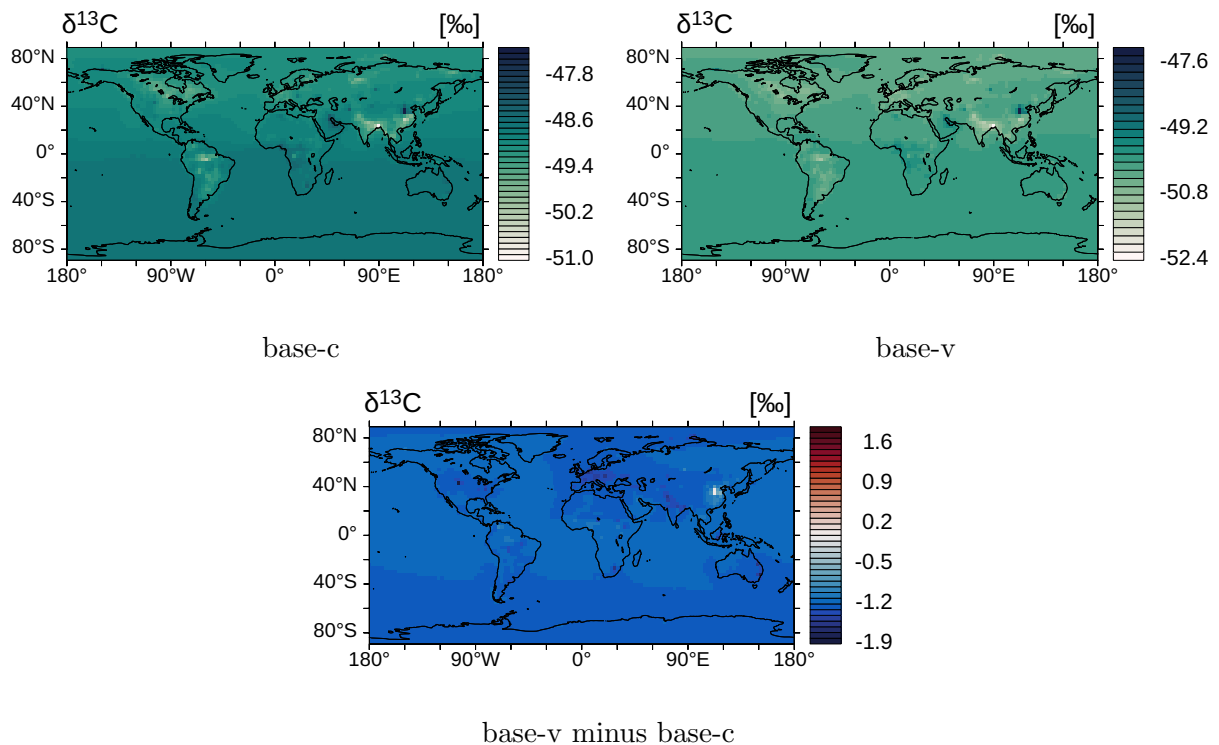


Figure 6.9: Global distribution of surface $\delta^{13}\text{C}$ in [‰] of the SDISO-base-c simulation (upper left panel), the SDISO-base-v simulation (upper right panel) and the difference: base-v minus base-c (lower panel). In each case the average is shown for the period 2000-2015.

Evaluation of the base simulation

Figure 6.10 (left panel) shows the global surface mixing ratios of methane averaged over the period 2000-2015 of the base simulation. The overall North-South gradient can be explained by the higher abundance of methane sources in the Northern Hemisphere. The good agreement with observations (see Figure 6.11, left panel) also reveals that SDISO-base-c simulates a realistic gradient between the Northern and Southern Hemisphere. Yet, observations at single measurement stations show locally enhanced methane mixing ratios, which are hardly comparable to the simulated global mean. Similar to the methane mixing ratios, a North-South gradient can also be seen in $\delta^{13}\text{C}_{surf}^{sim}$ (right panel). In the Southern Hemisphere $\delta^{13}\text{C}_{surf}^{sim}$ is enriched in the heavier carbon isotope. On the contrary, in the Northern Hemisphere $\delta^{13}\text{C}_{surf}^{sim}$ becomes isotopically more depleted, with lowest signatures in the high latitudes. This pattern can be explained by the fact that boreal emissions from pyrogenic and biogenic sources are isotopically more depleted than in the tropics. The relatively positive $\delta^{13}\text{C}$ in the Southern Hemisphere, where the comparable positive fossil

fuel sources are actually rare, is due to a net transport of more methane with positive $\delta^{13}\text{C}$ signature from North to South (Quay et al., 1999). Again, the gradient matches the observed gradient (see Figure 6.11, right panel). Still, $\delta^{13}\text{C}_{surf}^{sim}$ is underestimated in comparison to the observations. This bias has already been discussed in the previous section. The highest methane mixing ratios appear in Eastern China, where $\delta^{13}\text{C}_{surf}^{sim}$ is isotopically most enriched (see Figure 6.10). Chinese coal has a very high $\delta^{13}\text{C}$ signature (Miller et al., 2019) and methane emissions are probably dominated by coal mining in this area. Additionally, high methane mixing ratios can be observed in South East Asia, specifically in South East China and Bangladesh (see Figure 6.10). In this region, large emissions arise from rice cultivation (mainly in China, Vietnam, Bangladesh and India, Carlson et al., 2016) and from wetlands (e.g. in Bangladesh, India, Indonesia and China, Kirschke et al., 2013). The corresponding $\delta^{13}\text{C}_{surf}^{sim}$ is isotopically depleted, which is in good agreement with the generally lighter $\delta^{13}\text{C}$ of biogenic wetland and agricultural emissions. Similarly, enhanced surface mixing ratios and isotopically depleted $\delta^{13}\text{C}_{surf}^{sim}$ can be observed in the Amazonas region and in boreal regions, such as Canada and Siberia, where wetland emissions prevail (Kirschke et al., 2013). Furthermore, other locally enhanced mixing ratios and the corresponding $\delta^{13}\text{C}_{surf}^{sim}$ agree well with the associated methane source in the respective region. For example, high fossil fuel emissions in Alaska, Poland or the Persian/Arabian Gulf show $\delta^{13}\text{C}_{surf}^{sim}$ which is isotopically enriched. Overall, the regional refinement of the isotopic source signatures and the applied emission inventories of SDISO-base-c result in a realistic global distribution of $\delta^{13}\text{C}$. The simulated zonal mean methane mixing ratio and zonal mean $\delta^{13}\text{C}$ in Figure 6.12 again show that the North-South gradients at surface level are well represented in SDISO-base-c. The gradient becomes smaller with increasing altitude. Surface values depend on the distribution of the sources nearby. However with increasing altitude, mixing ratios and $\delta^{13}\text{C}$ are influenced by the abundance of the sink reactants. $\delta^{13}\text{C}$ is isotopically enriched due to the fractionation with OH in the troposphere and with Cl and O¹D in the stratosphere.

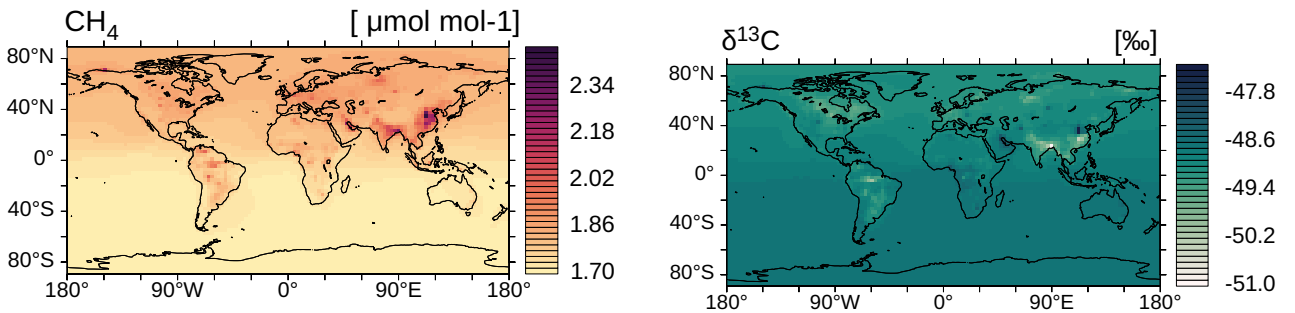


Figure 6.10: Global distribution of surface methane mixing ratio in [$\mu\text{mol mol}^{-1}$] (left panel) and surface $\delta^{13}\text{C}$ in [‰] (right panel) of SDISO-base-c. Shown in each case is the average for the period 2000-2015.

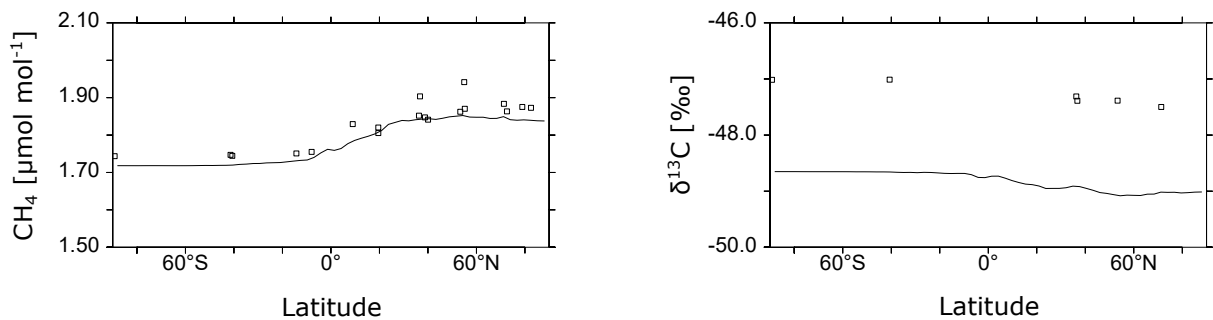


Figure 6.11: Zonal surface methane mixing ratio in $[\mu\text{mol mol}^{-1}]$ (left panel) and zonal surface $\delta^{13}\text{C}$ in $[\text{‰}]$ (right panel) of SDISO-base-c. In each case the average is shown for the period 2000-2015. The squares mark the respective observed mean methane mixing ratios and $\delta^{13}\text{C}$ at individual NOAA measurement stations for the same period. Only those stations where data for the whole time period was available are considered here.

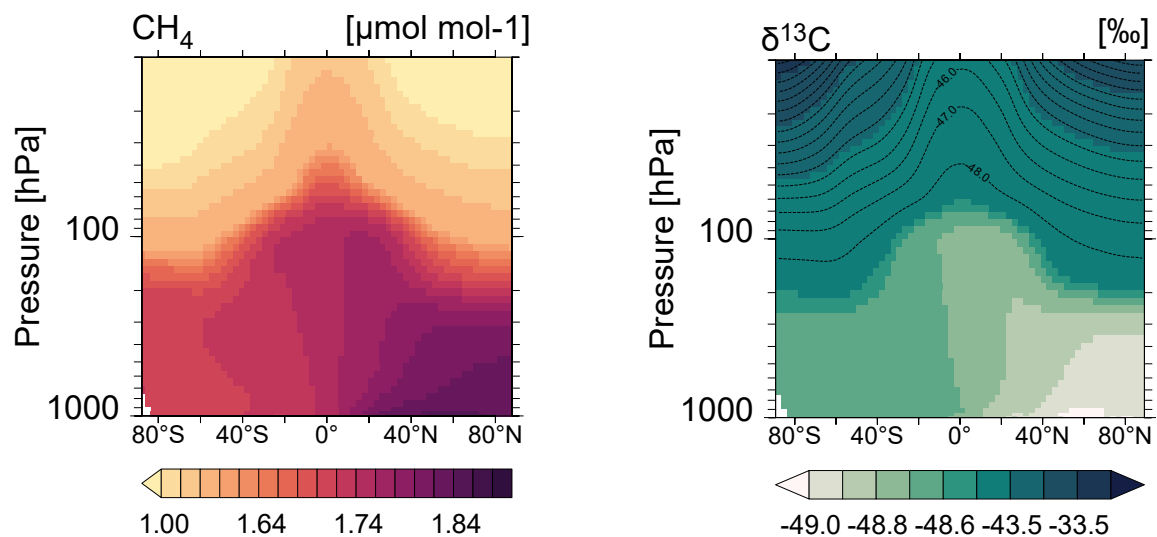


Figure 6.12: Zonal mean methane mixing ratio in $[\mu\text{mol mol}^{-1}]$ of SDISO-base (left panel) and zonal mean $\delta^{13}\text{C}$ in $[\text{‰}]$ of SDISO-base-c (right panel). Shown in each case is the average for the period 2000-2015.

Figure 6.13 (left panel) compares the simulated monthly-averaged global-mean surface CH_4 mixing ratios of the SDISO-base-c simulation to observations for the period between 1990 and 2019. Observations are monthly-averaged means from marine surface stations taken from Dlugokencky et al. (2020). Note that the simulated global-mean considers all surface grid boxes and not only the marine surface grid boxes. I justified this direct comparison between both data by the fact that the simulated mean using only marine surface grid boxes does not differ significantly from the total global-mean (see Appendix A.3.2).

The seasonal cycle of the SDISO-base-c simulation matches the observed seasonal cycle and shows that the seasonal cycle of atmospheric CH_4 mixing ratio is simulated correctly. The overall trends of the model results and observations agree well. The observed plateau between 2000 and 2007 is represented by the model, however with a slightly decreasing trend. As discussed earlier in this chapter, uncertainties in the OH concentration remain. The SDISO-base-c simulation uses a climatological mean of the OH field. Therefore a year-to-year variability is not presented. However, potential changes of the OH field between 2000 and 2007 could affect the methane mixing ratios. In order to cause a decrease in the atmospheric mixing ratio, the oxidation by OH must have increased, which would result in isotopically enriched methane. The monthly-averaged global-mean $\delta^{13}\text{C}_{surf}^{sim}$ (see Figure 6.13, right panel) contradicts this assumption, as $\delta^{13}\text{C}_{surf}^{sim}$ shows a slight decrease from 1998 to 2002. Wetland emissions for this period could also be underestimated. For the period 2000 to 2009, emission fluxes of 146 Tg(CH_4)/yr in the SDISO-base-c simulation agree well with the bottom up estimates by Saunio et al. (2020, see Table 6.1). In contrast, top down estimates in Saunio et al. (2020) and emission fluxes suggested by Poulter et al. (2017) between 2000 to 2012, exceed those used in SDISO-base-c (180 Tg(CH_4)/yr and 184 Tg(CH_4)/yr, respectively). However, increasing wetland emissions would lead to an overall more negative global $\delta^{13}\text{C}$. Figure 6.14 shows that the anthropogenic emissions of the applied EDGAR v5.0 inventory between 1998 and 2002 lie below those of the EMPA inventory (Frank, 2018). An underestimation of the anthropogenic, isotopically enriched fossil fuel emissions could be a possible explanation for the comparably low global-mean surface CH_4 mixing ratios. Still, this does not fully explain the decrease between 2000 and 2007. Moreover the monthly-averaged global-mean $\delta^{13}\text{C}_{surf}^{sim}$ shows a sudden increase after 2002, which corresponds to a sharp increase in coal emission and a peak in biomass burning at that time (see Figure 6.15). However, the overall observed increasing trend in methane mixing ratio is well represented by the model. This is also true for the monthly-averaged global-mean $\delta^{13}\text{C}_{surf}^{sim}$. Values increase until 2007 and indicate a larger proportion of isotopically enriched sources. In 1998 $\delta^{13}\text{C}_{surf}^{sim}$ shows a sudden rise, which is consistent with the observations. Indonesian wildfires as a response to the El Niño event have led to a large contribution of isotopically more positive biomass burning emissions in 1998 (Randerson et al., 2005). The observed decline after 2007 is well represented by the model, although $\delta^{13}\text{C}_{surf}^{sim}$ already stabilizes after 2012 and slightly increases 2015. This is due to the repetition (last year of the emission inventory) of natural emissions after 2012, followed by the repetition of anthropogenic emissions after 2015. After 2015, changes in CH_4 mixing ratios and $\delta^{13}\text{C}_{surf}^{sim}$ occur only due to changing biomass burning emissions.

The Taylor diagram in Figure 6.16 summarises the comparison of the model result and the individual observations at different sampling sites (see Figure 6.7) for the simulation period between 1990 and 2019/01. Section A.3.2 in the Appendix additionally shows a detailed illustration of the time series comparison at some selected sampling sites. Many observations are not available for the entire simulation period. In this case, the existing time series are compared to the corresponding period of the model results. Especially $\delta^{13}\text{C}$ data is sparse and only available after 1997. The simulated CH_4 mixing ratios (left

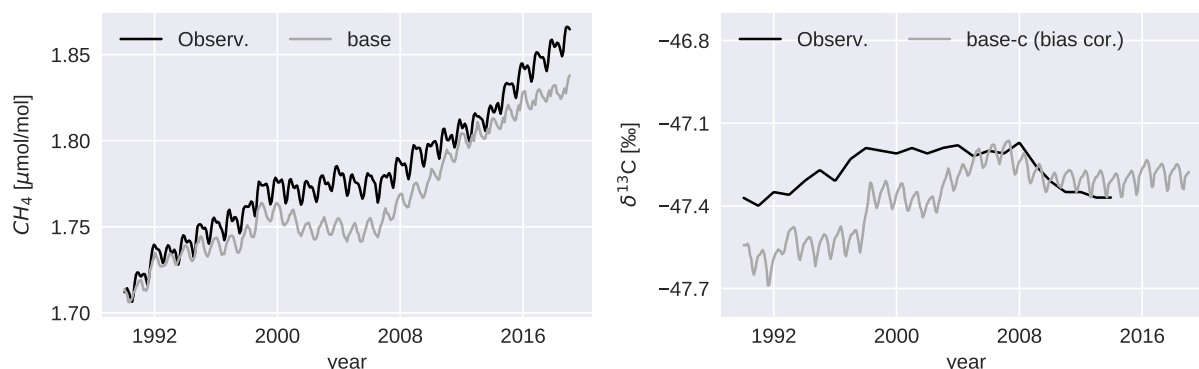


Figure 6.13: Global mean surface CH_4 mixing ratio in $[\text{nmol mol}^{-1}]$ of SDISO-base (light grey) and NOAA observations (black) from 1990 to 2019 (left panel). Globally averaged surface $\delta^{13}\text{C}$ in $[\text{‰}]$ of SDISO-base-c and observations (right panel). The observed global signatures are taken from Schaefer et al. (2016). A constant bias of 1.51 ‰ is added to SDISO-base-c $\delta^{13}\text{C}$.

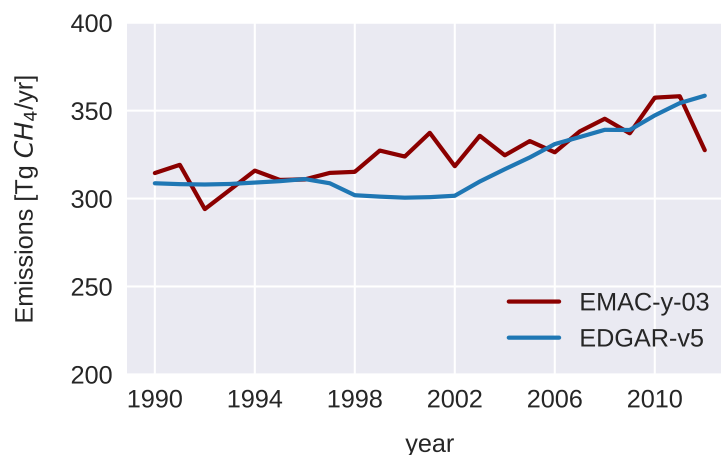


Figure 6.14: Comparison of anthropogenic emissions (including rice and ship emissions) of the EDGAR v5.0 inventory (blue) and the EMPA a-posteriori inventory (red).

panel) correlate well with the measurements. At nearly 75 % of the 67 sampling sites the correlation coefficient lies above 0.7, whereby for a large part it is even over 0.9. The normalized standard deviation is close to the reference line, indicating that the SDISO-base-c results display a similar variability as observed. This is especially true for sites in the Southern Hemisphere. However, in the Northern Hemisphere a few simulated CH_4 mixing ratios deviate strongly from the observations. At four sites the comparison shows a negative correlation coefficient and the corresponding data points lie outside the Taylor diagram. At some of these sampling sites observational data only cover a short time period (i.e. CMO, AMY), which makes interpretation difficult. A negative correlation is also found at Barrow in Alaska (BRW), where the SDISO setup assumes large emissions from fossil fuel extraction at the Northern Slope. Observational data exist here throughout the whole time span.

6. Simulation of the recent methane increase and the corresponding $\delta^{13}\text{C}(\text{CH}_4)$ decrease with EMAC

92

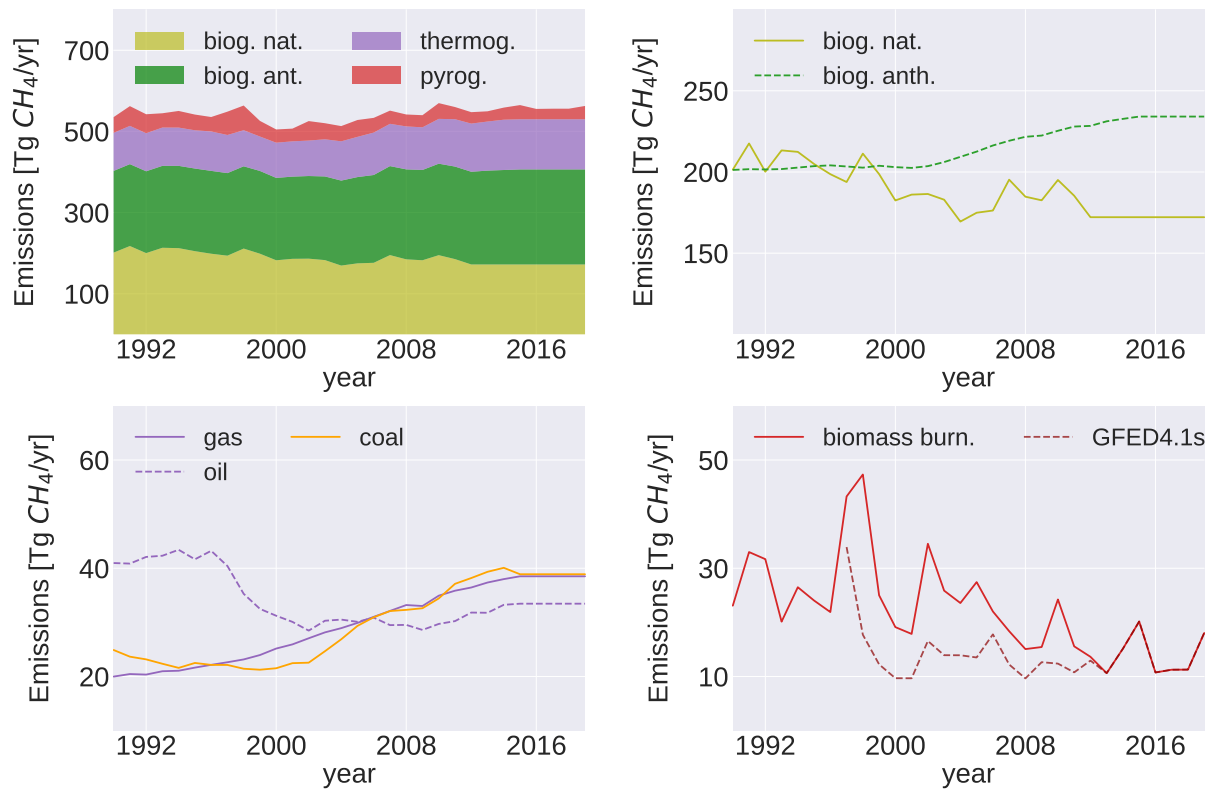


Figure 6.15: Total CH_4 emissions in [$\text{Tg CH}_4 / \text{yr}$] used in the SDISO setup between 1990 and 2019/01. The upper left panel shows all biogenic, thermogenic and pyrogenic emission fluxes. The upper right panel displays all biogenic emissions fluxes from natural and anthropogenic sources: natural emissions include wetlands and all minor sources, anthropogenic emissions include agricultural sources and landfills. The lower left panel displays the anthropogenic fossil fuel emission fluxes from coal, gas and oil extraction. The lower right panel shows the emission fluxes of biomass burning used in the SDISO setup and the emission fluxes of the GFED4.1s inventory (1997-2019).

Barrow is close to one of the largest drilling fields of Northern America, namely Prudhoe Bay Oil Field, which influences methane ratios during winter. Additionally Barrow is surrounded by wetlands associated with permafrost emissions during the summer time (Lawrence and Mao, 2019). The interplay of both sources may not be represented properly in the simulation. Furthermore, wetland emissions in the EMPA inventory, which are used in the SDISO setup, only exist until 2012. The surface $\delta^{13}\text{C}(\text{CH}_4)$ of the SDISO-base-c simulations are additionally isotopically enriched relative to the observations (see Appendix A.3.2). This indicates an underestimation of the isotopically lighter wetland emissions. Figure 6.16 (right panel) summarises the results for the comparison of the $\delta^{13}\text{C}(\text{CH}_4)$ time series. Contrary to the CH_4 mixing ratios, the SDISO-base-c simulation results agree best with the observations at sampling sites in Northern high latitudes. Overall, the correlation coefficients are smaller than those for the comparison of the CH_4 mixing ratios.

At many sampling sites observations show a larger decrease after 2007 than the SDISO-base-c simulation, which could be the reason for the low correlation. However, in many cases the seasonal cycle is well represented (see again Appendix A.3.2). Seasonality in the Northern Hemisphere is in general more pronounced than in the Southern Hemisphere. Despite the overall too small amplitudes (lower standard deviation), this is also seen in the model results.

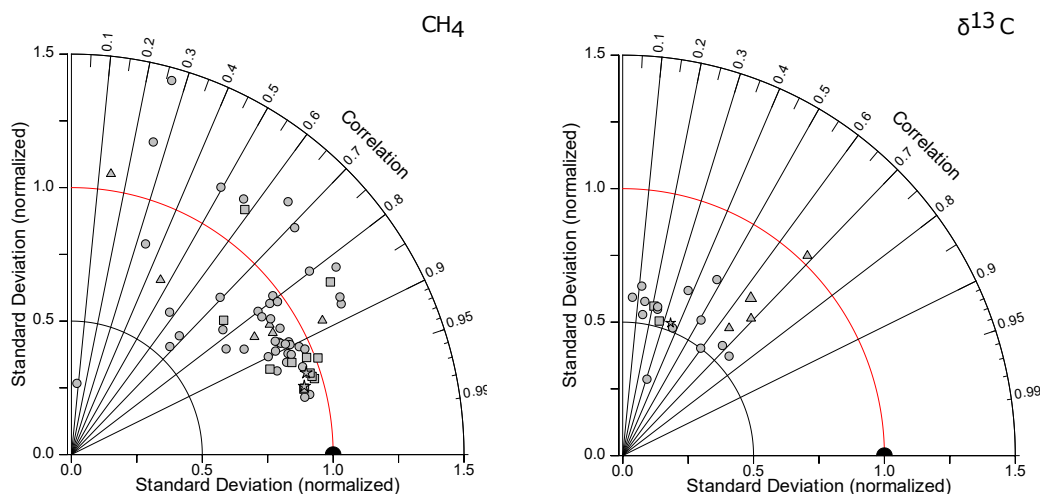


Figure 6.16: The Taylor diagram illustrates the statistical comparison between the surface CH_4 mixing ratios (left panel) and $\delta^{13}\text{C}(\text{CH}_4)$ (right panel) of the SDISO-base-c simulation and those of the observations at single sampling sites between 1990 and 2019. The diagram summarises the correlation coefficient (angle) and the normalized standard deviation (radius). The standard deviation is normalized, which makes it non-dimensional and allows for comparison of different sampling sites. The red line indicates a normalized standard deviation of 1. The black half circle on the horizontal axis marks the point where model results perfectly match the observations. The different symbols describe the climate zones where the sampling sites are located, i.e. Northern high latitudes (triangle), northern mid latitudes and tropics (circle), southern mid latitudes and tropics (square) and southern high latitudes (star). Note that for many sampling sites the observational data is not available throughout the whole time period.

Discussion of the post-stabilization period 2008 to 2014

This first part of the present study (Section 6.1.2) aims to find a suitable base simulation for the sensitivity studies. Furthermore, a key question is whether the base simulation, which uses state-of-the-art emission inventories and $\delta^{13}\text{C}$ source signatures, is already able to simulate the observed changes in the $\delta^{13}\text{C}(\text{CH}_4)$. As described above, the SDISO-base-c

simulation represents well the observed global increase in CH_4 mixing ratio after 2007. In order to define the contribution of the individual sources to the new increase, I compare the two periods 2000-2007 (stabilization period) and 2008-2014 (increase period) to each other. The two periods are chosen in order to compare the results with other studies analysing the same time periods (e.g. Hausmann et al. (2016); Worden et al. (2017); Howarth (2019)). Figure 6.17 shows the zonal-mean CH_4 mixing ratio averaged over both periods (left and middle panel, respectively) and the difference between both (right panel). The increase after 2007 is observed throughout the troposphere and is largest in the Northern Hemispheric mid and high latitudes. This indicates that tropical wetland emissions, predominantly located in the Southern Hemisphere, do not significantly contribute to the renewed methane increase in the SDISO-base-c setup. Other than in the troposphere, stratospheric methane decreased in the later period. This decrease is not conspicuous, but the corresponding zonal-mean $\delta^{13}\text{C}$ shows a more significant change (see Figure 6.18). $\delta^{13}\text{C}$ increased in the Northern Hemispheric lower stratosphere, which could indicate enhanced isotopic fractionation due to increasing sink reaction partners or sink reaction rates. However, sink reaction fields are prescribed in the SDISO setup using a climatological mean for the entire simulation time period and feedbacks on the sinks are not considered. Yet, the SDISO setup applies a water vapour feedback with respect to methane oxidation, which could cause a change in stratospheric water vapour. Winterstein et al. (2019) showed that strongly increased methane emissions lead to an increase in stratospheric water vapour and tropical upwelling accompanied by a stratospheric cooling and a change in dynamics. A change in dynamics might have led to a descending of less methane carrying air masses from the upper stratosphere. This methane is isotopically more enriched than the methane in the lower stratosphere (see upper two panels of Figure 6.18).

In contrast, little changes are observed for the tropospheric zonal-mean $\delta^{13}\text{C}$. In the tropics and in the Southern Hemisphere, $\delta^{13}\text{C}$ decreased by only 0.05 ‰. The other way round, in the Northern Hemispheric mid and high latitudes $\delta^{13}\text{C}$ increased by 0.05 ‰. As described in detail in the previous section, uncertainties remain with regard to the individual emission flux strengths between 2000 and 2007. The globally averaged $\delta^{13}\text{C}_{surf}^{sim}$ shows a slightly decreasing trend after 1998 and a sudden increase in 2002. The decrease after 2007 is comparatively small, which makes it difficult to analyse the relative changes between both time periods. However, the additional methane emission fluxes in the SDISO-base-c simulation after the stabilization period are comparable to other studies. The new increase consists of 19.7 Tg(CH_4)/yr fossil fuel emissions and 16.9 Tg(CH_4)/yr biogenic emissions (see Table 6.4), whereby the biogenic increase is mainly caused by anthropogenic agriculture and waste management. Jackson et al. (2020) also found that the major increase likely arises from anthropogenic biogenic emissions and fossil fuel emissions, equally. They further assume large fossil fuel emissions from China and from the United States, the former being consistent with the EDGAR v5.0 inventory used in the SDISO-base-c setup. Hausmann et al. (2016) assumes even larger fossil fuel emissions of 39 % of the total increase for the period 2007-2014. Worden et al. (2017) suggest a similar distribution with an increase in fossil fuel emissions by 16.4 (± 3.6) and only 12.0 (± 2.5) Tg(CH_4)/yr in biogenic emissions. On the contrary, biomass burning emission fluxes in the SDISO-base-c

simulation decreased by 7.9 Tg(CH₄)/yr, which is almost twice the amount as suggested by Worden et al. (2017) or by Thompson et al. (2018). Other studies such as Schwietzke et al. (2016) assume that fossil fuel emissions did not increase, although their contribution to the global methane budget is likely underestimated. Schaefer et al. (2016) found that predominantly emissions from agriculture lead to the observed increase. To the contrary, Thompson et al. (2018) suggest an increase of biogenic wetland and agricultural emissions by 24-48 Tg(CH₄)/yr between 2007 and 2014. Wetland emissions in the SDISO-base-c simulation are mostly constant for this period. This is consistent with the findings of Poulter et al. (2017), who report unchanged wetland emissions between 2000 and 2012. However, wetlands remain a source of uncertainties in the global methane budget and top down and bottom up estimates differ strongly from each other (Saunio et al., 2020; Jackson et al., 2020).

Summary and Conclusion

I performed two different base simulations (SDISO-base-c and SDISO-base-v) using state-of-the-art emission inventories and applying a regional refinement of the isotopic source signatures. The refinement of the isotopic signatures leads to a well represented global distribution of $\delta^{13}\text{C}_{surf}^{sim}$. This is shown by the fact that the vertical and meridional gradient of methane and $\delta^{13}\text{C}$ are simulated properly. Moreover, the regional $\delta^{13}\text{C}_{surf}^{sim}$ correspond to the sources associated with the respective location. The results also show that the simulations represent the observed plateau and the renewed increase of CH₄ after 2007. Furthermore, both simulations are able to simulate the general course of the observed global-mean surface $\delta^{13}\text{C}(\text{CH}_4)$, however, both with a constant offset towards the observations. The offset is partly explained by a likely too small KIE applied for OH oxidation in the troposphere. As the flux-weighted emitted mean $\delta^{13}\text{C}$ of the SDISO-base-c simulation agrees better with other literature values, I decided to concentrate on this simulation for further analysis. The comparison of the SDISO-base-c simulation to ground-based observations at different sampling sites reveals promising results regarding the surface CH₄ mixing ratios. In contrast, less correlation and an overall too small variability is observed for $\delta^{13}\text{C}_{surf}^{sim}$. However, continuous measurements of $\delta^{13}\text{C}$ are still sparse and additional data would be helpful to better evaluate the model results. As discussed in detail, the post-stabilization decrease of the global-mean $\delta^{13}\text{C}$ can be simulated by the SDISO-base-c simulation, although the decline is not as pronounced as in the observations and uncertainties also remain for the time period from 2000 to 2007. Nevertheless, the contribution of the individual sources to the renewed increase is similar to what is suggested in other studies. Only the decrease in biomass burning seems to be too large, especially when compared to emission fluxes presented in the GFED 4.1s inventory (see Figure 6.15, lower right panel). A detailed discussion concerning the biomass burning emissions is given in the following sections. Besides these uncertainties, the SDISO-base-c simulation gives realistic results and individual emissions can be further adjusted to test the influence of isotopically depleted shale gas emissions.

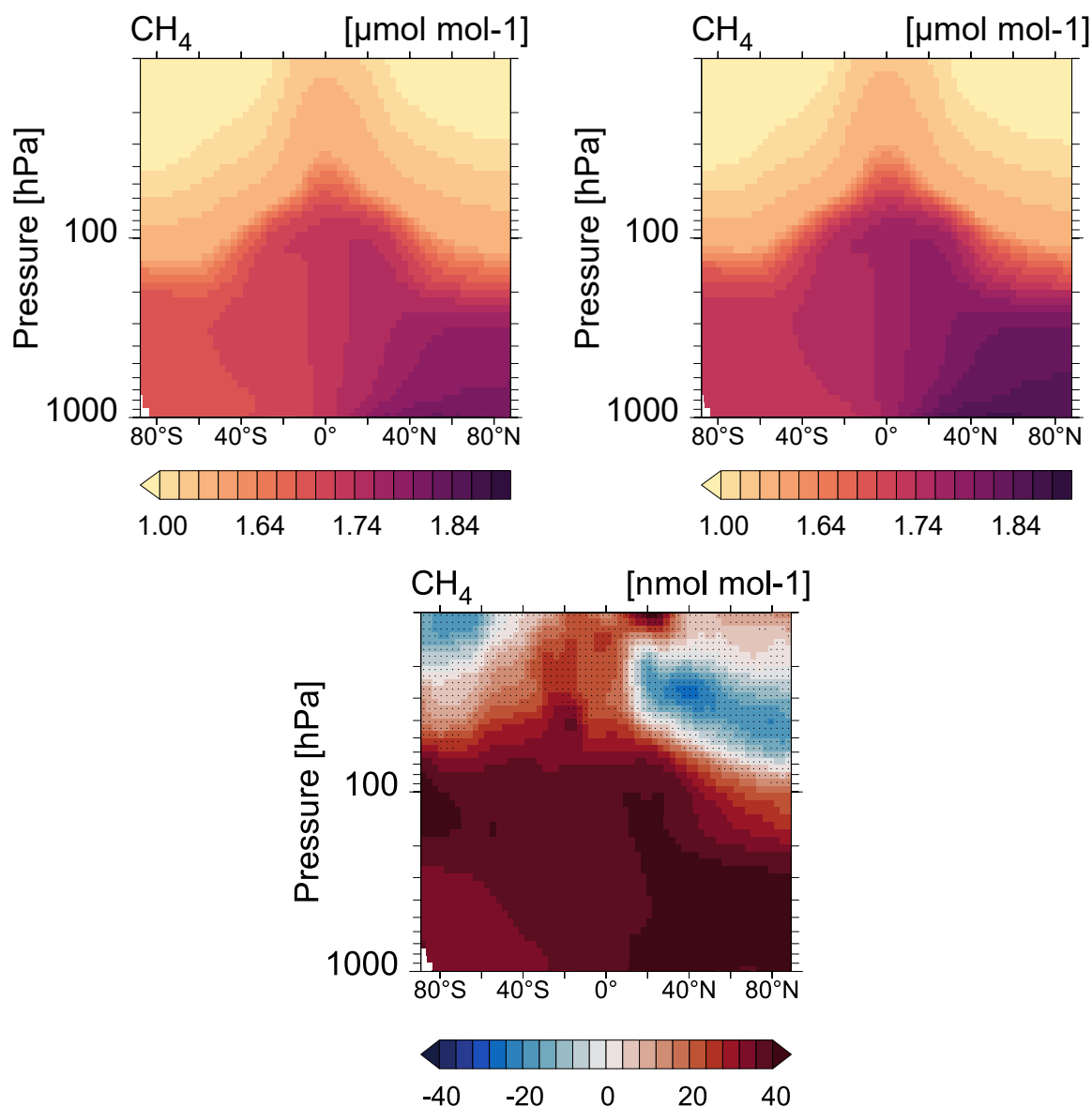


Figure 6.17: SDISO-base zonal mean CH_4 for the periods 2000-2007 (upper left panel) and 2008-2014 (upper right panel), as well as the difference: period 2008-2014 minus period 2000-2007 (lower panel). Non-dotted areas lie within a 95 % significance level according to the Student's t-test.

6.2 Sensitivities towards shale gas emissions

The study of Howarth (2019) is based on a methane increase of 28.4 CH_4 Tg/yr between 2008 until 2014 compared to the period 2000 to 2007. His base analysis assumes that emissions from shale gas production account for 33 % for the methane increase during the period 2008-2014. 30 % are derived from conventional gas and oil production or coal mining

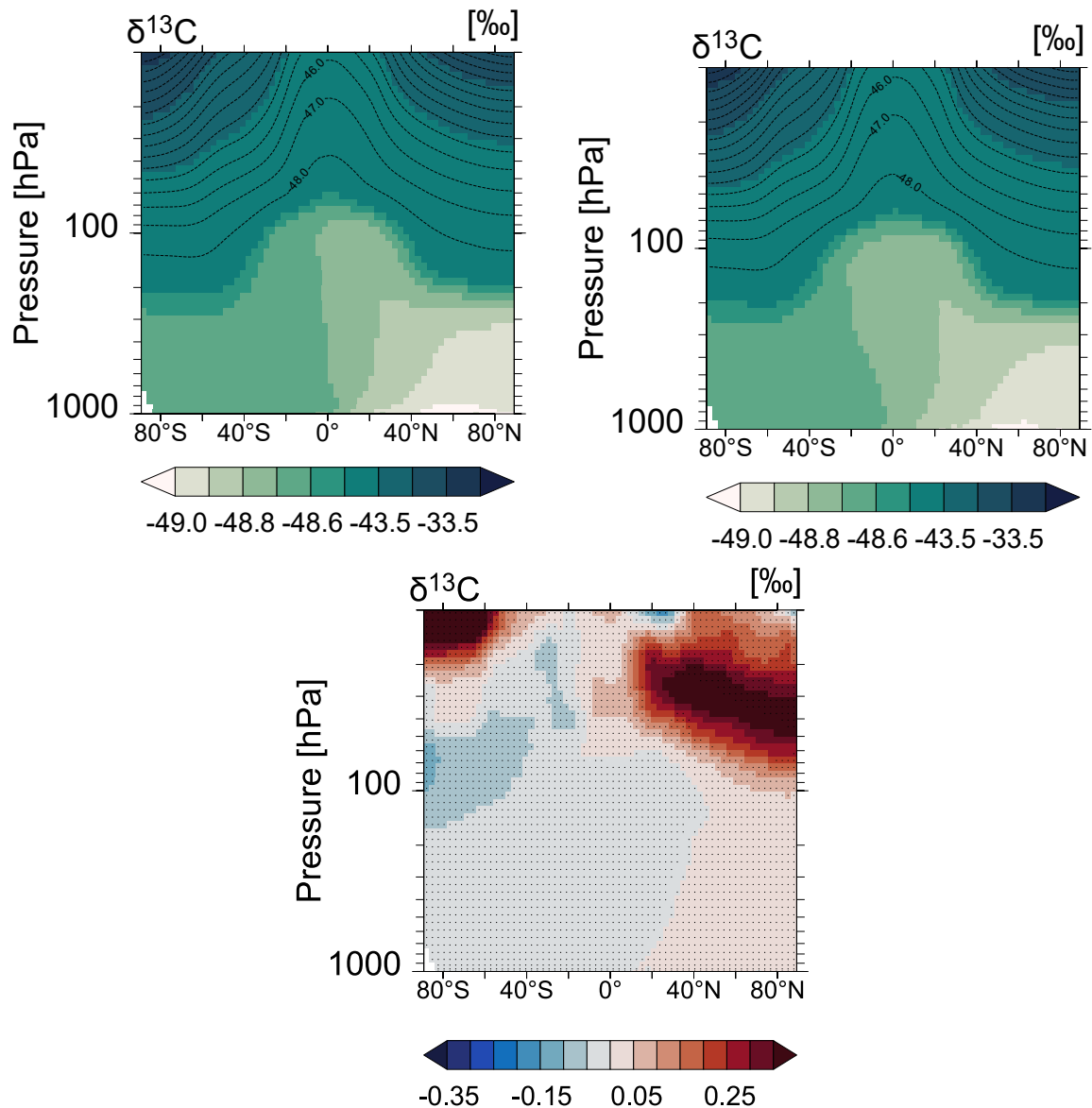


Figure 6.18: SDISO-base-c zonal mean $\delta^{13}\text{C}$ for the periods 2000-2007 (upper left panel) and 2008-2014 (upper right panel), as well as the difference: period 2008-2014 minus period 2000-2007 (lower panel). Non-dotted areas lie within a 95 % significance level according to the Student's t-test.

activities and another 37 % are due to biogenic emissions. Howarth (2019) also assumes a 3.7 Tg/yr decrease in biomass burning emissions, based on the findings by Worden et al. (2017). The idea of this study here is to test the hypothesis described by Howarth (2019) with the SDISO setup and to test under which assumptions the hypothesis can be supported or falsified. For this purpose, a new shale gas emission sector was introduced in 2008. Emission fluxes (F_{Shale}) increase linearly until 2015. Shale gas emission flux

6. Simulation of the recent methane increase and the corresponding $\delta^{13}\text{C}(\text{CH}_4)$ decrease with EMAC

98

files are created by flagging the yearly averaged 2007 emissions of the EDGAR v5.0 gas sector with a template of the US shale gas regions (see Figure 6.19; Source: US Energy Information Administration (Feb 2021)). Emissions are then scaled accordingly. Fossil fuel emission fluxes, excluding shale gas (F_{FF}) and biogenic emission fluxes (F_{Bio}), are consequently downscaled to maintain the total net increase during 2000-2015. I conducted three sensitivity simulations based on the SDISO-base-c simulation. These simulations are described and analysed in Section 6.2.1. Since biomass burning appeared to have a large influence on the global $\delta^{13}\text{C}$ in the previous sensitivity simulations, I additionally replaced the initial F_{BB} by the latest GFED 4.1s inventory. Another three simulations with the adjusted setup are performed and discussed in subsection 6.2.1. All results are further compared to observations at different sampling sites. Since the tropospheric lifetime of methane depends on the distribution of OH, $\delta^{13}\text{C}$ emitted in regions with less OH (e.g. in high latitudes) remains comparatively long in the atmosphere and may have a greater influence on the overall global-mean $\delta^{13}\text{C}$. On the contrary, $\delta^{13}\text{C}$ emitted in the mid latitudes in the Northern Hemisphere, like shale gas, has a relatively short lifetime. I test the effect of potential different lifetimes of the new shale gas emissions in Section 6.2.2.

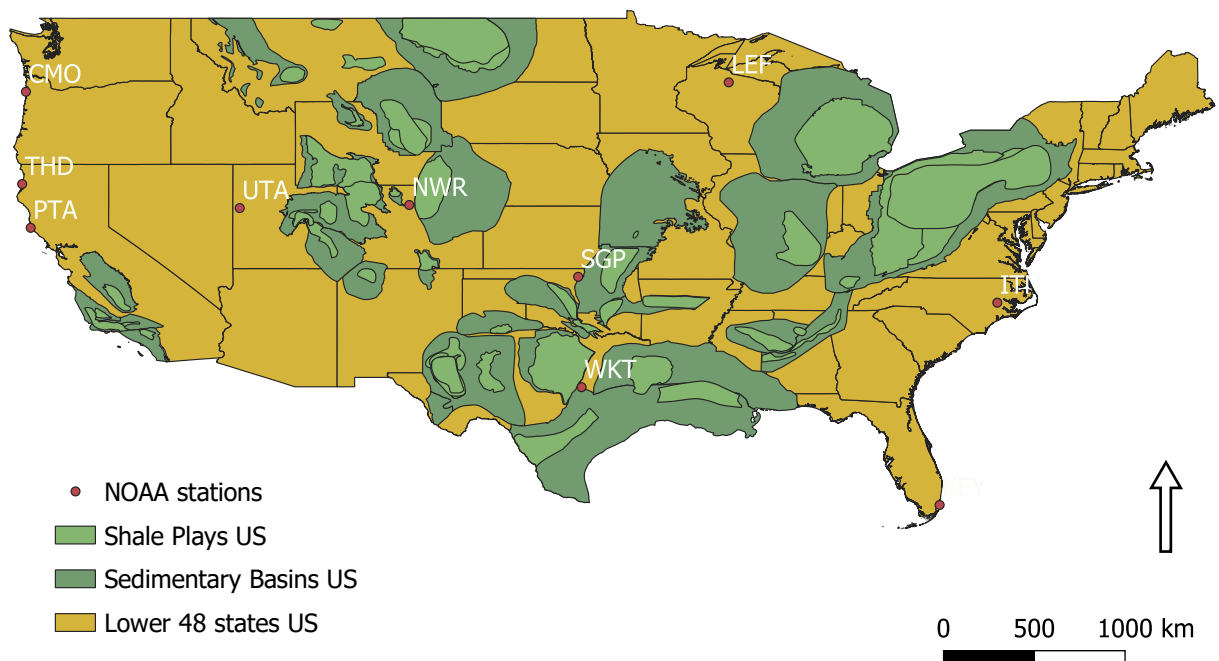


Figure 6.19: Map showing US low permeability oil and gas plays and sedimentary basins. Data derived from www.eia.gov, last access January 2020.

6.2.1 SDISO sensitivity simulations

Table 6.4 summarizes all SDISO-base-c emission fluxes for the two periods 2000-2007 and 2008-2014. It additionally lists the adjusted emissions from 2008-2014 for the first three sensitivity studies. Methane sources from transport, industry, biofuel, agricultural waste burning and volcanos are not listed here as they are not subject to modification in the sensitivity simulations. However, they are not excluded in the model and still contribute to the increase between 2008 and 2014. In the SDISO-sens1 and SDISO-sens2 simulations, F_{Bio} , F_{FF} and F_{Shale} are scaled to correspond to the assumption of Howarth (2019), i.e. F_{Bio} accounts for 37 %, F_{FF} for 30 % and F_{Shale} makes up the remaining 33 %. Individual fluxes within the three source categories are adjusted according to their initial fraction of the total source category increase. I added a constant flux of 4.2 Tg/yr to F_{BB} to consider the difference between the assumption of Howarth (2019) and of the SDISO-base-c setup. This flux is additionally subtracted in equal parts from F_{Bio} , F_{FF} and F_{Shale} . The simulations SDISO-sens1 and SDISO-sens2 differ with respect to their $\delta^{13}\text{C}_{\text{Shale}}$ signatures. For the SDISO-sens1 simulation, a $\delta^{13}\text{C}_{\text{Shale}}$ value of -44 ‰ (mean value for oil and gas) from Schwietzke et al. (2016) is applied. As indicated earlier in this chapter, isotopic signatures of shale gas emissions are not yet known without uncertainty. The purpose of SDISO-sens1 is to test the influence of increasing shale gas emissions independent from a depleted shale gas signature relative to the -44 ‰ mean. In the SDISO-sens2 simulation the specific value of -46.9 ‰ suggested by Howarth (2019) is applied. The SDISO-sens3 simulation equals the SDISO-sens2 simulation without the F_{BB} decrease reduction.

Results and discussion of SDISO-base sensitivity studies

Figure 6.20 displays the monthly-averaged global mean $\delta^{13}\text{C}_{\text{surf}}^{\text{sim}}$ of the sensitivity simulations compared to those of the SDISO-base-c simulation, which serves here as a reference for the $\delta^{13}\text{C}$ decline. The simulations SDISO-sens1 and SDISO-sens2, which include an F_{BB} decrease of 3.7 Tg(CH₄)/yr, branch from the base simulation and increase after 2009. In the SDISO-sens1 simulation $\delta^{13}\text{C}_{\text{surf}}^{\text{sim}}$ rises even more after 2012. The two simulations only differ in their applied $\delta^{13}\text{C}_{\text{Shale}}$ value with -44 ‰ and -46.9 ‰, respectively. The results show that an isotopically more depleted $\delta^{13}\text{C}$ source signature for shale gas indeed impacts the overall global-mean $\delta^{13}\text{C}$, although only after four years since the beginning of the sensitivity simulations, which raises the question of an earlier initiation of shale gas emissions. Shale gas production in the United States already started in the early nineties. However, the considerable share of shale gases production arises after 2007, and the resulting $\delta^{13}\text{C}_{\text{surf}}^{\text{sim}}$ of the SDISO-sens2 simulation does not decline after 2012, either. On the contrary, the SDISO-sens3 simulation decreases already in 2008 and follows the course of the base simulation. Since all sensitivity simulations include 33 % of shale gas emissions as well as an equal fraction of F_{Bio} and an equal fraction of the F_{FF} , the difference is caused by the larger decrease of biomass burning emissions in the SDISO-sens3 simulation. This reveals that a 33 % share of shale gas (with a $\delta^{13}\text{C}_{\text{Shale}}$ of 46.9 ‰) of the additional emissions, can be reconciled with a decline in $\delta^{13}\text{C}$. However, shale gas is presumably not the

6. Simulation of the recent methane increase and the corresponding $\delta^{13}\text{C}(\text{CH}_4)$ decrease with EMAC

Table 6.4: Fluxes (in $\text{Tg}(\text{CH}_4)/\text{yr}$) of the base simulation and the individual sensitivity simulations for the years 2008-2014. Δ shows the net increase of the fluxes compared to the period 2000-2007. The calculation of the resulting fluxes of the sensitivity simulations excludes pyrogenic emissions by biofuel or agricultural waste burning, which are not listed.

Source Categories	2000-2007			2008-2014			
	Flux	base-c		sens1/2*		sens3*	
		Flux	Δ	Flux	Δ	Flux	Δ
Thermogenic (excl. shale)	94.6	114.4	+19.7	104.4	+9.8	105.6	+11.0
- Coal	26.3	36.3	+10.0	30.5	+ 4.2	31.3	+5
- Gas & Oil	58.6	66.1	+7.4	61.9	+3.3	62.3	+3.7
- Other (minor)	9.7	12.0	+ 2.3	12.0	+2.3	12.0	+2.3
- Shale Gas	/	/	/	10.7	+10.7	12.1	+12.1
Biogenic (total)	390.8	407.7	+16.9	403.0	+12.2	404.4	+13.6
- Livestock	106.0	114.1	+8.1	111.9	+5.9	112.6	+6.6
- Landfills & Wwt	69.3	76.0	+6.7	74.3	+5.0	74.8	+5.5
- Rice	33.8	37.0	+3.2	36.2	+2.4	36.4	+ 2.6
- Natural (total)	181.7	180.6	-1.1	180.6	-1.1	180.6	-1.1
Biomass burning	23.6	15.7	-7.9	19.9	-3.7	15.7	-7.9

(*sens1/2 with F_{Bio} : 37 %, F_{FF} : 30 %, F_{Shale} : 33 % with bb increase of 4.2 $\text{Tg}(\text{CH}_4)/\text{yr}$, sens3 with F_{Bio} : 37 %, F_{FF} : 30 %, F_{Shale} : 33 % without bb increase)

driving force of the observed decline. Instead, low biomass burning emissions after 2008 caused the decrease in the global mean $\delta^{13}\text{C}_{\text{surf}}^{\text{sim}}$ of the SDISO-base-c and SDISO-sens3 simulations. Biomass burning emissions are most enriched in $\delta^{13}\text{C}$ and small changes in their emission flux strengths lead to relatively large changes in the overall global mean $\delta^{13}\text{C}$. A key question here is whether this decrease in biomass burning is consistent with other findings. As shown in the previous Chapter 6.1.2, biomass burning emissions in the SDISO setup decrease by 7.9 $\text{Tg}(\text{CH}_4)/\text{yr}$ in the period 2008 to 2014 compared to the period 2000 to 2007. In contrast, the GFED4.1s emission inventory (Randerson et al., 2017) shows a decline of only 1.4 $\text{Tg}(\text{CH}_4)/\text{yr}$ for the same period. Emissions in the SDISO setup are derived from the EMAC-y-03 inventory, combined with the data from GFED4.1s after 2012. Although GFED4.1s emissions are in general lower, the resulting emissions (see Figure 6.15) do not show any significant step in the time series around 2012. Furthermore, the EMAC-y-03 inventory is optimized towards observations (Frank, 2018) and biomass burning emissions in the SDISO setup are within the uncertainties reported by Saunio et al. (2020, see Table 6.1). However, the changes in biomass burning are not yet clearly defined and as already mentioned, other studies such as Worden et al. (2017) suggest a decrease of only 3.7 $\text{Tg}(\text{CH}_4)/\text{yr}$ for this period. The biomass burning emissions of EMAC-y-03 show a peak around 2001 and 2002 (see Figure 6.15), which might lead to larger differences

between the two compared periods. Matching with this, Earl and Simmonds (2018) found a peak in active fire activity in 2001, which was then again not found in a study based on burned area analysis (i.e. from Giglio et al. (2013)). Regardless of these discrepancies, many studies found a global decline in burned area or active fires over the past decades (Giglio et al., 2013; van Lierop et al., 2015; Doerr and Santín, 2016; Andela et al., 2017; Earl and Simmonds, 2018). Giglio et al. (2013) analysed the period between 2000 and 2012 and found a net trend of -4.3 Mha/yr in the annual burned area. Based on satellite data, Andela et al. (2017) estimated a decline of 24.3 ± 8.8 % of the global burned area from 1998 until 2015. Earl and Simmonds (2018) showed that the global fire activity decreased strongly between 2001 and 2016, with stable activities around 2002 and 2007 and a decline in 2008 and 2009. These findings are consistent with the overall course of the global-mean $\delta^{13}\text{C}$ between 2000 and 2009. The decline was dominated by less active fires in Northern Africa and the Amazonas region (Earl and Simmonds, 2018). Andela et al. (2017) links the reduced fires to the expansion of agriculture. Additionally, less deforestation appeared in South America and tropical Asia (Earl and Simmonds, 2018). Given the fact, that the decrease in biomass burning emissions in both simulation setups (SDISO-base-c and SDISO-sens3) is large compared to other studies, it is reasonable to assume that biomass burning emissions alone cannot be the reason for the observed $\delta^{13}\text{C}$ decrease. In fact, the SDISO-base-c and SDISO-sens3 simulations likely underestimate the isotopically more depleted biogenic emissions after 2007. Therefore, in order to test the hypothesis of Howarth (2019) with the SDISO setup and to identify the role of shale gas emissions, I performed three additional sensitivity simulations based on the recent GFED v4.1s inventory. The results are discussed in the next section.

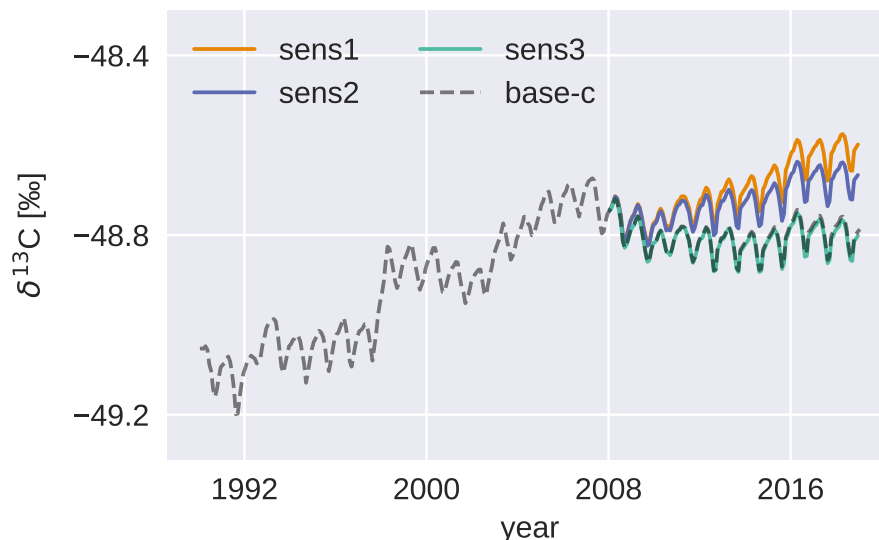


Figure 6.20: Global mean surface $\delta^{13}\text{C}$ of the SDISO-base-c and all three sensitivity simulations starting in 2008.

SDISO sensitivity simulation based on GFED4.1s

The previous section concluded that biomass burning emissions have a large influence on the global-mean $\delta^{13}\text{C}$ in the SDISO setup. Furthermore, a biomass burning decrease of such an extent is likely overestimated. In order to receive a best guess of the biomass burning emissions, I performed additional sensitivity simulations using the GFED v4.1s inventory already after 2007. Since SDISO-base-c uses the EMAC-y-03 a posteriori biomass burning emissions, which in general assumes a larger emission flux, GFED 4.1s emissions need to be scaled to match with the preceding EMAC-y-03 emissions in 2007. This changes the total decline in biomass burning to 4 Tg(CH₄)/yr from 2008-2014 compared to 2000-2007. Note that the GFED 4.1s inventory alone does not show such a decline (see previous section). The difference arises due to the combination with the EMAC-y-03 a posteriori inventory, which shows higher emissions between 2000 and 2007 than the GFED 4.1s inventory. Future studies could therefore include the recent biomass burning inventory already in the base simulations. Regardless, a decrease of 4 Tg(CH₄)/yr agrees with other studies (i.e. Worden et al. (2017)).

Table 6.5 lists the adjusted emissions for the sensitivity simulations from 2008 and 2014. F_{BB} is replaced by the latest GFED 4.1s emissions. The simulations start in 2008 and branch from SDISO-base-c. SDISO-gfed-c is equivalent to the SDISO-base-c simulation, where no shale gas emissions are applied. SDISO-gfed-01 is similar to SDISO-sens2 and includes 33 % shale gas emissions. SDISO-gfed-02 assumes ~46 % of the renewed rise between 2008 and 2014 to arise from biogenic sources and another ~54 % from fossil fuels. Shale gas emissions make up 50 % of the total fossil fuel emissions.

Results and discussion of SDISO-gfed sensitivity studies

Figure 6.21 shows the results of the new SDISO-gfed simulations compared to the SDISO-base-c simulation. Between 2008 and 2012, the monthly-averaged global mean $\delta^{13}\text{C}_{\text{surf}}^{\text{sim}}$ of all simulations decrease. After 2012 the SDISO-gfed simulations increase again relative to the base simulation. This also applies to the SDISO-gfed-c simulation, which does not include the new shale gas emissions. It equals the SDISO-gfed-01 simulation containing 33 % of shale gas emissions, although the results of the latter are slightly more negative. This apparently confirms the statement made with the previous sensitivity simulations; biomass burning emissions determine the course of the global mean $\delta^{13}\text{C}_{\text{surf}}^{\text{sim}}$ in the SDISO simulations. The new increase after 2012 can be attributed to greater fire activity against the overall decreasing trend. This is in agreement with the findings by Earl and Simmonds (2018), who found an active fire year in 2012, continuing until 2016.

Although shale gas emissions are not the main reason for a change in the global mean $\delta^{13}\text{C}$, an increase of shale gas can lead to a decrease in $\delta^{13}\text{C}$, if the isotopically more depleted biogenic emissions are not reduced instead. The SDISO-gfed-02 simulations clearly shows this effect. The resulting $\delta^{13}\text{C}_{\text{surf}}^{\text{sim}}$ is below that of the SDISO-gfed-c simulation. The additional emissions after 2007 in the SDISO-gfed-02 simulation consist of 46 % of biogenic emissions, which is the same in the SDISO-gfed-c simulation. Here, the remaining fossil

Table 6.5: Fluxes (in Tg(CH₄)/yr) of the gfed-c simulation and the individual sensitivity studies for the period 2008-2014. Δ shows the net increase of the fluxes compared to the period 2000-2007. The calculation of the resulting fluxes of the sensitivity simulations excludes pyrogenic emissions by biofuel or agricultural waste burning, which are not listed in the table.

Source Categories	2000-2007			2008-2014			
	Flux	gfed-c Flux	Δ	gfed-01* Flux	Δ	gfed-02* Flux	Δ
Thermogenic (excl. shale)	94.6	114.4	+19.7	105.6	+11.0	104.5	+9.9
- Coal	26.3	36.3	+10.0	31.3	+5	30.6	+4.3
- Gas & Oil	58.6	66.1	+7.4	62.3	+3.7	61.9	+3.3
- Other (minor)	9.7	12.0	+ 2.3	12.0	+2.3	12.0	+2.3
- Shale Gas	/	/	/	12.1	+12.1	9.9	+9.9
Biogenic (total)	390.8	407.7	+16.9	404.4	+13.6	407.7	+16.9
- Livestock	106.0	114.1	+8.1	112.6	+6.6	114.1	+8.1
- Landfills & Wwt	69.3	76.0	+6.7	74.8	+5.5	76.0	+6.7
- Rice	33.8	37.0	+3.2	36.4	+ 2.6	37.0	+3.2
- Natural (total)	181.7	180.6	-1.1	180.6	-1.1	180.6	-1.1
Biomass burning	23.6	19.6	-4.0	19.6	-4.0	19.6	-4.0

(* gfed -c / -01 / -02 with scaled GFED 4.1s bb emissions after 2007, gfed-01 with F_{Bio} : 37 %, F_{FF} : 30 % , F_{Shale} : 33 % , gfed-02 with F_{Bio} : 46 %, F_{FF} : 27 % , F_{Shale} : 27 %)

fuel emission fraction consists of more shale gas than conventional gas and oil. F_{Shale} is now 27 %, which is less than suggested by Howarth (2019), but still shows a clear impact on the global mean $\delta^{13}\text{C}$. However, similar to the previous SDISO-sens simulations, all monthly-averaged global mean $\delta^{13}\text{C}_{\text{surf}}^{\text{sim}}$ of the SDISO-gfed simulations increase relative to the base simulation. The observed changes in the global mean $\delta^{13}\text{C}$ cannot be simulated with the presented SDISO-gfed setups. These findings again imply a larger increase in biogenic emissions or changes in the atmospheric sinks, such as suggested by Rigby et al. (2017).

Comparison to individual sampling sites

So far I have focused on the resulting global mean $\delta^{13}\text{C}_{\text{surf}}^{\text{sim}}$ of the simulations and how they developed after 2008. Some of the simulations do not differ significantly on a global scale, but they might perform differently on a regional scale. The comparison to measurements at different sampling sites can help to assess the individual performances of the simulations, and further identify how well the simulations actually match with the observations. Here, I compare the monthly-averaged $\delta^{13}\text{C}_{\text{surf}}^{\text{sim}}$ of all SDISO simulations to observations at six different NOAA ground-base sampling sites (see Figure 6.22 and Figure 6.23, for

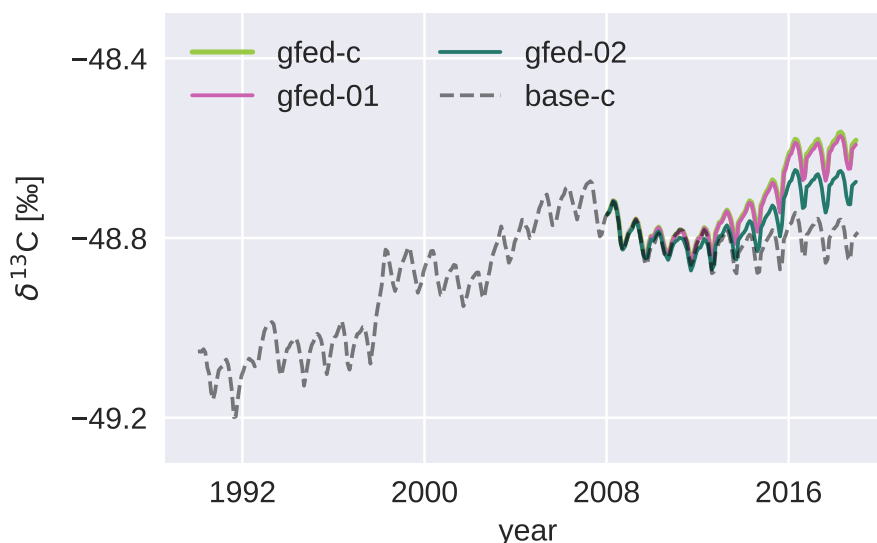


Figure 6.21: Global mean surface $\delta^{13}\text{C}$ of the SDISO-base-c and all three sensitivity simulations starting in 2008.

the SDISO-sens and SDISO-gfed simulation, respectively). Additional results at other sampling sites, as well as the corresponding Taylor diagrams summarizing the individual comparisons of surface CH_4 mixing ratios and surface $\delta^{13}\text{C}$, can be found in the Appendix A.3.3.

Figure 6.22 shows the results of the SDISO-sens simulations. Regarding the seasonal variability, the simulations best agree with the observations in the Northern high latitudes (ALT and BRW). This is also true for the SDISO-gfed simulations (see Figure 6.23, upper panels) and consistent with the finding in the previous Chapter (see Taylor diagram in Figure 6.16). At five sampling sites (excluding NWR) the differences between the resulting $\delta^{13}\text{C}_{surf}^{sim}$ of the simulations are comparable to the differences between the global mean values of the simulations (see previous section). The $\delta^{13}\text{C}_{surf}^{sim}$ of the sensitivity simulations SDISO-sens1 and SDISO-sens2 increase relative to the base simulation. Both include the shale gas emissions and a reduction of biomass burning emissions of only $3.7 \text{ Tg}(\text{CH}_4)/\text{yr}$ during the period 2008-2014 compared to the period 2000-2007. The $\delta^{13}\text{C}_{surf}^{sim}$ of the two simulations SDISO-sens3 and SDISO-base-c slightly decrease and are closest to the observations. Here, only SDISO-sens3 includes shale gas emissions, but in both simulations biomass burning emissions decrease by $7.9 \text{ Tg}(\text{CH}_4)/\text{yr}$. The $\delta^{13}\text{C}_{surf}^{sim}$ of the sensitivity simulations based on the GFED4.1s inventory increases after 2012. This is independent from the inclusion of shale gas emissions and can be attributed to the changed biomass burning emissions. It appears that, shale gas is not the major driver of the simulated changes in $\delta^{13}\text{C}$. The comparison to measurements at a regional scale therefore support the key findings, which were made based on the global mean $\delta^{13}\text{C}_{surf}^{sim}$. In each case, the observations show a stronger decline in $\delta^{13}\text{C}$ after 2008 than in the simulations. However, the general course

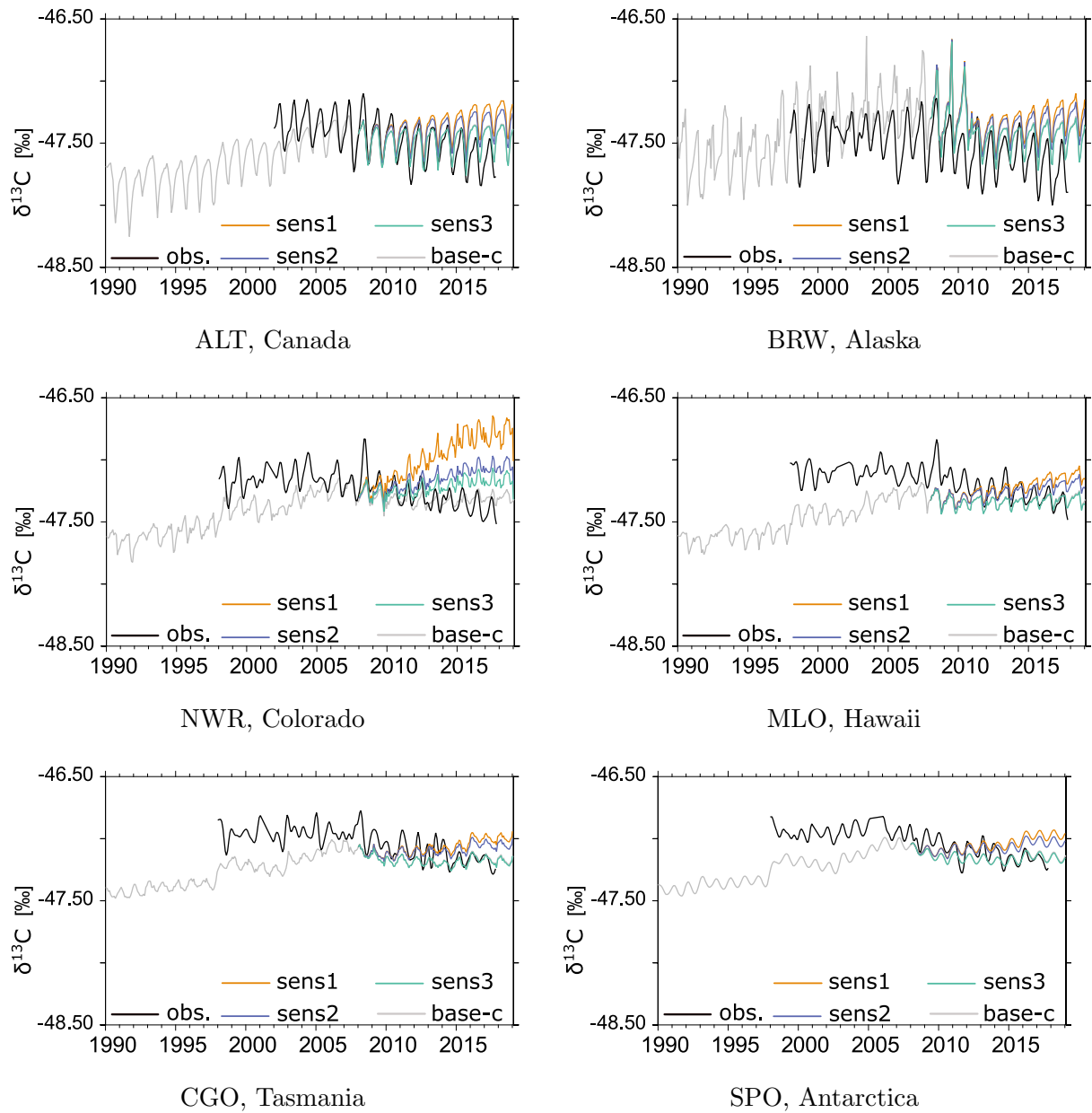


Figure 6.22: The monthly-averaged observed $\delta^{13}\text{C}$ at selected sampling sites are compared to the monthly-averaged $\delta^{13}\text{C}_{surf}^{sim}$ of the SDISO-base-c and all SDISO-sens simulations. The sampling sites depicted here cover the mid and high latitudes in both Hemispheres. Other sampling sites are also compared to the model results and can be found in the Appendix A.3.3. For a better comparison, the bias between observations and model results is reduced by adding a constant value of 1.51 ‰ to the latter.

of the observation can be simulated by the SDISO-base-c simulation and the SDISO-sens3 simulation. At the Niwot Ridge (NWR) in Colorado all sensitivity simulations deviate

6. Simulation of the recent methane increase and the corresponding $\delta^{13}\text{C}(\text{CH}_4)$ decrease with EMAC

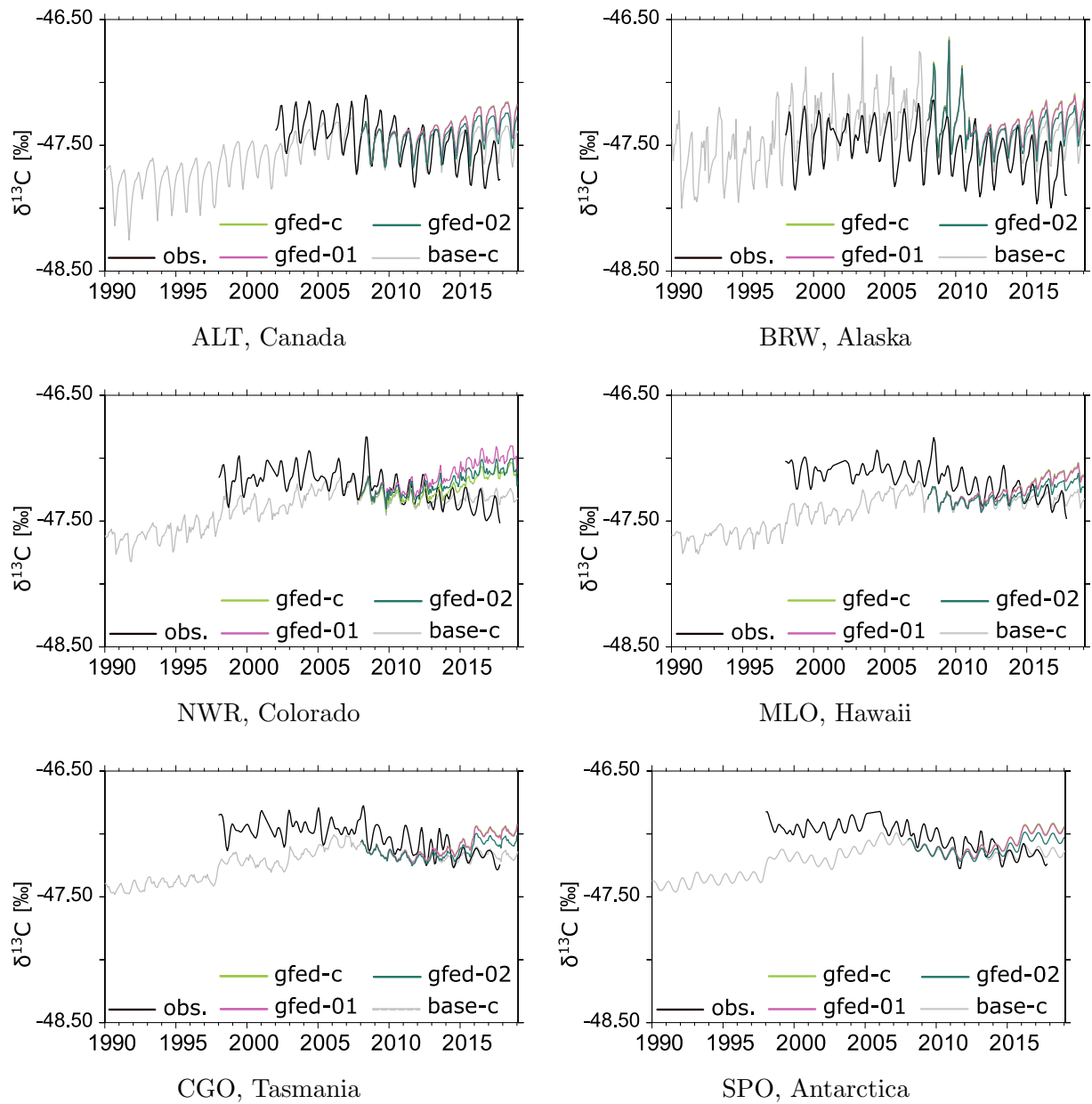


Figure 6.23: The monthly-averaged observed $\delta^{13}\text{C}$ at selected sampling sites are compared to the monthly-averaged $\delta^{13}\text{C}_{surf}^{sim}$ of the SDISO-base-c and all SDISO-gfed simulations. The sampling sites depicted here cover the mid and high latitudes in both Hemispheres. Other sampling sites are also compared to the model results and can be found in the Appendix A.3.3. For a better comparison, the bias between observations and model results is reduced by adding a constant value of 1.51 ‰ to the latter.

strongly from the observations, except for the SDISO-base-c simulation. The sampling site is close to a shale gas play (see map in Figure 6.19). Since all sensitivity simulations which

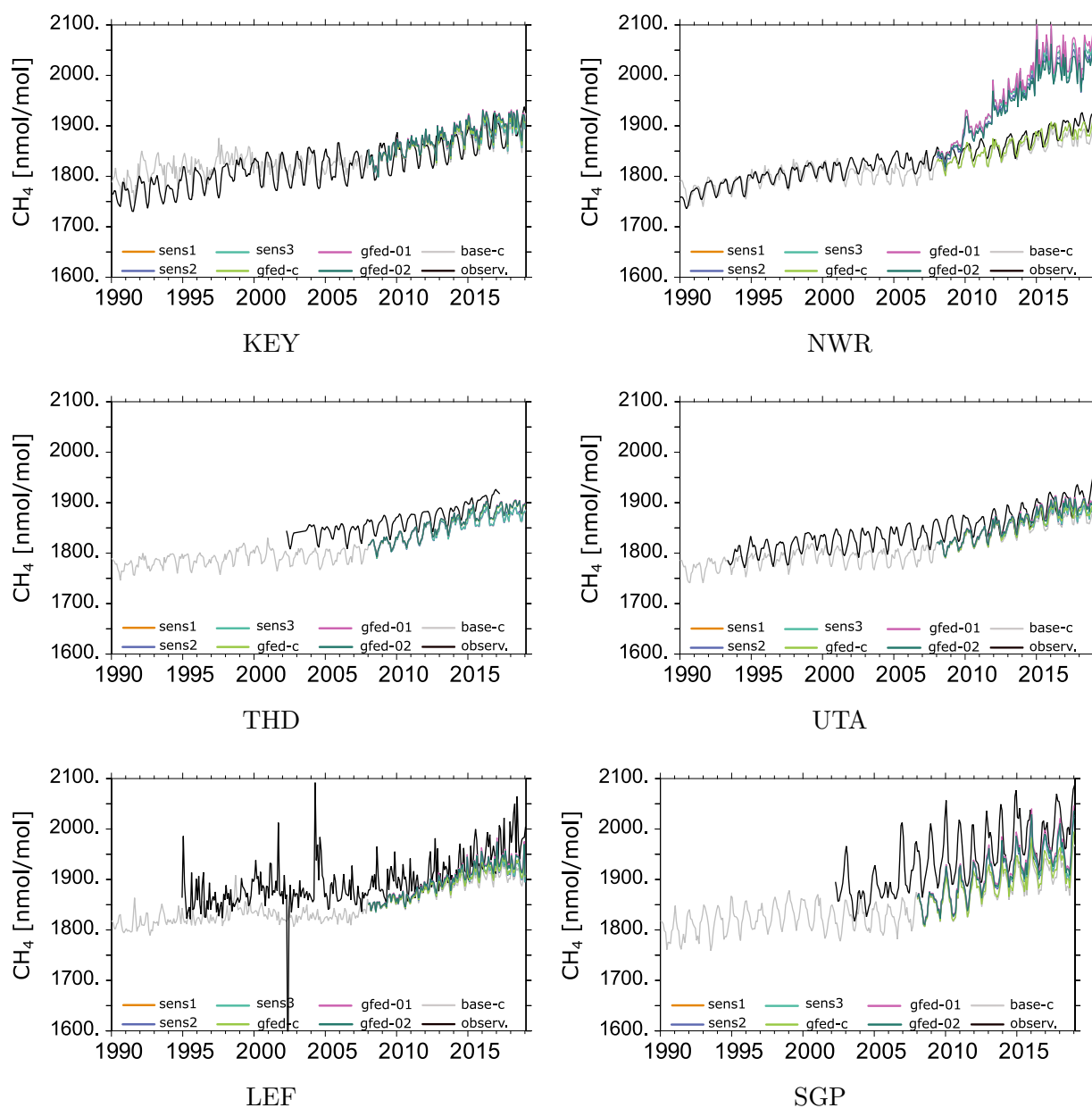


Figure 6.24: Monthly-averaged surface CH_4 mixing ratios simulated by the SDISO-base-c simulation and all sensitivity simulations at different US sampling sites. Additionally, the respective NOAA measurements are shown.

include shale gas emissions display a sharper increase in $\delta^{13}\text{C}_{surf}^{sim}$ compared to the other sampling sites, the shale gas emissions are likely overestimated here. Unfortunately, $\delta^{13}\text{C}$ measurements are sparse and one sampling site is not enough to manifest the statement that shale gas is in general overestimated. I therefore compared the ground-based CH_4 mixing ratios observed at different US sampling sites (see map in Figure 6.19) to the

model results (see Figure 6.24). Since only a few sites are close to the US shale plays and not all of them have continuous measurements, it is difficult to evaluate the model results with respect to the regional shale gas emissions. However, the simulations show similar surface CH_4 mixing ratios and match well with the observations at almost all sampling sites. Again, only the results at NWR indicate that shale gas emissions are overestimated. In all simulations, CH_4 mixing ratios clearly exceed the measurements, except for the SDISO-base-c and the SDISO-gfed-c simulations. Both do not contain any additional shale gas and match with the observations. The shale gas emissions in the SDISO setup are however, an approximation. As described in the beginning of Section 6.2, I use the shale gas plays as a mask for gas emissions of the EDGAR v5.0 inventory in 2007 in order to create a shale gas field for the sensitivity simulation. The proportion of the different shale plays of the total flux remains the same as in 2007. The NWR sampling site is close to Niobrara-Codell Shale, which is among those shale plays with a comparatively low level of shale gas production throughout the last decade. The largest production currently takes place in the Marcellus shale (North-Eastern shale in Figure 6.19), and between 2010 and 2014 the most productive shales were the Barnett shale and the Haynesville shale in the Southern part of the US (Texas) (EIA, 2019). Furthermore, the gas sector in the EDGAR v5.0 inventory does not distinguish between conventional and unconventional gas and may already include shale gas emissions. I account for the double counting by downscaling the gas emissions globally, however this can lead to mismatches on a regional scale. Nevertheless, quantifying the shale gas emissions on a regional scale is beyond the scope of this study. For the purpose of testing the influence on the global $\delta^{13}\text{C}$, these uncertainties can be neglected.

Summary and Conclusion

Based on the SDISO setup described in Section 6.1, I performed several sensitivity simulations. All simulations branch from the SDISO-base-c simulation and cover the period from 2008 until 2019. The sensitivity simulations are based on different assumptions regarding the contribution of the individual methane sources. Additionally, shale gas emissions are included in five of the six simulations. Biogenic and conventional fossil fuel emissions are then downscaled accordingly, in order to maintain the total sum of the methane emissions throughout the simulation period. As shown above, biomass burning emissions in the SDISO-base-c simulation decrease by $7.9 \text{ Tg}(\text{CH}_4)/\text{yr}$ between 2008 and 2014 compared to the period from 2000 to 2007. The decrease is large compared to estimates of Worden et al. (2017), who assumes a decrease of only $3.7 \text{ Tg}(\text{CH}_4)/\text{yr}$ for the same period. In two sensitivity simulations, biomass burning emissions are adjusted to match the estimates of Worden et al. (2017). Three additional simulations use the recent GFED v4.1s inventory for biomass burning emissions after 2007. In combination with the inventory used until 2007, this resulted in a similar decrease of $4 \text{ Tg}(\text{CH}_4)/\text{yr}$. For the shale gas emissions, I apply the isotopic signature of -46.9 ‰ suggested by Howarth (2019). For comparison, one sensitivity simulation uses a signature of -44 ‰ , which is the global mean for conventional oil and gas emissions (Schwietzke et al., 2016).

Results show that a decrease in the global mean $\delta^{13}\text{C}_{surf}^{sim}$ after 2007 is only achievable

with a decrease in biomass burning emissions of 7.9 Tg(CH₄)/yr. The global mean $\delta^{13}\text{C}_{surf}^{sim}$ decline is thereby independent from the inclusion of shale gas emissions. Shale gas emissions with an isotopic signature of -46.9 ‰, in fact, led to a slightly more negative global mean $\delta^{13}\text{C}_{surf}^{sim}$ when the conventional fossil fuel emissions were instead reduced. The effect is however, small and cannot explain the total decline in the observed $\delta^{13}\text{C}$. Moreover, the isotopic signature of shale gas emissions is not yet clearly known. Milkov et al. (2020) for example, estimated an isotopic signature of -41.8 ‰. Using higher isotopic signatures for shale gas emissions, such as -44 ‰, yields increasing global mean $\delta^{13}\text{C}_{surf}^{sim}$. Furthermore, the $\delta^{13}\text{C}_{surf}^{sim}$ of all simulations with a biomass burning decrease of only 3.7 or 4 Tg(CH₄)/yr increase relative to the base simulation. Consequently, shale gas emissions do not trigger the observed decrease in the global mean $\delta^{13}\text{C}$. Nevertheless, they cannot be excluded from the total methane increase. Shale gas production in the United States has prevailed during the last decades and recent studies suggest large fossil fuel emissions from Northern America (Helmig et al., 2016; Franco et al., 2016; Hausmann et al., 2016).

Similar to the SDISO-base-c simulation, the sensitivity simulations performed well on a regional scale and are comparable to local surface observations. The overall pattern of the six different global mean $\delta^{13}\text{C}_{surf}^{sim}$ can be observed at most sampling sites. Unfortunately $\delta^{13}\text{C}$ measurements in the United States are sparse. Only one sampling site close to a shale gas plain in Colorado could be compared to the simulations. The results revealed that shale gas emissions were clearly overestimated at the site. However, one sampling site is not sufficient to make any definite statements.

The present study could not confirm the ideas of Howarth (2019). Results show that shale gas emissions alone cannot be responsible for the observed global methane increase and the corresponding $\delta^{13}\text{C}$ decrease. In the SDISO setup, emissions from biomass burning seem to have a large influence on the $\delta^{13}\text{C}_{surf}^{sim}$. This is not surprising, since $\delta^{13}\text{C}$ signatures of biomass burning are much more positive than the atmospheric global mean $\delta^{13}\text{C}$. Small changes in their emission flux strength apparently lead to large changes in the global mean $\delta^{13}\text{C}$. However as discussed above in this section, the decrease in biomass burning is likely overestimated. This in turn implies larger biogenic emissions, which are generally more depleted in $\delta^{13}\text{C}$. The assumption is supported by several other studies (Schwietzke et al., 2016; Schaefer et al., 2016; Nisbet et al., 2019). Furthermore, changes of the atmospheric oxidation capacity may play an important role (Rigby et al., 2017; Turner et al., 2017). The impact on the global $\delta^{13}\text{C}$ due to changes of the atmospheric OH concentration is further investigated in Section 6.3. Although, as mentioned above, shale gas is not the major driver of the observed decline in the global $\delta^{13}\text{C}$, fossil fuel emissions likely increased after 2007 and shale gas emissions likely are a significant contributor to the global methane budget.

6.2.2 Influence of tropospheric lifetime on the global mean $\delta^{13}\text{C}$

Since the concentration of OH primarily defines the oxidation capacity in the troposphere, the tropospheric lifetime of methane mainly depends on the abundance and distribution

of OH. The highest OH concentrations appear in the tropics due to the formation of water vapour and the abundance of UV radiation (see Chapter 2 for more details). Consequently, tropical methane is removed faster from the atmosphere than in boreal regions, where the OH concentration is rather low. These differences may also have an influence on the global mean $\delta^{13}\text{C}$, since isotopic signatures emitted in the high latitudes could have a greater impact than those emitted in the tropics. In this section, I want to test whether individual methane sources contribute differently to the global mean $\delta^{13}\text{C}$, depending on their individual tropospheric lifetimes. In the CH₄ submodel each methane source can be simulated as a single methane tracer. The resulting CH₄ mixing ratios can be used to calculate the tropospheric lifetime with respect to the OH oxidation $\tau_{\text{CH}_4+\text{OH}}$. I calculated the mean lifetimes for each methane sector between 2008 and 2019 for the SDISO-sens2 simulation. The results are presented below. In the sensitivity setups I have reduced the biogenic and fossil fuel emissions globally, in order to introduce the new shale gas emissions locally. They are only emitted in the 48 US states between 25°N and 55°N. In order to see a potential impact on the global mean $\delta^{13}\text{C}$, I additionally calculated $\tau_{\text{CH}_4+\text{OH}}$ for all sensitivity simulations and the base simulation. The τ_{CH_4} with respect to OH is calculated with the formula from Jöckel et al. (2006):

$$\tau_{\text{CH}_4}(t) = \frac{\sum_{b \in B} M_{\text{CH}_4}(b, t)}{\sum_{b \in B} k_{\text{CH}_4+\text{OH}}(T(b, t)) \cdot c_{\text{air}}(T(b, t), q(b, t), p(b, t)) \cdot \text{OH}(b, t) \cdot M_{\text{CH}_4}(b, t)} \quad (6.1)$$

with $M_{\text{CH}_4}(b, t)$ being the mass of methane in kg, $k_{\text{CH}_4}(T(b, t))$ being the reaction rate of the methane oxidation with OH in $\text{cm}^3 \text{ s}^{-1}$, which is dependent on the temperature T , and $\text{OH}(b, t)$ being the mole fraction in mol mol^{-1} in a grid box b at time t . B is the number of grid boxes which are used for the calculation. In this case, B includes all grid boxes which lie below the tropopause in order to receive the tropospheric lifetime. $c_{\text{air}}(T(b, t), q(b, t), p(b, t))$ is the concentration of air in molecules cm^{-3} and depends on the temperature T , the specific humidity q and the pressure p in the respective grid box b at time t . It is calculated with the formula taken from Frank (2018):

$$c_{\text{air}}(T, p, q) = \frac{N_A}{10^6} \cdot \frac{p(b, t)}{R_{\text{gas}} \cdot T(b, t) \cdot (1 + (\frac{M_{\text{air}}}{M_{\text{H}_2\text{O}}} - 1) \cdot q(b, t))} \quad (6.2)$$

with $N_A = 6.02214129 \cdot 10^{23}$ (Avogadro's constant), $R_A = 8.3145 \frac{\text{J}}{\text{K} \cdot \text{mol}}$ (ideal gas constant) and $M_{\text{air}} = 28.987 \text{ g mol}^{-1}$ and $M_{\text{H}_2\text{O}} = 18.01 \text{ g mol}^{-1}$ being the molar mass of air and water, respectively.

Results and discussion of the tropospheric lifetime of the SDISO simulations

Table 6.6 lists the resulting lifetimes and their respective standard deviations for all methane sources between 2008/04 and 2019/01. Note that the first 3 months are excluded from the calculation, as shale gas emissions were introduced in January 2008 and

Table 6.6: The table lists the mean tropospheric lifetimes τ_{CH_4+OH} , the standard deviation of the annual averages (2009-2018) σ_y , and the standard deviation of the monthly averages σ_m for the individual methane sources in years for the period 2008/04-2019/01. The lifetimes are calculated based on the CH_4 mixing ratios simulated by the SDISO-sens2 simulation.

Source	τ_{CH_4} in [a]	σ_y	σ_m	Source	τ_{CH_4} in [a]	σ_y	σ_m
Livestock	9.003	0.0286	0.7579	Biomass burning	8.979	0.0298	0.7328
Landfills	9.002	0.0289	0.7857	Ocean	9.028	0.0290	0.7620
Rice	8.986	0.0284	0.7784	Termites	9.004	0.0287	0.7253
Coal	9.015	0.0280	0.7930	Volcanoes	8.999	0.0256	0.7750
Oil	8.997	0.0286	0.8052	Wild animals	9.015	0.0287	0.7539
Gas	9.007	0.0289	0.8136	Wetlands (temp./trop.)	9.004	0.0290	0.7307
Shale gas	8.958	0.0339	1.3850	Wetlands (boreal)	9.015	0.0309	0.8539
Awb	8.989	0.0289	0.7667				

Awb = Agricultural waste burning

therefore less exposed to oxidation in the first months of the simulation. This resulted in a large tropospheric lifetime of shale gas emissions which deteriorated the mean value.

The tropospheric lifetimes of the individual sources are similar, whereby the differences between them are less than a month. Since many of the sources are distributed over both climate zones, namely the tropics and the mid latitudes of the Northern Hemisphere, the expected differences are rather small. Instead, one would anticipate larger differences between sources in the tropics and sources in the high latitudes. Due to high concentrations of OH, the potential of methane removal is largest in the tropics. In Table 6.6, boreal wetland emissions are considered separately from tropical wetland emissions. Yet their tropospheric lifetime is not significantly larger. Additionally, the lifetime of shale gas, which is only emitted between 25°N and 55°N, does not stand out from the other lifetimes. This shows that the emitted methane is rapidly transported through the atmosphere and also oxidized in regions further away from the source. This is supported by Warwick et al. (2002), who showed that the transport of methane from mid and high latitudes to the tropics and the vertical transport in the troposphere influences the surface global growth rate of methane. Additionally, in a previous EMAC simulation, Frank (2018) tracked the evolution of individual methane sources by simulating monthly age classes, which is a feature of the CH_4 submodel (see Chapter 3.1.3). Results showed that regional emissions are distributed evenly and are added into the CH_4 background after only 5 months.

Yet, the here presented results differ from those presented by Zimmermann et al. (2020), who found distinct differences between the lifetimes of the individual sectors. Their calculation, however assumes steady state conditions, where the ratio between the atmospheric trace mass and the annual emissions equals the total sink of methane. These steady state conditions, however, cannot be assumed for the period from 2008 to 2019, which was investigated in the present work.

Most monthly standard deviations σ_m of the presented lifetimes vary between 8 to 10 months and show the inter-annual variability of the lifetimes, caused by the seasonality of OH. However, the standard deviation for the shale gas lifetime is larger than one year. This can be explained by the fact that in the first years since the initiation of shale gas, the global abundance of shale gas molecules is low relative to the abundance of shale gas molecules in the region where they are emitted. The majority of shale gas methane is therefore exposed to the variability of OH in the source region, namely in the mid latitudes of the Northern Hemisphere. The annual surface OH variability here is more pronounced than in the tropics or high latitudes. Nevertheless, the mean tropospheric lifetime of shale gas is comparable to those of the other sources. In line with this, all simulations (SDISO-base-c and sensitivity simulations) have the same global mean tropospheric lifetime of 9.021 yr. Introducing the new shale gas emissions locally did not influence the global mean tropospheric lifetime. Consequently, the localisation of a source does not determine the degree of its influence to the global mean $\delta^{13}\text{C}$ in the simulations. Moreover, this study concentrates on the surface global mean $\delta^{13}\text{C}$, which is dominated by sources rather than sink reactions. In reality, however, the regional methane emissions in turn affect the OH concentration and play an important role to the oxidation capacity. These potential feedbacks on OH are not considered in the SDISO simulations. Furthermore, methane lifetimes are not solely determined by the OH oxidation. About 30 Tg(CH₄)/yr (Dlugokencky et al., 2011) escapes into the stratosphere and is oxidized by Cl and O¹D. Another 5 % is lost by soil uptake, which depends on the temperature and moisture in the soil. The efficiency of soil uptake varies among latitudes (e.g. due to snow cover, Curry, 2009) and may therefore also influence the regional methane lifetimes.

6.3 Sensitivity simulations towards OH variations

So far in the present study I have focused on the recent methane rise due to changes in the emission fluxes and the individual sources that contribute to the additional emissions. The OH concentration was climatologically prescribed throughout the SDISO-base-c and sensitivity simulations. Understanding changes in tropospheric OH is, however, crucial for interpreting the global methane budget (Rigby et al., 2017; Turner et al., 2017; Zhao et al., 2020). This is especially true for top-down estimates in tropical regions (Zhao et al., 2020), where the interannual variability of OH is large. Yet temporal variations of OH concentrations in the atmosphere are poorly understood. Large uncertainties arise due to the complexity of the processes OH is involved in and due to difficulties in measuring OH concentrations in the atmosphere.

Apart from changes in the composition of methane sources, a change of the oxidation capacity in the troposphere is also likely to influence the global observed $\delta^{13}\text{C}$. Several studies already examined the influence of OH on the global methane budget with respect to $\delta^{13}\text{C}$. While Schaefer et al. (2016) ruled out the contribution of OH changes to the observed decline in $\delta^{13}\text{C}$, the studies of Rigby et al. (2017) and Turner et al. (2017) assume that a reduction of the OH concentration could be an explanation for the recent methane

increase and a simultaneous decline in $\delta^{13}\text{C}$. With decreasing OH concentrations, methane is less exposed to oxidation and the associated isotopic fractionation, which would lead to an enrichment in the heavier ^{13}C of the remaining methane, is reduced. This means in reverse, atmospheric methane remains isotopically more negative. Furthermore, a reduced oxidation capacity in turn means, that methane emissions are lower than originally assumed. Turner et al. (2017) considered, for example, that a decrease of emissions in the Southern Hemisphere, which are typically enriched in the heavier isotope, could result in a more negative global mean $\delta^{13}\text{C}$.

In this section I want to examine the effect of reduced isotopic fractionation on the global mean surface $\delta^{13}\text{C}$. This is done by assuming a moderate change in the tropospheric τ_{CH_4} of about 0.5 yr. I conducted two sensitivity simulations based on the SDISO-base-c simulation starting in 2008. Emissions are kept constant after 2007 to rule out the effect of variations in the emissions. The first simulation, named SDISO-base-OH, uses the OH field of the SDISO-base-c simulation. As shown above, the global mean tropospheric lifetime of the SDISO-base-c simulation is about 9 years. In the second simulation, named SDISO-base-OH-9.5, OH concentrations are scaled to obtain a global mean tropospheric lifetime of about 9.5 years.

Results and discussion of OH sensitivity simulations

Figure 6.25 shows the results of the simulation SDISO-base-c and the two sensitivity simulations SDISO-base-OH and SDISO-base-OH-9.5. The monthly averaged global mean surface CH_4 mixing ratio of the SDISO-base-OH simulation is similar to the SDISO-base-c simulation. Although emissions are kept constant, methane increases after 2007 and follows the course of the SDISO-base-c simulation. The methane level of the stabilisation period is not maintained throughout the simulation, since total methane emissions in 2007 are larger than those between 2000 and 2006. Holding emissions constant after the year 2006 would presumably have led to a state of equilibrium. The global mean CH_4 mixing ratio of the SDISO-base-OH-9.5 simulation increases sharply and exceeds that of the other simulation by far. This is explained by the reduced CH_4 oxidation. In order to correspond to the observed methane level in the atmosphere, methane emissions in the SDISO-base-OH-9.5 simulation would have to be lower. The global mean $\delta^{13}\text{C}_{\text{surf}}^{\text{sim}}$ of both sensitivity simulation decreases and lies below the result of the SDISO-base-c simulation (see Figure 6.25, right panel). The simulated decline possibly arises from larger wetland emissions in 2007 compared to the years 2008-2019 in the SDISO-base-c simulation (see also Figure 6.15). The two sensitivity simulations use the emissions of the year 2007 for the years 2008 until 2019. Consequently, the wetland emissions are larger than in the SDISO-base-c simulation. Although not further investigated in the present study, this supports the assumption that biogenic emissions are the primary cause for the observed methane increase. However, the SDISO-base-OH simulation and the SDISO-base-OH-9.5 simulation differ in their global mean $\delta^{13}\text{C}_{\text{surf}}^{\text{sim}}$, the latter being slightly more negative. The global mean tropospheric lifetime of the SDISO-base-OH-9.5 simulation between 2008 and 2019 is 9.451 (± 0.006) years. This represents an increase of the methane lifetime by about 0.45 yr and leads to

a decrease in the global mean $\delta^{13}\text{C}_{surf}^{sim}$ of about 0.03 ‰ compared to the SDISO-base-OH simulation. The influence of the isotopic fractionation seems to be small in the SDISO setup and cannot explain the total decline in the observed global mean $\delta^{13}\text{C}$. Nevertheless, as discussed in Section 6.1, also uncertainties in the applied KIE (OH oxidation) reveal in the SDISO setup. Moreover, a reduction of OH implies fewer emissions of methane. This could additionally change the flux-weighted emitted global mean $\delta^{13}\text{C}$ towards more negative values. As mentioned above, the current understanding of the temporal evolution of OH in the atmosphere is highly uncertain. By analysing various CCMI models, Zhao et al. (2020) found a positive OH trend between 1980 and 2010, and consistent therewith, Nicely et al. (2020) found a methane lifetime downward trend between 1980 and 2015. Nevertheless, the results show that OH plays an important role in the investigation of the recent methane rise and should not be ignored.

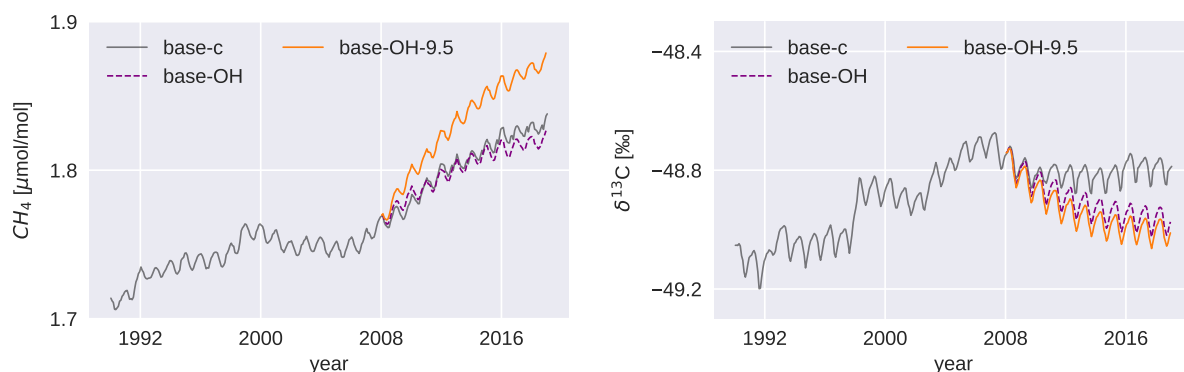


Figure 6.25: Global mean surface methane mixing ratios of the SDISO-base-c simulation and the two sensitivity simulations SDISO-base-OH and SDISO-base-OH-9.5 (left panel) and the resulting global mean surface $\delta^{13}\text{C}$ of each simulation (right panel).

6.4 Summary and outlook

The presented study aims to understand the global atmospheric methane increase after 2007 and the simultaneous global decrease in $\delta^{13}\text{C}$. In particular, I investigated the role of shale gas in this renewed methane increase by using the state-of-the-art chemistry climate model EMAC. In Section 6.1 I built the SDISO setup based on the most recent methane emission inventories and $\delta^{13}\text{C}$ source signatures. Instead of applying a global mean $\delta^{13}\text{C}$ for each source, I broke down the individual source signatures depending on source material and their type of formation. First simulations were successfully performed and their results are promising. The CH_4 mixing ratios are well represented in the model and comparable to the observations on both, regional and global scales. Despite showing a negative bias, the global mean surface $\delta^{13}\text{C}$ agrees well with the observed global mean.

In Section 6.2, I examined the role of shale gas emissions by testing the hypothesis proposed by Howarth (2019). Therein, shale gas emissions account for 33 % of the additional methane emissions after 2007. According to Howarth (2019), shale gas emissions

have a relatively negative isotopic signature compared to those of conventional fossil fuel emissions. Increasing shale gas emissions may therefore have contributed to the observed decline in the global atmospheric $\delta^{13}\text{C}$. I performed six sensitivity simulations with different assumptions on the contribution of conventional fossil fuel emissions, biogenic emissions and shale gas emissions. Furthermore, biomass burning emissions are modified in some of the sensitivity simulations. All simulations were then analysed with respect to their resulting global mean $\delta^{13}\text{C}_{surf}^{sim}$.

The ideas of Howarth (2019) were not confirmed with the SDISO setup. The results indicate that shale gas emissions do not primarily lead to the observed negative trend. Though they still may contribute to the renewed methane increase, since recent measurements of atmospheric ethane indicate increasing fossil fuel emissions from the United States (Helmig et al., 2016; Franco et al., 2016; Hausmann et al., 2016). Instead, biomass burning emissions played a larger role and a decrease of 7.9 Tg /yr resulted in a decrease of the global mean surface $\delta^{13}\text{C}$. However since this decrease is presumably too large, it is likely that biogenic emissions from agriculture or wetlands are the major driver of the new increase. Schaefer et al. (2016) suspected agricultural emissions as the main contributor. In the presented base simulation nearly 46 % of the additional emissions after 2007 are due to livestock, rice and landfills. In contrast, wetland emissions in the SDISO setup remain relatively constant after 2007. Constant wetland emissions agree with the findings of Poulter et al. (2017), but recent studies suggest a major contribution of wetlands after 2007 (Nisbet et al., 2019; Rosentreter et al., 2021). Studying the influence of wetland emissions was, however, beyond the scope of this study. The SDISO setup seems to be suitable for further sensitivity simulation towards wetland emissions. However future simulations should include the most recent GFED v4.1s inventory for biomass burning emissions throughout the whole simulation period from 1990 to 2019.

I further investigated the influence of the global OH distribution on the tropospheric lifetime of the individual methane sources in the SDISO setup. The tropospheric lifetimes with respect to OH do not differ significantly between the individual methane sources. This is possibly attributed to rapid and effective atmospheric transport through regions with different oxidation capacities. From these results it can be concluded that boreal emissions did not contribute more to the global mean $\delta^{13}\text{C}_{surf}^{sim}$ than tropical emissions. However, results might be different when applying an interactive chemistry with feedbacks on the OH concentrations.

The applied OH field is also crucial for the analysis of the global methane budget. Section 6.3 examines the influence on the global mean surface $\delta^{13}\text{C}$ when the tropospheric lifetime increases by 0.5 years. The effect of less isotopic fractionation due to less oxidation of methane is rather small and does not explain the total decline in the global mean $\delta^{13}\text{C}$. However, possible changes in the methane emission estimates are not considered here and further studies need to include temporal OH variations.

Chapter 7

Summary, discussion and conclusions

Methane (CH_4) is the second most important greenhouse gas, in terms of anthropogenic radiative forcing (Myhre et al., 2013). It is emitted at the Earth's surface from anthropogenic and natural sources, and mainly removed by the hydroxyl radical (OH) in the troposphere. Atmospheric mixing ratios have increased since the beginning of the industrialisation and continue to grow (Dlugokencky et al., 2011; Nisbet et al., 2014, 2019). Due to its the relatively short atmospheric lifetime, a reduction of methane emissions has great potential for climate change mitigation (Dlugokencky et al., 2011). After a period of stable mixing ratios since 2000, a strong increase has been observed since 2007. The causes of this renewed increase are not yet fully understood. The main drivers could be either biogenic sources (mainly wetlands, agriculture or waste management), thermogenic sources (mainly fossil fuels) or a combination of both (Hausmann et al., 2016; Schaefer et al., 2016; Schwietzke et al., 2016; Worden et al., 2017; Nisbet et al., 2019; Jackson et al., 2020; Rosentreter et al., 2021). Furthermore, changes in the major sink of CH_4 (i.e. OH) might play a role (Turner et al., 2016; Rigby et al., 2017). However, until today large uncertainties remain in the total emission estimates (Kirschke et al., 2013; Saunio et al., 2016, 2020). Understanding the global methane budget requires comprehensive measurements, as well as reliable regional and global numerical models. Moreover, studying stable isotopes provides a powerful tool to constrain atmospheric methane to individual sources.

The overall motivation for the presented thesis is, to contribute to the understanding of the global methane budget using regional and global modelling approaches, and by exploiting the additional information based on stable isotopes. The thesis comprises three main parts (i.e. Chapter 4, 5 and 6). Chapter 4 analyses hind- and forecasts of regional point source emissions from coal mining, simulated by a global/regional on-line nested chemistry climate model. In addition, stable methane isotopologues are simulated on regional scale (see Chapter 5). To do so, I use a simplified approach to calculate the basic chemistry and physics of CH_4 and its isotopologues (MESSy submodel CH4, Winterstein and Jöckel, 2021). The last section (Chapter 6) discusses the global atmospheric CH_4 and $\delta^{13}\text{C}(\text{CH}_4)$ evolution since 2007, using a state-of-the-art global chemistry climate model. Section 7.1 summarizes the different modelling approaches, and the preparations for the

individual simulations. Section 7.2 concludes the results with respect to the scientific questions raised in Chapter 1 and includes a short outlook.

7.1 Summary of the methodology

Regional modelling of CH₄ emissions

The first part of the presented study comprises the development of a forecast system with the global/regional on-line nested chemistry climate model “MESSyified ECHAM and COSMO models nested n times” (MECO(n), Kerkweg and Jöckel, 2012a; Mertens et al., 2016). Throughout the measurement campaign CoMet 1.0, this forecast system provided 6-day forecasts of regional methane emissions from coal mining ventilation shafts in the Upper Silesian Coal Basin (USCB) in Poland. Three regional model instances with progressing smaller spatial and temporal resolutions are nested into each other (down to a spatial resolution of 2.8 km), in order to simulate the small-scale features of the atmospheric CH₄ distribution within the study area. The regional model instances are driven by the global chemistry climate model ECHAM/MESSy (EMAC, Jöckel et al., 2010), which is constrained with the analysed and forecasted meteorology by Newtonian Relaxation. Each regional model domain receives its’ boundary conditions from the respective coarser-resolved model domain. The forecast products comprise the simulation of two independent CH₄ tracers: the first includes all methane emission fluxes, the second only considers the point source emissions from the coal mining ventilation shafts, without any background CH₄. After the campaign, these forecasts and an analysis simulation covering the whole campaigns’ time period, were conducted again. Thereby the model output along the measurement flight tracks was sampled. This model output is compared to the CoMet 1.0 observations, in order to evaluate the forecast skill and the general ability of MECO(3) to simulate regional methane emissions. The results are discussed in Chapter 4 and are already published in Nickl et al. (2020).

The second part, includes the simulation of stable CH₄ isotopologues with the MECO(3) model on regional scale. The CH₄ submodel extension described by Winterstein and Jöckel (2021) calculates the chemistry and physics of the stable isotopologues. Thereby it considers the isotopic fractionation during the sink processes of methane. I performed several analysis simulations of the CoMet 1.0 campaign, using different $\delta^{13}\text{C}(\text{CH}_4)$ signatures for the coal mining emissions in the USCB. The model results were examined for their ability to simulate $\delta^{13}\text{C}(\text{CH}_4)$ variability in methane plumes relative to the background on regional scale. The comparison of observations further helped to determine an overall source signature of coal mining emissions in the USCB. This is presented in Chapter 5.

Global modelling of stable CH₄ isotopologues and the recent CH₄ rise

Chapter 6 aims to understand the global CH₄ rise after 2007 and the simultaneous decline of the global mean surface $\delta^{13}\text{C}(\text{CH}_4)$. The main focus lies on testing the hypothesis of Howarth (2019), i.e. the contribution of CH₄ emissions due to shale gas extraction to

the observed global CH₄ rise. In light of this I built a model setup using the state-of-the-art global chemistry climate model EMAC. The setup is based on recent CH₄ emission inventories. The individual isotopic signatures of methane are a suitable tool to distinguish between biogenic, thermogenic and pyrogenic origin. Furthermore, $\delta^{13}\text{C}(\text{CH}_4)$ varies within individual emission sectors, e.g. wetlands, coal or biomass burning. This is for example due to different types of organic source material or different environmental conditions during the formation of CH₄ (Whiticar, 1999). Therefore, the preparation comprises a comprehensive breakdown of all isotope source signatures based on recent literature values. I conducted several transient sensitivity simulations of the years 1990 to 2019. A first base simulation is analysed with respect to the global atmospheric distribution of CH₄ and $\delta^{13}\text{C}(\text{CH}_4)$, and the observed global means since 2000. In a second step, I introduced shale gas emissions as an individual source category with different $\delta^{13}\text{C}(\text{CH}_4)$. These shale gas emissions were steadily increased since 2007 and sum up to 33 % of the total additional emissions between 2007 and 2014 (as suggested by Howarth, 2019). To maintain the total sum of the CH₄ emission fluxes, I reduced the remaining source category emission fluxes accordingly. Six sensitivity simulations were conducted.

In addition, I investigated if the atmospheric distribution of OH causes individual source emissions to contribute differently to the global mean surface $\delta^{13}\text{C}(\text{CH}_4)$. This consideration arises from the fact that the OH distribution in the troposphere varies greatly. Depending on where methane is emitted, it could be removed at different rates. To test this assumption, I calculated the tropospheric lifetime of CH₄ for each emission sector with respect to OH. In a last step, I explored the effect of a global OH reduction onto the global mean surface $\delta^{13}\text{C}(\text{CH}_4)$. The oxidation of methane leads to an isotopic fractionation and a more positive $\delta^{13}\text{C}(\text{CH}_4)$ of the remaining atmospheric methane. Consequently, less methane oxidation could be an explanation for the decline of the global mean surface $\delta^{13}\text{C}(\text{CH}_4)$ and the increase in the methane mixing ratios. I performed two sensitivity simulations with constant methane emissions and a reduction of the OH concentration after 2007.

7.2 Discussion and conclusions

Based on the applied methodology, I am able to answer the initially raised scientific questions:

How well do we understand the CH₄ distribution on regional scale? How well can we simulate and forecast regional CH₄ distributions with a regional model? Is there an improvement of the models' skill with increasingly finer model resolution?

The regional atmospheric CH₄ distribution depends on local CH₄ emissions from the Earths' surface, its chemical loss and atmospheric transport in the regarded area. Our current understanding of local emission estimates varies among regions and the associated

sources. Anthropogenic sources are usually better localized than natural sources, which makes it easier to quantify them. This is also evident, when comparing bottom-up and top-down inventories, which show smaller deviations from each other for anthropogenic sources (Saunois et al., 2020). Nevertheless, difficulties in accurate estimates remain, e.g. in poorly observed regions, or for emissions on very small-scales. In this modelling study, the focus is on modelling regional methane emissions from coal mining ventilation shafts in the USCB. The chemical sink is kept constant in all simulations. The answer to the above questions, therefore, only addresses this particular region and the respective emission estimates.

The results of the comparison with the CoMet 1.0 observations showed that the global and regional on-line nested chemistry climate model MECO(3) is able to simulate the CH₄ point source emissions from the coal mining ventilations shafts in the USCB reasonably well. This could not necessarily be expected, regarding the fact, that only the global EMAC model is “nudged” towards the ECMWF data, i.e. constrained with forecasted or observed meteorology. The finer model instances, in contrast, are only constrained at their boundaries by the next-coarser model instance. Therefore, they develop their own meteorology within the model domains.

The best agreements with observations are obtained for vertically integrated values and the vertical gradient of CH₄ in the atmosphere. This is deduced from the comparison with LIDAR measurements and airborne in-situ measurements along so-called “diving” flights, respectively. The simulation of smaller-scaled patterns (airborne high-frequency in-situ measurements), measured close to coal mining ventilations shafts, is, however, challenging. Nevertheless, MECO(3) provided good results when wind conditions were most stable and, therefore, favourable for detecting CH₄ plumes. The disagreements between model results and observations are mostly attributed to the applied emission inventories (i.e. use of emission from 2012 to simulate the 2018), and a too shallow Planetary Boundary Layer Height (PBLH) simulated by the model. Apart from that, methane emissions associated with coal mining can be well simulated by two individual methane tracers. The tracers either comprise only the point source emissions from the ventilation shafts, or the total CH₄ emission fluxes (i.e. background and point source emissions). Deviations in the amplitudes of individual methane peaks suggest different source strengths in the underlying emission inventories, i.e. CoMeT ED v1 based on E-PRTR (2014) and EDGAR v2FT2010 (Janssens-Maenhout et al., 2013), respectively. However, the position and timing of the methane peaks are in good agreement. This provides a good tool to distinguish between local source emissions from fluctuations in the background. Moreover, it implies that the emission sources of both inventories are consistent and reliable. A quicklook at more recent emission inventories reveals, that emission estimates have improved and better match with the amplitudes in the observed CH₄ mixing ratios.

Summarizing, this study suggest that – with our current understanding of local point sources – we can reproduce the observed methane distribution in the atmosphere on regional scales well. The MECO(3) model yields promising results and can produce supporting forecasts for future measurement campaigns. The evaluation of the forecast skill shows that MECO(3) provides reliable forecasts up to forecast day four. The finest-resolved model instance (spatial resolution of 2.8 km) shows no significant improvement compared to the

next coarser-resolved model instance (spatial resolution of 7 km). For the purpose of the campaigns' flight planning, equally good results can be achieved. However, the increasing resolution holds a benefit for a detailed consideration of the individual methane peaks. The presented study concentrated on very strong anthropogenic point source emissions, which were already localized. Current global emission estimates show that the largest uncertainties can be attributed to natural sources, such as wetland emissions, geological seepage and inland waters (Saunio et al., 2020). For example, the total natural source emissions between 2008-2017 are estimated to be 371 Tg(CH₄)/yr [245-488] in bottom-up, but only 218 Tg(CH₄)/yr [183-248] in top-down approaches (Saunio et al., 2020). With the MECO(3) model a tool has been established, which helps to verify emission estimates from local sources. The CoMet-like campaign MACIG (Monitoring of Atmospheric composition and Greenhouse gases through multi-Instrument Campaigns) carried out in 2021 and the future CoMet 2.0 campaign in 2022 aim on quantifying diffuse emissions from boreal wetlands. A model evaluation with respect to these measurements could provide further insights into how well current emission inventories resolve and estimate such diffuse emissions regionally. Future simulations should, however, include updated emission inventories to prevent biases between observations and simulations.

How well do we understand stable CH₄ isotopologues on regional scales and how well can we simulate them? Do we see differences in the isotopic signatures relative to the background signature?

The regional $\delta^{13}\text{C}(\text{CH}_4)$ distribution in the atmosphere depends on the emitted $\delta^{13}\text{C}(\text{CH}_4)$, the background $\delta^{13}\text{C}(\text{CH}_4)$ advecting into the regarded area, and the isotopic fractionation during sink processes. The $\delta^{13}\text{C}(\text{CH}_4)$ signatures are different for biogenic, thermogenic and pyrogenic methane. Depending on the emission source category (e.g. fossil fuel, livestock, wetlands, biomass burning), even finer $\delta^{13}\text{C}(\text{CH}_4)$ distinctions can be made. The here presented simulations use recent literature-based $\delta^{13}\text{C}(\text{CH}_4)$ signatures for the individual emission source categories.

Based on these isotopic signatures, the MECO(3) model is able to simulate the observed isotopic composition in the USCB. Moreover, differences relative to the background $\delta^{13}\text{C}(\text{CH}_4)$ are resolved. These differences of the $\delta^{13}\text{C}(\text{CH}_4)$ can be attributed to the local sources, i.e. coal mining ventilation shafts. The results prove that with the current emission inventories and knowledge of the individual isotope source signatures, we are able to reproduce the background $\delta^{13}\text{C}(\text{CH}_4)$ and $\delta^{13}\text{C}(\text{CH}_4)$ variability on regional scales.

In addition, this study has shown, that the simulations can support the interpretation of the measurements. By comparison with observations, an average $\delta^{13}\text{C}(\text{CH}_4)$ of -51 ‰ for coal mining emissions in the USCB was determined. This value is in accordance with other $\delta^{13}\text{C}(\text{CH}_4)$ signatures, reported for the USCB area (Zazzeri et al., 2016, -50.9 ± 0.6). However, the comparison with the observation also revealed several discrepancies. These are mainly attributed to the fact that small-scale observations were more difficult to simulate. As mentioned above, the accurate simulation of the local methane plumes strongly depends on the meteorological conditions and on the representation of the PBLH.

Comprehensive knowledge about local $\delta^{13}\text{C}(\text{CH}_4)$ signatures is crucial for further investigations of the global methane budget. Based on the comparison with airborne observations, the present study estimated an average $\delta^{13}\text{C}(\text{CH}_4)$ value for the USCB region. However, $\delta^{13}\text{C}(\text{CH}_4)$ source signatures can vary strongly among single point sources within one specific area (Kotarba, 2001; Zazzeri et al., 2016). For example, Kotarba (2001) reports $\delta^{13}\text{C}(\text{CH}_4)$ signatures between -79.9 and -44.5 ‰ for coalbeds in the USCB. The simulation of stable isotopologues with the MECO(3) model provides a suitable tool to assign observed methane plumes to individual point sources. The recently published CoMet ED v4 inventory (Gałkowski et al., 2021a) comprises emission fluxes and $\delta^{13}\text{C}(\text{CH}_4)$ of the individual ventilation shafts. A more precise assessment of the simulated $\delta^{13}\text{C}(\text{CH}_4)$ in methane plumes with respect to this inventory is therefore desirable. However, the investigation of individual methane plumes was beyond the scope of this thesis.

How do different CH_4 source categories, and in particular shale gas emissions, contribute to the global CH_4 budget?

A first base simulation with the global chemistry climate model EMAC was successfully performed. The regional breakdown of the $\delta^{13}\text{C}(\text{CH}_4)$ source signatures leads to a well represented global $\delta^{13}\text{C}(\text{CH}_4)$ distribution. Both, vertical and meridional gradients in the atmosphere are well reproduced. This is also true for the distribution of the CH_4 mixing ratios. Furthermore, regions with large expected emissions, such as the Amazon region, are clearly distinguishable from the background level. From that, it can be deduced, that the applied emission inventories (i.e. EDGAR v5.0, Crippa et al. (2020) and EMPA, Frank (2018)) and the isotopic source signatures from the literature enable our state-of-the-art chemistry climate model to reproduce the actual atmospheric methane and $\delta^{13}\text{C}(\text{CH}_4)$ distribution adequately. In addition, the observed temporal trend of the global mean surface CH_4 and $\delta^{13}\text{C}(\text{CH}_4)$ can be simulated well by the model. The simulation reflects the plateau between 2000 and 2007 and the new increase in CH_4 since 2007. The global mean surface $\delta^{13}\text{C}(\text{CH}_4)$ decline after 2007 is not as pronounced as in the observations. Moreover, a continuous offset between simulated and observed $\delta^{13}\text{C}(\text{CH}_4)$ exists. This is partly explained by uncertainties in the isotopic fractionation factor applied for the oxidation with OH.

Summarizing, these results are very promising. This study has built a comprehensive setup to assess the stable isotopologues of CH_4 and to constrain individual source contributions. The results of the base simulation provide a consistent picture for further investigations of the overall methane budget.

The ideas of Howarth (2019), i.e. that shale gas emissions could be a major driver of the global CH_4 rise since 2007 and the decline in global mean surface $\delta^{13}\text{C}(\text{CH}_4)$, were tested in several sensitivity simulations. A potential contribution of shale gas emissions to the new CH_4 rise cannot be discounted. Several studies suggest that emissions from fossil fuels in North America must have increased in the last decade (Helmig et al., 2016; Franco

et al., 2016; Hausmann et al., 2016). In addition, shale gas production has become more important, particularly in the United States (EIA, 2015, 2019). However, results of the sensitivity simulations in the present study show that the decrease in the global mean surface $\delta^{13}\text{C}(\text{CH}_4)$ is not achievable with increasing shale gas emissions alone. Instead, the results show that the global mean surface $\delta^{13}\text{C}(\text{CH}_4)$ is very sensitive to changes in biomass burning emissions. The presented approach assumes a very strong decrease in biomass burning emissions, which leads to the observed global mean surface $\delta^{13}\text{C}(\text{CH}_4)$ decline. Although, reduced biomass burning emissions after 2007 are likely (Worden et al., 2017), such a strong decrease is not supported by other studies (Worden et al., 2017; Randerson et al., 2017). Consequently, the biogenic emissions after 2007 must be larger than I assume in the present setup (i.e. 46 % of the additional emissions between 2007 and 2014 due to emissions from livestock, rice farming and landfills). Biogenic sources have in general more negative $\delta^{13}\text{C}(\text{CH}_4)$ signatures than fossil fuel emissions, and might explain the observed global mean surface $\delta^{13}\text{C}(\text{CH}_4)$ decline. A more dominant role of biogenic emissions compared to fossil fuel emissions is also supported by several other studies, e.g. Schwietzke et al. (2016); Schaefer et al. (2016); Nisbet et al. (2019). In addition, a reduced atmospheric oxidation capacity (mainly OH sink) could lead to increasing CH_4 mixing ratios and the decreasing $\delta^{13}\text{C}(\text{CH}_4)$ (Rigby et al., 2017; Turner et al., 2017). The effect of OH onto the global mean surface $\delta^{13}\text{C}(\text{CH}_4)$ is discussed as part of the subsequent research question, see below.

In the presented EMAC setup, the wetland emissions are kept relatively constant after 2007. This is in accordance with findings of Poulter et al. (2017), who suggest no significant contribution of wetland emissions to the renewed global CH_4 increase. In contrast, other studies suggest that wetlands might contribute largely (Nisbet et al., 2019; Rosentreter et al., 2021). Natural emissions are strongly associated with climate feedbacks and wetland emissions will presumably increase as a result of rising temperatures and higher water tables (Gedney et al., 2004; Zhang et al., 2017). The presented EMAC setup has been proven to be a suitable tool for further investigations, which could involve the role of wetlands. Future studies should, however, include updated biomass burning emissions (e.g. GFED 4.1s inventory).

Understanding the contribution of natural and anthropogenic emissions is urgently needed for climate change mitigation strategies and in order to reach policy-relevant temperature targets. Reducing anthropogenic emissions is more feasible than reducing natural emissions. Beyond that, reduced anthropogenic emissions will have a rapid impact on the global methane burden. This in turn, mitigates global warming and presumably lowers the feedbacks on natural wetlands emissions. Consequently, even in the case of large natural emissions, the reduction of anthropogenic emissions should be the target of action.

How does the global OH concentration and its atmospheric distribution influence the global mean surface $\delta^{13}\text{C}(\text{CH}_4)$ signature?

OH is the major sink of CH_4 in the atmosphere and plays an important role in the investigation of the recent methane rise. The atmospheric lifetime of methane mainly depends

on the OH concentration. Since the latter varies with latitudes, methane emitted at different regions of the Earth could have different atmospheric lifetimes. I calculated the tropospheric lifetimes with respect to OH for each individual emission source category (e.g. wetlands boreal, wetlands tropical, fossil fuels, biomass burning) in the presented simulations. As they are emitted at different latitudes, they could contribute differently to the global CH₄ rise and the global mean surface $\delta^{13}\text{C}(\text{CH}_4)$. The calculated mean tropospheric lifetime of all emissions is 9.021 years (for the period between 2008 and 2019). This lies within the range of other reported lifetime estimates (e.g. Prinn et al., 2005; Jöckel et al., 2006; Frank, 2018; Prather et al., 2012; Voulgarakis et al., 2013). The tropospheric lifetimes of the individual emission source categories do not differ significantly. This is due to a rapid and efficient atmospheric transport through regions with different oxidation capacities (i.e. OH concentrations). The results show, that the latitudinal OH distribution does not impact the relative contribution of different emission source categories to the global CH₄ rise and the global mean surface $\delta^{13}\text{C}(\text{CH}_4)$. However, it should be mentioned, that the OH field in the simulation is pre-defined. Consequently, potential feedbacks on the OH concentration were not considered.

The methane oxidation with OH results in an isotopic fractionation of the remaining methane in the atmosphere. In a further sensitivity simulation, I tested the influence of an OH reduction on the global mean surface $\delta^{13}\text{C}(\text{CH}_4)$. Therefore, the methane emissions have been hold constant since 2007. The reduction of OH resulted in a prolonged tropospheric CH₄ lifetime of 0.5 years. The effect of this OH reduction is rather small and does not explain the total decline in the global mean surface $\delta^{13}\text{C}(\text{CH}_4)$.

Since tropospheric OH is the most important sink of CH₄, the applied OH field in global models is crucial for understanding the global CH₄ budget. Nevertheless, atmospheric OH is difficult to measure and highly uncertain in global climate models (Zhao et al., 2020; Nicely et al., 2020). Here, I used pre-defined OH concentrations, which are not subject to any feedbacks. Possible temporal OH variations should be considered in future studies. Moreover, investigations should be carried out with interactive chemistry considering potential feedbacks on the OH concentration.

Bibliography

Allan, W., H. Struthers, and D. C. Lowe

2007. Methane carbon isotope effects caused by atomic chlorine in the marine boundary layer: Global model results compared with Southern Hemisphere measurements. *Journal of Geophysical Research: Atmospheres*, 112(D4).

Amediek, A., G. Ehret, A. Fix, M. Wirth, C. Büdenbender, M. Quatrevalet, C. Kiemle, and C. Gerbig

2017. CHARM-F – a new airborne integrated-path differential-absorption lidar for carbon dioxide and methane observations: measurement performance and quantification of strong point source emissions. *Applied Optics*, 56(18):5182–5197.

Andela, N., D. C. Morton, L. Giglio, Y. Chen, G. R. van der Werf, P. S. Kasibhatla, R. S. DeFries, G. J. Collatz, S. Hantson, S. Kloster, D. Bachelet, M. Forrest, G. Lasslop, F. Li, S. Mangeon, J. R. Melton, C. Yue, and J. T. Randerson

2017. A human-driven decline in global burned area. *Science*, 356(6345):1356–1362.

Bigeleisen, J.

2005. *Isotopic Effects in Chemistry and Biology, Chapter 01: Theoretical Basis of Isotope Effects from an Autobiographical Perspective*, Pp. 1–40.

Bousquet, P., P. Ciais, J. Miller, E. Dlugokencky, D. Hauglustaine, C. Prigent, G. Werf, P. Peylin, E.-G. Brunke, C. Carouge, R. Langenfelds, J. Lathière, F. Papa, M. Ramonet, M. Schmidt, L. Steele, S. Tyler, and J. White

2006. Contribution of anthropogenic and natural sources to atmospheric methane variability. *Nature*, 443:439–443.

Cantrell, C. A., R. E. Shetter, A. H. McDaniel, J. G. Calvert, J. A. Davidson, D. C. Lowe, S. C. Tyler, R. J. Cicerone, and J. P. Greenberg

1990. Carbon kinetic isotope effect in the oxidation of methane by the hydroxyl radical. *Journal of Geophysical Research: Atmospheres*, 95(D13):22455–22462.

Carlson, K., J. Gerber, N. Mueller, M. Herrero, G. MacDonald, K. Brauman, P. Havlík, C. Connell, J. Johnson, S. Saatchi, and P. West

2016. Greenhouse gas emissions intensity of global croplands. *Nature Climate Change*, 7.

- Chanton, J., P. Crill, K. Bartlett, and C. Martens
1989. Amazon Capims (floating grassmats): A source of ^{13}C enriched methane to the troposphere. *Geophysical Research Letters*, 16(8):799–802.
- Chen, J., C. Gerbig, J. Marshall, and K. U. Totsche
2020. Short-term forecasting of regional biospheric CO_2 fluxes in Europe using a light-use-efficiency model (vprm, mpi-bgc version 1.2). *Geoscientific Model Development*, 13(9):4091–4106.
- Cicerone, R. and R. Oremland
1988. Biogeochemical aspects of atmospheric methane. *Global Biogeochemical Cycles*, 2:299.
- Crippa, M., D. Guizzardi, M. Muntean, E. Schaaf, F. Dentener, J. Aardenne, S. Monni, U. Doering, J. Oliver, V. Pagliari, and G. Janssens-Maenhout
2018. Gridded emissions of air pollutants for the period 1970–2012 within EDGAR v4.3.2. *Earth System Science Data*, 10:1987–2013.
- Crippa, M., E. Solazzo, G. Huang, D. Guizzardi, E. Koffi, M. Muntean, C. Schieberle, R. Friedrich, and G. Janssens-Maenhout
2020. High resolution temporal profiles in the Emissions Database for Global Atmospheric Research. *Scientific data*, 7(1):121.
- Crutzen, P. J.
1995. Introductory lecture. Overview of tropospheric chemistry: developments during the past quarter century and a look ahead. *Faraday Discuss.*, 100:1–21.
- Curry, C.
2007. Modeling the soil consumption of atmospheric methane at the global scale. *Global Biogeochemical Cycles*, 21.
- Curry, C.
2009. The consumption of atmospheric methane by soil in a simulated future climate. *Biogeosciences*, 6.
- Dean, J. F., J. J. Middelburg, T. Röckmann, R. Aerts, L. G. Blauw, M. Egger, M. S. M. Jetten, A. E. E. de Jong, O. H. Meisel, O. Rasigraf, C. P. Slomp, M. H. in't Zandt, and A. J. Dolman
2018. Methane Feedbacks to the Global Climate System in a Warmer World. *Reviews of Geophysics*, 56(1):207–250.
- Dee, D. P., S. M. Uppala, A. J. Simmons, P. Berrisford, P. Poli, S. Kobayashi, U. Andrae, M. A. Balmaseda, G. Balsamo, P. Bauer, P. Bechtold, A. C. M. Beljaars, L. van de Berg, J. Bidlot, N. Bormann, C. Delsol, R. Dragani, M. Fuentes, A. J. Geer, L. Haimberger, S. B. Healy, H. Hersbach, E. V. Hólm, L. Isaksen, P. Kållberg, M. Köhler, M. Matricardi, A. P. McNally, B. M. Monge-Sanz, J.-J. Morcrette, B.-K. Park, C. Peubey, P. de Rosnay,

- C. Tavolato, J.-N. Thépaut, and F. Vitart
2011. The ERA-Interim reanalysis: configuration and performance of the data assimilation system. *Quarterly Journal of the Royal Meteorological Society*, 137(656):553–597.
- Dentener, F., S. Kinne, T. Bond, O. Boucher, J. Cofala, S. Generoso, P. Ginoux, S. Gong, J. J. Hoelzemann, A. Ito, L. Marelli, J. E. Penner, J.-P. Putaud, C. Textor, M. Schulz, G. R. van der Werf, and J. Wilson
2006. Emissions of primary aerosol and precursor gases in the years 2000 and 1750 prescribed data-sets for AeroCom. *Atmospheric Chemistry and Physics*, 6(12):4321–4344.
- Dlugokencky, E., A. Crotwell, J. Mund, M. Crotwell, and K. Thoning
2020. Atmospheric Methane Dry Air Mole Fractions from the NOAA GML Carbon Cycle Cooperative Global Air Sampling Network, 1983-2019, Version: 2020-07.
- Dlugokencky, E. J., K. A. Masaire, P. M. Lang, P. P. Tans, L. P. Steele, and E. G. Nisbet
1994. A dramatic decrease in the growth rate of atmospheric methane in the northern hemisphere during 1992. *Geophysical Research Letters*, 21(1):45–48.
- Dlugokencky, E. J., E. G. Nisbet, R. Fisher, and D. Lowry
2011. Global atmospheric methane: budget, changes and dangers. *Philosophical Transactions of the Royal Society A: Mathematical, Physical and Engineering Sciences*, 369(1943):2058–2072.
- Doerr, S. H. and C. Santín
2016. Global trends in wildfire and its impacts: perceptions versus realities in a changing world. *Philosophical Transactions of the Royal Society B: Biological Sciences*, 371(1696):20150345.
- Dutton, E. G. and J. R. Christy
1992. Solar radiative forcing at selected locations and evidence for global lower tropospheric cooling following the eruptions of El Chichón and Pinatubo. *Geophysical Research Letters*, 19(23):2313–2316.
- E-PRTR
2014. European Pollutant Release and Transfer Register. Retrieved from <http://prtr.eea.europa.eu>, last access Feb 08, 2017.
- E-PRTR
2016. European Pollutant Release and Transfer Register. Retrieved from <http://prtr.eea.europa.eu>, last access Nov 07, 2018.
- Earl, N. and I. Simmonds
2018. Spatial and Temporal Variability and Trends in 2001–2016 Global Fire Activity. *Journal of Geophysical Research: Atmospheres*, 123(5):2524–2536.

Ehleringer, J. and T. Cerling

2002. C3 and C4 Photosynthesis. *Encyclopedia of Global Environmental Change*, 2.

Ehleringer, J., T. Cerling, and B. Helliker

1997. C-4 photosynthesis, atmospheric CO₂ and climate. *Oecologia*, 112:285–299.

EIA

2015. Energy Information Administration, US Department of Energy: Shale gas and tight oil are only commercially produced in just four countries, available at <https://www.eia.gov/todayinenergy/detail.php?id=19991>, last access May 2021.

EIA

2019. EIA, Energy Information Administration, US Department of Energy: EIA adds new play production data to shale gas and tight oil reports, available at <https://www.eia.gov/todayinenergy/detail.php?id=38372>, last access May 2021.

Eichinger, R., P. Jöckel, S. Brinkop, M. Werner, and S. Lossow

2015. Simulation of the isotopic composition of stratospheric water vapour – Part 1: Description and evaluation of the EMAC model. *Atmospheric Chemistry and Physics*, 15(10):5537–5555.

Etheridge, D. M., L. P. Steele, R. J. Francey, and R. L. Langenfelds

1998. Atmospheric methane between 1000 A.D. and present: Evidence of anthropogenic emissions and climatic variability. *Journal of Geophysical Research: Atmospheres*, 103(D13):15979–15993.

Etminan, M., G. Myhre, E. J. Highwood, and K. P. Shine

2016. Radiative forcing of carbon dioxide, methane, and nitrous oxide: A significant revision of the methane radiative forcing. *Geophysical Research Letters*, 43(24):12,614–12,623.

Farquhar, G. D., J. R. Ehleringer, and K. T. Hubick

1989. Carbon Isotope Discrimination and Photosynthesis. *Annual Review of Plant Physiology and Plant Molecular Biology*, 40(1):503–537.

Feinberg, A. I., A. Coulon, A. Stenke, S. Schwietzke, and T. Peter

2018. Isotopic source signatures: Impact of regional variability on the $\delta^{13}\text{C}$ trend and spatial distribution. *Atmospheric Environment*, 174:99 – 111.

Fiehn, A., J. Kostinek, M. Eckl, T. Klausner, M. Gałkowski, J. Chen, C. Gerbig, T. Röckmann, H. Maazallahi, M. Schmidt, P. Korbeń, J. Neęki, P. Jagoda, N. Wildmann, C. Mallaun, R. Bun, A.-L. Nickl, P. Jöckel, A. Fix, and A. Roiger

2020. Estimating CH₄, CO₂ and CO emissions from coal mining and industrial activities in the Upper Silesian Coal Basin using an aircraft-based mass balance approach. *Atmospheric Chemistry and Physics*, 20(21):12675–12695.

- Filges, A., C. Gerbig, H. Chen, H. Franke, C. Klaus, and A. Jordan
2015. The IAGOS-core greenhouse gas package: a measurement system for continuous airborne observations of CO₂, CH₄, H₂O and CO. *Tellus Series B Chemical and Physical Meteorology B*, 67:27989.
- Fischer, H., M. Behrens, M. Bock, U. Richter, J. Schmitt, L. Louergue, J. Chappellaz, R. Spahni, T. Blunier, M. Leuenberger, and T. Stocker
2008. Changing boreal methane sources and constant biomass burning during the last termination. *Nature*, 452 (7189):864 – 867. Publisher: Nature Publishing Group.
- Fletcher, S. E. M. and H. Schaefer
2019. Rising methane: A new climate challenge. *Science*, 364(6444):932–933.
- Franco, B., E. Mahieu, L. K. Emmons, Z. A. Tzompa-Sosa, E. V. Fischer, K. Sudo, B. Bovy, S. Conway, D. Griffin, J. W. Hannigan, K. Strong, and K. A. Walker
2016. Evaluating ethane and methane emissions associated with the development of oil and natural gas extraction in North America. *Environmental Research Letters*, 11(4):044010.
- Frank, F. I.
2018. Atmospheric methane and its isotopic composition in a changing climate, available at: <http://nbn-resolving.de/urn:nbn:de:bvb:19-225789>, last access August 2021.
- Fry, B.
2006. *Isotope Notation and Measurement*. In: *Stable Isotope Ecology*. Springer, New York, NY. https://doi.org/10.1007/0-387-33745-8_2.
- Gałkowski, M., A. Fiehn, J. Swolkien, M. Stanisavljevic, P. Korben, M. Menoud, J. Necki, A. Roiger, T. Röckmann, C. Gerbig, and A. Fix
2021a. Emissions of CH₄ and CO₂ over the Upper Silesian Coal Basin (Poland) and its vicinity.
- Gałkowski, M., A. Jordan, M. Rothe, J. Marshall, F.-T. Koch, J. Chen, A. Agustí-Panareda, A. Fix, and C. Gerbig
2021b. In situ observations of greenhouse gases over Europe during the comet 1.0 campaign aboard the halo aircraft. *Atmospheric Measurement Techniques*, 14(2):1525–1544.
- Ganesan, A. L., A. C. Stell, N. Gedney, E. Comyn-Platt, G. Hayman, M. Rigby, B. Poulter, and E. R. C. Hornibrook
2018. Spatially Resolved Isotopic Source Signatures of Wetland Methane Emissions. *Geophysical Research Letters*, 45(8):3737–3745.
- Garny, H., R. Walz, M. Nützel, and T. Birner
2020. Extending the Modular Earth Submodel System (MESSy v2.54) model hierarchy: the ECHAM/MESSy Idealized (EMIL) model setup. *Geoscientific Model Development*, 13(11):5229–5257.

- Gedney, N., P. M. Cox, and C. Huntingford
2004. Climate feedback from wetland methane emissions. *Geophysical Research Letters*, 31(20).
- Gerilowski, K., A. Tretner, T. Krings, M. Buchwitz, P. P. Bertagnolio, F. Belemzov, J. Erzinger, J. P. Burrows, and H. Bovensmann
2011. MAMAP – a new spectrometer system for column-averaged methane and carbon dioxide observations from aircraft: instrument description and performance analysis. *Atmospheric Measurement Techniques*, 4(2):215–243.
- Giglio, L., J. T. Randerson, and G. R. van der Werf
2013. Analysis of daily, monthly, and annual burned area using the fourth-generation global fire emissions database (GFED4). *Journal of Geophysical Research: Biogeosciences*, 118(1):317–328.
- Gromov, S., C. A. M. Brenninkmeijer, and P. Jöckel
2018. A very limited role of tropospheric chlorine as a sink of the greenhouse gas methane. *Atmospheric Chemistry and Physics*, 18(13):9831–9843.
- Gupta, M. L., M. P. McGrath, R. J. Cicerone, F. S. Rowland, and M. Wolfsberg
1997. $^{12}\text{C}/^{13}\text{C}$ kinetic isotope effects in the reactions of CH_4 with OH and Cl. *Geophysical Research Letters*, 24(22):2761–2764.
- Hausmann, P., R. Sussmann, and D. Smale
2016. Contribution of oil and natural gas production to renewed increase in atmospheric methane (2007–2014): top-down estimate from ethane and methane column observations. *Atmospheric Chemistry and Physics*, 16(5):3227–3244.
- Helmig, D., S. Rossabi, J. Hueber, P. Tans, S. Montzka, K. Masarie, K. Thoning, C. Plass-Duelmer, A. Claude, L. Carpenter, A. Lewis, S. Punjabi, S. Reimann, M. Vollmer, R. Steinbrecher, J. Hannigan, L. Emmons, E. Mahieu, B. Franco, and A. Pozzer
2016. Reversal of global atmospheric ethane and propane trends largely due to US oil and natural gas production. *Nature Geoscience*, 9.
- Höök, M., J. Li, K. Johansson, and S. Snowden
2012. Growth Rates of Global Energy Systems and Future Outlooks. *Natural Resources Research*, 22:23–41.
- Hornibrook, E.
2009. The Stable Carbon Isotope Composition of Methane Produced and Emitted from Northern Peatlands. *Washington DC American Geophysical Union Geophysical Monograph Series*, 184:187–203.
- Howarth, R. W.
2019. Ideas and perspectives: is shale gas a major driver of recent increase in global atmospheric methane? *Biogeosciences*, 16(15):3033–3046.

- Jackson, R. B., M. Saunio, P. Bousquet, J. G. Canadell, B. Poulter, A. R. Stavert, P. Bergamaschi, Y. Niwa, A. Segers, and A. Tsuruta
2020. Increasing anthropogenic methane emissions arise equally from agricultural and fossil fuel sources. *Environmental Research Letters*, 15(7):071002.
- Janssens-Maenhout, G., M. Crippa, D. Guizzardi, M. Muntean, and E. Schaaf
2013. Emissions Database for Global Atmospheric Research, version v4.2 FT2010 (grid-maps). European Commission, Joint Research Centre.
- Jöckel, P., A. Kerkweg, A. Pozzer, R. Sander, H. Tost, H. Riede, A. Baumgaertner, S. Gromov, and B. Kern
2010. Development cycle 2 of the Modular Earth Submodel System (MESSy2). *Geoscientific Model Development*, 3(2):717–752.
- Jöckel, P., R. Sander, A. Kerkweg, H. Tost, and J. Lelieveld
2005. Technical Note: The Modular Earth Submodel System (MESSy) - a new approach towards Earth System Modeling. *Atmospheric Chemistry and Physics*, 5(2):433–444.
- Jöckel, P., H. Tost, A. Pozzer, C. Brühl, J. Buchholz, L. Ganzeveld, P. Hoor, A. Kerkweg, M. G. Lawrence, R. Sander, B. Steil, G. Stiller, M. Tanarhte, D. Taraborrelli, J. van Aardenne, and J. Lelieveld
2006. The atmospheric chemistry general circulation model ECHAM5/MESSy1: consistent simulation of ozone from the surface to the mesosphere. *Atmospheric Chemistry and Physics*, 6(12):5067–5104.
- Jöckel, P., H. Tost, A. Pozzer, M. Kunze, O. Kirner, C. A. M. Brenninkmeijer, S. Brinkop, D. S. Cai, C. Dyroff, J. Eckstein, F. Frank, H. Garny, K.-D. Gottschaldt, P. Graf, V. Grewe, A. Kerkweg, B. Kern, S. Matthes, M. Mertens, S. Meul, M. Neumaier, M. Nützel, S. Oberländer-Hayn, R. Ruhnke, T. Runde, R. Sander, D. Scharffe, and A. Zahn
2016. Earth System Chemistry integrated Modelling (ESCiMo) with the Modular Earth Submodel System (MESSy) version 2.51. *Geoscientific Model Development*, 9(3):1153–1200.
- Kaiser, J. C., J. Hendricks, M. Righi, N. Riemer, R. A. Zaveri, S. Metzger, and V. Aquila
2014. The MESSy aerosol submodel MADE3 (v2.0b): description and a box model test. *Geoscientific Model Development*, 7(3):1137–1157.
- Keeling, C. D.
1958. The concentration and isotopic abundances of atmospheric carbon dioxide in rural areas. *Geochimica et Cosmochimica Acta*, 13(4):322–334.
- Keeling, C. D.
1961. The concentration and isotopic abundances of carbon dioxide in rural and marine air. *Geochimica et Cosmochimica Acta*, 24(3):277–298.

- Kerkweg, A., J. Buchholz, L. Ganzeveld, A. Pozzer, H. Tost, and P. Jöckel
2006a. Technical Note: An implementation of the dry removal processes DRY DEPosition and SEDImentation in the Modular Earth Submodel System (MESSy). *Atmospheric Chemistry and Physics*, 6(12):4617–4632.
- Kerkweg, A. and P. Jöckel
2012a. The 1-way on-line coupled atmospheric chemistry model system MECO(n) – Part 1: Description of the limited-area atmospheric chemistry model COSMO/MESSy. *Geoscientific Model Development*, 5(1):87–110.
- Kerkweg, A. and P. Jöckel
2012b. The 1-way on-line coupled atmospheric chemistry model system MECO(n) – Part 2: On-line coupling with the Multi-Model-Driver (MMD). *Geoscientific Model Development*, 5(1):111–128.
- Kerkweg, A. and P. Jöckel
2015. The infrastructure MESSy submodels GRID (v1.0) and IMPORT (v1.0). *Geoscientific Model Development Discussions*, 8:8607–8633.
- Kerkweg, A., R. Sander, H. Tost, and P. Jöckel
2006b. Technical note: Implementation of prescribed (OFFLEM), calculated (ONLEM), and pseudo-emissions (TNUDGE) of chemical species in the Modular Earth Submodel System (MESSy). *Atmospheric Chemistry and Physics*, 6(11):3603–3609.
- Kirschke, S., P. Bousquet, P. Ciais, M. Saunois, J. G. Canadell, E. J. Dlugokencky, P. Bergamaschi, D. Bergmann, D. R. Blake, L. Bruhwiler, P. Cameron-Smith, S. Castaldi, F. Chevallier, L. Feng, A. Fraser, M. Heimann, E. L. Hodson, S. Houweling, B. Josse, P. J. Fraser, P. B. Krummel, J.-F. Lamarque, R. L. Langenfelds, C. Le Quéré, V. Naik, S. O’Doherty, P. I. Palmer, I. Pison, D. Plummer, B. Poulter, R. G. Prinn, M. Rigby, B. Ringeval, M. Santini, M. Schmidt, D. T. Shindell, I. J. Simpson, R. Spahni, L. P. Steele, S. A. Strode, K. Sudo, S. Szopa, G. R. van der Werf, A. Voulgarakis, M. van Weele, R. F. Weiss, J. E. Williams, and G. Zeng
2013. Three decades of global methane sources and sinks. *Nature Geosci.*, 6:813–823.
- Kiyosu, Y.
1983. Hydrogen isotopic compositions of hydrogen and methane from some volcanic areas in northeastern Japan. *Earth and Planetary Science Letters*, 62(1):41–52.
- Kostinek, J., A. Roiger, K. J. Davis, C. Sweeney, J. P. DiGangi, Y. Choi, B. Baier, F. Hase, J. Groß, M. Eckl, T. Klausner, and A. Butz
2019. Adaptation and performance assessment of a quantum and interband cascade laser spectrometer for simultaneous airborne in situ observation of CH₄, C₂H₆, CO₂, CO and N₂O. *Atmospheric Measurement Techniques*, 12(3):1767–1783.

- Kostinek, J., A. Roiger, M. Eckl, A. Fiehn, A. Luther, N. Wildmann, T. Klausner, A. Fix, C. Knote, A. Stohl, and A. Butz
2021. Estimating Upper Silesian coal mine methane emissions from airborne in situ observations and dispersion modeling. *Atmospheric Chemistry and Physics*, 21(11):8791–8807.
- Kotarba, M. J.
2001. Composition and origin of coalbed gases in the Upper Silesian and Lublin basins, Poland. *Organic Geochemistry*, 32(1):163–180.
- Krautwurst, S., K. Gerilowski, J. Borchardt, N. Wildmann, M. Galkowski, J. Swolkien, J. Marshall, A. Fiehn, A. Roiger, T. Ruhtz, C. Gerbig, J. Necki, J. P. Burrows, A. Fix, and H. Bovensmann
2021. Quantification of CH₄ coal mining emissions in Upper Silesia by passive airborne remote sensing observations with the MAMAP instrument during CoMet. *Atmospheric Chemistry and Physics Discussions*, 2021:1–39.
- Kunze, M., M. Godolt, U. Langematz, J. Grenfell, A. Hamann-Reinus, and H. Rauer
2014. Investigating the early Earth faint young Sun problem with a general circulation model. *Planetary and Space Science*, 98:77–92. Planetary evolution and life.
- Lawrence, C. and H. Mao
2019. Anthropogenic and Natural Factors Affecting Trends in Atmospheric Methane in Barrow, Alaska. *Atmosphere*, 10:187.
- Lelieveld, J., P. Crutzen, and F. Dentener
1998. Changing concentration, lifetime and climate forcing of atmospheric methane. *Tellus B*, 50.
- Lelieveld, J., F. J. Dentener, W. Peters, and M. C. Krol
2004. On the role of hydroxyl radicals in the self-cleansing capacity of the troposphere. *Atmospheric Chemistry and Physics*, 4(9/10):2337–2344.
- Luther, A., R. Kleinschek, L. Scheidweiler, S. Defratyka, M. Stanisavljevic, A. Forstmaier, A. Dandocsi, S. Wolff, D. Dubravica, N. Wildmann, J. Kostinek, P. Jöckel, A.-L. Nickl, T. Klausner, F. Hase, M. Frey, J. Chen, F. Dietrich, J. Necki, J. Swolkien, A. Fix, A. Roiger, and A. Butz
2019. Quantifying CH₄ emissions from hard coal mines using mobile sun-viewing Fourier transform spectrometry. *Atmospheric Measurement Techniques*, 12(10):5217–5230.
- Mailler, S., D. Khvorostyanov, and L. Menut
2013. Impact of the vertical emission profiles on background gas-phase pollution simulated from the EMEP emissions over Europe. *Atmospheric Chemistry and Physics*, 13(12):5987–5998.

- Maxfield, P., E. Hornibrook, N. Dildar, and R. Evershed
2009. Stable isotope probing of the physical and biological controls that influence the fate and isotopic composition of carbon derived from the terrestrial methane sink. *Environmental Science Technology*, 42(21):7824–7830.
- McKinney, C. R., J. M. McCrea, S. Epstein, H. A. Allen, and H. A. Urey
1950. Improvements in mass spectrometers for the measurement of small differences in isotope abundance ratios. *Review of Scientific Instruments*, 21:724–730.
- Mertens, M., A. Kerkweg, P. Jöckel, H. Tost, and C. Hofmann
2016. The 1-way on-line coupled model system MECO(n) – Part 4: Chemical evaluation (based on MESSy v2.52). *Geoscientific Model Development*, 9(10):3545–3567.
- Mikaloff-Fletcher, S., P. Tans, L. Bruhwiler, J. Miller, M. Heimann, and M. Fletcher
2004. CH₄ sources estimated from atmospheric observations of CH₄ and its ¹³C/¹²C isotopic ratios: 1. Inverse modeling of source processes. *Global Biogeochemical Cycles*, 18.
- Milkov, A., S. Schwietzke, G. Allen, O. Sherwood, and G. Etiope
2020. Using global isotopic data to constrain the role of shale gas production in recent increases in atmospheric methane. *Scientific Reports*, 10(1):4199.
- Miller, S., A. Michalak, R. Detmers, O. Hasekamp, L. Bruhwiler, and S. Schwietzke
2019. China’s coal mine methane regulations have not curbed growing emissions. *Nature Communications*, 10.
- Monteil, G., S. Houweling, E. J. Dlugokenky, G. Maenhout, B. H. Vaughn, J. W. C. White, and T. Rockmann
2011. Interpreting methane variations in the past two decades using measurements of CH₄ mixing ratio and isotopic composition. *Atmospheric Chemistry and Physics*, 11(17):9141–9153.
- Mook, W., J. Bommerson, and W. Staverman
1974. Carbon isotope fractionation between dissolved bicarbonate and gaseous carbon dioxide. *Earth and Planetary Science Letters*, 22(2):169–176.
- Mook, W. G.
2000. Environmental isotopes in the hydrological cycle. *Technical Documents in Hydrology*, UNESCO, 1(39).
- Myhre, G., D. Shindell, F.-M. BrÄ©on, W. Collins, J. Fuglestedt, J. Huang, D. Koch, J.-F. Lamarque, D. Lee, B. Mendoza, T. Nakajima, A. Robock, G. Stephens, T. Takemura, and H. Zhang
2013. *Anthropogenic and natural radiative forcing*, Pp. 659–740. Cambridge, UK: Cambridge University Press.

- Nair, H., M. E. Summers, C. E. Miller, and Y. L. Yung
2005. Isotopic fractionation of methane in the martian atmosphere. *Icarus*, 175(1):32–35.
- Nicely, J. M., B. N. Duncan, T. F. Hanisco, G. M. Wolfe, R. J. Salawitch, M. Deushi, A. S. Haslerud, P. Jöckel, B. Josse, D. E. Kinnison, A. Klekociuk, M. E. Manyin, V. Marécal, O. Morgenstern, L. T. Murray, G. Myhre, L. D. Oman, G. Pitari, A. Pozzer, I. Quaglia, L. E. Revell, E. Rozanov, A. Stenke, K. Stone, S. Strahan, S. Tilmes, H. Tost, D. M. Westervelt, and G. Zeng
2020. A machine learning examination of hydroxyl radical differences among model simulations for CCMI-1. *Atmospheric Chemistry and Physics*, 20(3):1341–1361.
- Nickl, A.-L., M. Mertens, A. Roiger, A. Fix, A. Amediek, A. Fiehn, C. Gerbig, M. Galkowski, A. Kerkweg, T. Klausner, M. Eckl, and P. Jöckel
2020. Hindcasting and forecasting of regional methane from coal mine emissions in the Upper Silesian Coal Basin using the online nested global regional chemistry–climate model MECO(n) (MESSy v2.53). *Geoscientific Model Development*, 13(4):1925–1943.
- Nisbet, E. G., E. J. Dlugokencky, and P. Bousquet
2014. Methane on the Rise—Again. *Science*, 343(6170):493–495.
- Nisbet, E. G., E. J. Dlugokencky, M. R. Manning, D. Lowry, R. E. Fisher, J. L. France, S. E. Michel, J. B. Miller, J. W. C. White, B. Vaughn, P. Bousquet, J. A. Pyle, N. J. Warwick, M. Cain, R. Brownlow, G. Zazzeri, M. Lanoisellé, A. C. Manning, E. Gloor, D. E. J. Worthy, E.-G. Brunke, C. Labuschagne, E. W. Wolff, and A. L. Ganesan
2016. Rising atmospheric methane: 2007–2014 growth and isotopic shift. *Global Biogeochemical Cycles*, 30(9):1356–1370.
- Nisbet, E. G., M. R. Manning, E. J. Dlugokencky, R. E. Fisher, D. Lowry, S. E. Michel, C. L. Myhre, S. M. Platt, G. Allen, P. Bousquet, R. Brownlow, M. Cain, J. L. France, O. Hermansen, R. Hossaini, A. E. Jones, I. Levin, A. C. Manning, G. Myhre, J. A. Pyle, B. H. Vaughn, N. J. Warwick, and J. W. C. White
2019. Very Strong Atmospheric Methane Growth in the 4 Years 2014–2017: Implications for the Paris Agreement. *Global Biogeochemical Cycles*, 33(3):318–342.
- Pandey, S., S. Houweling, M. Krol, I. Aben, N. Nechita-Banda, K. Thoning, T. Röckmann, Y. Yin, A. Segers, and E. Dlugokencky
2019. Influence of Atmospheric Transport on Estimates of Variability in the Global Methane Burden. *Geophysical Research Letters*, 46:2302–2311.
- Poulter, B., P. Bousquet, J. G. Canadell, P. Ciais, A. Peregon, M. Saunois, V. K. Arora, D. J. Beerling, V. Brovkin, C. D. Jones, F. Joos, N. Gedney, A. Ito, T. Kleinen, C. D. Koven, K. McDonald, J. R. Melton, C. Peng, S. Peng, C. Prigent, R. Schroeder, W. J. Riley, M. Saito, R. Spahni, H. Tian, L. Taylor, N. Viovy, D. Wilton, A. Wiltshire, X. Xu, B. Zhang, Z. Zhang, and Q. Zhu
2017. Global wetland contribution to 2000–2012 atmospheric methane growth rate dynamics. *Environmental Research Letters*, 12(9):094013.

- Pozzer, A., P. Jöckel, B. Kern, and H. Haak
2011. The Atmosphere-Ocean General Circulation Model EMAC-MPIOM. *Geoscientific Model Development*, 4(3):771–784.
- Prather, M., C. D. Holmes, and J. Hsu
2012. Reactive greenhouse gas scenarios: Systematic exploration of uncertainties and the role of atmospheric chemistry. *Geophysical Research Letters*, 39(9).
- Pringle, K., H. Tost, S. Message, B. Steil, D. Giannadaki, A. Nenes, C. Fountoukis, S. P. V. E, and L. J
2010. Description and evaluation of GMXe: A new aerosol submodel for global simulations (v1). *Geoscientific Model Development*, 3:391–412.
- Prinn, R. G., J. Huang, R. F. Weiss, D. M. Cunnold, P. J. Fraser, P. G. Simmonds, A. McCulloch, C. Harth, S. Reimann, P. Salameh, S. O’Doherty, R. H. J. Wang, L. W. Porter, B. R. Miller, and P. B. Krummel
2005. Evidence for variability of atmospheric hydroxyl radicals over the past quarter century. *Geophysical Research Letters*, 32(7).
- Quay, P., J. Stutsman, D. Wilbur, A. Snover, E. Dlugokencky, and T. Brown
1999. The isotopic composition of atmospheric methane. *Global Biogeochemical Cycles*, 13(2):445–461.
- Randerson, J., G. Van Der Werft, L. Giglio, G. Collatz, and P. Kasibhatla
2017. Global Fire Emissions Database, Version 4.1 (GFEDv4).
- Randerson, J. T., G. R. van der Werf, G. J. Collatz, L. Giglio, C. J. Still, P. Kasibhatla, J. B. Miller, J. W. C. White, R. S. DeFries, and E. S. Kasischke
2005. Fire emissions from C3 and C4 vegetation and their influence on interannual variability of atmospheric CO₂ and $\delta^{13}\text{CO}_2$. *Global Biogeochemical Cycles*, 19(2).
- Ravishankara, A. R.
1988. Kinetics of Radical Reactions in the Atmospheric Oxidation of CH₄. *Annual Review of Physical Chemistry*, 39(1):367–394.
- Rigby, M., A. J. Manning, and R. G. Prinn
2012. The value of high-frequency, high-precision methane isotopologue measurements for source and sink estimation. *Journal of Geophysical Research: Atmospheres*, 117(D12).
- Rigby, M., S. A. Montzka, R. G. Prinn, J. W. C. White, D. Young, S. O’Doherty, M. F. Lunt, A. L. Ganesan, A. J. Manning, P. G. Simmonds, P. K. Salameh, C. M. Harth, J. Mühle, R. F. Weiss, P. J. Fraser, L. P. Steele, P. B. Krummel, A. McCulloch, and S. Park
2017. Role of atmospheric oxidation in recent methane growth. *Proceedings of the National Academy of Sciences*, 114(21):5373–5377.

- Rockel, B., A. Will, and A. Hense
2008. The Regional Climate Model COSMO-CLM (CCLM). *Meteorologische Zeitschrift*, 17(4):347–348.
- Roeckner, E., R. Brokopf, M. Esch, M. Giorgetta, S. Hagemann, L. Kornblueh, E. Manzini, U. Schlese, and U. Schulzweida
2006. Sensitivity of Simulated Climate to Horizontal and Vertical Resolution in the ECHAM5 Atmosphere Model. *Journal of Climate*, 19(16):3771–3791.
- Roeckner, E., T. Siebert, and J. Feichter
1995. Climatic response to anthropogenic sulfate forcing simulated with a general circulation model. *Aerosol Forcing of Climate*, Pp. 349–362.
- Rosentreter, J., A. Borges, B. Deemer, M. Holgerson, S. Liu, C. Song, J. Melack, P. Raymond, C. Duarte, G. Allen, D. Olefeldt, B. Poulter, T. Battin, and B. Eyre
2021. Half of global methane emissions come from highly variable aquatic ecosystem sources. *Nature Geoscience*, 14(4):225–230.
- Sander, R., A. Baumgaertner, S. Gromov, H. Harder, P. Jöckel, A. Kerkweg, D. Kubistin, E. Regelin, H. Riede, A. Sandu, D. Taraborrelli, H. Tost, and Z.-Q. Xie
2011. The atmospheric chemistry box model CAABA/MECCA-3.0. *Geoscientific Model Development*, 4(2):373–380.
- Sander, R., P. Jöckel, O. Kirner, A. T. Kunert, J. Landgraf, and A. Pozzer
2014. The photolysis module JVAL-14, compatible with the MESSy standard, and the JVal PreProcessor (JVPP). *Geoscientific Model Development*, 7(6):2653–2662.
- Sander, R., A. Kerkweg, P. Jöckel, and J. Lelieveld
2005. Technical note: The new comprehensive atmospheric chemistry module MECCA. *Atmospheric Chemistry and Physics*, 5(2):445–450.
- Saueressig, G., P. Bergamaschi, J. N. Crowley, H. Fischer, and G. W. Harris
1995. Carbon kinetic isotope effect in the reaction of CH₄ with Cl atoms. *Geophysical Research Letters*, 22(10):1225–1228.
- Saueressig, G., P. Bergamaschi, J. N. Crowley, H. Fischer, and G. W. Harris
1996. D/H kinetic isotope effect in the reaction CH₄+Cl. *Geophysical Research Letters*, 23(24):3619–3622.
- Saueressig, G., J. N. Crowley, P. Bergamaschi, C. Brühl, C. A. M. Brenninkmeijer, and H. Fischer
2001. Carbon 13 and D kinetic isotope effects in the reactions of CH₄ with O(1 D) and OH: New laboratory measurements and their implications for the isotopic composition of stratospheric methane. *Journal of Geophysical Research: Atmospheres*, 106(D19):23127–23138.

- Saunio, M., P. Bousquet, B. Poulter, A. Peregon, P. Ciais, J. G. Canadell, E. J. Dlugokencky, G. Etiope, D. Bastviken, S. Houweling, G. Janssens-Maenhout, F. N. Tubiello, S. Castaldi, R. B. Jackson, M. Alexe, V. K. Arora, D. J. Beerling, P. Bergamaschi, D. R. Blake, G. Brailsford, V. Brovkin, L. Bruhwiler, C. Crevoisier, P. Crill, K. Covey, C. Curry, C. Frankenberg, N. Gedney, L. Höglund-Isaksson, M. Ishizawa, A. Ito, F. Joos, H.-S. Kim, T. Kleinen, P. Krummel, J.-F. Lamarque, R. Langenfelds, R. Locatelli, T. Machida, S. Maksyutov, K. C. McDonald, J. Marshall, J. R. Melton, I. Morino, V. Naik, S. O'Doherty, F.-J. W. Parmentier, P. K. Patra, C. Peng, S. Peng, G. P. Peters, I. Pison, C. Prigent, R. Prinn, M. Ramonet, W. J. Riley, M. Saito, M. Santini, R. Schroeder, I. J. Simpson, R. Spahni, P. Steele, A. Takizawa, B. F. Thornton, H. Tian, Y. Tohjima, N. Viovy, A. Voulgarakis, M. van Weele, G. R. van der Werf, R. Weiss, C. Wiedinmyer, D. J. Wilton, A. Wiltshire, D. Worthy, D. Wunch, X. Xu, Y. Yoshida, B. Zhang, Z. Zhang, and Q. Zhu
2016. The global methane budget 2000–2012. *Earth System Science Data*, 8(2):697–751.
- Saunio, M., A. R. Stavert, B. Poulter, P. Bousquet, J. G. Canadell, R. B. Jackson, P. A. Raymond, E. J. Dlugokencky, S. Houweling, P. K. Patra, P. Ciais, V. K. Arora, D. Bastviken, P. Bergamaschi, D. R. Blake, G. Brailsford, L. Bruhwiler, K. M. Carlson, M. Carrol, S. Castaldi, N. Chandra, C. Crevoisier, P. M. Crill, K. Covey, C. L. Curry, G. Etiope, C. Frankenberg, N. Gedney, M. I. Hegglin, L. Höglund-Isaksson, G. Hugelius, M. Ishizawa, A. Ito, G. Janssens-Maenhout, K. M. Jensen, F. Joos, T. Kleinen, P. B. Krummel, R. L. Langenfelds, G. G. Laruelle, L. Liu, T. Machida, S. Maksyutov, K. C. McDonald, J. McNorton, P. A. Miller, J. R. Melton, I. Morino, J. Müller, F. Murguía-Flores, V. Naik, Y. Niwa, S. Noce, S. O'Doherty, R. J. Parker, C. Peng, S. Peng, G. P. Peters, C. Prigent, R. Prinn, M. Ramonet, P. Regnier, W. J. Riley, J. A. Rosentreter, A. Segers, I. J. Simpson, H. Shi, S. J. Smith, L. P. Steele, B. F. Thornton, H. Tian, Y. Tohjima, F. N. Tubiello, A. Tsuruta, N. Viovy, A. Voulgarakis, T. S. Weber, M. van Weele, G. R. van der Werf, R. F. Weiss, D. Worthy, D. Wunch, Y. Yin, Y. Yoshida, W. Zhang, Z. Zhang, Y. Zhao, B. Zheng, Q. Zhu, Q. Zhu, and Q. Zhuang
2020. The global methane budget 2000–2017. *Earth System Science Data*, 12(3):1561–1623.
- Schaefer, H., S. E. M. Fletcher, C. Veidt, K. R. Lassey, G. W. Brailsford, T. M. Bromley, E. J. Dlugokencky, S. E. Michel, J. B. Miller, I. Levin, D. C. Lowe, R. J. Martin, B. H. Vaughn, and J. W. C. White
2016. A 21st-century shift from fossil-fuel to biogenic methane emissions indicated by $^{13}\text{CH}_4$. *Science*, 352(6281):80–84.
- Schwietzke, S., O. Sherwood, L. Bruhwiler, J. Miller, G. Etiope, E. Dlugokencky, S. Englund Michel, V. A. Arling, B. Vaughn, J. White, and P. P. Tans
2016. Upward revision of global fossil fuel methane emissions based on isotope database. *Nature*, 538:88–91.
- Shackleton, N. J.

1974. Attainment of isotopic equilibrium between ocean water and the benthonic foraminifera genus *Uvigerina*: isotopic changes in the ocean during the last glacial.
- Sherwood, O. A., S. Schwietzke, V. A. Arling, and G. Etiope
2017. Global Inventory of Gas Geochemistry Data from Fossil Fuel, Microbial and Burning Sources, version 2017. *Earth System Science Data*, 9(2):639–656.
- Snover, A. K. and P. D. Quay
2000. Hydrogen and carbon kinetic isotope effects during soil uptake of atmospheric methane. *Global Biogeochemical Cycles*, 14(1):25–39.
- Snover, A. K., P. D. Quay, and W. M. Hao
2000. The D/H content of methane emitted from biomass burning. *Global Biogeochemical Cycles*, 14(1):11–24.
- Solomon, S., K. Rosenlof, R. Portmann, J. Daniel, S. Davis, T. Sanford, and G.-K. Plattner
2010. Contributions of Stratospheric Water Vapor to Decadal Changes in the Rate of Global Warming. *Science (New York, N.Y.)*, 327:1219–23.
- Spahni, R., R. Wania, L. Neef, M. van Weele, I. Pison, P. Bousquet, C. Frankenberg, P. N. Foster, F. Joos, I. C. Prentice, and P. van Velthoven
2011. Constraining global methane emissions and uptake by ecosystems. *Biogeosciences*, 8(6):1643–1665.
- Sperlich, P., N. A. M. Uitslag, J. M. Richter, M. Rothe, H. Geilmann, C. van der Veen, T. Röckmann, T. Blunier, and W. A. Brand
2016. Development and evaluation of a suite of isotope reference gases for methane in air. *Atmospheric Measurement Techniques*, 9(8):3717–3737.
- Stecher, L., F. Winterstein, M. Dameris, P. Jöckel, M. Ponater, and M. Kunze
2021. Slow feedbacks resulting from strongly enhanced atmospheric methane mixing ratios in a chemistry–climate model with mixed-layer ocean. *Atmospheric Chemistry and Physics*, 21(2):731–754.
- Still, C., J. Berry, G. Collatz, and R. DeFries
2009. ISLSCP II C4 Vegetation Percentage. Available on-line [<http://daac.ornl.gov/>] from Oak Ridge National Laboratory Distributed Active Archive Center, Oak Ridge, Tennessee, USA.
- Taylor, K. E.
2001. Summarizing multiple aspects of model performance in a single diagram. *Journal of Geophysical Research: Atmospheres*, 106(D7):7183–7192.
- Thompson, R. L., E. G. Nisbet, I. Pisso, A. Stohl, D. Blake, E. J. Dlugokencky, D. Helmig, and J. W. C. White
2018. Variability in Atmospheric Methane From Fossil Fuel and Microbial Sources Over the Last Three Decades. *Geophysical Research Letters*, 45(20):11,499–11,508.

- Thompson, R. L., A. Stohl, L. X. Zhou, E. Dlugokencky, Y. Fukuyama, Y. Tohjima, S.-Y. Kim, H. Lee, E. G. Nisbet, R. E. Fisher, D. Lowry, R. F. Weiss, R. G. Prinn, S. O'Doherty, D. Young, and J. W. C. White
2015. Methane emissions in East Asia for 2000–2011 estimated using an atmospheric Bayesian inversion. *Journal of Geophysical Research: Atmospheres*, 120(9):4352–4369.
- Tost, H., P. Jöckel, A. Kerkweg, R. Sander, and J. Lelieveld
2006. Technical note: A new comprehensive SCAVenging submodel for global atmospheric chemistry modelling. *Atmospheric Chemistry and Physics*, 6(3):565–574.
- Turco, R.
1975. Photodissociation rates in the atmosphere below 100km. *Geophysical Surveys*, 2:153–192.
- Turner, A. J., C. Frankenberg, P. O. Wennberg, and D. J. Jacob
2017. Ambiguity in the causes for decadal trends in atmospheric methane and hydroxyl. *Proceedings of the National Academy of Sciences*, 114(21):5367–5372.
- Turner, A. J., D. J. Jacob, J. Benmergui, S. C. Wofsy, J. D. Maasakkers, A. Butz, O. Hasekamp, and S. C. Biraud
2016. A large increase in U.S. methane emissions over the past decade inferred from satellite data and surface observations. *Geophysical Research Letters*, 43(5):2218–2224.
- van Lierop, P., E. Lindquist, S. Sathyapala, and G. Franceschini
2015. Global forest area disturbance from fire, insect pests, diseases and severe weather events. *Forest Ecology and Management*, 352:78–88. Changes in Global Forest Resources from 1990 to 2015.
- Voulgarakis, A., V. Naik, J.-F. Lamarque, D. T. Shindell, P. J. Young, M. J. Prather, O. Wild, R. D. Field, D. Bergmann, P. Cameron-Smith, I. Cionni, W. J. Collins, S. B. Dalsøren, R. M. Doherty, V. Eyring, G. Faluvegi, G. A. Folberth, L. W. Horowitz, B. Josse, I. A. MacKenzie, T. Nagashima, D. A. Plummer, M. Righi, S. T. Rumbold, D. S. Stevenson, S. A. Strode, K. Sudo, S. Szopa, and G. Zeng
2013. Analysis of present day and future OH and methane lifetime in the ACCMIP simulations. *Atmospheric Chemistry and Physics*, 13(5):2563–2587.
- Warwick, N. J., S. Bekki, K. S. Law, E. G. Nisbet, and J. A. Pyle
2002. The impact of meteorology on the interannual growth rate of atmospheric methane. *Geophysical Research Letters*, 29(20):8–1–8–4.
- Werner, R. A. and W. A. Brand
2001. Referencing strategies and techniques in stable isotope ratio analysis. *Rapid Communications in Mass Spectrometry*, 15(7):501–519.
- White, J., B. Vaughn, and S. Michel
2018. University of Colorado, Institute of Arctic and Alpine Research (INSTAAR), Stable

- Isotopic Composition of Atmospheric Methane (^{13}C) from NOAA ESRL Carbon Cycle Cooperative Global Air Sampling Network, 1998-2017, Version: 2018-09-24.
- Whiticar, M., E. Faber, and M. Schoell
1986. Biogenic methane formation in marine and freshwater environments: CO_2 reduction vs. acetate fermentation—Isotope evidence. *Geochimica et Cosmochimica Acta*, 50(5):693–709.
- Whiticar, M. and H. Schaefer
2007. Constraining past global tropospheric methane budgets with carbon and hydrogen isotope ratios in ice. *Philosophical Transactions of the Royal Society A: Mathematical, Physical and Engineering Sciences*, 365(1856):1793–1828.
- Whiticar, M. J.
1999. Carbon and hydrogen isotope systematics of bacterial formation and oxidation of methane. *Chemical Geology*, 161(1):291 – 314.
- Wildmann, N., E. Päschke, A. Roiger, and C. Mallaun
2020. Towards improved turbulence estimation with Doppler wind lidar velocity-azimuth display (VAD) scans. *Atmospheric Measurement Techniques*, 13(8):4141–4158.
- Winterstein, F. and P. Jöckel
2021. Methane chemistry in a nutshell – the new submodels CH₄ (v1.0) and TRSYNC (v1.0) in MESSy (v2.54.0). *Geoscientific Model Development*, 14(2):661–674.
- Winterstein, F., F. Tanalski, P. Jöckel, M. Dameris, and M. Ponater
2019. Implication of strongly increased atmospheric methane concentrations for chemistry–climate connections. *Atmospheric Chemistry and Physics*, 19(10):7151–7163.
- Wolff, S., G. Ehret, C. Kiemle, A. Amediek, M. Quatrevalet, M. Wirth, and A. Fix
2021. Determination of the emission rates of CO_2 point sources with airborne lidar. *Atmospheric Measurement Techniques*, 14(4):2717–2736.
- Worden, J., A. Bloom, and S. e. a. Pandey
2017. Reduced biomass burning emissions reconcile conflicting estimates of the post-2006 atmospheric methane budget. *Nature Communications*, 8(2227).
- Wyższy Urząd Gorniczy 2014, .
Retrieved from <http://www.wug.gov.pl/download/5710.pdf>, last access Feb 08, 2017.
- Zazzeri, G., D. Lowry, R. Fisher, J. France, M. Lanoisellé, and E. Nisbet
2015. Plume mapping and isotopic characterisation of anthropogenic methane sources. *Atmospheric Environment*, 110.
- Zazzeri, G., D. Lowry, R. E. Fisher, J. L. France, M. Lanoisellé, B. F. J. Kelly, J. M. Necki, C. P. Iverach, E. Ginty, M. Zimnoch, A. Jasek, and E. G. Nisbet
2016. Carbon isotopic signature of coal-derived methane emissions to the atmosphere:

- from coalification to alteration. *Atmospheric Chemistry and Physics*, 16(21):13669–13680.
- Zhang, Z., N. E. Zimmermann, A. Stenke, X. Li, E. L. Hodson, G. Zhu, C. Huang, and B. Poulter
2017. Emerging role of wetland methane emissions in driving 21st century climate change. *Proceedings of the National Academy of Sciences*, 114(36):9647–9652.
- Zhao, Y., M. Saunois, P. Bousquet, X. Lin, A. Berchet, M. I. Hegglin, J. G. Canadell, R. B. Jackson, M. Deushi, P. Jöckel, D. Kinnison, O. Kirner, S. Strode, S. Tilmes, E. J. Dlugokencky, and B. Zheng
2020. On the role of trend and variability in the hydroxyl radical (OH) in the global methane budget. *Atmospheric Chemistry and Physics*, 20(21):13011–13022.
- Zimmermann, P. H., C. A. M. Brenninkmeijer, A. Pozzer, P. Jöckel, F. Winterstein, A. Zahn, S. Houweling, and J. Lelieveld
2020. Model simulations of atmospheric methane (1997–2016) and their evaluation using NOAA and AGAGE surface and IAGOS-CARIBIC aircraft observations. *Atmospheric Chemistry and Physics*, 20(9):5787–5809.

Appendix A

Appendix

A.1 Additional material: Hind- and forecasting of regional methane emissions with MECO(n)

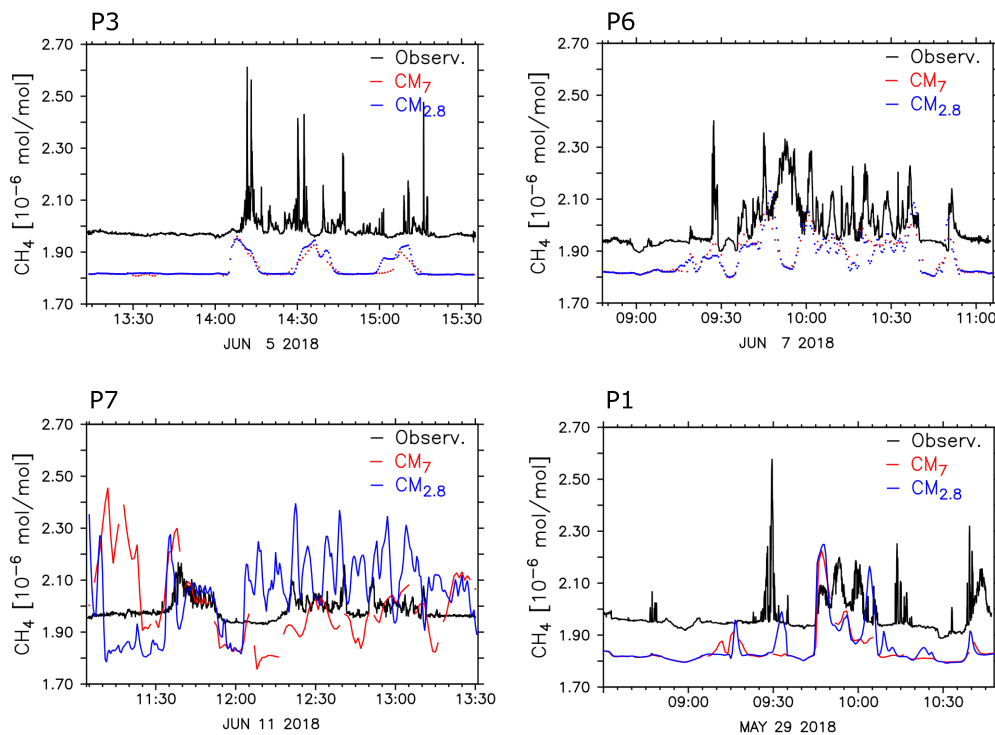


Figure A.1: Comparison of the S4D model output ($\text{CH}_4\text{-FX}$ tracer) and observations sampled along the flight tracks of P3, P6, P7 and P1. Black: observed CH_4 mixing ratios, measured in-situ on board D-FDLR. Red and blue: CH_4 mixing ratios simulated by the CM7 and CM2.8 model instance, respectively.

A.2 Additional material: Simulation of $\delta^{13}C(CH_4)$ in coal mining emissions with the regional model MECO(3)

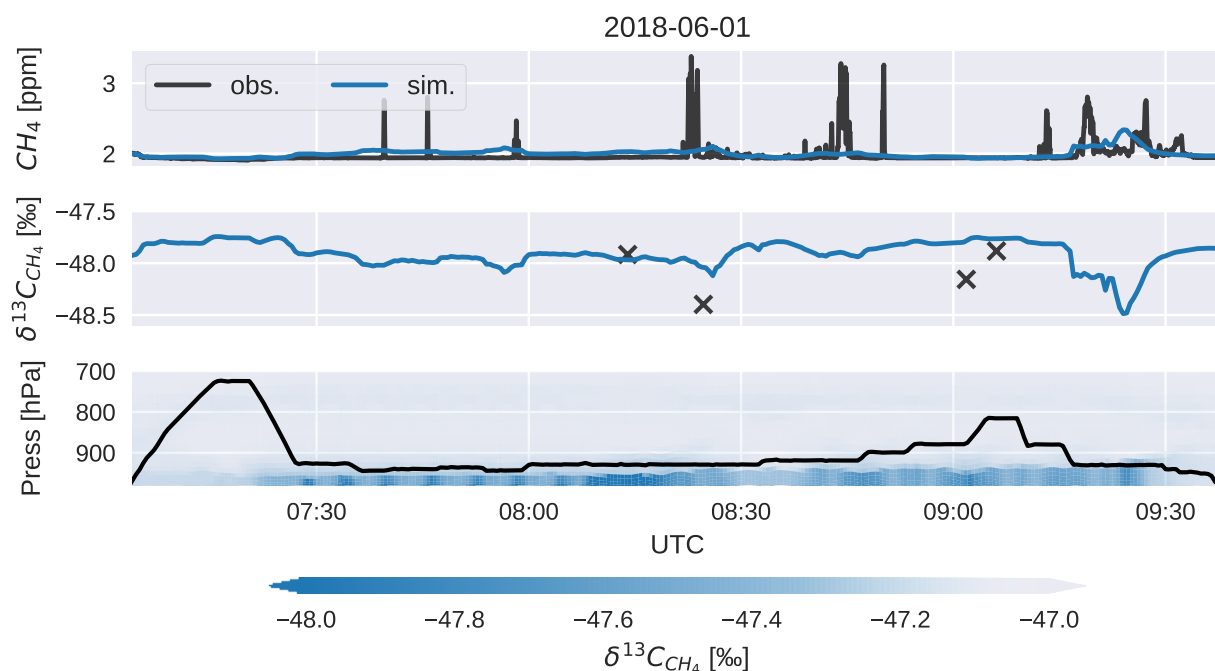


Figure A.2: Comparison of the ANA.ISO simulation (-51 ‰) and the observations along the flight track of P2. Upper panel: CH_4 mixing ratios of in-situ measurements (black) and simulated CH_4 FX tracer (blue). Middle panel: simulated $\delta^{13}C$ (blue) and $\delta^{13}C$ of flask samples (black). Note that a constant value of -0.63 ‰ is added to the simulation results. Lower panel: Flight height (black) and vertical distribution of simulated $\delta^{13}C$ along the flight track.

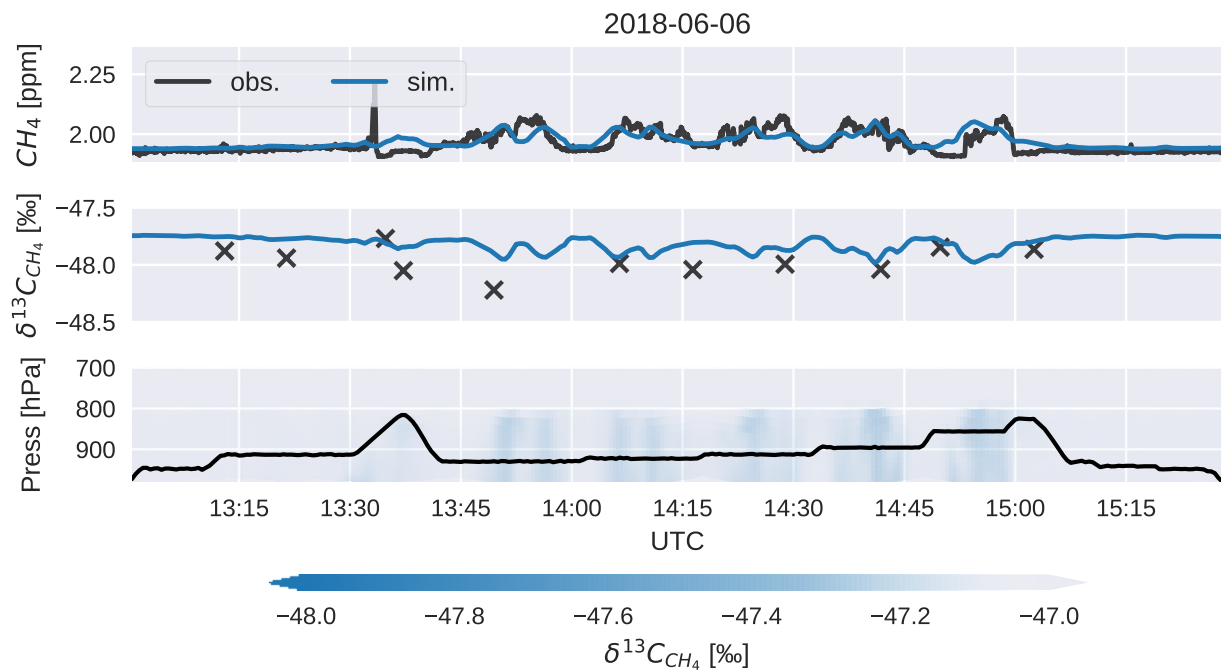


Figure A.3: Similar to Figure A.2, but for flight track of P5.

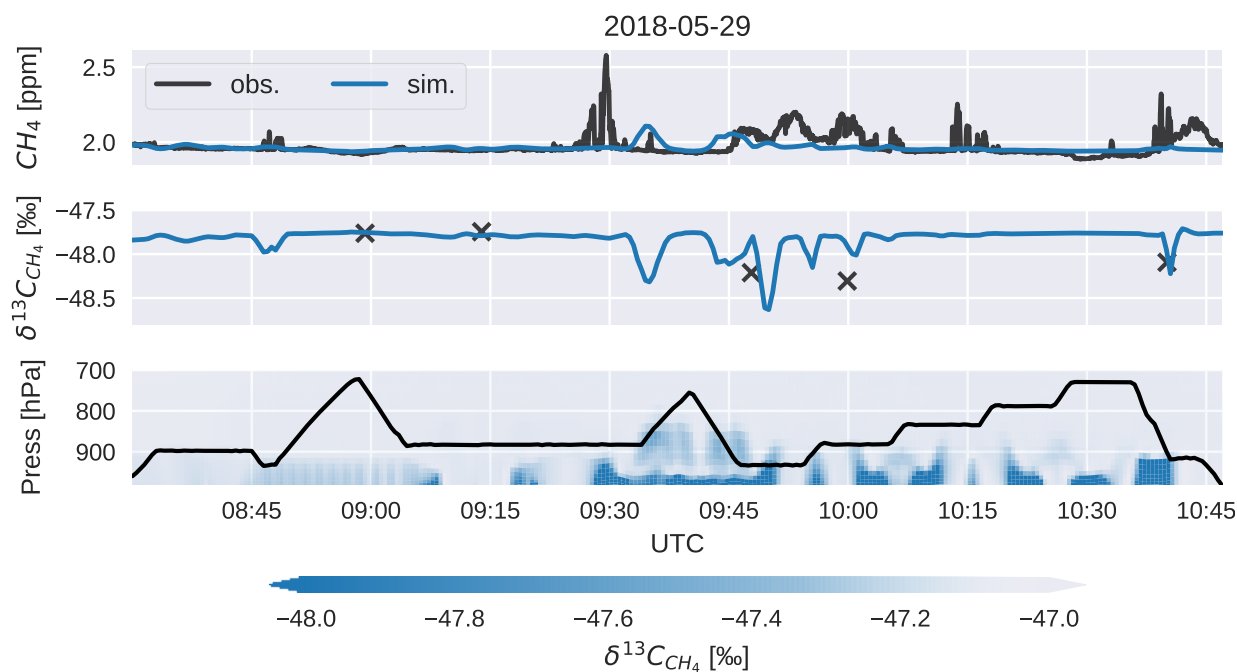


Figure A.4: Similar to Figure A.2, but for ANA.ISO simulation #3 (USCB) and flight track of P1.

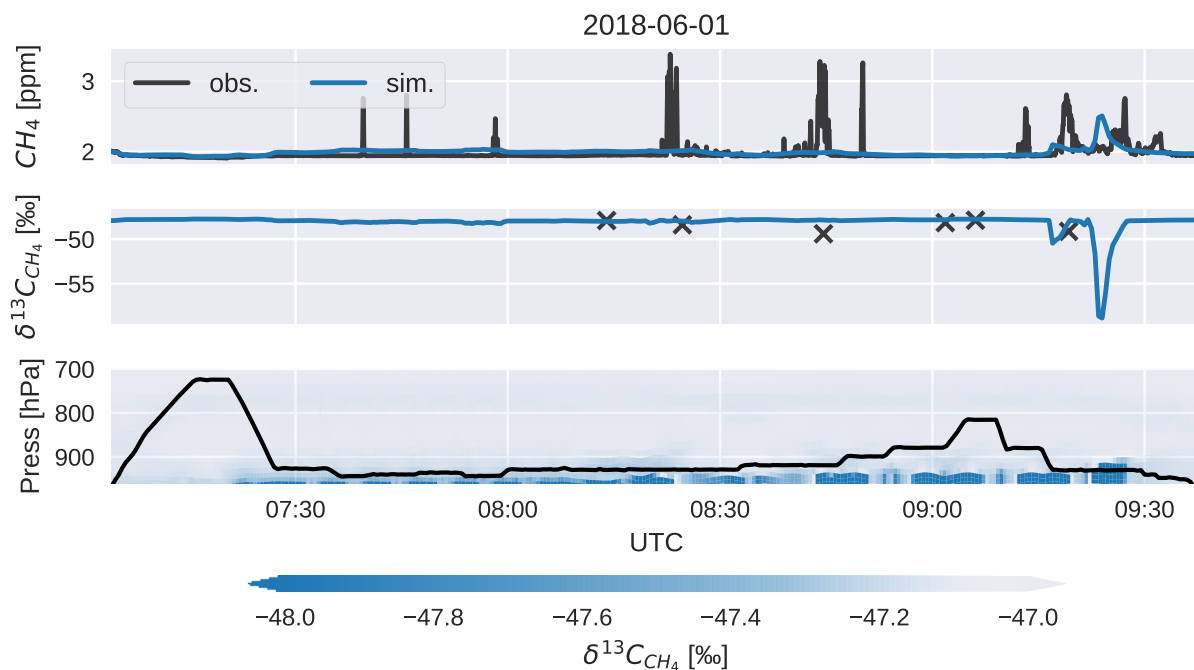


Figure A.5: Similar to Figure A.2, but for ANA.ISO simulation #3 (USCB) and flight track of P2.

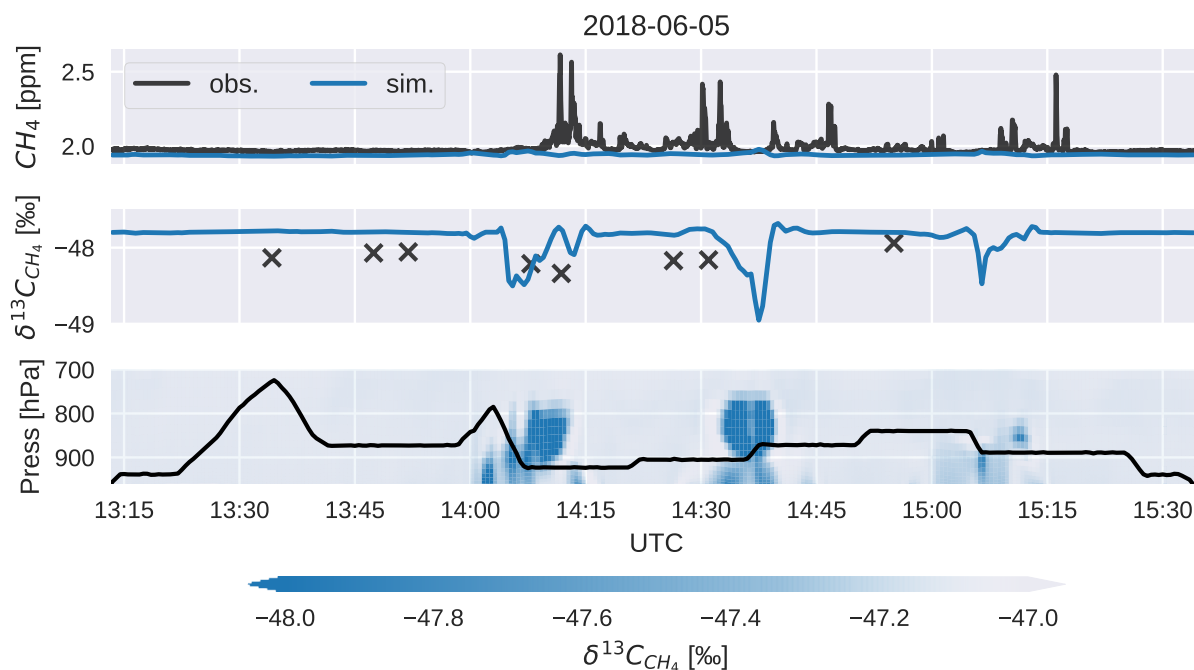


Figure A.6: Similar to Figure A.2, but for ANA.ISO simulation #3 (USCB) and flight track of P3.

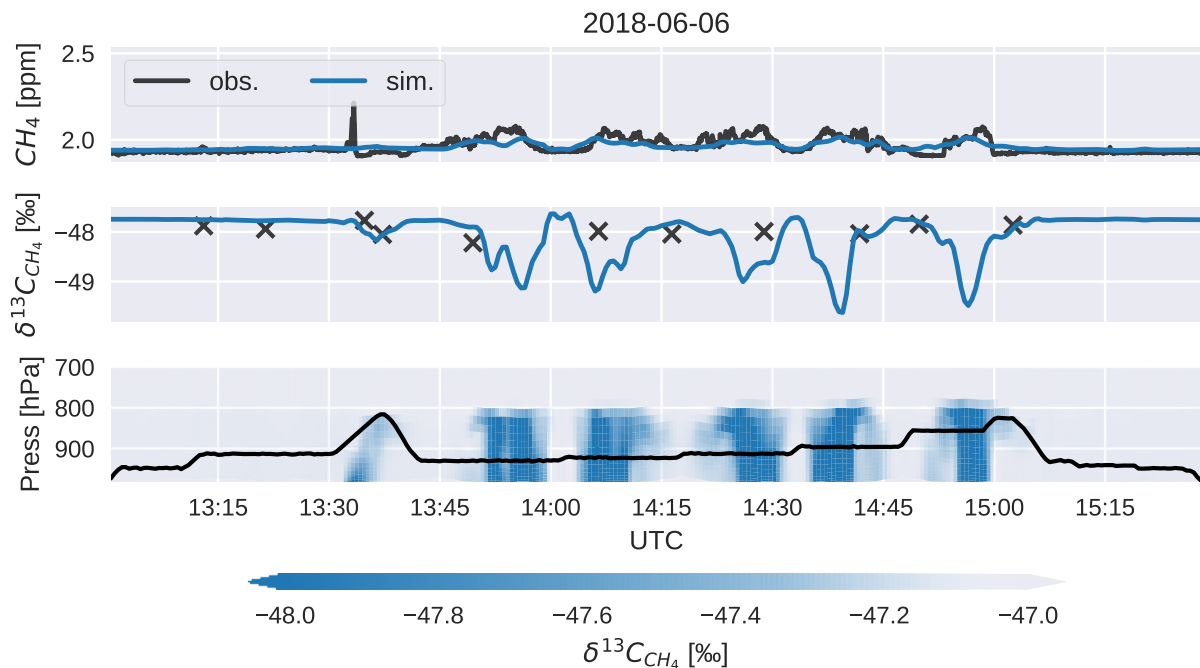


Figure A.7: Similar to Figure A.2, but for ANA.ISO simulation #3 (USCB) and flight track of P5.

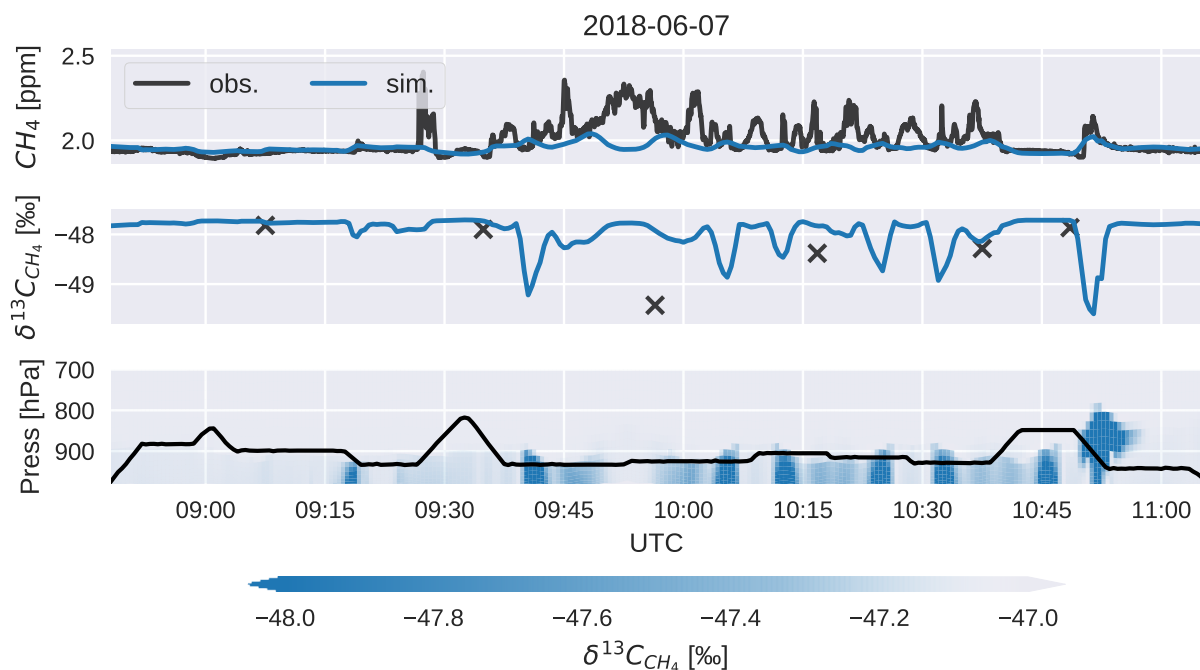


Figure A.8: Similar to Figure A.2, but for ANA.ISO simulation #3 (USCB) and flight track of P6.

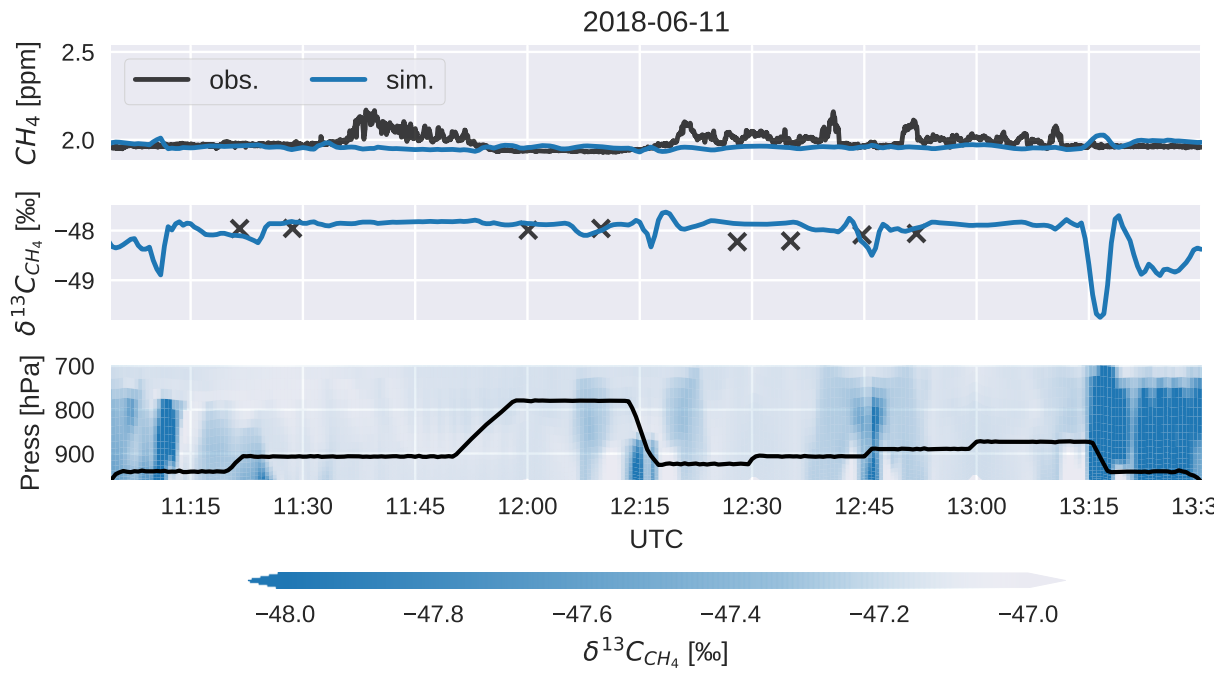


Figure A.9: Similar to Figure A.2, but for ANA.ISO simulation #3 (USCB) and flight track of P7.

A.3 Additional material: Simulation of the recent methane increase and the corresponding $\delta^{13}\text{C}(\text{CH}_4)$

A.3.1 Model setup

Calculation of the number of rare and abundant molecules to split emission fluxes according to their specific $\delta^{13}\text{C}(\text{CH}_4)$ and $\delta\text{D}(\text{CH}_4)$ signatures.

Anthropogenic emissions of the EDGAR v5.0 inventory are provided in $\text{kg}(\text{CH}_4) \text{ m}^{-2} \text{ s}^{-1}$ and need to be converted into to molecules $\text{m}^{-2} \text{ s}^{-1}$.

Equations for $\delta^{13}\text{C}(\text{CH}_4)$:

$$n_{12\text{CH}_4,i} = \frac{(\text{flux}_i * A)}{Mw_{12\text{CH}_4} + (\delta^{13}\text{C}_i/1000 + 1) * R_C * Mw_{13\text{CH}_4}} \quad (\text{A.1})$$

$$n_{13\text{CH}_4,i} = (\delta^{13}\text{C}_i/1000 + 1) * R_C * n_{12\text{CH}_4,i} \quad (\text{A.2})$$

Equations for $\delta\text{D}(\text{CH}_4)$:

$$q_i = R_D * (\delta\text{D}_i/1000 + 1) \quad (\text{A.3})$$

$$n_{\text{CH}_4\text{D}0,i} = \frac{(\text{flux}_i * N_A) * (1 - 3 * q_i)}{(Mw_{\text{CH}_4\text{D}0} * (1 - 3 * q_i) + (4 * Mw_{\text{CH}_3\text{D}} + q_i))} \quad (\text{A.4})$$

$$n_{\text{CH}_3\text{D},i} = \frac{4 * n_{\text{CH}_4\text{D}0,i} * q_i}{1 - 3 * q_i} \quad (\text{A.5})$$

With n^*_i being the number of molecules of the specific isotopologues per grid i , flux_i being the methane flux per grid in g , Mw^* being the molar weights of the specific molecules, N_A being Avogadro's constant, and R_C and R_D being the isotopic ratios of the two standards VPDB and VSMOW, respectively.

Bias calculation for initial $\delta^{13}\text{C}$ adjustment

The SDISO-base-c and SDISO-base-v simulations are initialized in order to account for the bias between the simulated and observed $\delta^{13}\text{C}$ signatures after the spin up time. Instead of reducing the bias, initial conditions are scaled to correspond to this bias from the beginning of the simulations (as explained in Chapter 6). As a reference I use the ground-based observational global mean $\delta^{13}\text{C}$ calculated by Schaefer et al. (2016)) between 2000 and 2007. The bias is defined as the median of the differences between simulated (test simulations) and observed surface global mean $\delta^{13}\text{C}$ during the respective time period.

A.3.2 SDISO-base-c and SDISO-base-v discussion

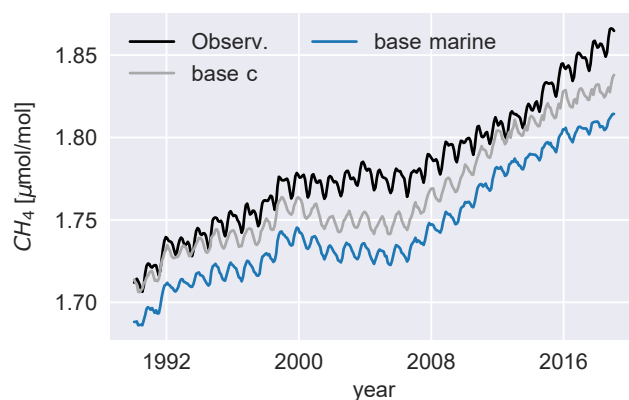


Figure A.10: Comparison of the simulated SDISO-base-c global averaged surface CH_4 mixing ratios (gray), the simulated SDISO-base-c global averaged marine surface CH_4 mixing ratios (blue) and the observed global averaged marine near surface CH_4 mixing ratios (black) taken from Dlugokencky et al. (2020).

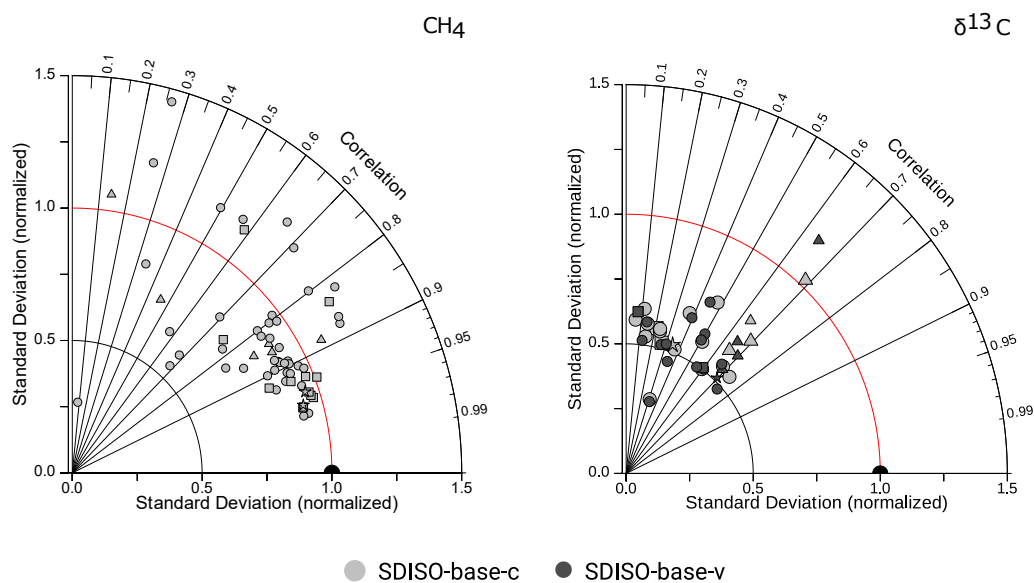


Figure A.11: Taylor diagrams summarizing the time series comparison of observed and simulated methane mixing ratios (left panel) and $\delta^{13}\text{C}$ (right panel) simulated by SDISO-base-c / -v at specific NOAA stations. Different shapes refer to the different zones of latitudes on Northern Hemisphere (NH) and Southern Hemisphere (SH). Triangle: high latitudes on NH, circle: mid and low latitudes on NH, square: mid and low latitudes on SH, star: high latitudes on SH.

Mid latitudes - NH

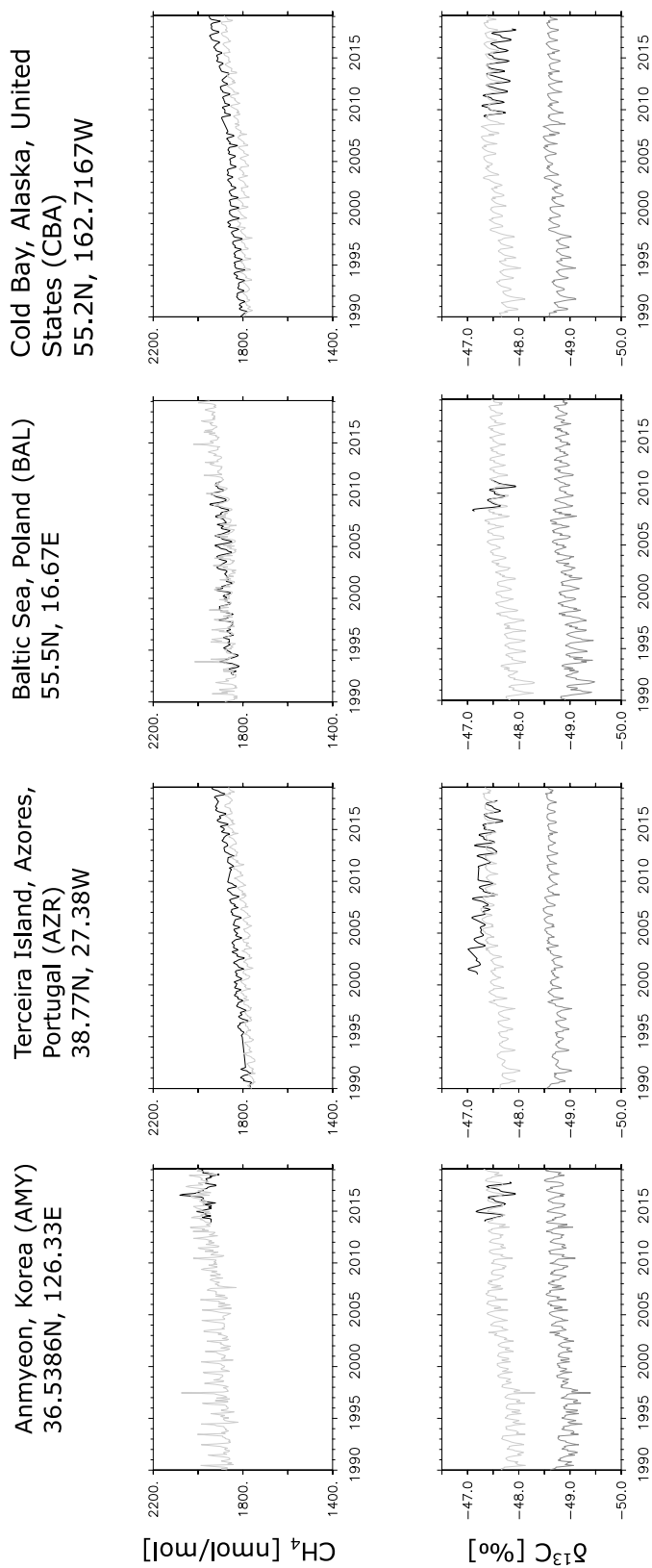


Figure A.12: Comparison of the SDISO-base-c (in light gray) and SDISO-base-v (in dark gray) monthly averaged CH_4 mixing ratios and $\delta^{13}\text{C}$ with observations (in black) at different mid latitudinal sampling sites on the Northern Hemisphere. Note that the SDISO-base-c and the SDISO-base-v simulations only differ in their $\delta^{13}\text{C}$. CH_4 mixing ratios are the same.

Mid latitudes - NH

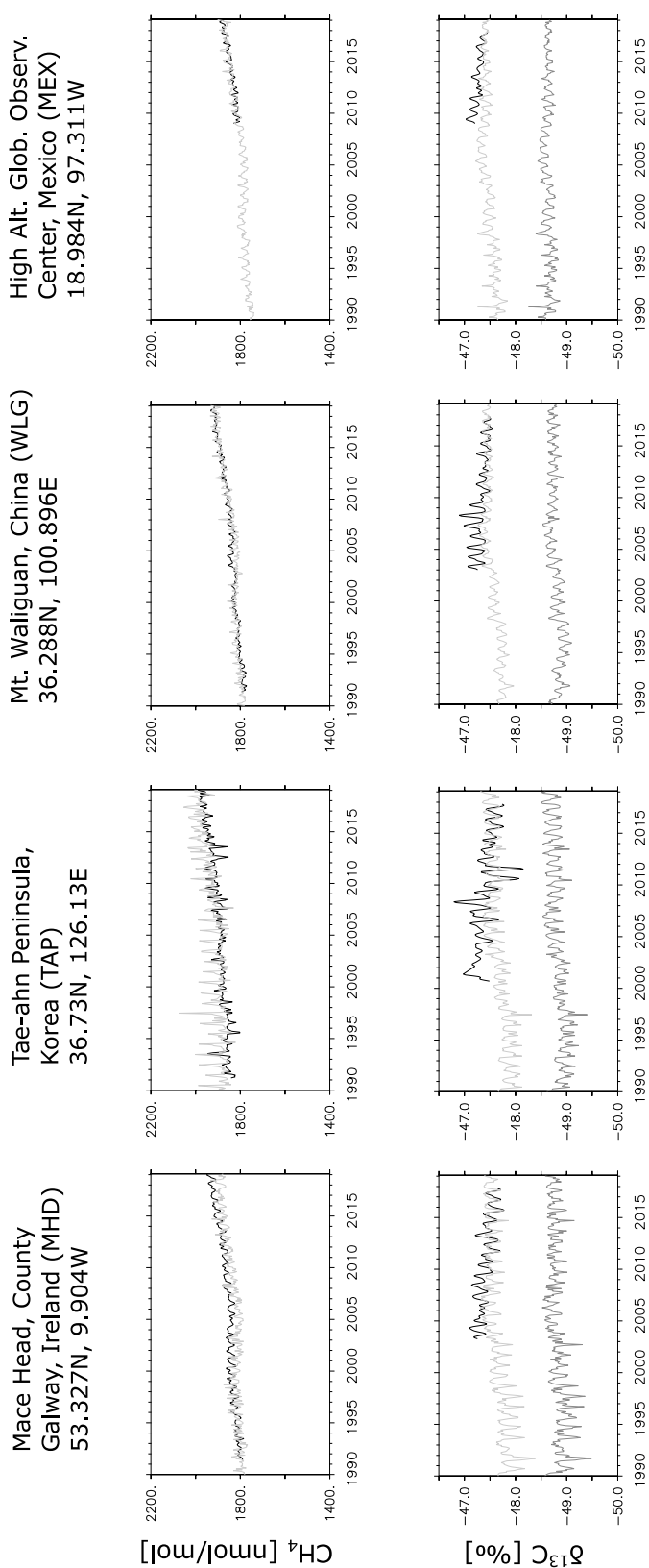
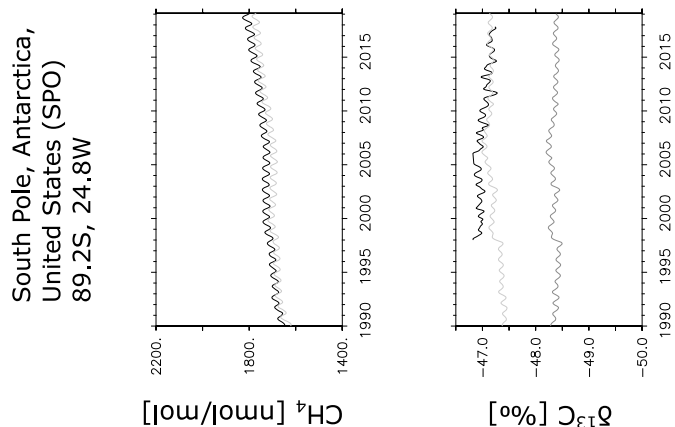


Figure A.13: Comparison of the SDISO-base-c (in light gray) and SDISO-base-v (in dark gray) monthly averaged CH_4 mixing ratios and $\delta^{13}\text{C}$ with observations (in black) at different mid latitudinal sampling sites on the Northern Hemisphere. Note that the SDISO-base-c and the SDISO-base-v simulations only differ in their $\delta^{13}\text{C}$. CH_4 mixing ratios are the same.

High latitudes - SH



Mid latitudes - SH

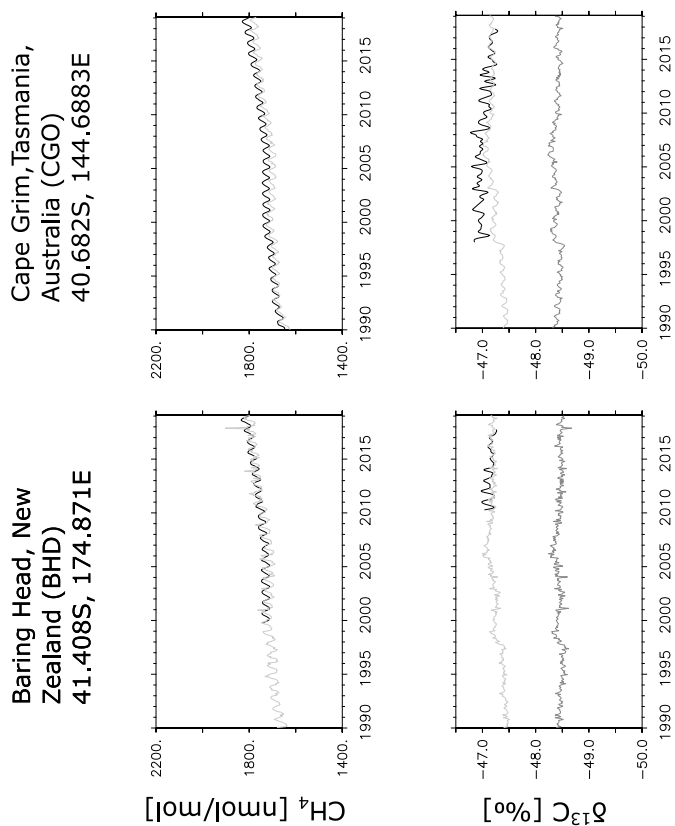


Figure A.14: Comparison of the SDISO-base-c (in light gray) and SDISO-base-v (in dark gray) monthly averaged CH_4 mixing ratios and $\delta^{13}\text{C}$ with observations (in black) at different mid latitudinal (right panels) and high latitudinal (left panels) sampling sites on the Southern Hemisphere. Note that the SDISO-base-c and the SDISO-base-v simulations only differ in their $\delta^{13}\text{C}$. CH_4 mixing ratios are the same.

A.3.3 Sensitivity studies towards shale gas emissions

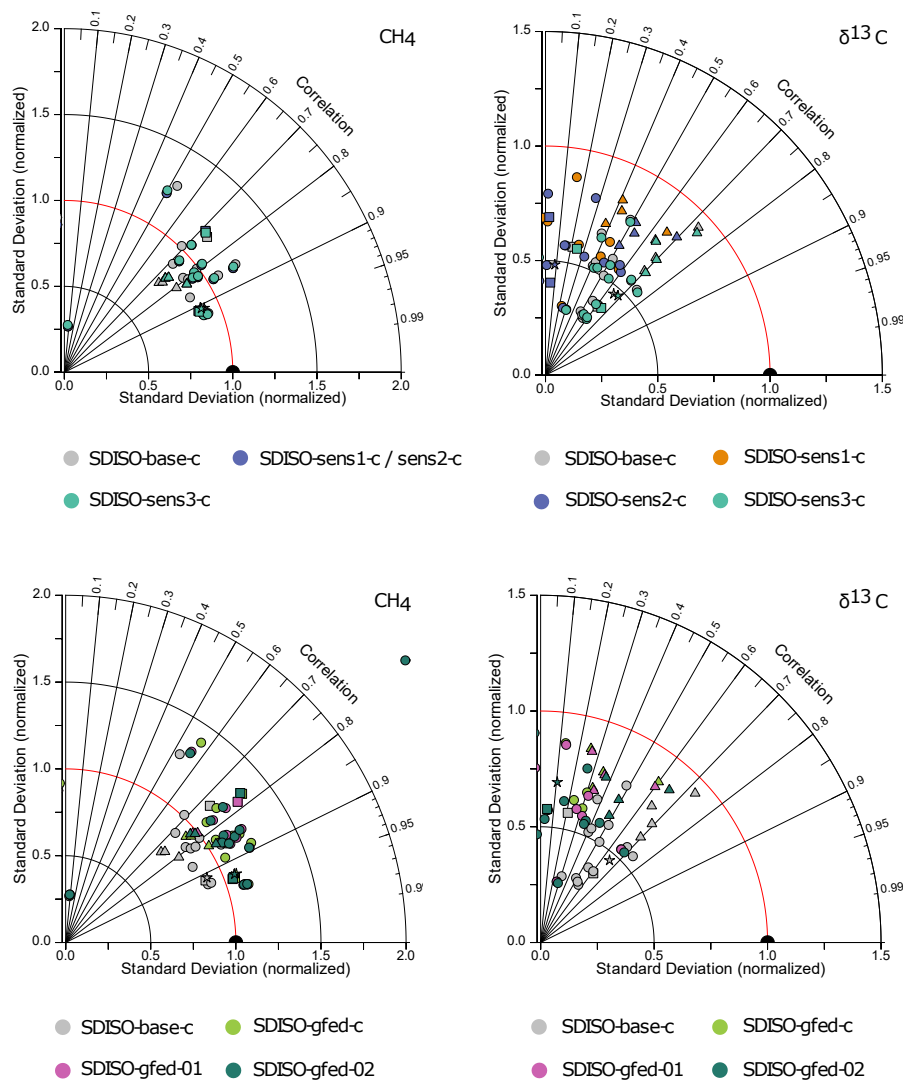


Figure A.15: The Taylor diagram illustrates the statistical comparison between the surface CH_4 mixing ratios (left panel) and $\delta^{13}\text{C}(\text{CH}_4)$ (right panel) of the SDISO-base-c and SDISO-sens (upper panels) or SDISO-gfed (lower panels) simulations and those of the observations at single sampling sites between 2008 and 2019. The different symbols describe the climate zones where the sampling sites are located, i.e.: Northern high latitudes (triangle), northern mid latitudes and tropics (circle), southern mid latitudes and tropics (square) and southern high latitudes (star). I used only those sampling sites, where both, CH_4 mixing ratios and $\delta^{13}\text{C}(\text{CH}_4)$ measurements are available (indicated by the orange dots on the map in Fig. 6.7). Note, that for many sampling sites the observational data is not available throughout the whole time period.

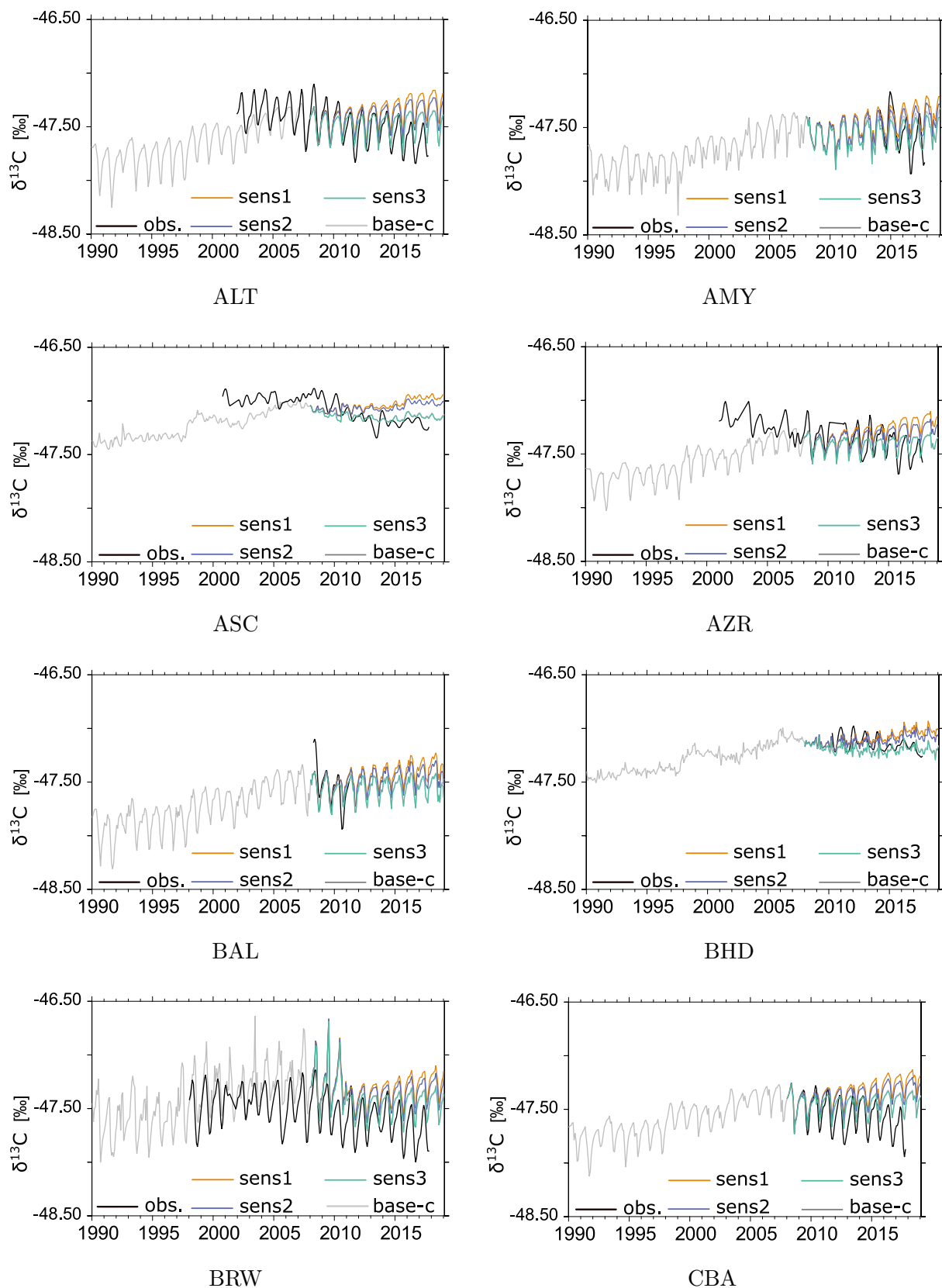


Figure A.16: Comparison of the SDISO-base-c (in light gray) and SDISO-sens (coloured) monthly averaged $\delta^{13}\text{C}$ with observations (in black) at different sampling sites.

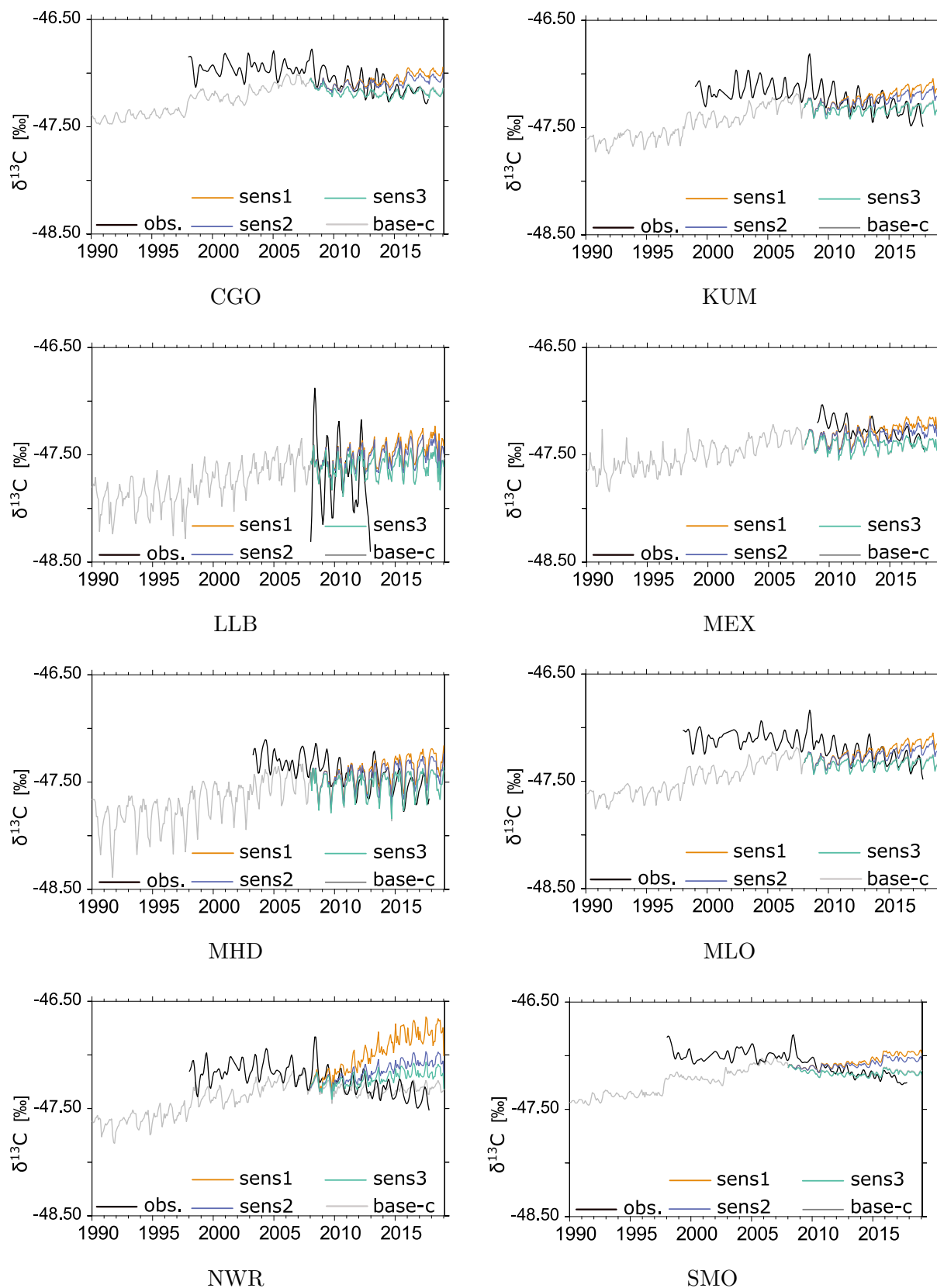


Figure A.17: Comparison of the SDISO-base-c (in light gray) and SDISO-sens (coloured) monthly averaged $\delta^{13}\text{C}$ with observations (in black) at different sampling sites.

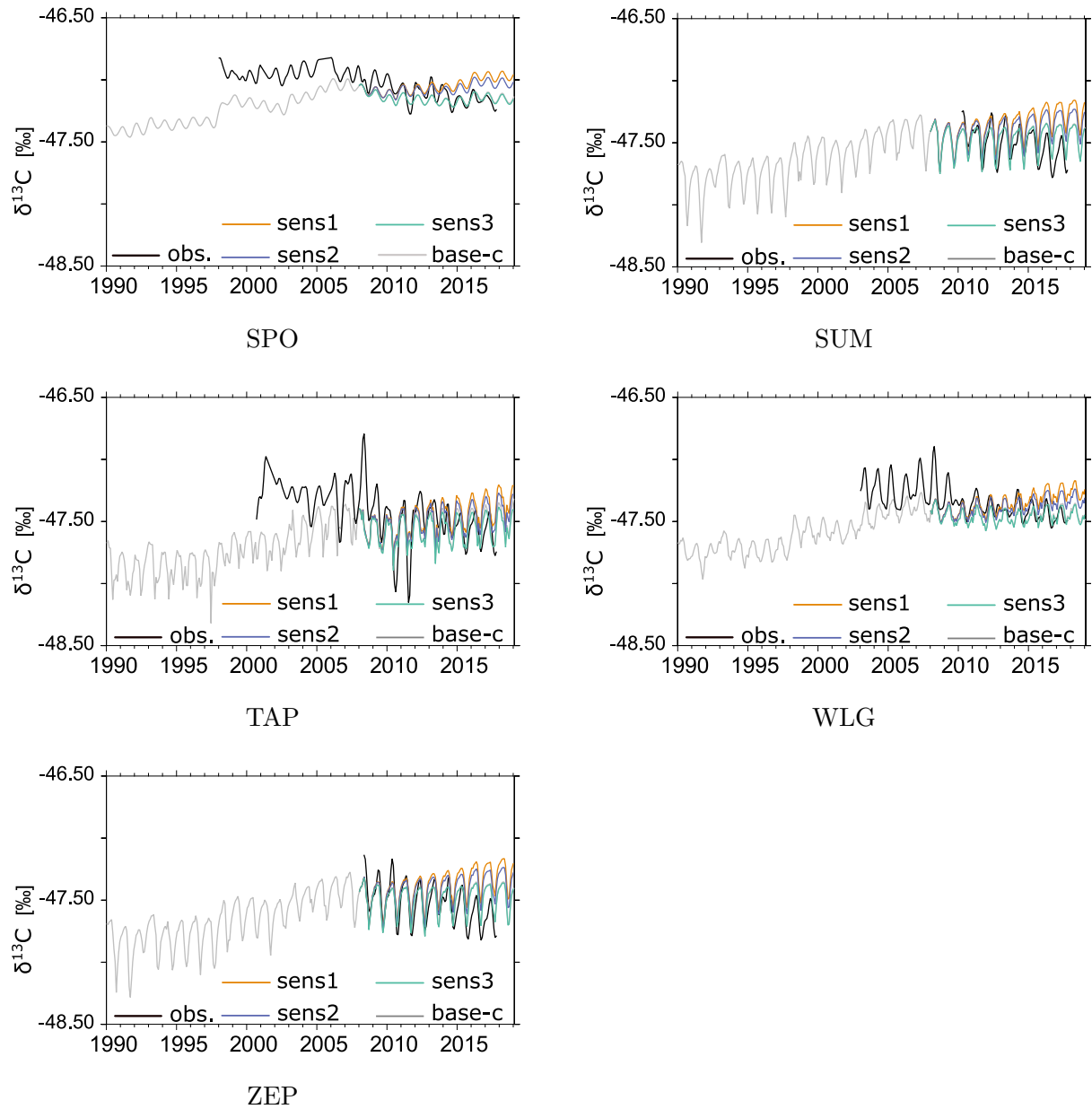


Figure A.18: Comparison of the SDISO-base-c (in light gray) and SDISO-sens (coloured) monthly averaged $\delta^{13}\text{C}$ with observations (in black) at different sampling sites.

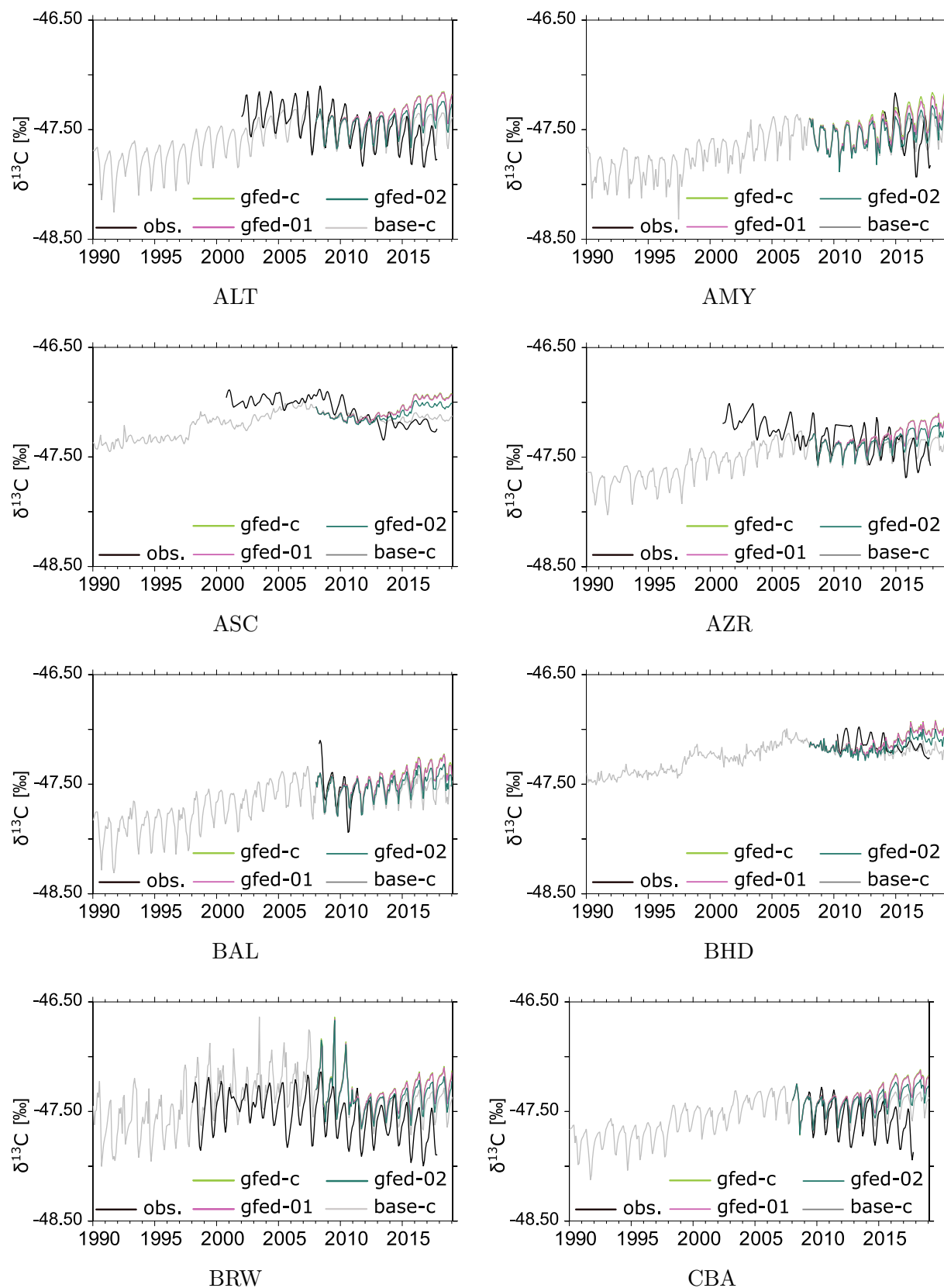


Figure A.19: Comparison of the SDISO-base-c (in light gray) and SDISO-gfed (coloured) monthly averaged $\delta^{13}\text{C}$ with observations (in black) at different sampling sites.

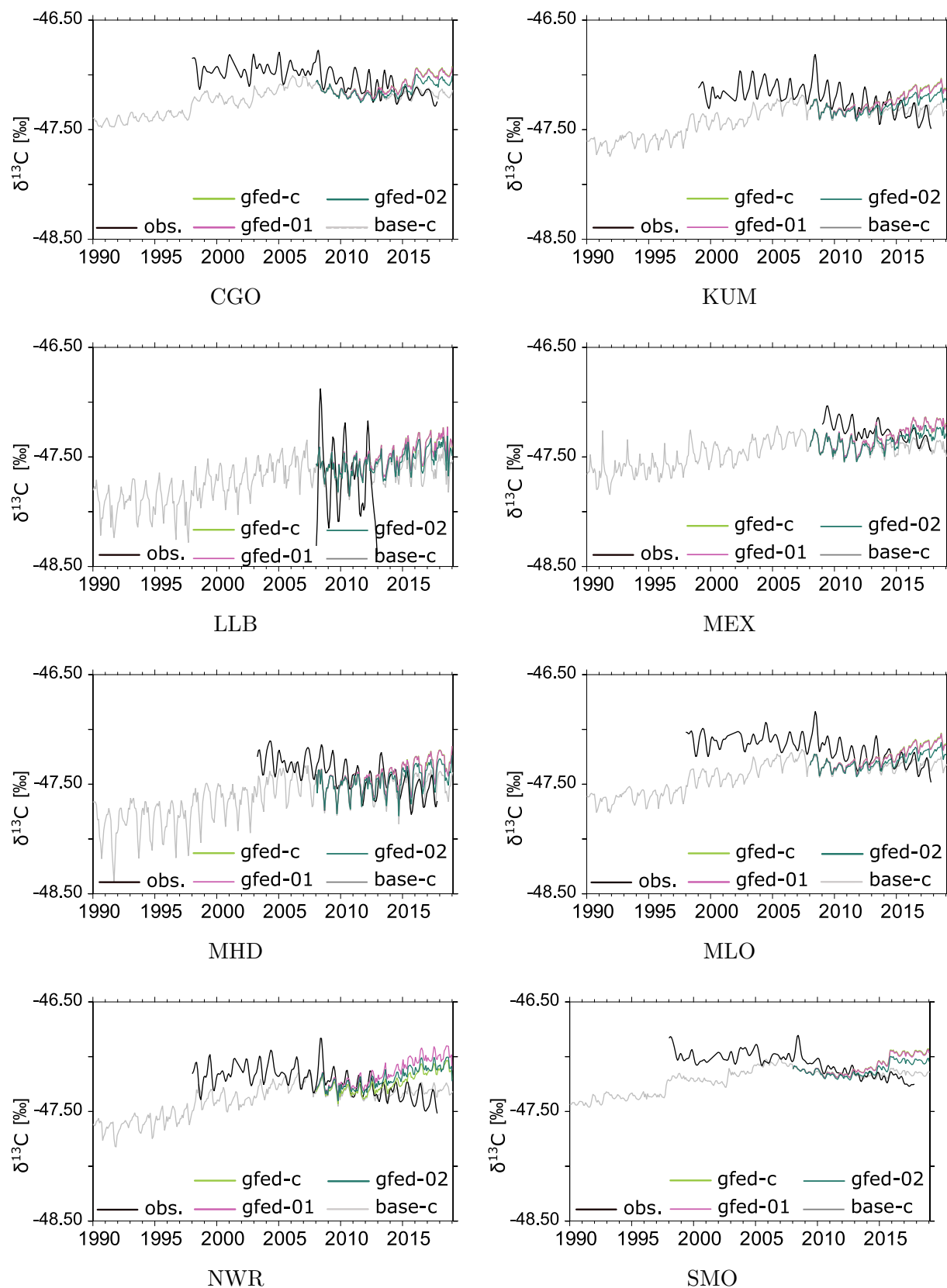


Figure A.20: Comparison of the SDISO-base-c (in light gray) and SDISO-gfed (coloured) monthly averaged $\delta^{13}\text{C}$ with observations (in black) at different sampling sites.

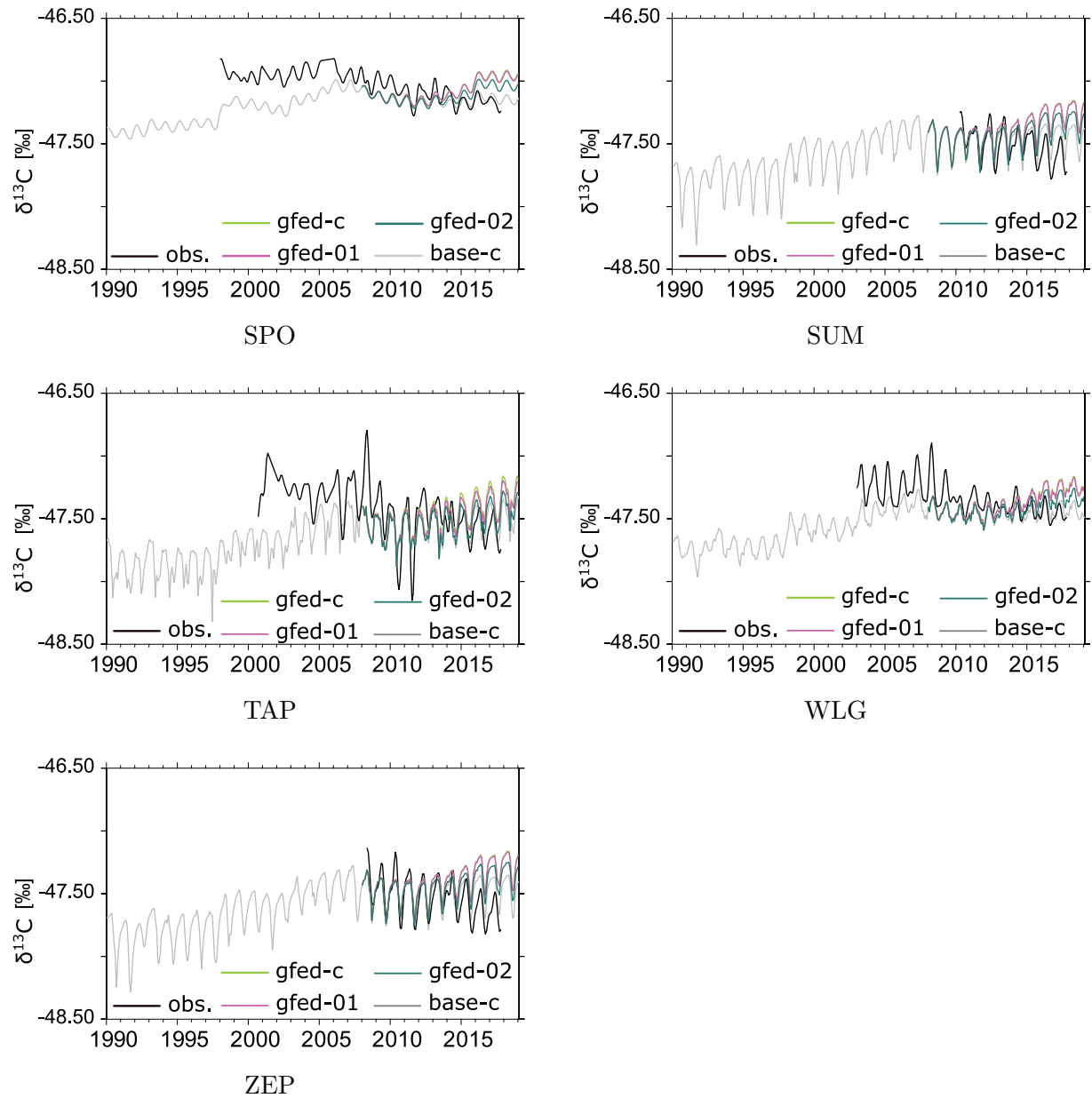


Figure A.21: Comparison of the SDISO-base-c (in light gray) and SDISO-gfed (coloured) monthly averaged $\delta^{13}\text{C}$ with observations (in black) at different sampling sites.

Danksagung

Ich möchte mich ganz herzlich bei Professor Hans Peter Schmid für sein Interesse an meiner Arbeit, die Anregung für neue Forschungsfragen und sein wertvolles Feedback bedanken. Professor Robert Sausen danke ich für seine vielen Ratschläge und die kontinuierliche Unterstützung während des gesamten Projekts.

Ein besonderer Dank gilt meinem Betreuer Dr. Patrick Jöckel, ohne dessen Unterstützung und Ermutigung dieses Projekt nicht möglich gewesen wäre. Ich danke ihm für die viele Zeit die er sich genommen hat, um meine Fragen zu beantworten und Probleme zu besprechen. Seine Anleitung während der gesamten Zeit, sowie die wertvollen Ideen und Anmerkungen haben viel zu dieser Arbeit beigetragen.

Bei meinen Kolleginnen und Kollegen des Instituts für Physik der Atmosphäre (DLR) und insbesondere bei der Abteilung Erdsystem Modellierung möchte ich mich für die schöne Zeit und tollen Gespräche bedanken. Ein besonderer Dank gilt an dieser Stelle Franziska für ihre fachliche Begleitung und ihr Interesse an meiner Arbeit, sowie Mariano für das Beantworten unzähliger MECO(n) Fragen. Ich möchte mich auch bei allen Beteiligten der CoMet Kamapgne bedanken. Insbesondere bei Alina, Axel und Michal für die Zusammenarbeit und die Bereitstellung der CoMet Messdaten.

Ein großer Dank gilt außerdem Marius, Laura und Sheena, ohne die unsere gemeinsame Zeit im Büro nur halb so schön gewesen wäre. Danke an Laura, die immer ein offenes Ohr hat, an Sheena, die sich viel Zeit zum Korrekturlesen genommen hat, und an Marius für unterhaltsame Tetrispausen und den unerschöpflichen Vorrat an Schokolade. Ich danke auch Monica und Joggy für die großartige Gelegenheit am Ammersee ein Schreibexil einzurichten.

Ich danke den vielen Menschen die mich in den letzten Jahren sowohl privat als auch im Studium begleitet haben. Ohne deren Inspiration und Unterstützung hätte ich nur halb so viel Freude auf meinem Weg bis zu dieser Arbeit gehabt. Danke an Fiona für die Ermutigung zu Beginn meiner Zeit als Doktorandin. Danke an Max und Kathi für die vielen schönen Abendessen. Danke an Katrina für aufmunternde Gespräche und Kaffeepausen während der Homeoffice-Zeit. Ein besonderer Dank geht an Lena, die mir in allen Phasen beistand. Und an Bas für viele Stunden Zuhören, noch mehr Geduld und das Fachsimpeln über die schönste Farbkombination meiner Plots.

Ganz besonders möchte ich mich bei meiner Familie für ihre unendliche Unterstützung bedanken. Insbesondere bei meinen Eltern, für ihr Vertrauen in mich und für die Möglichkeit und Freiheit meinen eigenen Weg zu gehen und die Welt zu entdecken.